

Ministry of Education and Science of the Russian Federation  
Saint Petersburg National Research University of Information  
Technologies, Mechanics, and Optics

***NANOSYSTEMS:***  
***PHYSICS, CHEMISTRY, MATHEMATICS***

**2020, volume 11(5)**

**Наносистемы: физика, химия, математика**

**2020, том 11, № 5**



# NANOSYSTEMS:

## PHYSICS, CHEMISTRY, MATHEMATICS

### ADVISORY BOARD MEMBERS

**Chairman:** V.N. Vasiliev (*St. Petersburg, Russia*),  
V.M. Buznik (*Moscow, Russia*); V.M. Ievlev (*Voronezh, Russia*), P.S. Kop'ev (*St. Petersburg, Russia*), N.F. Morozov (*St. Petersburg, Russia*), V.N. Parmon (*Novosibirsk, Russia*),  
A.I. Rusanov (*St. Petersburg, Russia*),

### EDITORIAL BOARD

**Editor-in-Chief:** I.Yu. Popov (*St. Petersburg, Russia*)

#### Section Co-Editors:

Physics – V.M. Uzdin (*St. Petersburg, Russia*),  
Chemistry, material science – V.V. Gusarov (*St. Petersburg, Russia*),  
Mathematics – I.Yu. Popov (*St. Petersburg, Russia*).

#### Editorial Board Members:

V.M. Adamyan (*Odessa, Ukraine*); O.V. Al'myasheva (*St. Petersburg, Russia*);  
A.P. Alodjants (*Vladimir, Russia*); S. Bechta (*Stockholm, Sweden*); J. Behrndt (*Graz, Austria*);  
M.B. Belonenko (*Volgograd, Russia*); A. Chatterjee (*Hyderabad, India*); S.A. Chivilikhin  
(*St. Petersburg, Russia*); A.V. Chizhov (*Dubna, Russia*); A.N. Enyashin (*Ekaterinburg, Russia*),  
P.P. Fedorov (*Moscow, Russia*); E.A. Gudilin (*Moscow, Russia*); V.K. Ivanov  
(*Moscow, Russia*), H. Jónsson (*Reykjavik, Iceland*); A.A. Kiselev (*Durham, USA*);  
Yu.S. Kivshar (*Canberra, Australia*); S.A. Kozlov (*St. Petersburg, Russia*); P.A. Kurasov  
(*Stockholm, Sweden*); A.V. Lukashin (*Moscow, Russia*); I.V. Melikhov (*Moscow, Russia*);  
G.P. Miroshnichenko (*St. Petersburg, Russia*); I.Ya. Mittova (*Voronezh, Russia*); Nguyen  
Anh Tien (*Ho Chi Minh, Vietnam*); V.V. Pankov (*Minsk, Belarus*); K. Pankrashkin (*Orsay, France*);  
A.V. Ragulya (*Kiev, Ukraine*); V. Rajendran (*Tamil Nadu, India*); A.A. Rempel  
(*Ekaterinburg, Russia*); V.Ya. Rudyak (*Novosibirsk, Russia*); D Shoikhet (*Karmiel, Israel*);  
P Stovicek (*Prague, Czech Republic*); V.M. Talanov (*Novocherkassk, Russia*); A.Ya. Vul'  
(*St. Petersburg, Russia*); A.V. Yakimansky (*St. Petersburg, Russia*), V.A. Zagrebnev  
(*Marseille, France*).

#### Editors:

I.V. Blinova; A.I. Popov; A.I. Trifanov; E.S. Trifanova (*St. Petersburg, Russia*),  
R. Simoneaux (*Philadelphia, Pennsylvania, USA*).

**Address:** University ITMO, Kronverkskiy pr., 49, St. Petersburg 197101, Russia.

**Phone:** +7(812)312-61-31, **Journal site:** <http://nanojournal.ifmo.ru/>,

**E-mail:** [popov1955@gmail.com](mailto:popov1955@gmail.com)

### AIM AND SCOPE

The scope of the journal includes all areas of nano-sciences. Papers devoted to basic problems of physics, chemistry, material science and mathematics inspired by nanosystems investigations are welcomed. Both theoretical and experimental works concerning the properties and behavior of nanosystems, problems of its creation and application, mathematical methods of nanosystem studies are considered.

The journal publishes scientific reviews (up to 30 journal pages), research papers (up to 15 pages) and letters (up to 5 pages). All manuscripts are peer-reviewed. Authors are informed about the referee opinion and the Editorial decision.

# CONTENT

**FROM THE EDITORIAL BOARD** 500

## **MATHEMATICS**

M.S. Duraisami, K. Parasuraman

**Computational analysis of some degree based topological indices of cubic structured tungsten trioxide [l,m,n] nanomultilayer** 501

## **PHYSICS**

V.D. Krevchik, A.V. Razumov, P.V. Krevchik,

M.B. Semenov, A.V. Shorokhov, A.P. Shkurinov,

I.A. Ozheredov, Y.H. Wang, T.R. Li, A.K. Malik

**Influence effect of an external electric field and dissipative tunneling on intracenter optical transitions in quantum molecules with  $D_2$  states** 510

## **CHEMISTRY AND MATERIAL SCIENCE**

Jitendra Borse, Arun Garde

**Influence of complexing agent, pH of solution and thickness on morphological and optical properties of ZnS particles layer prepared by electrochemical deposition technique** 519

N.S. Kozhevnikova, L.N. Maskaeva, E.E. Lekomtseva, L.A. Pasechnik,

A.Yu. Chufarov, O.A. Lipina, A.N. Enyashin, V.F. Markov

**A facile low-temperature deposition of Sn-rich tin (II) monosulfide colloid particles** 529

B. Abadllah, B. Assfour, M. Kakhia, Ali Bumajdad

**HRTEM, XPS and XRD characterization of ZnS/PbS nanorods prepared by thermal evaporation technique** 537

Sanjay Prakash Kaushik, Satyendra Singh, Ram-Krishna Thakur

**Stability and electronic properties of ZnSe nanowires: An ab initio approach** 546

Yu.V. Rudyak, F.A. Doronin, G.O. Rytikov, E.K. Filyugina, V.G. Nazarov

**Nanotexture effect of the fiber surface on the sorption capacity of nonwoven fabrics** 553

A.V. Dmitriev, E.V. Vladimirova, M.A. Semkin, A.V. Korolev

**Spin-glass transition in porous spheres  $\text{BiFeO}_3$**  565

E.V. Vladimirova, O.I. Gyrdasova, A.V. Dmitriev <b>Synthesis of nanostructured hollow microspheres of vanadium (III, V) oxides</b>	572
M.S. Duraisami, K. Parasuraman <b>High sensitive room temperature ammonia sensor based on dopant free m-WO<sub>3</sub> nanoparticles: Effect of calcination temperature</b>	578
Deepika Pal, Anil Kumar Choubey <b>Photocatalytic properties of persistent luminescent rare earth doped SrAl<sub>2</sub>O<sub>4</sub> phosphor under solar radiation</b>	590
K.D. Martinson, D.D. Sakhno, V.E. Belyak, I.B. Panteleev, I.V. Kochurov, Yu.E. Zevatskiy, V.I. Popkov <b>Synthesis of Ni<sub>0.4</sub>Zn<sub>0.6</sub>Fe<sub>2</sub>O<sub>4</sub> spinel ferrite and microwave adsorption of related polymer composite</b>	595
E.V. Polyakov, R.R. Tzukanov, I.V. Volkov, L.Yu. Buldakova, I.V. Baklanova, O.A. Lipina, V.P. Zhukov, Yu.V. Kuznetsova, A.P. Tutyunnik, M.A. Maximova <b>Synthesis and comparative photocatalytic activity of CuO layers on SiO<sub>2</sub> substrates</b>	601
A.A. Lobinsky, M.V. Kaneva <b>Synthesis Ni-doped CuO nanorods via successive ionic layer deposition method and their capacitive performance</b>	608
<b>Information for authors</b>	615

## FROM THE EDITORIAL BOARD



### Obituary

Dr. Sergey A. Chivilikhin (1947 – 2020)

The Editorial Board regrettably announce that Doctor Sergey A. Chivilikhin, a member of the Editorial Board of the journal, passed away on September 29, 2020.

Doctor Chivilikhin was an internationally known and respected physicist. His scientific interests were very wide. He obtained remarkable results in many fields from viscous flows to quantum communications. He was consummate specialist in the modeling of physical processes. All colleagues were sure that he could create a good model for any phenomenon. He was a longtime employee at Saint Petersburg National Research University ITMO, where he was an excellent teacher. His enthusiasm and knowledge attracted many students and young scientists. He was very popular with students of all subjects due to his enthusiasm and knowledge and, because of his great commitment as a supervisor of numerous bachelor and master theses, he was highly sought as a mentor. He demonstrated students and young scientists that science is not only hard labor but also could be a tremendous pleasure. As one of his enduring legacies, he was one of the founders of the journal “Nanosystems: Physics, Chemistry, Mathematics”.

Above all, however, he will be remembered for his assistance to those colleagues and students having problems, his patience and his openness to listen to all the difficulties encountered by his students and colleagues. The loss of Sergey leaves a large gap in our community.

In conclusion, we would like to offer our most sincere condolences to his family.

## Computational analysis of some degree based topological indices of cubic structured tungsten trioxide [l,m,n] nanomultilayer

M. S. Duraisami\*, K. Parasuraman

PG & Research Department of Physics, Poompuhar College (Autonomous), Melaiyur – 609107, Tamilnadu, India  
 Affiliated to Bharathidasan University, Tiruchirappalli

\*tharmamithran@gmail.com

PACS 02.10.Ox, 61.48.-c

DOI 10.17586/2220-8054-2020-11-5-501-509

Topological indices are numerical invariants of molecular graphs and are beneficial for predicting the physicochemical properties of chemical compounds. In this view, a topological index can be considered as a score function which maps each molecular structure to a real number. In the past two decades, tungsten trioxide ( $\text{WO}_3$ ) nanostructures have been extensively studied for their diverse technological applications. They have received greater attention by researchers, owing to their novel functionalities and unique physicochemical properties. We, for the first time, compute the Sum Connectivity index, Variable Sum index, ABC index, Harmonic index, Ordinary Geometric Arithmetic index, SK indices, Forgotten index, Symmetric Division index, Augmented Zagreb index, Inverse sum index, IRM index, Modified second Zagreb index, Inverse Randić index, Albertson and Bell topological indices of cubic structured  $\text{WO}_3$  [l, m, n] nanomultilayer. We also present a graphical analysis of all indices with respect to the dimension of this nanomultilayer.

**Keywords:** topological index, chemical graph, cubic  $\text{WO}_3$ , nanomultilayer.

*Received:* 31 August 2020

*Revised:* 8 September 2020

### 1. Introduction

Let  $G = (V, E)$  be a molecular graph of order  $p$  (number of vertices) with size  $q$  (number of edges). Denote  $uv$ , the link (edge) joining the nodes (vertices)  $u$  and  $v$ . The degree of a vertex  $u \in V(G)$  is denoted by  $d_u$  and is the number of vertices that are adjacent to  $u$ . Molecular graphs are a unique type of chemical graphs, which describe the constitution of molecules [1]. Molecular graph considered in this article is finite, undirected, connected, loopless, and without multiple edges.

#### 1.1. Background

Testing of new reagents in chemical physics and physical chemistry is always a major concern. One of the prominent strategies to address this issue is the graph theoretic approach, which performs to model the characteristics of novel and proposed chemical compounds to save time and costs. Chemical graph theory plays a crucial role in molecular topology and computational nanomaterials to determine the structure of molecular graphs [2–4]. Topological characterization is a standout approach provided by chemical graph theory to predict certain physicochemical properties like molecular weight, density, risk assessment, toxicity and determine regularity decisions and so forth [2–6]. Topological indices (molecular descriptors) are numerical values associated with chemical constitution and are applied in the development of quantitative structure-activity relationships (QSARs), Quantitative Structure Property Relationships (QSPRs) and Quantitative Structure-Toxicity Relationships (QSTRs) [7, 8]. They preserve the symmetry of molecular structures and act as a bridging tool between mathematics and chemistry. Until recently, several kinds of topological indices are introduced like distance-based, degree-based and spectrum-based indices and so on. Among them, degree based topological indices are robust in nature, because they can be directly derived from the structure of chemical graphs. The concept of topological indices in chemical graph theory was first introduced by Weiner in 1947, to predict the heats of formation, chromatographic retention time, boiling point and strain energy [2]. In recent times, many authors employed topological indices of various nanostructures involving Pent-Heptagonal Nanosheets [9], poly-hex nanotubes [10] and nanostar dendrimers [11]. For more about the significance of topological indices in molecular chemistry and the graph theoretical tools used in this article, we refer [12, 13] and references therein.

## 1.2. Degree based Topological Indices

In this part, we shall enumerate some degree-based topological indices (as explicated in Table 3) that will be needed in the main result section. Gutman et al. [3] established a pair of topological indices namely, first Zagreb ( $M_1(G)$ ) and second Zagreb ( $M_2(G)$ ) indices for predicting total  $\pi$  electron energy of compounds. In mathematical chemistry, there is a large number of topological indices of the form

$$TI = TI(G) = \sum_{x_i x_j \in E(G)} F(d_i, d_j).$$

Another important degree-based topological index called Randić index (connectivity index or branching index), which is given by Milan Randić in 1975 [32]. It has found manifold applications in drug designing field. Later, Amić et al. [29] proposed the generalized version of Inverse Randić index (for any real number  $\alpha$ ). For  $\alpha = -1$ ,  $RR_\alpha$  turns out to be a second Zagreb index; for  $\alpha = 1$ ,  $RR_\alpha$  will be a modified second Zagreb index and  $RR_\alpha$  becomes a Reciprocal Randić index if  $\alpha = -\frac{1}{2}$ .

## 1.3. A brief sketch on $WO_3$ nanomaterial

Today has witnessed the prompt advancements in nanotechnology, which keeps in pace with the emergence of novel nanomaterials and interdisciplinary approaches.  $WO_3$  is one such nanomaterial which has drawn considerable attention of research community due to their various applications in chemical sensors, field emission devices, electrochromic, photocatalysts [33] and photo-electrochemical water splitting [34]. For more details we refer [35] and references therein.

## 1.4. Proposed work and organization

Motivated by the formation of  $WO_3$  nanomultilayer reported in [36], here, we construct a molecular graph for cubic  $WO_3$  nanomultilayer and compute certain degree based topological indices to reveal its mathematical aspects. The partitions of the edge set and the vertex set of cubic  $WO_3$  nanomultilayer have been well discussed in Section 2. In Section 3, we established our new results about cubic  $WO_3$  nanomultilayer in terms of the parameters  $l$ ,  $m$  and  $n$ . In order to disclose the trends of dependency among the values of indices and the dimensions of the nanomultilayer, some relevant graphical representations are provided in Section 4.

## 2. Methods

It is evident from Fig. 1 and Fig. 2 that, each tungsten atom is closely bound to six oxygen atoms, and each oxygen atom and two tungsten atoms are nearly adjacent, then each tungsten atom is a sub-neighbor with another one. As seen in Fig. 2(a), the intervening portion between two horizontal linear arrangements of connected tungsten trioxide molecules can be taken as a single row ( $l = 1$ ). The same vertical alignment of this pattern forms a single column ( $m = 1$ ) and these two parameters joined together to form a single layer ( $n = 1$ ). Consider a 3-D cubic system of  $WO_3$  nanomultilayer with  $l$  rows,  $m$  columns and  $n$  layers, and each layer contains  $l$  rows and  $m$  columns as shown in Fig. 3. Such a typical molecular system, atoms and bonds can be represented by vertices and edges, respectively. We reserve the notation c- $WO_3$  [ $l, m, n$ ] for cubic  $WO_3$  nanomultilayer, where  $l, m, n \geq 1$ . The construction of c- $WO_3$  [1, 1, 2] and c- $WO_3$  [1, 3, 2] are illustrated in Fig. 2(b) and Fig. 2(c).

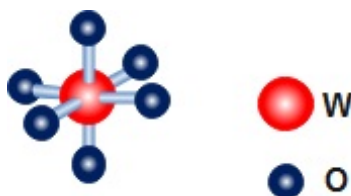


FIG. 1. A 3-D structure of  $WO_3$  molecule

Observe that, c- $WO_3$  [ $l, m, n$ ] consist of 1,2 and 6 degrees vertices, and the total number of vertices are  $4lmn + 6n + 15(ln + mn) + lm + l + m + 1$ . Further, we partition the edge set of c- $WO_3$  [ $l, m, n$ ] into two disjoint sub-classes with respect to the degrees of the end vertices of each edge namely,  $\{1,6\}$  and  $\{2,6\}$ , and the total number of edges are  $6n(lm + l + m + 1)$ . In other words, all surface O atoms bound to W atoms can be shown by the edge type  $E_{(1,6)}$

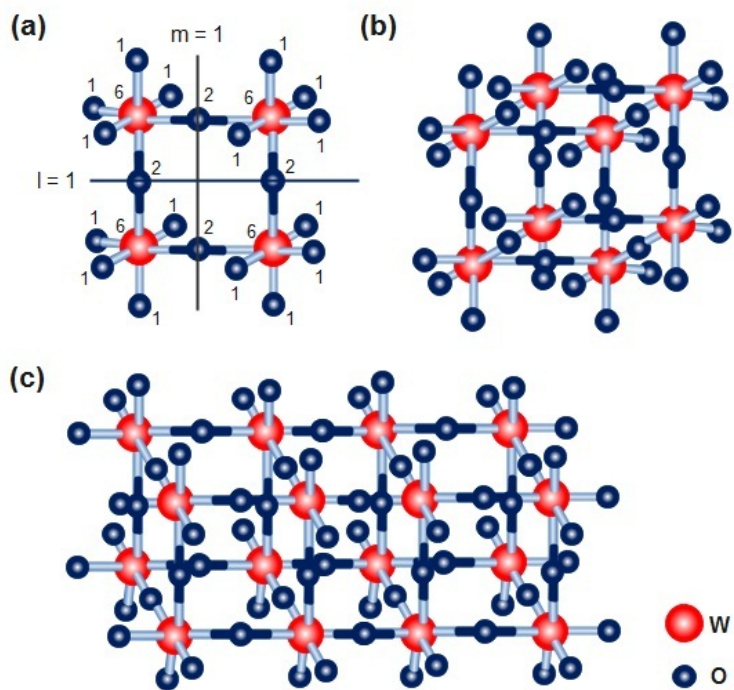


FIG. 2. (a) Vertices of  $c\text{-WO}_3$  [1, 1, 1] labelled with degrees  $\{1,2,6\}$ ; (b)  $c\text{-WO}_3$  [1, 1, 2] and (c)  $c\text{-WO}_3$  [1, 3, 2] nanomultilayer

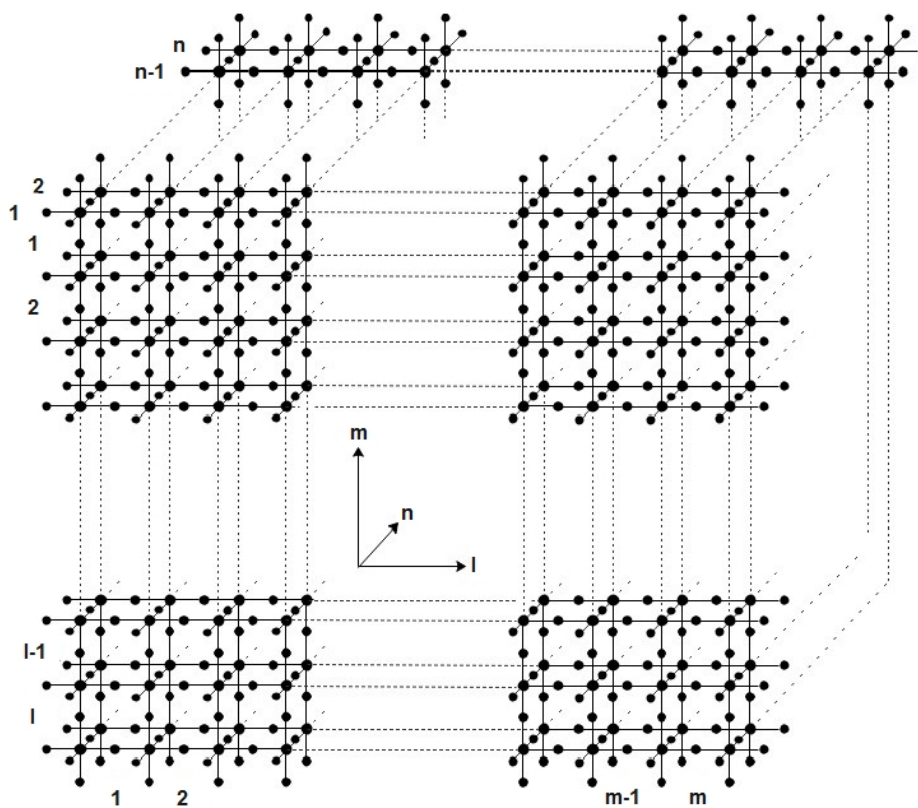


FIG. 3. Molecular graph of cubic  $\text{-WO}_3$  [ $l, m, n$ ] nanomultilayer

TABLE 1. Edge partition of c-WO<sub>3</sub> [l, m, n] nanomultilayer based on the degree of end vertices of each edge

Type of edges	$E_{(1, 6)}$	$E_{(2, 6)}$
$(d_u, d_v), u, v \in E(G)$	(1, 6)	(2, 6)
Number of Edges $ E_{(d_u, d_v)} $	$2(lm + mn + ln + l + m + 2n + 1)$	$6lmn + 4(ln + mn) + 2n - 2(lm + l + m + 1)$

TABLE 2. Vertex partition of c-WO<sub>3</sub> [l, m, n] nanomultilayer based on the degree of end vertices of each edge

Vertex partition $V_{d_u}$	$V_1$	$V_2$	$V_6$
$d_u, u \in V(G)$	1	2	6
Number of Vertices $ V_{d_u} $	$2(lm + mn + ln + l + m + 2n + 1)$	$3lmn + 2(ln + mn) - (lm + l + m + n + 1)$	$(lm + l + m + 1)n$

and the intermediated O atoms connected with W atoms are represented by the edge type  $E_{(2, 6)}$ . Table 1 and Table 2 represent the degree based edge partition and vertex partition of c-WO<sub>3</sub> [l, m, n].

The edge set c-WO<sub>3</sub> [l, m, n] nanomultilayer with  $l, m, n \geq 1$  has following two partitions:

$$E_{(1, 6)} = \{e = uv \in E(c - \text{WO}_3 [l, m, n]) | d_u = 1, d_v = 6\}$$

and

$$E_{(2, 6)} = \{e = uv \in E(c - \text{WO}_3 [l, m, n]) | d_u = 2, d_v = 6\}.$$

The vertex set of c-WO<sub>3</sub> [l, m, n] nanomultilayer with  $l, m, n \geq 1$  has following three partitions:

$$V_1 = \{v \in V(c - \text{WO}_3 [l, m, n]) | d_v = 1\}, \quad V_2 = \{v \in V(c - \text{WO}_3 [l, m, n]) | d_v = 2\}$$

and

$$V_6 = \{v \in V(c - \text{WO}_3 [l, m, n]) | d_v = 6\}.$$

### 3. Main results

**Theorem 3.1.** Let c-WO<sub>3</sub> [l, m, n] be the cubic structured WO<sub>3</sub> nanomultilayer of dimensions l, m, and  $n \geq 1$ . Then

(1)

$$\text{SCI}(c - \text{WO}_3 [l, m, n]) = \chi(c - \text{WO}_3 [l, m, n]) = \frac{2(lm + mn + nl + l + m + 2n + 1)}{\sqrt{7}} + \frac{6lmn + 4(ln + mn) + 2n - 2(lm + l + m + 1)}{2\sqrt{2}}.$$

(2)

$$\chi_\alpha(c - \text{WO}_3 [l, m, n]) = 2(lm + mn + nl + l + m + 2n + 1)(7)^\alpha + (6lmn + 4(ln + mn) + 2n - 2(lm + l + m + 1))(8)^\alpha.$$

(3)

$$\text{SEI}_\alpha(c - \text{WO}_3 [l, m, n]) = 2\alpha(lm + mn + nl + l + m + 2n + 1) + \alpha^2(3lmn + 2(ln + mn) - (lm + l + m + n + 1)) + \alpha^6(lm + l + m + 1)n,$$

where  $\alpha$  is any positive real number such that  $\alpha \neq 1$ .

(4)

$$ABC(c - WO_3 [l, m, n]) = 2\sqrt{\frac{5}{6}}(lm + mn + nl + l + m + 2n + 1) + \sqrt{\frac{1}{2}}(6lmn + 4(ln + mn) + 2n - 2(lm + l + m + 1)).$$

(5)

$$H(c - WO_3 [l, m, n]) = \frac{4}{7}(lm + mn + nl + l + m + 2n + 1) + \frac{1}{4}(6lmn + 4(ln + mn) + 2n - 2(lm + l + m + 1)).$$

(6)

$$OGA(c - WO_3 [l, m, n]) = \frac{4\sqrt{6}}{7}(lm + mn + nl + l + m + 2n + 1) + \frac{\sqrt{3}}{2}(6lmn + 4(ln + mn) + 2n - 2(lm + l + m + 1)).$$

$$(7) SK(c - WO_3 [l, m, n]) = 24lmn + 23(ln + mn) + (22n - lm) - (l + m + 1).$$

$$(8) SK_1(c - WO_3 [l, m, n]) = 36lmn + 30(ln + mn) + 6(4n - lm) - 6(l + m + 1).$$

$$(9) SK_2(c - WO_3 [l, m, n]) = 96lmn + 88.5(ln + mn) + (81n - 7.5lm) - 7.5(l + m + 1).$$

$$(10) F(c - WO_3 [l, m, n]) = 240lmn + 234(ln + mn) + 6(38n - lm) - 6(l + m + 1).$$

$$(11) SDD(c - WO_3 [l, m, n]) = 20lmn + \frac{77}{3}(ln + mn) + \frac{1}{3}(94n + 17lm) + \frac{17}{3}(l + m + 1).$$

$$(12) AZI(c - WO_3 [l, m, n]) = 48lmn + 35.456(ln + mn) + (22.912n - 12.544lm) - 12.544(l + m + 1).$$

$$(13) ISI(c - WO_3 [l, m, n]) = 9lmn + 7.714(ln + mn) + 1.29(5n - lm) - 1.29(l + m + 1).$$

$$(14) IRM(c - WO_3 [l, m, n]) = 96lmn + 114(ln + mn) + (132n - 18lm) + 18(l + m + 1).$$

$$(15) {}^m M_2(c - WO_3 [l, m, n]) = \left(\frac{1}{6}\right)(3lmn + 4(ln + mn) + (5n + lm) + (l + m + 1)).$$

(16)

$$RR_\alpha(c - WO_3 [l, m, n]) = \frac{2}{(6)^\alpha}(lm + mn + nl + l + m + 2n + 1) + \frac{1}{(12)^\alpha}(6lmn + 4(ln + mn) + 2n - 2(lm + l + m + 1)).$$

$$(17) A(c - WO_3 [l, m, n]) = 24lmn + 26(ln + mn) + 2(14n + lm) + 2(l + m + 1).$$

(18)

$$B(c - WO_3 [l, m, n]) = 2(lm + mn + nl + l + m + 2n + 1) \left(1 - \frac{12n(lm + l + m + 1)}{4lmn + 6n + 15(ln + mn) + lm + l + m + 1}\right)^2 + (3lmn + 2(ln + mn) - (lm + l + m + n + 1)) \left(2 - \frac{12n(lm + l + m + 1)}{4lmn + 6n + 15(ln + mn) + lm + l + m + 1}\right)^2 + (lm + l + m + 1)n \left(6 - \frac{12n(lm + l + m + 1)}{4lmn + 6n + 15(ln + mn) + lm + l + m + 1}\right)^2.$$

*Proof.* One can make calculations in accordance with the rules presented in Table 3.

#### 4. Index analysis and description

In this part, we present index analysis of computed indices of cubic  $WO_3 [l, m, n]$  nanomultilayer. Fig. 4(a) suggests that  $IRM$ , Albertson and Bell indices are linearly related with number of vertices in nanomultilayer of dimensions  $l, m$  and  $n$ . These three indices really correlate the tendency of irregularity in structure [27, 30, 31]. However  $B(G)$  progresses very slowly. On the other hand,  $IRM(G)$  increases sharply, indicating that the nanomultilayer structure becomes more irregular and complex as dimension increases. The graph in Fig. 4(b) illustrates the dependence of  $ABC(G)$ ,  $OGA(G)$  and  $AZI(G)$  on nanomultilayer dimension. It is now an established fact that, these indices are more sensitive to predict thermodynamic properties of compounds [18, 21, 25].

TABLE 3. Formula for degree-based topological indices of a graph  $G$ 

S. No	Topological Index	Notation	Formula of Topological Index
1.	Sum Connectivity Index [14]	$SCI(G) = \chi(G)$	$\sum_{u,v \in E(G)} \frac{1}{\sqrt{d_u + d_v}}$
2.	General Sum Connectivity Index [15]	$\chi_\alpha(G)$	$\sum_{u,v \in E(G)} (d_u + d_v)^\alpha$
3.	Variable Sum exdeg Index [16, 17]	$SEI_\alpha(G)$	$\sum_{u \in V(G)} d_u(\alpha)^{d_u}$ , and $\alpha \neq 1$
4.	Atomic Bond Connectivity Index [18]	$ABC(G)$	$\sum_{u,v \in E(G)} \sqrt{\frac{d_u + d_v - 2}{d_u \cdot d_v}}$
5.	Harmonic Index [19, 20]	$H(G)$	$\sum_{u,v \in E(G)} \frac{2}{d_u + d_v}$
6.	Ordinary Geometric Arithmetic Index [21]	$OGA(G)$	$\sum_{u,v \in E(G)} \frac{2\sqrt{d_u \cdot d_v}}{d_u + d_v}$
7.	SK Index [22]	$SK(G)$	$\sum_{u,v \in E(G)} \frac{d_u + d_v}{2}$
8.	$SK_1$ Index [22]	$SK_1(G)$	$\sum_{u,v \in E(G)} \frac{d_u \cdot d_v}{2}$
9.	$SK_2$ Index [22]	$SK_2(G)$	$\sum_{u,v \in E(G)} \left(\frac{d_u + d_v}{2}\right)^2$
10.	Forgotten Index [23]	$F(G)$	$\sum_{u,v \in E(G)} [(d_u)^2 + (d_v)^2]$
11.	Symmetric Division (Deg) Index [24]	$SDD(G)$	$\sum_{u,v \in E(G)} \left[ \frac{\min\{d_u, d_v\}}{\max\{d_u, d_v\}} + \frac{\max\{d_u, d_v\}}{\min\{d_u, d_v\}} \right]$
12.	Augmented Zagreb Index [25]	$AZI(G)$	$\sum_{u,v \in E(G)} \left(\frac{d_u \cdot d_v}{d_u + d_v - 2}\right)^3$
13.	Inverse sum (Indeg) Index [26]	$ISI(G)$	$\sum_{u,v \in E(G)} \frac{d_u \cdot d_v}{d_u + d_v}$
14.	IRM Index [27]	$IRM(G)$	$\sum_{u,v \in E(G)} (d_u - d_v)^2$
15.	Modified Second Zagreb Index [28]	${}^m M_2(G)$	$\sum_{u,v \in E(G)} \frac{1}{d_u \cdot d_v}$
16.	Inverse Randić Index [29]	$RR_\alpha(G)$	$\sum_{u,v \in E(G)} \frac{1}{(d_u \cdot d_v)^\alpha}$
17.	Albertson Index [30]	$A(G)$	$\sum_{u,v \in E(G)}  d_u - d_v $
18.	Bell Index [31]	$B(G)$	$\sum_{u \in V(G)} \left(d_u - \frac{2q}{p}\right)^2$

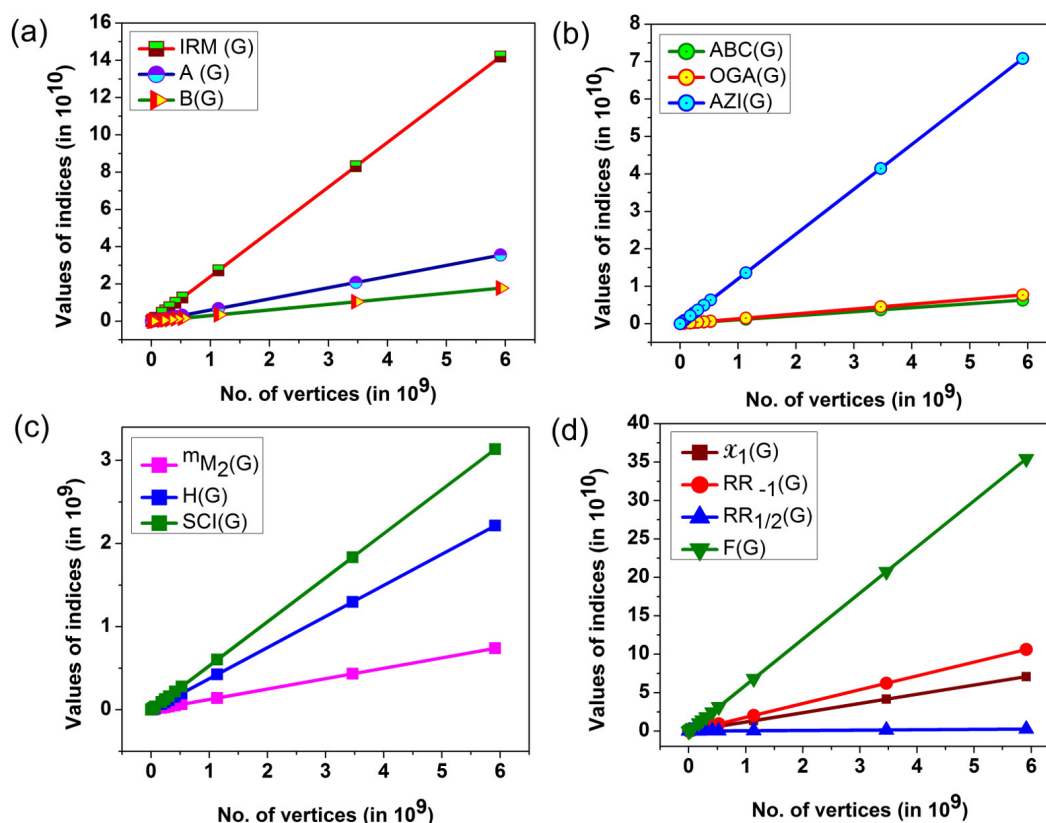


FIG. 4. Comparison of values of different topological indices (a)  $IRM(G)$ ,  $A(G)$  and  $B(G)$ ; (b)  $ABC(G)$ ,  $OGA(G)$  and  $AZI(G)$ ; (c)  ${}^mM_2(G)$ ,  $H(G)$  and  $SCI(G)$  and (d)  $\chi_1(G)$ ,  $RR_{-1}(G)$ ,  $RR_{1/2}(G)$  and  $F(G)$  with respect to number of vertices in c-WO<sub>3</sub> [l, m, n] nanomultilayer

The indices graphically represented in Fig. 4(c) and Fig. 4(d) are actually related with the total  $\pi$  electron energy of compounds [14, 15, 19, 20, 28, 29]. Clearly, Forgotten index responds promptly as compared to other indices, suggesting that which has the higher prediction capacity of this energy. It is evident from Fig. 4(c) that,  ${}^mM_2(G)$  has the least prediction potential with respect to the dimension. The indices plotted in Fig. 5(a) are considered to predict the total surface area of a structure [24, 26]. The prediction performance of  $SDD(G)$  is greater than  $ISI(G)$ . Fig. 5(b) and Fig. 6 clearly show that,  $SK_2(G)$  increases quickly as a function of dimensions [l, m, n].

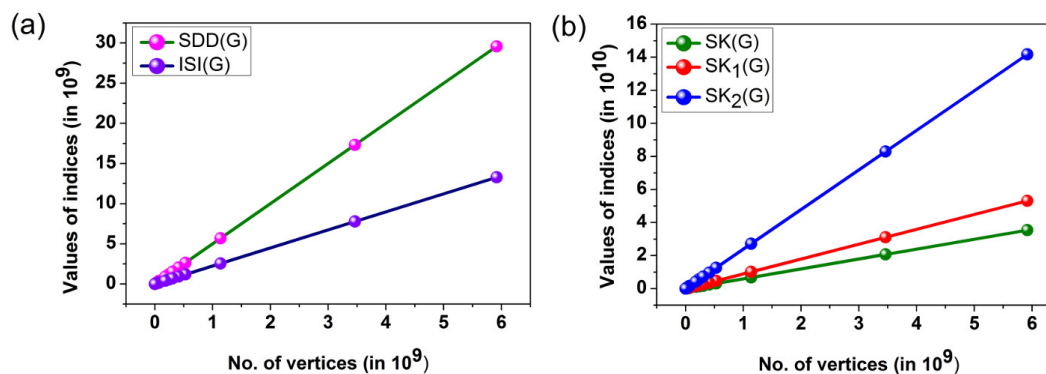


FIG. 5. Comparison of the topological indices (a)  $SDD(G)$  and  $ISI(G)$ ; (b)  $SK(G)$ ,  $SK_1(G)$  and  $SK_2(G)$  with respect to number of vertices in c-WO<sub>3</sub> [l, m, n] nanomultilayer

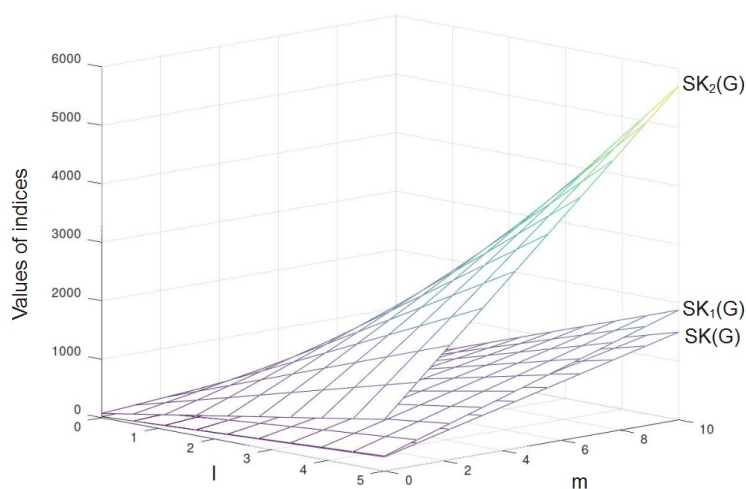


FIG. 6. A 3-D surface plot showing the comparison of  $SK(G)$ ,  $SK_1(G)$  and  $SK_2(G)$  indices with respect to number of vertices in  $c\text{-WO}_3 [l, m, n]$  monolayer; where  $l \in [1, 5]$  and  $m \in [1, 10]$  using Octave software

## 5. Conclusion

We successfully computed some important degree based topological indices for cubic structured  $\text{WO}_3 [l, m, n]$  nanomultilayer and accurate expressions have been obtained. We also presented index analysis graphically with a view to understand the dependence on the involved parameters  $[l, m, n]$ . From an applicative point of view, the indices reported in this literature are really correlated with physicochemical properties of  $\text{WO}_3$  nanomultilayer and will be helpful for people employed within nanotechnology industries.

## References

- [1] West D.B. *Introduction to Graph Theory*, 2nd Edition, Prentice Hall, 2000.
- [2] Wiener H.J. Structural determination of paraffin boiling points. *Journal of the American Chemical Society*, 1947, **69** (1), P. 17–20.
- [3] Gutman I., Trinajstić N. Graph theory, and molecular orbitals total  $\pi$ -electron energy of alternant hydrocarbons. *Chem. Phys. Lett.*, 1972, **17**, P. 535–538.
- [4] Rucker G., Rucker C. On topological indices, boiling points, and cycloalkanes. *J. Chem. Inf. Comput. Sci.*, 1999, **39**, P. 788.
- [5] Gutman I. Molecular graphs with minimal and maximal Randić indices. *Croatica Chem. Acta.*, 2002, **75**, P. 357–369.
- [6] Gutman I. Degree-based topological indices. *Croat. Chem. Acta.*, 2013, **86**, P. 351–361.
- [7] Dearden J.C. The Use of Topological Indices in QSAR and QSPR Modeling. In: *Advances in QSAR Modeling. Challenges and Advances in Computational Chemistry and Physics*, Roy K. (ed.), 2017, **24**, P. 57–88.
- [8] Samir A. Senior, Magdy D. Madbouly., Abdel-Moneim Elmassry. QSTR of the toxicity of some organophosphorus compounds by using the quantum chemical and topological descriptors. *Chemosphere*, 2011, **85** (1), P. 7–12.
- [9] Fei Deng, Xiujun Zhang, et al. Topological Indices of the Pent-Heptagonal Nanosheets  $\text{VC}_5\text{C}_7$  and  $\text{HC}_5\text{C}_7$ . *Advances in Materials Science and Engineering*, 2019, 9594549.
- [10] Munir M., Nazeer W., Rafique S., Kang S.M. MPolynomial and Degree-Based Topological Indices of Polyhex Nanotubes. *Symmetry*, 2016, **8** (12), P. 149.
- [11] Munir M., Nazeer W., Rafique S., Kang S.M. Mpolynomial and degree- based topological indices of Nano star dendrimers. *Symmetry*, 2016, **8** (9), P. 97.
- [12] Diudea M.V., Gutman I., Lorentz J. *Molecular topology*, Nova Science Publishers, Huntington, NY, 2001.
- [13] Trinajstić N. *Chemical Graph theory*, CRC Press, Boca Raton, 1992.
- [14] Zhou B., Trinajstić N. On a novel connectivity index. *J. Math. Chem.*, 2009, **46**, P. 1252–1270.
- [15] Zhou B., Luo W. A note on general Randić index. *Match Commun. Math. Comput. Chem.*, 2009, **62**, P. 155–162.
- [16] Vukičević D. Bond Additive Modeling 4. QSPR and QSAR studies of the variable Adriatic indices. *Croat. Chem. Acta.*, 2011, **84** (1), P. 87–91.
- [17] Vukičević D. Bond additive modeling 5. mathematical properties of the variable sum exdeg index. *Croat. Chem. Acta.*, 2011, **84** (1), P. 93–101.
- [18] Estrada E., Torres L., Rodriguez L., Gutman I. An atom-bond connectivity index: modelling the enthalpy of formation of alkanes. *Indian Journal of Chemistry*, 1998, **37A**, P. 849–855.
- [19] Favaron O., Maheó M., Saclé J.-F. Some eigenvalue properties in graphs (conjectures of graffiti-II). *Discrete Mathematics*, 1993, **111** (1–3), P. 197–220.
- [20] Fajtlowicz S. On conjectures of graffiti-ii. *Congr. Numer.*, 1987, **60**, P. 187–197.
- [21] Vukičević D., Furtula B. Topological index based on the ratios of geometrical and arithmetical means of end-vertex degrees of edges. *J. Math. Chem.*, 2009, **46**, P. 1369–1376.
- [22] Shighhalli V.S., Kanabur R. Computation of new degree-based topological indices of graphene. *Journal of Nanomaterials*, 2016, 4341919.

- [23] Furtula B., Gutman I. A forgotten topological index. *J. Math. Chem.*, 2015, **53**, P. 184–1190.
- [24] Vukičević D., Gašperov M. Bond additive modeling 1. Adriatic indices. *Croatica Chemica Acta*, 2010, **83** (3), P. 243–260.
- [25] Furtula B., Graovac A., Vukičević D. Augmented zagreb index. *Journal of Mathematical Chemistry*, 2010, **48** (2), P. 370–380.
- [26] Sedlar J., Stevanović D., Vasilyev A. On the inverse sum indeg index. *Discrete Applied Mathematics*, 2015, **184**, P. 202–212.
- [27] Hamzeh A., Réti T. An Analogue of Zagreb Index Inequality Obtained from Graph Irregularity Measures. *Match Commun. Math. Comput. Chem.*, 2014, **72**, P. 669–683.
- [28] Miličević A., Nikolić S., Trinajstić N. On reformulated zagreb indices. *Molecular Diversity*, 2004, **8**, P. 393–399.
- [29] Amić D., Bešlo D., et al. The vertex-connectivity index revisited. *Journal of Chemical Information and Computer Sciences*, 1998, **38** (5), P. 819–822.
- [30] Albertson M. The irregularity of a graph. *Ars. Combin.*, 1997, **46**, P. 219–225.
- [31] Bell F. A note on the irregularity of graphs. *Linear Algebra Appl.*, 1992, **161**, P. 45–54.
- [32] Randić M. Characterization of molecular branching. *Journal of the American Chemical Society*, 1975, **97** (23), P. 6609–6615.
- [33] Haidong Zheng, Jian Zhen Ou, et al. Nanostructured Tungsten Oxide-Properties, Synthesis, and Applications. *Adv. Funct. Mater.*, 2011, **21**, P. 2175–2196.
- [34] Liu X., Wang F., Wang Q. Nanostructure-based WO<sub>3</sub> Photoanodes for Photoelectrochemical Water Splitting. *Phys. Chem. Chem. Phys.*, 2012, **14**, P. 7894–7911.
- [35] Chang-Mou Wu., Saba Naseem, et al. Recent Advances in Tungsten-Oxide-Based Materials and Their Applications. *Front. Mater.*, 2019, **6** (49), P. 1–17.
- [36] Jijie Zhang, Peng Zhang, Tuo Wang, Jinlong Gong. Monoclinic WO<sub>3</sub> nanomultilayers with preferentially exposed (002) facets for photoelectrochemical water splitting. *Nano Energy*, 2015, **11**, P. 189–195.

## Influence effect of an external electric field and dissipative tunneling on intracenter optical transitions in quantum molecules with $D_2^-$ states

V. D. Krevchik<sup>1</sup>, A. V. Razumov<sup>1</sup>, P. V. Krevchik<sup>1</sup>, M. B. Semenov<sup>1</sup>, A. V. Shorokhov<sup>1,2,3,4</sup>,  
A. P. Shkurinov<sup>5,1</sup>, I. A. Ozheredov<sup>5,1</sup>, Y. H. Wang<sup>6</sup>, T. R. Li<sup>6</sup>, A. K. Malik<sup>7</sup>

<sup>1</sup>Penza State University, Krasnaya str., 40, Penza, 440026, Russia

<sup>2</sup>University of Jyväskylä, P.O. Box 35 (YFL), Jyväskylä, 40014, Finland

<sup>3</sup>National Research Mordovia State University, Saransk, 430005, Russia

<sup>4</sup>International Research Centre Mag Top, Institute of Physics, Polish Academy of Sciences,  
Aleja Lotnikow 32/46, Warsaw, PL-02668, Poland

<sup>5</sup>Institute for Problems of Laser and Information Technologies RAS, Moscow reg., 140700, Russia

<sup>6</sup>Lanzhou University, Lanzhou, 730000, China

<sup>7</sup>Multanimal Modi College Modinagar, Uttar Pradesh, 201204, India

Misha29.02.1@gmail.com

PACS 73.40.Gk, 03.65.Xp

DOI 10.17586/2220-8054-2020-11-5-510-518

In the zero-range potential model and in the effective mass approximation, dispersion equations have been obtained, that describe dependence of the average binding energies of the quasistationary g- and u-states of the  $D_2^-$ -center in the QD, as well as the widths of energy levels on the magnitude of the external electric field and the parameters of 1D-dissipative tunneling. Dips in the field dependences of the binding energies average values for quasi-stationary g- and u-states have been revealed. It is shown that the field dependences of the energy level widths for the g- and u- states of the  $D_2^-$ -center have a resonance structure at the external electric field strengths corresponding to the dips in the field dependences of the average binding energies.

In the dipole approximation, the field dependence of the probability of the electron radiative transition from a quasistationary u-state to a quasi-stationary g-state of the  $D_2^-$ -center in a QD in the presence of dissipative tunneling with the participation of two local phonon modes has been calculated. It was found that the curve of the radiative transition probability (RTP) dependence on the strength of the external electric field contains three peaks.

**Keywords:** dissipative tunneling, quantum molecules, optical transitions.

*Received:* 4 August 2020

*Revised:* 1 September 2020

*Final revision:* 7 September 2020

### 1. Introduction

In recent years there has been an increasing interest in the optical properties of tunnel-coupled semiconductor nanostructures with impurity quasistationary states (a review is given in [1]). This interest is twofold, since, on the one hand, tunneling structures with impurity states are attractive from the point of view of creating new sources of stimulated emission based on intracenter optical transitions, and the further development of optoelectronics requires the search for effective methods for controlling the lifetime of impurity states. On the other hand, the combination of optical and tunneling measurements can serve as an important tool for investigating new effects associated with electron - phonon interactions and interparticle correlations in low-dimensional systems.

The problem of tunneling decay of quasistationary states in mesosystems of different nature (in various problems of physics, chemistry, and biology) is the subject of many monographs, reviews, and articles (see, for example [2–12]). Typical shapes of potential energy surfaces are quite universal in various applications. The problem of controlled tunnel transport in low-dimensional systems is relevant and is represented by a fairly wide range of experimental works [7–13]. Currently, an alternative to quantum methods for calculating the tunneling probability can be the instanton method proposed by A. M. Polyakov [14] and S. Coleman [15] (a review is given in [2, 3]), which allows one to take into account the influence of the heat bath on the tunneling transfer process. The theory of dissipative quantum tunneling as applied to systems with Josephson contacts was developed by E. J. Legget, A. I. Larkin, Yu. N. Ovchinnikov and others [2, 3]. In the works of V. A. Bendersky, E. V. Vetoshkin and E. I. Kats (see, for example [16]) on basis of the instanton approach, E. Kats developed a quasi-classically exact method that makes it possible to solve the problem of tunneling splitting for symmetric double-well potentials in a wide energy range from the ground state to states located near the top of the barrier. The instanton method turned out to be productive in calculating the tunneling probability for QMs with  $H^-$ -like quasistationary impurity states [17], where, in combination with the zero-range

potential method, it was possible to obtain the main results in an analytical form and to analyze the effect of tunneling decay on the optical properties of QDs. The need to take into account the QM interaction in a quasi-zero-dimensional structure, as well as the influence of local phonon modes on the field dependence of the probability of dissipative tunneling, requires further development of the instanton method as applied to the optics of low-dimensional tunneling structures with impurity quasi-stationary states.

The aim of this work is to study theoretically the features of intracenter radiative transitions in quantum molecules with quasi-stationary impurity  $D_2^-$ -states associated with the presence of 1D-dissipative tunneling, taking into account the influence of two local phonon modes in an external electric field.

## 2. Model: Dispersion equations describing quasi-stationary states of the $D_2^-$ -center in a quantum dot in the presence of an external electric field and dissipative tunneling, taking into account the influence of two local phonon modes.

Let us consider the problem of bound states of an electron localized at a  $D_2^-$ -center with quasistationary g- and u-states in a QD with a parabolic confinement potential in the presence of an external electric field.

Let  $D^0$  are the centers of the ion, which are localized at points with coordinates  $R_{a1} = (x_{a1}, y_{a1}, z_{a1})$  and  $R_{a2} = (x_{a2}, y_{a2}, z_{a2})$ , here  $R_{ai} = (x_{ai}, y_{ai}, z_{ai})$  ( $i = 1, 2$ ) – rectangular Cartesian coordinates of  $D^0$ -centers in QD. Let us assume that the external electric field  $E_0$  is directed along the  $x$  coordinate axis.

The two-center point perturbation potential  $V_\delta$  can be written correctly in the form of a pseudopotential [18] as:

$$V_\delta(\mathbf{r}; \mathbf{R}_{a1}, \mathbf{R}_{a2}) = \sum_{i=1}^2 \alpha_i \delta(\mathbf{r} - \mathbf{R}_{ai}) [1 + (\mathbf{r} - \mathbf{R}_{ai}) \nabla_{\mathbf{r}}]. \quad (1)$$

Here,  $\alpha_i$  is determined by the energy  $E_i = -\hbar^2 \alpha_i^2 / (2m^*)$  of the electronic bound state at the same  $D^0$ -centers in the bulk semiconductor;  $m^*$  is the effective mass of an electron.

For one-electron states, unperturbed by impurities in a longitudinal electric field, the Hamiltonian in the chosen model of the parabolic confinement potential has the form:

$$\mathbf{H} = -\frac{\hbar^2}{(2m^*)} \nabla^2 + \frac{1}{2} m^* \omega_0^2 (x^2 + y^2 + z^2) - |e| E_0 x, \quad (2)$$

where  $\omega_0$  – characteristic frequency of the QD confinement potential;  $|e|$  – absolute value of the electron charge.

The eigenvalues  $E_{n_1, n_2, n_3}$  and the corresponding eigenfunctions  $\Psi_{n_1, n_2, n_3}(x, y, z)$  of the Hamiltonian (2) are given by expressions of the form [19]:

$$E_{n_1, n_2, n_3} = \hbar \omega_0 \left( n_1 + n_2 + n_3 + \frac{3}{2} \right) - \frac{|e|^2 E_0^2}{2m^* \omega_0^2}, \quad (3)$$

$$\Psi_{n_1, n_2, n_3}(x, y, z) = 2^{-\frac{n_1+n_2+n_3}{2}} (n_1! n_2! n_3!)^{-\frac{1}{2}} \pi^{-\frac{3}{4}} a^{-\frac{3}{2}} \exp\left(-\left[\frac{(x-x_0)^2}{a^2} + y^2 + z^2\right]\right) \times \quad (4)$$

where  $n_1, n_2, n_3 = 0, 1, 2, \dots$  are the quantum numbers corresponding to the energy levels of an oscillatory spherically symmetric potential well;  $a = \sqrt{\hbar / (m^* \omega_0)}$  is the characteristic length of the confinement potential;  $x_0 = |e| E_0 / (m^* \omega_0^2)$ ;  $H_n(x)$  are the Hermite polynomials.

In the effective mass approximation, the wave function of an electron  $\Psi_\lambda(r; R_{a1}, R_{a2})$ , localized at the  $D_2^-$ -center, satisfies the Lippmann–Schwinger equation:

$$\Psi_\lambda(\mathbf{r}; \mathbf{R}_{a1}, \mathbf{R}_{a2}) = \int d\mathbf{r}_1 G(\mathbf{r}, \mathbf{r}_1; E_\lambda) V_\delta(\mathbf{r}_1; \mathbf{R}_{a1}, \mathbf{R}_{a2}) \Psi_\lambda(\mathbf{r}_1; \mathbf{R}_{a1}, \mathbf{R}_{a2}) \quad (5)$$

and has the form of a linear combination

$$\Psi_\lambda(r; R_{a1}, R_{a2}) = \sum_{k=1}^2 \gamma_k c_k G(r; R_{ak}; E_\lambda), \quad (6)$$

where  $c_k = \lim_{\mathbf{r} \rightarrow \mathbf{R}_{ak}} [1 + (\mathbf{r} - \mathbf{R}_{ak}) \nabla_{\mathbf{r}}] \Psi_\lambda$  ( $k = 1, 2$ );  $G(\mathbf{r}, \mathbf{R}_{ak}; E_\lambda)$  is the one-electron Green's function corresponding to a source at the point  $\mathbf{R}_{ai}$  and the complex energy  $E_\lambda = \hbar^2 \lambda^2 / (2m^*)$ .

The one-electron Green's function has the form:

$$G(\mathbf{r}, \mathbf{r}_1; E_\lambda) = \sum_{n_1, n_2, n_3} \frac{\Psi_{n_1, n_2, n_3}^*(\mathbf{r}_1) \Psi_{n_1, n_2, n_3}(\mathbf{r})}{E_\lambda - E_{n_1, n_2, n_3} - i\hbar\Gamma_0}. \quad (7)$$

Using expressions for the energy spectrum (3) and for one-particle wave functions (4), for the Green's function (7) we obtain:

$$\begin{aligned} G(\mathbf{r}, \mathbf{R}_{ak}; E_\lambda) = & -(2\pi)^{-\frac{3}{2}} \beta^{-\frac{1}{2}} a_d^{-3} \times \\ & \exp \left[ -\frac{(x_{ak} - x_0)^2 + y_{ak}^2 + z_{ak}^2 + (x - x_0)^2 + y^2 + z^2}{2a^2} \right] \sum_{n_1=0}^{\infty} \left( \frac{1}{2} \right)^{n_1} \times \\ & \frac{H_{n_1} \left( \frac{x_{ak} - x_0}{a} \right) H_{n_1} \left( \frac{x - x_0}{a} \right)}{n_1!} \sum_{n_2=0}^{\infty} \left( \frac{1}{2} \right)^{n_2} \frac{H_{n_2} \left( \frac{y_{ak}}{a} \right) H_{n_2} \left( \frac{y}{a} \right)}{n_2!} \sum_{n_3=0}^{\infty} \left( \frac{1}{2} \right)^{n_3} \times \\ & \frac{H_{n_3} \left( \frac{z_{ak}}{a} \right) H_{n_3} \left( \frac{z}{a} \right)}{n_3!} \left( E_\lambda - \hbar\omega_0 \left( n_1 + n_2 + n_3 + \frac{2}{3} \right) + \frac{|e|^2 E_0^2}{2m^* \omega_0^2} - i\hbar\Gamma_0 \right)^{-1}. \quad (8) \end{aligned}$$

Green's function (8) can be conveniently written in units of the effective Bohr radius ( $a_d = 4\pi\epsilon_0\epsilon\hbar^2/(m^*|e|^2)$ , ( $\epsilon_0$  is the electric constant,  $\epsilon$  is the static relative dielectric permeability of the QD) and the effective Bohr energy  $E_d = \hbar^2/(2m^*a_d^2)$ . Let's use the obvious expression:

$$\begin{aligned} & \left( E_\lambda - \hbar\omega_0 \left( n_1 + n_2 + n_3 + \frac{3}{2} \right) + \frac{|e|^2 E_0^2}{2m^* \omega_0^2} - i\hbar\Gamma_0 \right)^{-1} = \\ & E_d^{-1} \int_0^{+\infty} \exp \left( -E_d^{-1} \left( E_\lambda - \hbar\omega_0 \left( n_1 + n_2 + n_3 + \frac{3}{2} \right) + \frac{|e|^2 E_0^2}{2m^* \omega_0^2} + i\hbar\Gamma_0 \right) t \right) dt = \\ & E_d^{-1} \int_0^{+\infty} \exp \left[ -(\epsilon_q + n_1 + n_2 + n_3) t \right] dt, \quad (9) \end{aligned}$$

where  $\epsilon_q = -\beta\eta_q^2 + 3/2 - \beta W_0^* + i\Gamma_0\hbar\beta/E_d$ ;  $\eta_q^2 = E_\lambda/E_d$ ;  $\beta = R_0^*/(4\sqrt{U_0^*})$ ;  $W_0^* = e^2 E_0^2 a_d^2 \beta^2 / E_d$ ;  $R_0^* = 2R_0/a_d$ ;  $R_0$  is the QD radius;  $U_0^* = U_0/E_d$ ;  $U_0$  is the amplitude of the QD confinement potential, satisfying the relation  $2U_0 = m^* \omega_0^2 R_0^2$ ;  $\Gamma_0$  is the dissipative tunneling probability.

Then expression (8) can be represented as:

$$\begin{aligned} G(\mathbf{r}, \mathbf{R}_{ak}; E_\lambda) = & -(2\pi)^{-\frac{3}{2}} \beta^{-\frac{1}{2}} E_d^{-1} a_d^{-3} \times \exp \left[ -\frac{(x_{ak} - x_0)^2 + y_{ak}^2 + z_{ak}^2 + (x - x_0)^2 + y^2 + z^2}{2a^2} \right] \times \\ & \int_0^{\infty} dt \exp[-\epsilon_q t] \times \sum_{n_1=0}^{\infty} \left( \frac{e^{-t}}{2} \right)^{n_1} \frac{H_{n_1} \left( \frac{x_{ak} - x_0}{a} \right) H_{n_1} \left( \frac{x - x_0}{a} \right)}{n_1!} \sum_{n_2=0}^{\infty} \left( \frac{e^{-t}}{2} \right)^{n_2} \times \\ & \frac{H_{n_2} \left( \frac{y_{ak}}{a} \right) H_{n_2} \left( \frac{y}{a} \right)}{n_2!} \sum_{n_3=0}^{\infty} \left( \frac{e^{-t}}{2} \right)^{n_3} \frac{H_{n_3} \left( \frac{z_{ak}}{a} \right) H_{n_3} \left( \frac{z}{a} \right)}{n_3!}. \quad (10) \end{aligned}$$

Summation in (10) over quantum numbers  $n_1, n_2, n_3$  can be performed using Mehler's formula [20]:

$$\sum_{n=0}^{\infty} \left( \frac{e^{-t}}{2} \right)^n \frac{H_n \left( \frac{z_a}{a} \right) H_n \left( \frac{z}{a} \right)}{n!} = \frac{1}{\sqrt{1 - e^{-2t}}} \exp \left\{ \frac{2z_a z e^{-t} - (z_a^2 + z^2) e^{-2t}}{a^2 (1 - e^{-2t})} \right\}. \quad (11)$$

As a result, for the Green's function, we have [17]:

$$\begin{aligned} G(\mathbf{r}, \mathbf{R}_{ak}; E_\lambda) = & -(2\pi)^{-\frac{3}{2}} \beta^{-\frac{1}{2}} E_d^{-1} a_d^{-3} \times \int_0^{\infty} dt \exp[-\epsilon_q t] \left\{ (1 - e^{-2t})^{-\frac{3}{2}} \times \right. \\ & \left. \exp \left[ -\frac{(\mathbf{r} - \mathbf{R}_{ak})^2}{2a^2} \coth(t) \right] \exp \left( -\frac{(x_{ak} - x_0)(x - x_0) + y_{ak}y + z_{ak}z}{a^2} \tanh \left( \frac{t}{2} \right) \right) \right\}. \quad (12) \end{aligned}$$

Using the procedure of the zero-range potential method, we obtain a dispersion equation that determines the dependence of the average binding energy of the resonant g- and u-states and the width of resonance levels on the coordinates for  $D^0$ -centers, parameters of the confinement potential of QDs, the strength of the external electric field, and parameters of dissipative tunneling. Applying the limits  $\lim_{\mathbf{r} \rightarrow \mathbf{R}_{ak}} [1 + (\mathbf{r} - \mathbf{R}_{ak}) \nabla_r]$  to both sides of expression (6), we obtain the following system of algebraic equations of the form [17]:

$$\begin{cases} c_1 = \gamma_1 a_{11} c_1 + \gamma_2 a_{12} c_2, \\ c_2 = \gamma_1 a_{21} c_1 + \gamma_2 a_{22} c_2, \end{cases} \quad (13)$$

where  $a_{kj} = \lim_{\mathbf{r} \rightarrow \mathbf{R}_{ak}} [1 + (\mathbf{r} - \mathbf{R}_{ak}) \nabla_r] G(\mathbf{r}, \mathbf{R}_{aj}; E_\lambda)$  ( $k, j = 1, 2$ ).

Eliminating the coefficients  $c_i$ , containing the unknown wave function  $\Psi_\lambda(\mathbf{r}; \mathbf{R}_{a1}, \mathbf{R}_{a2})$ , from the system (13), we obtain the desired dispersion equation:

$$\gamma_1 a_{11} + \gamma_2 a_{22} - 1 = \gamma_1 \gamma_2 (a_{11} a_{22} - a_{12} a_{21}). \quad (14)$$

Let us find explicit expressions for the coefficients  $a_{ii}$  and  $a_{ij}$ .

To isolate the diverging part in (12), we use the Weber integral [20]:

$$\int_0^{+\infty} x^{-\frac{3}{2}} \exp\left[-\frac{\rho^2}{2x} - \mu x\right] dx = \frac{\sqrt{2\pi}}{|\rho|} \exp\left[-\sqrt{2\mu} |\rho|\right], \quad [\Re(\rho^2) > 0, \Re\mu > 0], \quad (15)$$

which in the notation adopted here has the form:

$$\int_0^\infty t^{-\frac{3}{2}} dy \exp(-\varepsilon_q t) \exp\left(-\frac{|\mathbf{r} - \mathbf{R}_a|^2}{2a^2 t}\right) = \frac{\beta}{(2\pi)^2 \sqrt{\pi} E_d a_d^2} \frac{e^{-\sqrt{\varepsilon_q} |\mathbf{r} - \mathbf{R}_a|}}{|\mathbf{r} - \mathbf{R}_a|}. \quad (16)$$

In this case, the Green's function can be represented as:

$$\begin{aligned} G(\mathbf{r}, \mathbf{R}_{ak}; E_\lambda) = & -(2\pi)^{-\frac{3}{2}} \beta^{-\frac{1}{2}} E_d^{-1} a_d^{-3} \times \int_0^\infty dt \exp[-\varepsilon_q t] \left\{ (1 - e^{-2t})^{-\frac{3}{2}} \times \right. \\ & \exp\left(-\frac{(x_{ak} - x_0)(x - x_0) + y_{ak}y + z_{ak}z}{a^2} \tanh\left(\frac{t}{2}\right) - \frac{(\mathbf{r} - \mathbf{R}_{ak})^2}{2a^2} \coth(t)\right) - \\ & \left. t^{-\frac{3}{2}} \exp\left[-\frac{(\mathbf{r} - \mathbf{R}_{ak})^2}{2a^2 t} \coth(t)\right] \right\} - \frac{\beta}{(2\pi)^2 \sqrt{\pi} E_d a_d^2} \frac{\exp(-\sqrt{\varepsilon_q} |\mathbf{r} - \mathbf{R}_a|)}{|\mathbf{r} - \mathbf{R}_a|}. \quad (17) \end{aligned}$$

Again, applying the limits  $\lim_{\mathbf{r} \rightarrow \mathbf{R}_{ak}} [1 + (\mathbf{r} - \mathbf{R}_{ak}) \nabla_r]$  to both sides of this expression, we obtain [17]:

$$\begin{aligned} a_{kk} = & -(2\pi)^{-\frac{3}{2}} \beta^{-\frac{1}{2}} E_d^{-1} a_d^{-3} \left\{ \int_0^{+\infty} dt \exp[-\varepsilon_q t] \left( (1 - e^{-2t})^{-\frac{3}{2}} \times \right. \right. \\ & \left. \left. \exp\left[-\frac{((x_{ak} - x_0)^2 + y_{ak}^2 + z_{ak}^2) \tanh(t/2)}{a^2} - (2t)^{-\frac{3}{2}}\right] - \sqrt{\frac{\pi}{2}} \sqrt{\varepsilon_q} \right) \right\} \quad (18) \end{aligned}$$

and

$$\begin{aligned}
a_{kj} = & - (2\pi)^{-\frac{3}{2}} \beta^{-\frac{1}{2}} E_d^{-1} a_d^{-3} \left\{ \int_0^{+\infty} dt \exp[-\varepsilon_q t] \left[ (1 - e^{-2t})^{-\frac{3}{2}} \times \right. \right. \\
& \exp \left[ - \frac{\left( (x_{ak} - x_{aj})^2 + (y_{ak} - y_{aj})^2 + (z_{ak} - z_{aj})^2 \right) \coth(t)}{2a^2} \right] \times \\
& \exp \left[ - \frac{(x_{ak} - x_0)(x_{aj} - x_0) + y_{ak}y_{aj} + z_{ak}z_{aj}}{a^2} \tanh\left(\frac{t}{2}\right) \right] - \\
& \left. \left. t^{-\frac{3}{2}} \exp \left[ - \frac{\left( (x_{ak} - x_{aj})^2 + (y_{ak} - y_{aj})^2 + (z_{ak} - z_{aj})^2 \right) \coth(t)}{2a^2 t} \right] \right] \right\} - \\
& \frac{\beta}{(2\pi)^2 \sqrt{\pi} E_d a_d^2} \left( (x_{ak} - x_{aj})^2 + (y_{ak} - y_{aj})^2 + (z_{ak} - z_{aj})^2 \right)^{-1} \times \\
& \exp \left( - \sqrt{\varepsilon_q \left( (x_{ak} - x_{aj})^2 + (y_{ak} - y_{aj})^2 + (z_{ak} - z_{aj})^2 \right)} \right). \quad (19)
\end{aligned}$$

In the case when  $\gamma_1 = \gamma_2 = \gamma$  equation (14) splits into two equations that determine the symmetric (g-term) and antisymmetric (u-term) states of the electron, respectively, we obtain:

$$\gamma a_{11} + \gamma a_{12} = 1, \quad (c_1 = c_2) \quad (20)$$

$$\gamma a_{11} - \gamma a_{12} = 1. \quad (c_1 = -c_2) \quad (21)$$

In this case, the average binding energies of quasistationary g- and u-states are determined, respectively, as  $\bar{E}_g = E_{0,0,0} - \Re E_{2\lambda u}$ ,  $\bar{E}_u = E_{0,0,0} - \Re E_{2\lambda g}$ , and the broadening of impurity levels:  $\Delta E_g = 2\Im E_{2\lambda g}$ ,  $\Delta E_u = 2\Im E_{2\lambda u}$ , respectively.

### 3. Dependence of the average binding energies of quasistationary g- and u-states of the $D_2^-$ -center and the width of impurity levels on the magnitude of the external electric field and parameters of dissipative tunneling.

Figure 1 shows dependence of the average values of the binding energies for the quasistationary g- and u-states of the QD  $D_2^-$ -center on the magnitude of the external electric field and the parameters of 1D-dissipative tunneling, obtained by numerical analysis of equations (20) and (21). The field dependences of the binding energies average values for the quasistationary g- and u-states show dips that appear at the values of the parameters of 1D-dissipative tunneling and the external electric field strengths corresponding to the maxima in the field dependences of 1D-dissipative tunneling, with the participation.

Let us normalize the wave functions of quasistationary g- and u-states. From the normalization condition for the wave function  $\Psi_\lambda(\mathbf{r}; \mathbf{R}_{a1}, \mathbf{R}_{a2})$ , we have:

$$\begin{aligned}
\int_V dV |\Psi_\lambda(\mathbf{r}; \mathbf{R}_{a1}, \mathbf{R}_{a2})|^2 = & \gamma_1^2 C_1^2 \int_{-\infty}^{\infty} \int_{-\infty}^{\infty} \int_{-\infty}^{\infty} |G(\mathbf{r}, \mathbf{R}_{a1}; E_\lambda)|^2 dx dy dz + \\
& 2\gamma_1 \gamma_2 C_1 C_2 \int_{-\infty}^{\infty} \int_{-\infty}^{\infty} \int_{-\infty}^{\infty} G(\mathbf{r}, \mathbf{R}_{a1}; E_\lambda) G(\mathbf{r}, \mathbf{R}_{a2}; E_\lambda) dx dy dz + \\
& \gamma_2^2 |C_2|^2 \int_{-\infty}^{\infty} \int_{-\infty}^{\infty} \int_{-\infty}^{\infty} |G(\mathbf{r}, \mathbf{R}_{a2}; E_\lambda)|^2 dx dy dz = 1. \quad (22)
\end{aligned}$$

The integrals in expression (22) are calculated using the Green's function (7), i.e.:

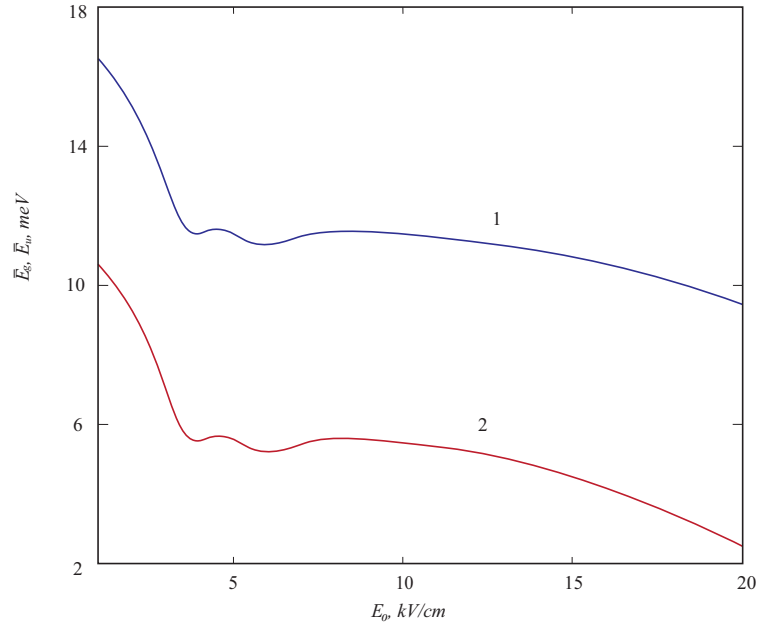


FIG. 1. Dependence of the average binding energy of quasistationary g-state  $\bar{E}_g$  (curve 1), and u-state  $\bar{E}_u$  (curve 2) for  $D_2^-$ -center on the strength of the external electric field  $E_0$  in the presence of 1D-dissipative tunneling with allowance for the influence of two local phonon modes at  $R_0 = 50$  nm;  $U_0 = 0.35$  eV;  $\eta_i = 8.5$ ;  $\rho_{12} = 4.8$  nm;  $\epsilon_T^* = 1.3$ ;  $\epsilon_{L1}^* = 1.4$ ;  $\epsilon_{L2}^* = 1.6$ ;  $\epsilon_C^* = 2.2$

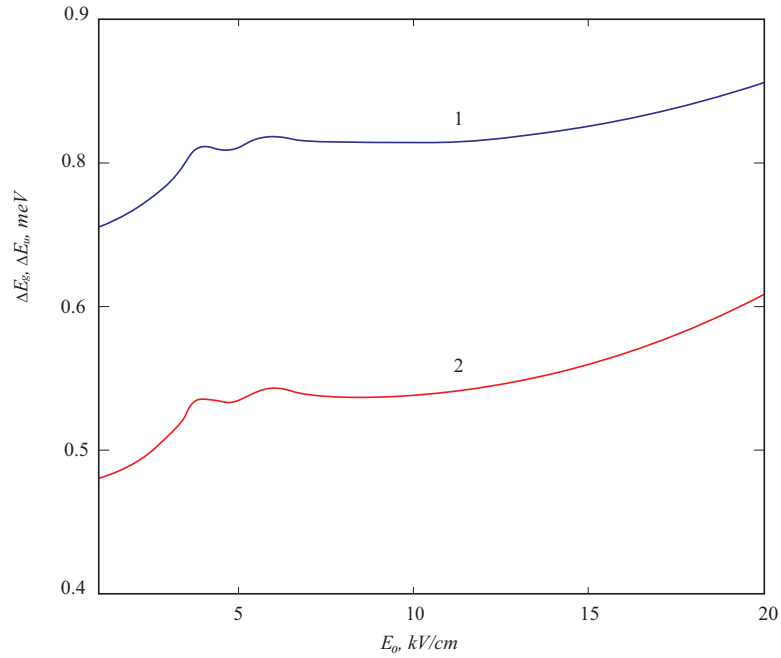


FIG. 2. Dependence of the broadening for impurity levels of quasistationary g- (curve 1), and u-states (curve 2) for  $D_2^-$ -center on the strength of an external electric field  $E_0$  in the presence of 1D-dissipative tunneling taking into account the influence of two local phonon modes at  $R_0 = 50$  nm;  $U_0 = 0.35$  eV;  $\eta_i = 8.5$ ;  $\rho_{12} = 4.8$  nm;  $\epsilon_T^* = 1.3$ ;  $\epsilon_{L1}^* = 1.4$ ;  $\epsilon_{L2}^* = 1.6$ ;  $\epsilon_C^* = 2.2$

$$\int_{-\infty}^{\infty} \int_{-\infty}^{\infty} \int_{-\infty}^{\infty} G(\mathbf{r}, \mathbf{R}_{aj}; E_\lambda) G(\mathbf{r}, \mathbf{R}_{ak}; E_\lambda) dx dy dz = \sum_{n_1, n_2, n_3} \sum_{n'_1, n'_2, n'_3} \frac{\Psi_{n_1 n_2 n_3}(\mathbf{R}_{aj}) \Psi_{n'_1, n'_2, n'_3}^*(\mathbf{R}_{ak})}{(E_\lambda - E_{n_1, n_2, n_3}) (E_\lambda - E_{n'_1, n'_2, n'_3})} \times \int_{-\infty}^{\infty} \int_{-\infty}^{\infty} \int_{-\infty}^{\infty} \Psi_{n_1, n_2, n_3}^*(\mathbf{r}) \Psi_{n'_1, n'_2, n'_3}(\mathbf{r}) dx dy dz. \quad (23)$$

We calculate the integral in (23) using the orthogonality condition for the eigenwave functions:

$$\int_{-\infty}^{\infty} \int_{-\infty}^{\infty} \int_{-\infty}^{\infty} \Psi_{n_1, n_2, n_3}^*(\mathbf{r}) \Psi_{n'_1, n'_2, n'_3}(\mathbf{r}) dx dy dz = \delta_{n_1, n'_1} \times \delta_{n_2, n'_2} \times \delta_{n_3, n'_3}, \quad (24)$$

as a result, we have:

$$\int_{-\infty}^{\infty} \int_{-\infty}^{\infty} \int_{-\infty}^{\infty} G(\mathbf{r}, \mathbf{R}_{aj}; E_\lambda) G(\mathbf{r}, \mathbf{R}_{ak}; E_\lambda) dx dy dz = \sum_{n_1, n_2, n_3} \frac{\Psi_{n_1, n_2, n_3}(\mathbf{R}_{aj}) \Psi_{n_1, n_2, n_3}^*(\mathbf{R}_{ak})}{(E_\lambda - E_{n_1, n_2, n_3})^2}, \quad (25)$$

where  $j, k = 1, 2$ .

The right-hand side of expression (25) can be written as:

$$\sum_{n_1, n_2, n_3} \frac{\Psi_{n_1, n_2, n_3}(\mathbf{R}_{aj}) \Psi_{n_1, n_2, n_3}^*(\mathbf{R}_{ak})}{(E_\lambda - E_{n_1, n_2, n_3})^2} = -\frac{\partial G(\mathbf{R}_{aj}, \mathbf{R}_{ak}; E_\lambda)}{\partial E_\lambda} = (\hbar\omega_0)^{-2} a^{-3} \frac{\partial G_0(\mathbf{R}_{aj}, \mathbf{R}_{ak}; \varepsilon_s)}{\partial \varepsilon_s}, \quad (26)$$

where  $G_0(\mathbf{r}, \mathbf{R}_a; E_\lambda)$  – dimensionless Green's function.

Taking into account (23) – (26), we write down the normalization condition for the wave function  $\Gamma_\lambda(\mathbf{r}; \mathbf{R}_{a1}, \mathbf{R}_{a2})$  of the quasistationary  $D_2^-$ -state:

$$\int_V dV |\Psi_\lambda(\mathbf{r}; \mathbf{R}_{a1}, \mathbf{R}_{a2})|^2 = -\gamma^2 \left( C_1^2 \frac{\partial G(\mathbf{R}_{a1}, \mathbf{R}_{a1}; E_\lambda)}{\partial E_\lambda} + 2C_1 C_2 \frac{\partial G(\mathbf{R}_{a1}, \mathbf{R}_{a2}; E_\lambda)}{\partial E_\lambda} + C_2^2 \frac{\partial G(\mathbf{R}_{a2}, \mathbf{R}_{a2}; E_\lambda)}{\partial E_\lambda} \right) = 1. \quad (27)$$

Then the expressions for the normalization factors of the symmetric ( $C_1 = C_2$ ) and antisymmetric ( $C_1 = -C_2$ )  $D_2^-$ -states take the form:

$$C_1^2 = -\gamma^2 \left\{ \frac{\partial G(\mathbf{R}_{a1}, \mathbf{R}_{a2}; E_\lambda)}{\partial E_\lambda} \pm 2 \frac{\partial G(\mathbf{R}_{a1}, \mathbf{R}_{a2}; E_\lambda)}{\partial E_\lambda} + \frac{\partial G(\mathbf{R}_{a2}, \mathbf{R}_{a2}; E_\lambda)}{\partial E_\lambda} \right\}^{-1}, \quad (28)$$

here the upper and lower signs refer to the g- and u-states, respectively. Let us calculate the derivatives in formula (28), passing to the dimensionless Green's function  $G_0(\mathbf{r}, \mathbf{R}_a; E_\lambda)$  by a simple transformation:

$$G(\mathbf{r}, \mathbf{R}_a; E_\lambda) = a^{-3} (\hbar\omega_0)^{-1} G_0(\mathbf{r}, \mathbf{R}_a; \varepsilon_q), \quad (29)$$

where

$$G_0(\mathbf{r}, \mathbf{R}_a; \varepsilon_q) = -2^{-1} \pi^{-\frac{3}{2}} \exp\left(-\frac{(x_a - x_0)(x - x_0) + y_a y + z_a z}{a^2}\right) \exp\left[-\frac{(\mathbf{r} - \mathbf{R}_a)^2}{2a^2}\right] B\left(\frac{\varepsilon_q}{2}, -\frac{1}{2}\right). \quad (30)$$

As a result, we have:

$$\frac{\partial G_0(\mathbf{r}, \mathbf{R}_a; \varepsilon_q)}{\partial \varepsilon_q} = -2^{-1} \pi^{-\frac{3}{2}} \exp\left(-\frac{(x_a - x_0)(x - x_0) + y_a y + z_a z}{a^2}\right) \frac{\partial B\left(\frac{\varepsilon_q}{2}, -\frac{1}{2}\right)}{\partial \varepsilon_q} = 2^{-1} \pi^{-1} \exp\left(-\frac{(x_a - x_0)(x - x_0) + y_a y + z_a z}{a^2}\right) \frac{\Gamma\left(\frac{\varepsilon_q}{2}\right)}{\Gamma\left(\frac{\varepsilon_q}{2} - \frac{1}{2}\right)} \left(\psi\left(\frac{\varepsilon_q}{2}\right) - \psi\left(\frac{\varepsilon_q}{2} - \frac{1}{2}\right)\right), \quad (31)$$

where  $\psi(x) = \Gamma'(x)/\Gamma(x)$  is the logarithmic derivative of the Euler gamma function  $\Gamma(x)$ .

Let us write down the final expression for the normalization factors of the wave functions  $\Psi_\lambda(\mathbf{r}; \mathbf{R}_{a1}, \mathbf{R}_{a2})$  for the symmetric and antisymmetric states:

$$C_1 = 2^{\frac{5}{4}} \pi^{\frac{1}{2}} \beta^{-\frac{1}{4}} E_d a_d^{\frac{3}{2}} \gamma \left( \frac{\Gamma\left(\frac{\varepsilon_q}{2}\right)}{\Gamma\left(\frac{\varepsilon_q}{2} - \frac{1}{2}\right)} \left( \psi\left(\frac{\varepsilon_q}{2}\right) - \psi\left(\frac{\varepsilon_q}{2} - \frac{1}{2}\right) \right) \right)^{-\frac{1}{2}} \times \\ \left\{ \exp\left(-\frac{(x_{a1} - x_0)^2 + y_{a1}^2 + z_{a1}^2}{a^2}\right) \pm 2 \exp\left(-\frac{(x_{a1} - x_0)(x_{a2} - x_0) + y_{a1}y_{a2} + z_{a1}z_{a2}}{a^2}\right) + \right. \\ \left. \exp\left(-\frac{(x_{a2} - x_0)^2 + y_{a2}^2 + z_{a2}^2}{a^2}\right) \right\}^{-\frac{1}{2}}. \quad (32)$$

Using expression (32) for the wave function of the quasi-stationary  $D_2^-$  - state in a QD in an external electric field, we obtain:

$$\Psi_\lambda(\mathbf{r}; \mathbf{R}_{a1}, \mathbf{R}_{a2}) = -2^{-\frac{1}{4}} \pi^{-1} \beta^{-\frac{1}{4}} a_d^{-\frac{3}{2}} \left( \frac{\Gamma\left(\frac{\varepsilon_q}{2}\right) \left( \psi\left(\frac{\varepsilon_q}{2}\right) - \psi\left(\frac{\varepsilon_q-1}{2}\right) \right)}{\Gamma\left(\frac{\varepsilon_q-1}{2}\right)} \right)^{-\frac{1}{2}} \times \\ \left\{ \exp\left(-\frac{(x_{a1} - x_0)^2 + y_{a1}^2 + z_{a1}^2}{a^2}\right) \pm 2 \exp\left(-\frac{(x_{a1} - x_0)(x_{a2} - x_0) + y_{a1}y_{a2} + z_{a1}z_{a2}}{a^2}\right) + \right. \\ \left. \exp\left(-\frac{(x_{a2} - x_0)^2 + y_{a2}^2 + z_{a2}^2}{a^2}\right) \right\}^{-\frac{1}{2}} \times \\ \left( \int_0^\infty dt \exp[-\varepsilon_q t] (1 - \exp(-2t))^{-\frac{3}{2}} \exp\left(-\frac{(x - x_{a1})^2 + (y - y_{a1})^2 + (z - z_{a1})^2}{2a^2} \coth(t)\right) \right) \times \\ \exp\left(-\frac{(x_{a1} - x_0)(x - x_0) + y_{a1}y + z_{a1}z}{a^2} \tanh\left(\frac{t}{2}\right)\right) \pm \int_0^\infty dt \exp[-\varepsilon_q t] (1 - \exp(-2t))^{-\frac{3}{2}} \times \\ \exp\left(-\frac{(x - x_{a2})^2 + (y - y_{a2})^2 + (z - z_{a2})^2}{2a^2} \coth(t)\right) \times \\ \exp\left(-\frac{(x_{a2} - x_0)(x - x_0) + y_{a2}y + z_{a2}z}{a^2} \tanh\left(\frac{t}{2}\right)\right). \quad (33)$$

Here, the signs "+" and "-" determine the g- and u-states, respectively.

Expression (33) for the wave functions of quasistationary g- and u-states will make it possible to calculate the probabilities of radiative transitions of an electron in a quantum molecule in an external electric field.

#### 4. Conclusions

In the model of the zero-range potential in the effective mass approximation, dispersion equations have been obtained that describe dependence of the average binding energies of the quasistationary g- and u-states of the  $D_2^-$  - center in the QD, as well as the energy levels width on the magnitude of the external electric field and the parameters of 1D-dissipative tunneling. Dips in the field dependences of the average values of the binding energies of quasistationary g- and u-states have been revealed. The dips are caused by a significant decrease in the lifetime of the impurity quasi-stationary states at values of the dissipative tunneling parameters and external electric field strengths corresponding to the maxima on the field dependences of the 1D-dissipative tunneling probability. It is shown that the field dependences of the energy levels widths for the g- and u- states of the  $D_2^-$ -center have a resonance structure at the external electric field strengths corresponding to the dips in the field dependences of the average binding energies.

In the dipole approximation, the field dependence of the radiative transition probability (RTP) of an electron from a quasistationary u-state to a quasi-stationary g-state of the  $D_2^-$ -center in a QD in the presence of dissipative tunneling with the participation of two local phonon modes has been calculated. It was found that the curve of the RTP dependence on the strength of the external electric field contains three peaks. The leftmost peak corresponds to the RTP with the energy of the emitted photon comparable to the energy of the optical transition of an electron from

the quasistationary u-state to the quasi-stationary g-state of the  $D_2^-$ -center. The other two peaks are separated by a dip and are due to the presence of two local phonon modes; moreover, with a decrease in the phonon frequency, the peaks are smoothed out and the dip is transformed into a horizontal section, the length of which substantially depends on the constant of interaction with the contact medium.

### Acknowledgements

This work was supported by the Ministry of Education and Science of the Russian Federation (project 0748-2020-0012) and RFBR (project no. 18-42-130007 p.a). The research was partially supported by the Foundation for Polish Science through the IRA Programme co-financed by EU within SG OP.

### References

- [1] Aleshkin V.Y., Gavrilenko L.V., Odnoblyudov M.A., Yassievich I.N. Impurity resonance states in semiconductors. *Semiconductors*, 2008, **42**, P. 880–904.
- [2] Ovchinnikov A.A., Dakhnovsky Yu.I., et al. *Principles of controlled modulation of low-dimensional structures*. UNC DO (a publishing company at Moscow State University), Moscow, 2003, 510 p.
- [3] Leggett A.J. (Ed.) *Controllable dissipative tunneling. Tunnel transport in low-dimensional systems*. Fizmatlit, Moscow, 2012, 495 p.
- [4] Mantsevich V.N. Nonequilibrium effects and non-stationary electron transport in semiconductor nanostructures with interparticle interaction. PhD Thesis, Moscow, 2014, 337 p.
- [5] Mantsevich V.N., Maslova N.S. Spatial effects of Fano resonance in local tunneling conductivity in vicinity of impurity on semiconductor surface. *JETP Lett.*, 2010, **91**, P. 139–142.
- [6] Maltezopoulos T., Bolz A., et al. Wave-function mapping of InAs quantum dots by scanning tunneling spectroscopy. *Phys. Rev. Lett.*, 2003, **91**, 196804.
- [7] Tserkovnyak Y., Halperin B.I., Auslaender O.M., Yacoby A. Finite-size effects in tunneling between parallel quantum wires. *Phys. Rev. Lett.*, 2002, **89**, 136805.
- [8] Bomze Yu., Mebrahtu H., et al. Resonant tunneling in a dissipative environment. *Phys. Rev. B*, 2009, **79**, 241402.
- [9] Qin H., Holleitner A.W., Eberl K., Blick R.H. Coherent superposition of photon- and phonon-assisted tunneling in coupled quantum dots. *Phys. Rev. B*, 2001, **64**, 241302.
- [10] Trocha P., Rudziński W. Phonon-assisted electronic transport through double quantum dot system coupled to ferromagnetic leads. *Acta Physica Polonica A*, 2013, **124**, P. 843–845.
- [11] Liu L., Du Y., Zhou H., Lin T. Resonant tunneling through a coupled double quantum well in the presence of electron-phonon interaction. *Phys. Rev. B*, 1996, **54**, P. 1953–1958.
- [12] Kang K., Min B.I. Effect of quantum confinement on electron tunneling through a quantum dot. *Phys. Rev. B*, 1997, **55**, P. 15412–15415.
- [13] Kusmartsev F.V., Krevchik V.D., et al. Phonon assisted resonant tunneling and its phonons control. *JETP Lett.*, 2016, **104**, P. 392–397.
- [14] Polyakov A.M. *Gauge Fields and Strings*. Routledge, London, 1987. 312 p.
- [15] Coleman S. *Aspects of Symmetry: Selected Erice Lectures*. Cambridge University Press, Cambridge, 1985, 402 p.
- [16] Benderskii V.A., Vetoshkin E.V., Kats E.I. Semiclassical quantization of bound and quasistationary states beyond the adiabatic approximation. *Phys. Rev. A*, 2004, **69**, 062508.
- [17] Zhukovsky V.Ch., Krevchik V.D., et al. The effect of an external electric field on the optical properties of a quantum-dot molecule with a resonant state of the  $D_2^-$  center. *Moscow University Physics Bulletin*, 2013, **68**, P. 397–404.
- [18] Baz' A.I., Zeldovich Ya.B., Perelomov A.M. *Scattering, Reactions and Decays in Nonrelativistic Quantum Mechanics*. Jerusalem: Israel Program for Scientific Translations, 1969, 246 p.
- [19] Galitski V., Karnakov B., Kogan V., Galitski V. (Jr). *Exploring Quantum Mechanics: A Collection of 700+ Solved Problems for Students, Lecturers, and Researchers*. Oxford University Press, Oxford, 2013, 904 p.
- [20] Bateman H. *Higher Transcendental Functions* [Vol. 1–3]. McGraw-Hill Book Company, New York, 1953.

## Influence of complexing agent, pH of solution and thickness on morphological and optical properties of ZnS particles layer prepared by electrochemical deposition technique

Jitendra Borse<sup>1</sup>, Arun Garde<sup>2</sup>

<sup>1</sup>Department of Physics, Late Pushpadevi Patil Arts & Science College, Risod 444506, India

<sup>2</sup>Department of Physics, SPH Arts, Science and Commerce College, Nampur 423204, India

jaborse@gmail.com, arungarde@yahoo.co.in

DOI 10.17586/2220-8054-2020-11-5-519-528

Zinc sulfide particles layer were grown on FTO glass and stainless steel substrates by electrode position technique from aqueous solution that contained 0.1 N zinc sulfate, 0.1 N sodium thiosulfate and 0.1 N triethanolamine was used as complexing agent. The depositing potential was analyzed by cyclic voltammetry technique. The ZnS particle growth was studied in the range of deposition time from 10 to 40 minutes. The thickness of layer was found to be the highest, 3.92  $\mu\text{m}$ , at 20 min. The various percentage of complexing agent, pH of solution and thicknesses of film were characterized by scanning electron microscope (SEM) and UV-Visible spectrophotometer. The effects of complexing agent, pH of solution and thickness of layer on morphological and optical properties of ZnS were investigated. The Electrical resistivity of ZnS was found thickness dependent. The Chemical Composition of ZnS particles analysed by EDAX (Energy Dispersive Analysis by X-ray).

**Keywords:** complexing agent, electrodeposition, pH of bath, resistivity, thickness of ZnS particles layer.

*Received:* 14 May 2020

*Revised:* 29 May 2020

*Final revision:* 21 September 2020

### 1. Introduction

The research of chalcogenide semiconductor materials for solar energy conversion and other related photovoltaic applications has been recently initiated. ZnS belongs to group II–VI semiconductor material. It has cubic and hexagonal crystal structure [1]. It is semiconductor material with a large band gap greater than 3.5 eV [2]. ZnS films have been prepared by using various techniques such as electrochemical deposition, chemical bath deposition, spray pyrolysis [3]. Amongst these various deposition methods, electrochemical deposition is more attractive, being a simple, low temperature and inexpensive technique. The prepared films have been widely used in variety of application such as window layer of solar cell, laser materials, sensors, photoconductors, anti-reflection coating [4]. The Chalcogenide semiconductor material show unique optical behavior due to quantum size effect and widely studied because of their applications in optoelectronic devices [5]. The ZnS material is suitable as a window layer in hetero junction photovoltaic solar cells [6–10]. In this research, we have reported deposition of ZnS film on stainless steel substrate by an electrode position technique [11, 12]. The main aim of this research is to study the effect of triethanolamine as complexing agent and pH of bath on the morphological and optical properties of ZnS material respectively.

### 2. Method

ZnS particles were deposited on stainless steel substrate by an electrochemical deposition technique shown in Fig. 1. The type of AISI 316 stainless steel plate/FTO glass was used as the working electrode with graphite as the counter electrode and Ag/AgCl working as reference electrode to measured depositing potential of ZnS with respect to working electrode. All the precursors were used for the deposition as AR grade. Zinc sulfide particles layer were electrode positioned on to the stainless steel substrate for 10 to 40 min at room temperature from a solution containing 0.1 N Zinc sulfate ( $\text{ZnSO}_4$ ), 0.1 N sodium thiosulfate ( $\text{Na}_2\text{S}_2\text{O}_3$ ) at pH = 3.5. The 0.1 N solution of triethanolamine (TEA) was added in bath as complexing agent. The role of complexing agent to formation of complex stoichiometric compound of Zn and S ions and substrate is fully covered. The cyclic voltammetry technique was used to study the electrochemical property such as depositing potential of ZnS materials. The stainless steel substrates of 2.25  $\text{cm}^2$  dimension area were cleaned by acetone and distilled water before deposition. The distance between the working electrode and counter electrode was kept constant as 1 cm during deposition of materials. The ZnS particles are formed on the stainless steel substrate according to reaction. This is electrochemical reaction of thiosulfate ion. The process of disproportionate of  $\text{S}_2\text{O}_3^{2-}$  to S and  $\text{SO}_3^{2-}$  is possible,



Zinc ions are involved in reduction and oxidation reaction with transfer of two electrons

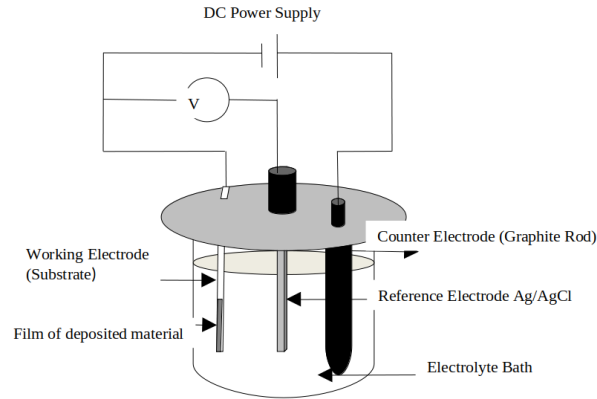
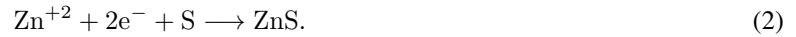


FIG. 1. Electrochemical deposition set-up for deposition of ZnS particles layer

The formation of ZnS material according to reaction (2).

The electrical parameters such as DC voltage and current density were adjusted at 1700 mV and 4.4 mA/cm<sup>2</sup> respectively. The zinc sulfide films were prepared at deposition time (10 to 40 min) and thickness of layer studied [13]. The pH of electrolyte bath was adjusted from 3.5 to 5 by adding 0.1 N sodium hydroxide (NaOH). The ZnS films were prepared at different percentage of 0.1 N triethanolamine (TEA). The layer of ZnS was further characterized by UV-Visible spectrophotometer. Energy dispersive analysis by X-ray diffraction (EDAX) and Scanning electron microscopy (SEM). The chemical bonding of functional groups was analysed by FT-IR technique. The electrical resistivity of ZnS was estimated by two point probe method.

### 3. Result and discussion

#### 3.1. Energy dispersive analysis by X-ray spectroscopy

Figure 2 shows energy dispersive analysis by X-ray spectroscopy of ZnS particles. It showed the elemental composition for the Zn and S ions in the sample. The ZnS particles were shown to be deposited successfully. The EDX spectrum in Fig. 3 revealed that as grown layer composed of only Zn and S species. The At% ratio of Zn, S and O was found 62.48, 6.76 and 30.76 respectively.

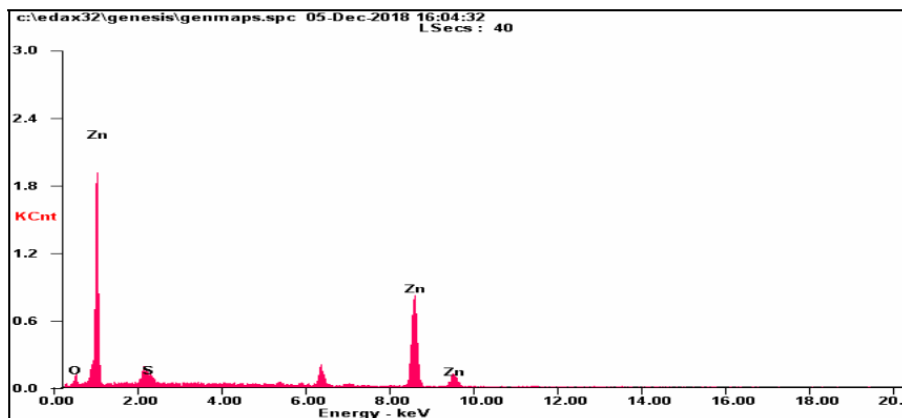


FIG. 2. Energy dispersive analysis of ZnS particles

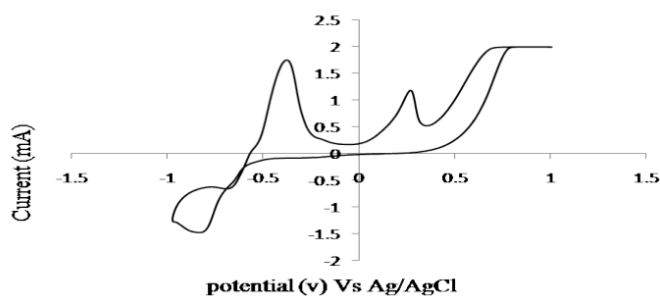


FIG. 3. Cyclic voltammetry of measured current versus applied potential of electrolyte bath containing  $\text{ZnSO}_4$  and  $\text{Na}_2\text{S}_2\text{O}_3$  with scan speed 25 mv/sec

### 3.2. Cyclic voltammetry

Figure 3 shows cyclic voltammetry of electrolyte bath at scan speed 25 mv/sec. Cyclic voltammetry (CV) was used to determine the optimal deposition potential of ZnS and study of the corresponding deposition mechanism. It indicates variation of potential with current to find suitable depositing potential of ZnS material. The first and second anodic peak was found at +0.25 V, +0.80 V at scan speed 25 mV/s. Dissolution of sulfide and zinc ions in the solution has been observed respectively. At that instant, the deposition of ZnS takes place when cathodic potential was reached  $-0.80$  V against Ag/AgCl (Reference Electrode). Therefore, the optimal potential range for deposition of ZnS is  $-0.8$  to  $-1$  V.

### 3.3. Estimation of layer thickness

Figure 4 shows the deposition time versus thickness of ZnS film.

The thickness of film variation was estimated by using mass difference method:

$$t = \frac{\Delta m}{A \cdot \rho}, \quad (3)$$

where  $\Delta m$  is mass difference of stainless steel substrate before deposition and after deposition,  $t$  is thickness of film,  $A$  is area of deposition,  $\rho$  is density of deposited material. The standard density of ZnS particles was  $4.090 \text{ g/cm}^3$ . The process of layer formation was found to be time dependent. The ZnS particle growth was studied over the range of deposition times from 10 to 40 min. It has been observed that thickness of layer increased up to 20 min, and after that, it was decreased by co-deposition. The optimized thickness of the layer was  $3.92 \mu\text{m}$  at 20 min. The thickness of the ZnS layer was found to be highest at 20 min. The real thickness of the layer will be higher than the calculated values. Because layers may have some porosity, there exists uncertainty in layer thickness.

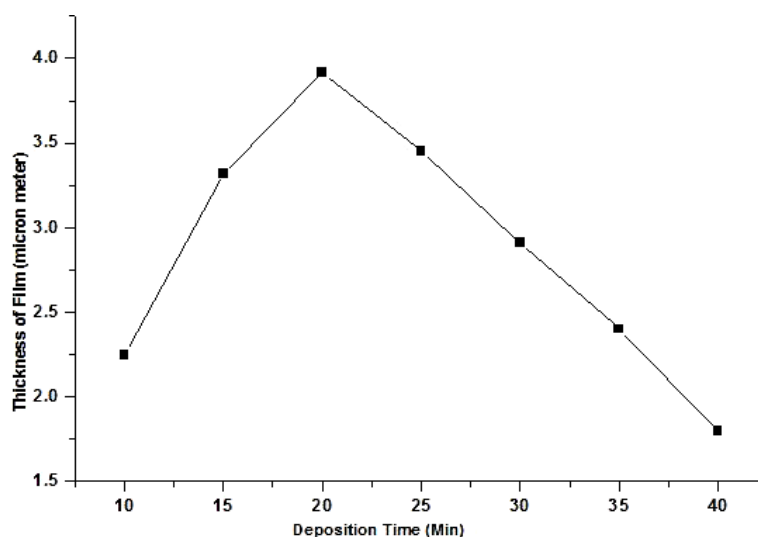


FIG. 4. Deposition time (min) versus thickness of layer

### 3.4. Effect of complexing agent

In this report triethanolamine (TEA) was used as a complexing agent to prepare ZnS film at optimized time 20 min [14]. The ZnS film deposited at pH 3.5 at different percentage of 0.1 N triethanolamine such as 1, 2, 3, and 4 % of total 80 ml electrolytic bath. The prepared films of ZnS were characterized by using Field Emission Scanning Electron Microscope (FESEM). The SEM image indicated that high dense ZnS film was deposited at 4 % TEA if compared to those prepared in the 1 % TEA of complexing agent [14]. It has been observed in Fig. 5. The ZnS film deposited with 4 % TEA was optimized. It showed high dense and good surface coverage of substrate. It can be seen that ZnS film was found densely covered full substrate area if percentage of complexing agent are increased.

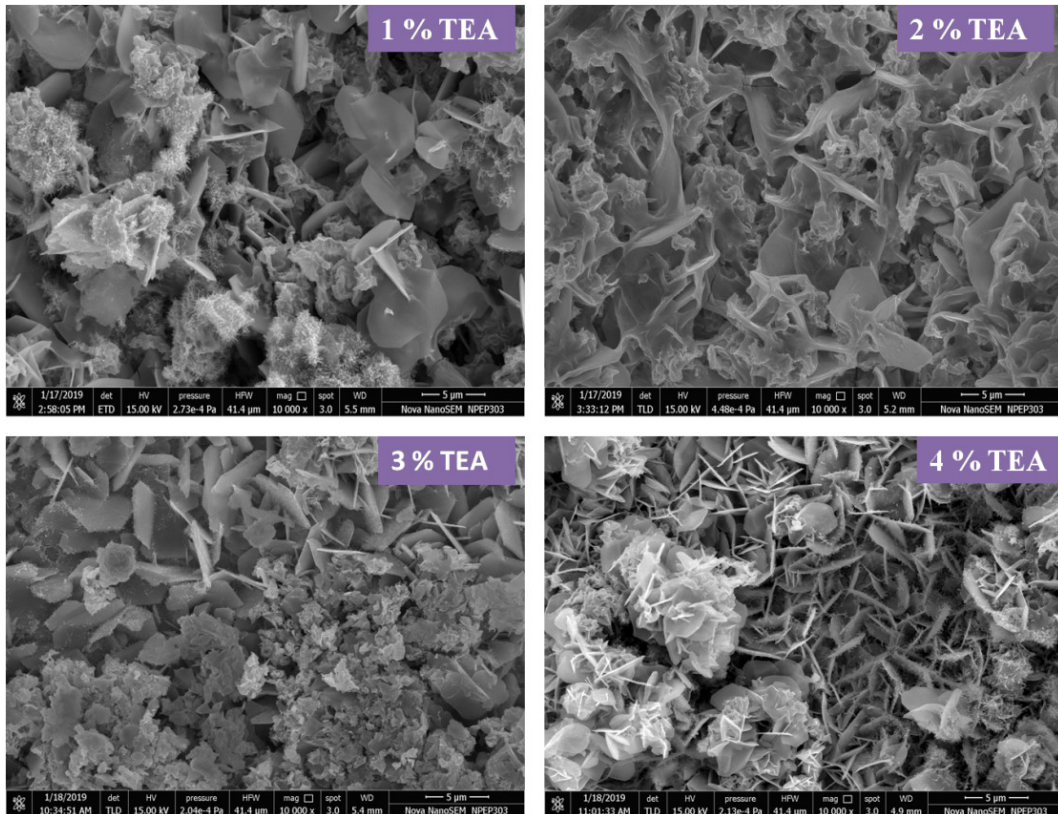


FIG. 5. Scanning electron microscopy image of deposited layer of ZnS particles with complexing agent triethanolamine (TEA) (a) 1 % TEA; (b) 2 % TEA; (c) 3 % TEA; (d) 4 % TEA

### 3.5. Effect of pH

Figure 6 shows SEM images of deposited ZnS particle layers with different pH. The SEM was carried out to study the effect of different pH values of solution on surface morphology of ZnS particles. The pH of solution varied from 3.5 to 5; it introduced crystallite defect. It has been observed that two types of particles were found, namely nanorods and lamellar. The average diameter of nanorods was estimated by using image-J software. The nanorods diameter was found to decrease in order to increased pH of solution [15]. It has been shown in Table 1.

The optical absorbance spectra of the ZnS particles by the electrode position method with different pH solution are shown in Fig. 7. The optical absorbance data of the particles were carried out by using UV-Visible spectrophotometer in the wavelength range from 100 to 1100 nm. It is shown that a sharp rise in absorbance occurs between 330 and 360 nm. These are fundamental absorption edges. It is indicated to excitation of electron from valence band to conduction band.

Figure 8 shows optical transmission spectra of ZnS particles deposited by electrode position method with different pH solution [15]. All films showed sharp absorption edges at near 330 nm which correspond to optical band gap of films. It can be observed that average transmission values are 80 % in the wavelength range after 330 nm. The absorption of light in the wavelength region of 330 nm to 360 nm is caused by crystalline defects. The crystalline defects were found to be responsible for reduction in optical transmission. It can be seen that varying pH introduces crystalline defects in ZnS particles as shown in Fig. 6.

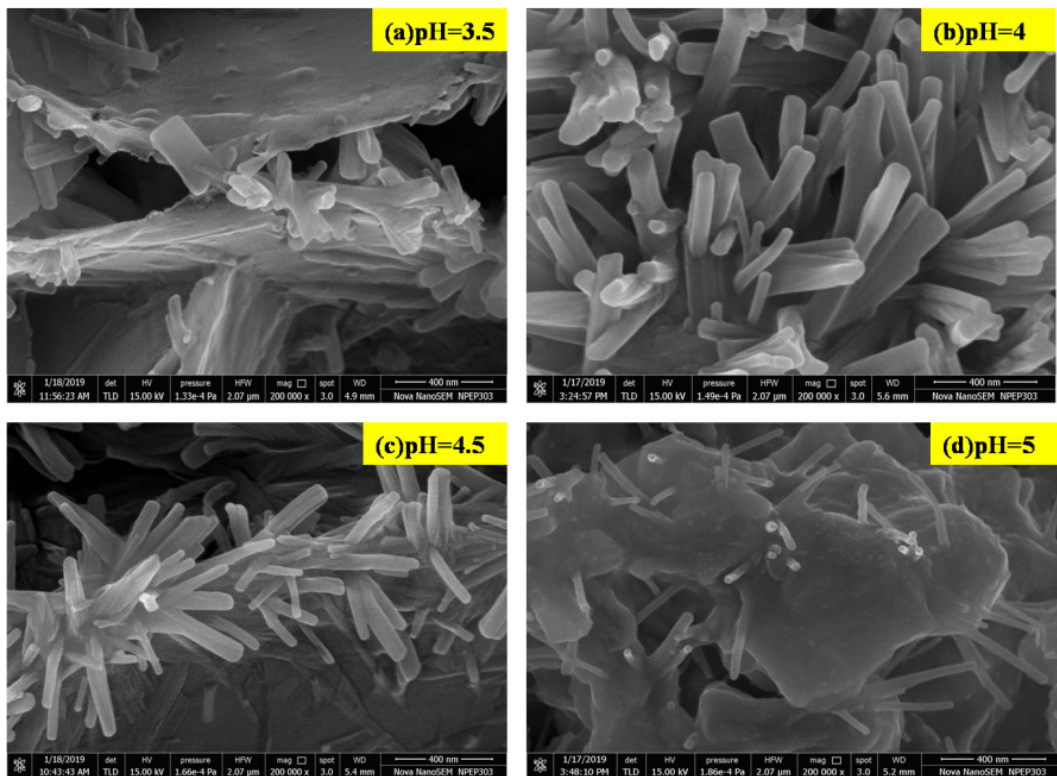


FIG. 6. Scanning electron microscope image of deposited layer of ZnS particles at (a) pH = 3.5; (b) pH = 4; (c) pH = 4.5; (d) pH = 5

TABLE 1. Estimated values of average diameter of nanorods and band gap of ZnS at different pH of bath

Sr. No	pH of solution	Average diameter of nanorod (nm)	Energy Band gap (eV)
1	3.5	160.12 ± 0.5 nm	3.98
2	4	100.15 ± 0.5 nm	3.91
3	4.5	60.10 ± 0.5 nm	3.87
4	5	40.22 ± 0.5 nm	3.74

Figure 9 shows energy band gap of ZnS particles deposited with varying pH of solution from 3.5 to 5. The band gap energies of the deposited particles were calculated with the help of an optical absorption spectrum, i.e. Taucplot. The absorption coefficient ( $\alpha$ ) was calculated by using equation:

$$\alpha = \frac{\text{Absorbance}}{\text{Thickness of film}} \quad (4)$$

The optical band gap energy of ZnS particles were calculated by plotting graph  $(\alpha h\nu)^2$  versus  $h\nu$  [16–19]. The band gaps were determined by the intercept of straight line portion of the  $(\alpha h\nu)^2$  versus  $h\nu$  graph on the  $h\nu$  axis. The direct band gap was calculated to be 3.98 eV and decreased to 3.74 eV after increasing pH of solution. The effect of crystallite defects on band gap of ZnS at different pH of solution as shown in Table 1.

### 3.6. Effect of deposited layer thickness

The various thicknesses of layer characterized by UV-visible spectrophotometer. Fig. 10 shows optical absorption spectra of ZnS particles deposited by the electrode position method at different thicknesses [20]. The sharp rise of absorption occurs between 300 to 350 nm of thickness range 2400 to 3920 nm.

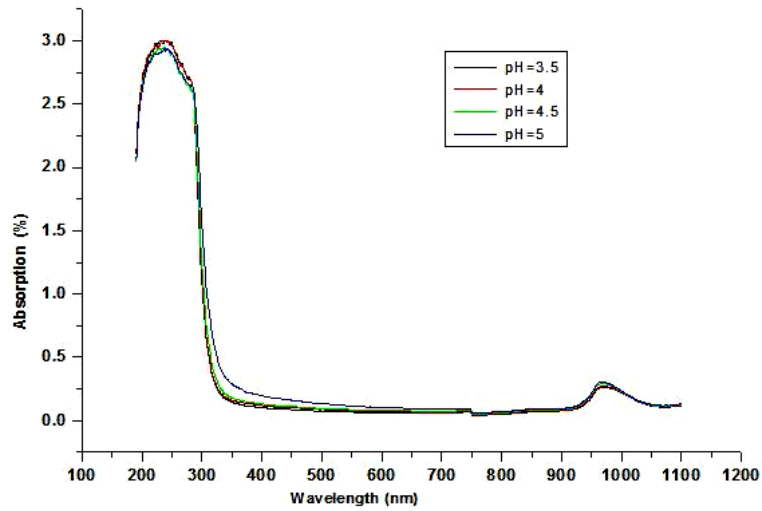


FIG. 7. Optical absorbance spectra of ZnS films deposited at different pH solution

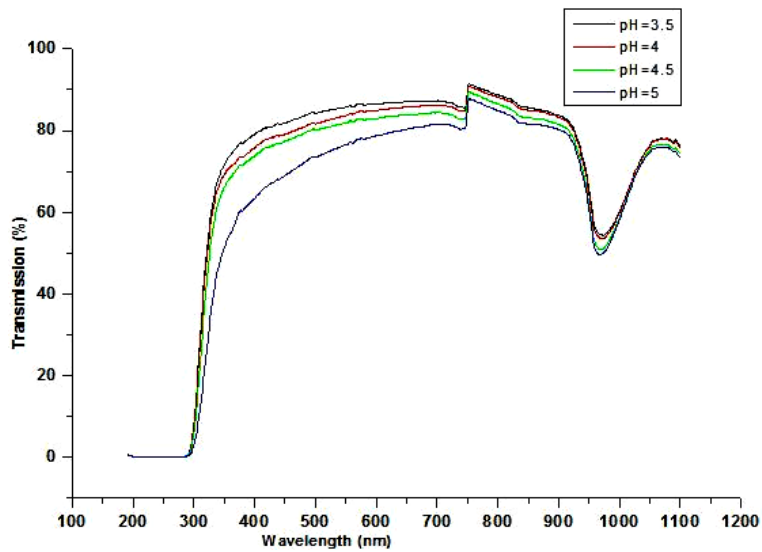


FIG. 8. Optical transmittance spectra of ZnS films deposited at different pH solution

Figure 11 shows transmittance spectra of ZnS particles with various thicknesses. It has been observed that 80 % transmittance occurs for all thickness above wavelengths of 350 nm. The maximum absorption at various layer thicknesses was found to be at wavelengths lower than 350 nm.

Figure 12 shows the optical band gap energies for various particle layer thicknesses. The optical band gap energy of ZnS particles of various thicknesses were calculated by plotting graph  $(\alpha h\nu)^2$  versus  $h\nu$  [21]. The band gap values varied from 4.10 to 3.78 eV. Of varied thickness 2400 to 3920 nm. It showed band gap energy decreased with increased thickness of layer [22, 23]. The effect of thickness on band gap energy as shown in Table 2.

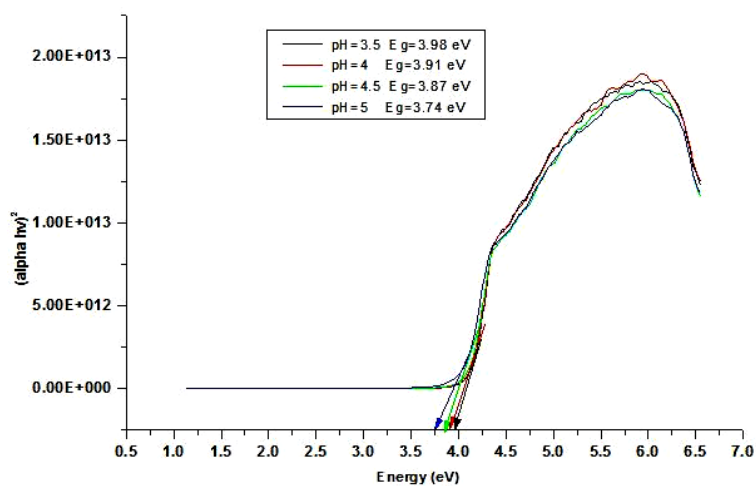


FIG. 9. Energy gap of ZnS films deposited with different pH solution

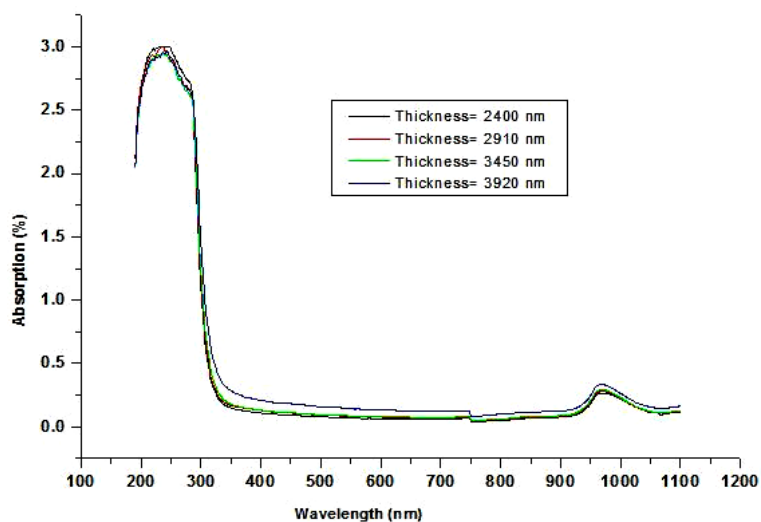


FIG. 10. Optical absorbance spectra of ZnS particles with different thickness

TABLE 2. Estimated values of band gap with different thickness of films

Sr. No.	Thickness of layer (nm)	Band gap energy (eV)
1	2400	4.10
2	2910	3.99
3	3450	3.90
4	3920	3.78

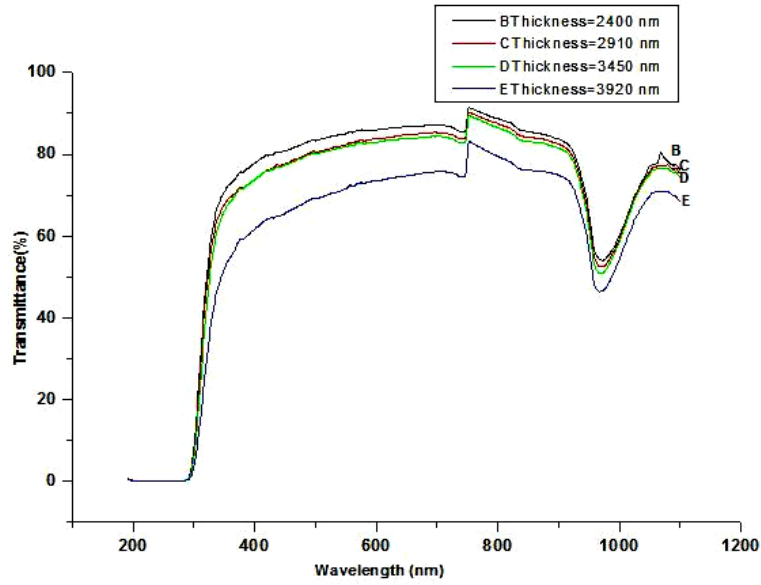


FIG. 11. Transmittance spectra of ZnS particles with different thickness

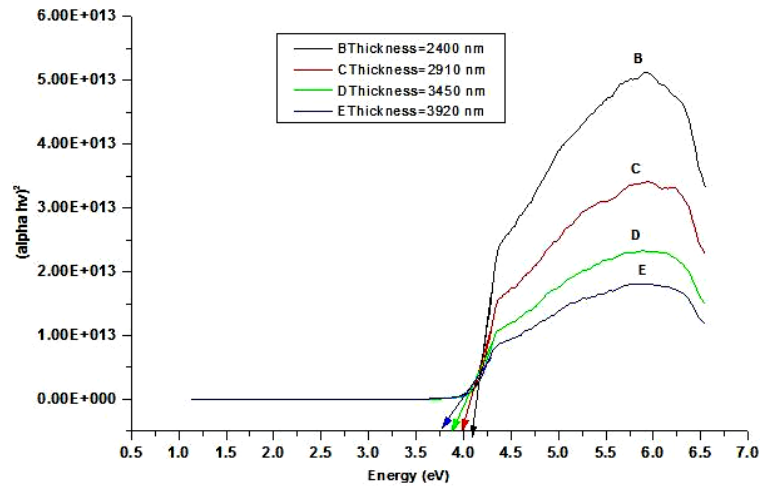


FIG. 12. Energy band gap of ZnS particles with different thickness

### 3.7. Electrical resistivity

A direct current two point probe technique in air was implemented for characterized the ZnS particles resistivity. The electrical resistivity was estimated by using eq. (3):

$$R = \frac{\rho \cdot L}{dW}, \quad (5)$$

where  $R$  – resistance of film,  $\rho$  – resistivity of film,  $L$  – length of rectangular substrate,  $dW$  – element of width.

The resistivity of particles depends on resistance of layer and its thickness. It has been observed that a change in thickness of layer gives variation in electrical resistivity.

The resistivity of various layer thicknesses estimated as shown in Table 3.

It confirmed the resistivity of ZnS particles decreases from  $1.782 \cdot 10^6$  to  $0.462 \cdot 10^6$  ( $\Omega$ -cm) as layer thickness increases from 2400 to 3920 nm, due to the improved crystallinity of ZnS particles. The size effect in semiconductor thin films was introduced for this behavior. Fig. 13 shows the variation of resistivity with thickness of ZnS particles.

The ZnS particles deposited on substrate with high concentration of  $\text{Zn}^{2+}$  ions as compared to S ions and this is n-type ZnS film hence it has been observed in edax spectra as Zn:S =9.24:1.

TABLE 3. Illustrate the variation of electrical resistivity with thickness of ZnS particles layer

Sr.No.	Thickness of layer (nm)	Resistivity ( $\Omega\cdot\text{cm}$ )
1	2400	$1.782 \cdot 10^6$
2	2910	$1.396 \cdot 10^6$
3	3450	$0.868 \cdot 10^6$
4	3920	$0.462 \cdot 10^6$

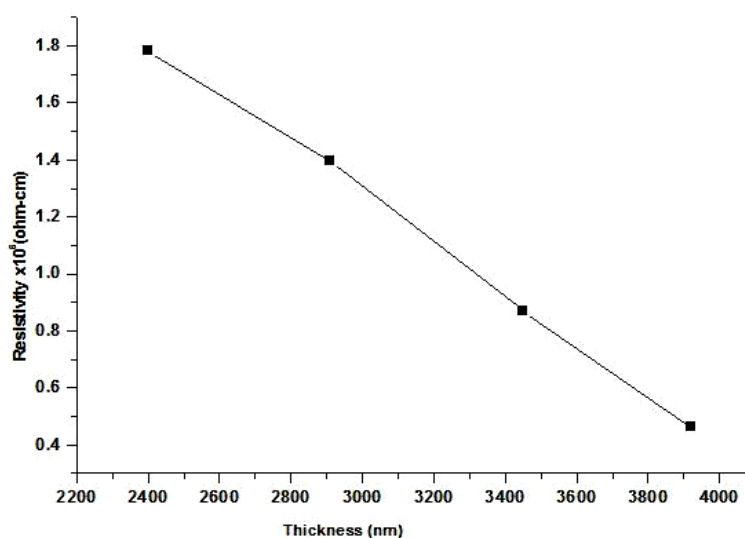


FIG. 13. Variation of resistivity with film thickness of ZnS films

During the growth process of ZnS, not only the Zn and S were found, but also the presence of oxygen appeared, actually there was a significant amount of oxygen present in the ZnS layer. The impure Zn included in deposited layer because ZnS include oxygen element. There is impact of this additional phase on electrical behavior. The resistivity value decreases as the oxygen content is increased in ZnS. It maybe owing to the higher defect existed in ZnS and surface state density existed in the higher oxygen incorporated. The thickness of the layer increases when more oxygen is introduced in ZnS and resistivity will decrease.

#### 4. Conclusion

The ZnS particles were successfully deposited on FTO/stainless steel substrate by an electrode position technique in the presence of triethanolamine as complexing agent. By using scanning electron microscope and UV-Visible spectrophotometer ZnS layers were studied. The SEM images showed that the layer was found good quality and fully substrate coverage at 4 % triethanolamine as compared to film in absence of triethanolamine. The effects of pH on surface morphology, optical properties of ZnS particles were investigated. It was shown that the average crystalline nanorod diameter and band gap decreases with increasing the pH values in range 3.5 to 5. The crystalline nanorod diameter of ZnS particles were found to be between 160.12 – 40.22 nm. The pH values were found to be responsible for crystal defect. The optical band gap values of ZnS particles were found to be 3.98 to 3.74 eV. The thickness of layer was also affected on optical properties. The thickness of layer varied from 2400 to 3920 nm. The optical band gaps were found to range from 4.10 to 3.78 eV. The thickness of layer increases with decreasing band gap energy. The complexing agent, pH of solution and thickness has an important role in controlling morphological and optical properties of the ZnS particles layer. The resistivity of layer was found to thickness dependent. The thickness of layer ranged from 2400 to 3920 nm the resistivity were measured in range  $1.782 \cdot 10^6$  to  $0.462 \cdot 10^6$  ( $\Omega\cdot\text{cm}$ ). It confirmed that the resistivity of layer decreases as layer thickness increases.

## Acknowledgements

The authors wish to thank the Physics Research centre M.S.G. College Malegaon camp Malegaon for giving instrument facilities to carry out this research work. Authors also thanks to SAIF IIT Madras and The CIF, Savitribai phule Pune University for providing EDAX and SEM characterization results.

## References

- [1] Farjami Shayesteh S., Kolahi S., Azizian Kalandarragh Y. Effect of pH on structural and optical properties of ZnS nanoparticles embedded in PVA matrix. *Indian journal of pure and applied physics*, 2013, **51**, P. 780–783.
- [2] Aybek A.S., Ruzgar H. Effect of the pH on crystal structure, optical and surface morphological properties of the CdS films deposited by chemical bath deposition. *Chalcogenide Letters*, 2016, **13** (8), P. 339–350.
- [3] Guzeldir B., Saglam M., Ates A. Deposition and characterization of CdS, CuS and ZnS thin Films deposited by SILAR method. *Proceedings of the International Congress on Advances in Applied Physics and Materials Science*, Antalya, 2012, **121**, P. 33–35.
- [4] Nabyouni G., Sahraei R. et al. Preparation and characterization of nanostructures thin films grown on glass and n-type Si substrates using a new chemical bath deposition technique. *Rev. Adv. Mater. Sci.*, 2011, **27**, P. 52–57.
- [5] Echendu, Weerasinghe O.K., et al. Characterization of n-type and p-type ZnS thin layers grown by an electrochemical method. *J. Electron. Mater.*, 2013, **42**, P. 692–700.
- [6] Miyawaki T., Ichimura M. Fabrication of ZnS thin films by an improved photochemical deposition method and application to ZnS/SnS heterojunction cells. *Mater. Lett.*, 2007, **61**, P. 4683–4686.
- [7] Saravanan Nagalingam, Geok Bee Teh, Rong-Fuh Louh, Kai Tung Chee. Cyclic voltammetry studies of cadmium zinc sulfide aqueous solution. *International Journal of the Physical Sciences*, 2011, **6** (31), P. 7166–7170.
- [8] Ojo A.A., Dharmadasa I.M. Analysis of the electronic properties of all-electroplated ZnS, CdS and CdTe graded bandgap photovoltaic device configuration. *Sol. Energy*, 2017, **158**, P. 721–727.
- [9] Olusola O.I., Madugu M.L., Dharmadasa I.M. Investigating the electronic Properties of multi-junction ZnS/CdS/CdTe graded band gap solar cells. *Mater. Chem. Phys.*, 2016, **191**, P. 145–150.
- [10] Kassim A., Tan W.T., Ho S.M., Saravanan N. Influence of pH on the structural and morphological properties of ZnS thin films. *Anadolu University Journal of Science and Technology A*, 2010, **11** (1), P. 17–22.
- [11] Senthil Kumar Vellingiri. Study on physical properties of ZnS thin films prepared by chemical bath deposition. *Asia Pacific Journal of Research*, 2013, **1** (8), P. 5–14.
- [12] Chung H.V., Huy P.T., An T.T. Synthesis and optical properties of ZnS Nanostructures. *Journal of the Korean Physical Society*, 2008, **52**, 1562.
- [13] Acharya S.A., Maheshwari N., et al. Ethylenediamine-mediated wurtzite phase formation in ZnS. *Cryst. Growth Des.*, 2013, **13**, 1369.
- [14] Dutta A., Panda S.K., Chaudhuri S. Phase transformation and optical properties of Cu-doped ZnS nanorods. *Journal of Solid State Chemistry*, 2008, **181**, 2332.
- [15] Nabyony G., Sahraei R., et al. Preparation and characterization of nanostructured ZnS thin films grown on glass and n-type Si substrates using a new chemical bath deposition technique. *Rev. Adv. Mater. Sci.*, 2011, **27**, P. 52–57.
- [16] Ben Bacha K., Timoumi A., Bitri N., Bouzouitastructural H. Morphological and optical properties of sprayed ZnS thin films on various substrate natures. *Optik*, 2015, **126** (21), P. 3020–3024.
- [17] Ghezali K., Mentar L., Boudine B., Azizi A. Electrochemical deposition of ZnS thin films and their structural, morphological and optical properties. *Journal of Electro Analytical Chemistry*, 2017, **794**, P. 212–220.
- [18] Azmand A., Kafashan H. Physical and electrochemical properties of electrodeposited undoped and Se-doped ZnS thin films. *Ceramics International*, 2018, **44** (14), P. 17124–17137.
- [19] Azmand A., Kafashan H. Al-doped ZnS thin films: physical and electrochemical characterizations. *Journal of Alloys and Compounds*, 2019, **779**, P. 301–313.
- [20] Seyed Mostafa Mosavi, Hosein Kafashan. Physical properties of Cd-doped ZnS thin films. *Superlattices and Microstructures*, 2019, **126**, P. 139–149.
- [21] Asghar M., Mahmood K., et al. Effect of annealing temperature on the structural and optical properties of ZnS thin films. *Materials Today*, 2015, **2**, P. 5430–5435.
- [22] Lopez M.C., Espinos J.P., et al. Growth of ZnS thin films obtained by chemical spray pyrolysis: the influence of precursors. *Journal of Crystal Growth*, 2005, **285** (1–2), P. 66–75.
- [23] Hernandez-Fenollosa M.A., Lopez M.C., et al. Role of precursor on morphology and optical properties of ZnS thin films prepared by chemical spray pyrolysis. *Thin Solid Films*, 2008, **516**, P. 1622–1625.

## A facile low-temperature deposition of Sn-rich tin (II) monosulfide colloid particles

N. S. Kozhevnikova<sup>1</sup>, L. N. Maskaeva<sup>2,3</sup>, E. E. Lekomtseva<sup>2</sup>, L. A. Pasechnik<sup>1</sup>, A. Yu. Chufarov<sup>1</sup>,  
O. A. Lipina<sup>1</sup>, A. N. Enyashin<sup>1</sup>, V. F. Markov<sup>2,3</sup>

<sup>1</sup>Institute of Solid State Chemistry of Ural Branch of the Russian Academy of Sciences, Pervomayskaya, 91,  
Ekaterinburg, 620990, Russia

<sup>2</sup>Ural Federal University named B. N. Yeltsin, Mira, 9, Ekaterinburg, 620002, Russia

<sup>3</sup>Ural Institute of State Fire Service of EMERCOM of Russia, Mira str. 22, 620062, Ekaterinburg  
kozhevnikova@ihim.uran.ru, larisamaskaeva@yandex.ru, danserkatya13@mail.ru, pasechnik@ihim.uran.ru,  
circulchufa@gmail.com, lipinaolgaa@yandex.ru, enyashin@ihim.uran.ru, v.f.markov@urfu.ru

PACS 81.10.Dn, 82.60.Lf, 82.70.Dd, 81.05.Hd

DOI 10.17586/2220-8054-2020-11-5-529-536

A novel, eco-friendly and low temperature synthesis of tin (II) monosulfide colloid particles is described. Chemical bath deposition was successfully applied for the deposition of polynanocrystalline SnS from acidic aqueous solutions. The characterization of the prepared samples was accomplished through elemental analysis, scanning electron microscopy, X-ray powder diffraction, and optical spectroscopy. The composition of tin (II) monosulfide colloids assembled of nanoparticles was found to be Sn-rich. Several simple scenarios for Sn surplus within SnS lattice (S-vacancies at S-sublattice, Sn-atoms intercalated between SnS layers and Sn-doping of S-sites) have been analyzed by means of quantum chemical calculations. The potential application of the Sn<sub>1+x</sub>S colloid particles in solar cells as absorber material and as photocatalyst was demonstrated by measuring the optical properties.

**Keywords:** tin (II) sulfide, chemical bath deposition, optical band gap, Sn-rich.

*Received: 18 September 2020*

### 1. Introduction

Metal sulfides represent one of the most important compounds among chalcogenide semiconductor materials due to their unique chemical and electronic properties. SnS is typically a *p*-type semiconductor with ideal parameters for solar cell absorbers. SnS has attracted much attention in the solar energy conversion due to its near-optimal direct band gap ( $E_g \sim 1.3$  eV) [1], a high absorption coefficient of  $\sim 10^4$ – $10^5$  cm<sup>-1</sup> [2] for photons with energies greater than the bandgap energy, the high hole densities of  $10^{15}$ – $10^{18}$  cm<sup>-3</sup> and mobilities  $\sim 90$  cm<sup>2</sup>/(Vs) [3]. Recently, SnS has also been proven to be an attractive photocatalyst for dye degradation under visible light [4] and for photoelectrochemical splitting of water [5]. The constituent elements, Sn and S, are nontoxic, cost affordable and relatively abundant in nature. Diverse methods for SnS deposition have been developed including vacuum and chemical deposition techniques, namely, vacuum evaporation [6], sputtering [7], vapor transport deposition and epitaxy [8], atomic layer deposition [9], sulfurization of Sn metal films [10], chemical spray pyrolysis [1,11], electrochemical deposition [3,12] and bath deposition [13,14]. Though, these numerous approaches are capable for producing thin film materials only.

Recently, the synthesis of SnS in the form of nanocrystals and quantum dots through a single-source precursor route has attracted much attention because of its potential advantages and possibility to tune the size, size distribution, and morphologies of the powder products by controlling the reaction conditions [15]. The precursors employed are usually metal complexes prepared from a Sn salt and ligands in organic media. In the present work, colloid nanoparticles of tin (II) monosulfide have been grown by the chemical bath deposition (CBD) technique. CBD is a solution-based technique providing simple and low-cost pathway to produce both uniform, adherent, reproducible large area thin films and nanostructured powders. CBD is based on the reaction between metal salt and sulfur agent in aqueous solutions. The structural and optical properties of CBD-deposited SnS colloid particles have been studied with the objective to establish the optimum parameters for forming single phase nanostructured SnS for application as a photo-absorber layer in solar cells and in natural sunlight-driven photocatalytic processes.

### 2. Experimental

#### 2.1. Synthesis and characterization

The nanostructured SnS colloid particles were precipitated by chemical bath deposition. The SnS-1, SnS-2, SnS-3 and SnS-4 samples were synthesized over 30, 60, 90 and 120 min, respectively. The aqueous solutions of tin chloride SnCl<sub>2</sub> (0.06 M) and sodium thiosulfate Na<sub>2</sub>S<sub>2</sub>O<sub>3</sub> (0.06 M) were used as Sn<sup>2+</sup> and S<sup>2-</sup> sources. In order to adjust the concentration of free Sn<sup>2+</sup> cations, the complexing agent sodium citrate Na<sub>3</sub>Cit was added into the reaction mixture.

The pH value was maintained at  $4.6 \pm 0.2$ . All used chemical reagents were of analytical grade and used without further purification. After SnS deposition, the powders were taken out of the beaker, filtered, washed with distilled water and dried in air at ambient temperature.

Scanning electron microscopy (SEM) images were recorded on a scanning electron microscope JEOL-JSM LA 6390 at 20 kV. Energy dispersive X-ray (EDX) analysis was performed by using a JEOL JED-2300 detector. X-ray powder diffraction (XRPD) patterns were collected on Shimadzu XRD-7000 automatic diffractometer ( $\text{CuK}\alpha$  radiation) in the angle range  $2\theta$  of  $5\text{--}80^\circ$  with step  $0.03^\circ$  and an exposure time of 5 sec. The unit cell parameters of SnS were refined by Rietveld method using XRD data. The diffuse reflectance spectra of the SnS powders were recorded on a Shimadzu UV-3600 UV-VIS-NIR spectrophotometer using  $\text{BaSO}_4$  as a reference.

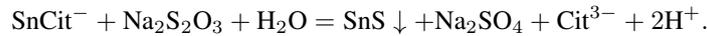
## 2.2. Computational details

The DFT calculations were performed using the SIESTA 4.0 implementation [16, 17]. Generalized Gradient Approximation (GGA) with the Perdew–Burke–Ernzerhof parametrization was used for description of exchange–correlation potential. The core electrons were treated within the frozen core approximation, applying norm-conserving Troullier–Martins pseudopotentials. In all calculations, the double- $\zeta$  basis set was used. The k-point mesh was generated by the method of Monkhorst and Pack with a cutoff  $15 \text{ \AA}$  for the k-point sampling. The real-space grid used for the numeric integrations was set to correspond to the energy cutoff of 300 Ry. All calculations were performed using variable-cell and atomic position relaxations, with convergence criteria corresponding to the maximum residual stress of 0.1 GPa for each component of the stress tensor, and the maximum residual force component of  $0.01 \text{ eV/\AA}$ .

## 3. Results and discussion

### 3.1. Concentration regions of SnS solid phase formation by CBD

The formation of SnS solid phase during CBD is a complex multistage process, which is based on the chemical reaction between a complex tin ion  $\text{SnCit}^-$  and a sulfide ion  $\text{S}^{2-}$  released during the hydrolytic decomposition of  $\text{Na}_2\text{S}_2\text{O}_3$ . The chemical reaction can be represented as follows:



The concentration regions for the formation of SnS and competitive hydroxide phase  $\text{Sn(OH)}_2$  as impurity were calculated for the “ $\text{SnCl}_2 - \text{Na}_3\text{Cit} - \text{Na}_2\text{S}_2\text{O}_3$ ” system (Fig. 1). The determination of the minimum concentration of metal salt  $C_{in}$  required for solid phase either SnS (1) or  $\text{Sn(OH)}_2$ (2) depositions was carried out using the relations:

$$pC_{in} = pK_{sp,SnS} - p\alpha_{Sn^{2+}} - \left( \frac{1}{2}pK_{TS} - \text{pH} + \frac{1}{2}p \left[ \text{S}_2\text{O}_3^{2-} \right]_{in} \right) - \frac{0.86 \cdot \sigma \cdot V_M}{R \cdot T \cdot r_{cr}}, \quad (1)$$

$$pC_{in} = pK_{sp,Sn(OH)_2} - p\alpha_{Sn^{2+}} - 2pK_w + 2\text{pH}, \quad (2)$$

where  $p$  is the negative decimal logarithm;  $K_{sp,SnS} = 6.92 \cdot 10^{-30}$  is the SnS solubility product;  $\alpha_{Sn^{2+}}$  is the fractional concentration of free  $\text{Sn}^{2+}$  ions;  $K_{TS} = 1.99 \cdot 10^{-27}$  is the constant of  $\text{Na}_2\text{S}_2\text{O}_3$  hydrolytic decomposition;  $[\text{Na}_2\text{S}_2\text{O}_3]_{in}$  is the initial  $\text{Na}_2\text{S}_2\text{O}_3$  concentration in solution;  $\sigma = 1.75 \text{ J/m}^2$  is the SnS specific surface energy;  $V_M = 28.88 \text{ kg/m}^3$  is the molar volume of synthesized SnS phase;  $r_{cr}$  is the radius of the nucleus of critical size,  $3.2 \text{ nm}$ ;  $R$  is the universal gas constant;  $T$  is the bath temperature;  $pK_{sp,Sn(OH)_2} = 6.31 \cdot 10^{-27}$  is the  $\text{Sn(OH)}_2$  solubility product;  $K_w$  is the  $\text{H}_2\text{O}$  ionic product [18, 19].

As shown in Fig. 1, the presence of the  $\text{Na}_3\text{Cit}$  ligand with the concentration of  $0.15 \text{ M}$  may lead to the co-precipitation of SnS and  $\text{Sn(OH)}_2$  solid phases in the pH range from 6 to 12, while  $C_{in}$  remains constant with a change of  $\text{Na}_2\text{S}_2\text{O}_3$  concentration from  $0.05$  to  $0.2 \text{ M}$ . Thermodynamic calculations and the plotted dependence in three-dimensional coordinates “ $pC_{in} - [\text{Na}_2\text{S}_2\text{O}_3] - \text{pH}$ ” showed that the acidic region  $\text{pH} = 3\text{--}5$  is the most preferable for obtaining solid phase of SnS.

### 3.2. Phase identification

The as-deposited layers were brownish black. The XRPD patterns of the SnS particles synthesized at different times are given in Fig. 2. The XRPD data showed the colloid particles to be tin(II) monosulfide SnS. The characteristic diffraction lines (111), (131) and (141) at  $2\theta$  positions  $31.8^\circ$ ,  $38.4^\circ$  and  $44.7^\circ$  match with the JCPDS reference database # 00-039-0354, which is herzenbergite SnS or  $\alpha$ -SnS (orthorhombic; space group  $Pnma$ ). The unit cell parameters were estimated to be  $a = 11.290(8) \text{ \AA}$ ,  $b = 3.989(3) \text{ \AA}$ ,  $c = 4.280(3) \text{ \AA}$ ; cell volume =  $192.8(3) \text{ \AA}^3$ . No other impurities were found in the samples, indicating that the products are a pure SnS phase. The average crystalline sizes in the SnS-1, SnS-2, SnS-3 and SnS-4 samples were determined as 19, 21, 23 and 20 nm, respectively. The change of crystallite size with deposition time was insignificant. This can be attributed to a rapid growth of the SnS crystallites during the first 30 min of CBD process. A longer deposition time is inefficient to produce the larger particles.

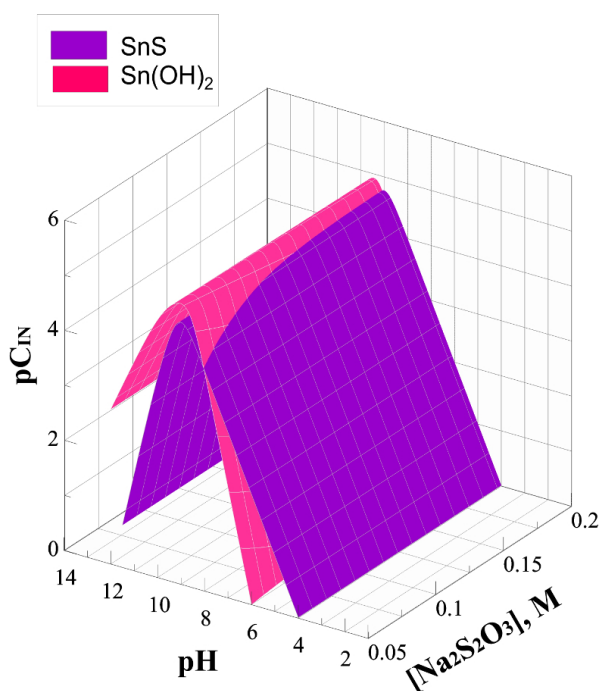


FIG. 1. Schematic diagram of concentration regions for formation of SnS and Sn(OH)<sub>2</sub> solid phases. The calculations were carried out at different initial pH and Na<sub>2</sub>S<sub>2</sub>O<sub>3</sub> concentration for the “SnCl<sub>2</sub>–Na<sub>3</sub>Cit–Na<sub>2</sub>S<sub>2</sub>O<sub>3</sub>” system at  $T = 298$  K

### 3.3. Grain morphology and elemental composition

The morphology and microstructure of SnS samples synthesized by CBD were visualized by scanning electron microscopy. The typical SEM micrograph shown in Fig. 3a corresponds to the powder SnS-1 synthesized during 30 min. Fig. 3 reveals that synthesized powders consist of nearly spherical particles of similar sizes  $\sim 1$   $\mu\text{m}$ . Taking into account the XRPD data, the observed SnS colloid particles are polycrystals assembled of nanoparticles with the size of about 19 nm. The EDX analysis (Fig. 3b) confirmed that particles consist of tin, sulfur and oxygen with an average content of  $53 \pm 1$ ,  $42 \pm 1$ , and  $5 \pm 1$  at.%, respectively. The presence of oxygen might be due to water molecules adsorbed on the surface of SnS nanoparticles.

Therefore, the synthesized SnS colloid particles are found also to be Sn-rich. Despite of the initial reaction bath had an equimolar Sn<sup>2+</sup>/S<sub>2</sub>O<sub>3</sub><sup>2-</sup> ratio, the disclosure of Sn-rich particles suggest a partial reduction of Sn atoms embedded in SnS lattice through the reactions of Sn<sup>2+</sup> + 2e = Sn<sup>0</sup> ( $E = -0.140$  V) and 2SO<sub>4</sub><sup>2-</sup> + 10H<sup>+</sup> + 8e = S<sub>2</sub>O<sub>3</sub><sup>2-</sup> + 5H<sub>2</sub>O ( $E = 0.29$  V) [17]. Hence, it appeals that correct chemical formula for the synthesized colloid particles might be written here and thereafter as Sn<sub>1+x</sub>S (Fig. 3).

### 3.4. Optical properties

The diffuse reflectance spectra of the SnS-1, SnS-2, SnS-3, and SnS-4 samples measured at 780–1800 nm wavelength range are presented in Fig. 4. The synthesized Sn<sub>1+x</sub>S colloid particles do not absorb radiation with  $\lambda = 1450$ –1800 nm; and the diffuse reflectance is approximately 100 % in this spectral region. However, at  $\lambda < 1450$  nm the significant decrease in the diffuse reflectance value takes place. The observed wide absorption band may be divided into two components at 780–880 nm and 880–1450 nm, and the contribution of the latter increases with the deposition time.

The diffuse reflectance data were analyzed to determine the optical band gap energy ( $E_g$ ) of the samples. For a long time SnS had been considered as either direct and indirect allowed transition material until DFT calculations of electronic band structure of SnS in the bulk form as well as the in the bilayer and monolayer limit were performed [20–22]. Calculations showed that the bulk and bilayer SnS have an indirect band gap, while for the monolayer possible direct transitions that are close in energy to the indirect gaps occur. Thus, the  $E_g$  value was estimated taking into account the indirect allowed type of transitions. For this purpose, the Kubelka-Munk functions [23] were calculated

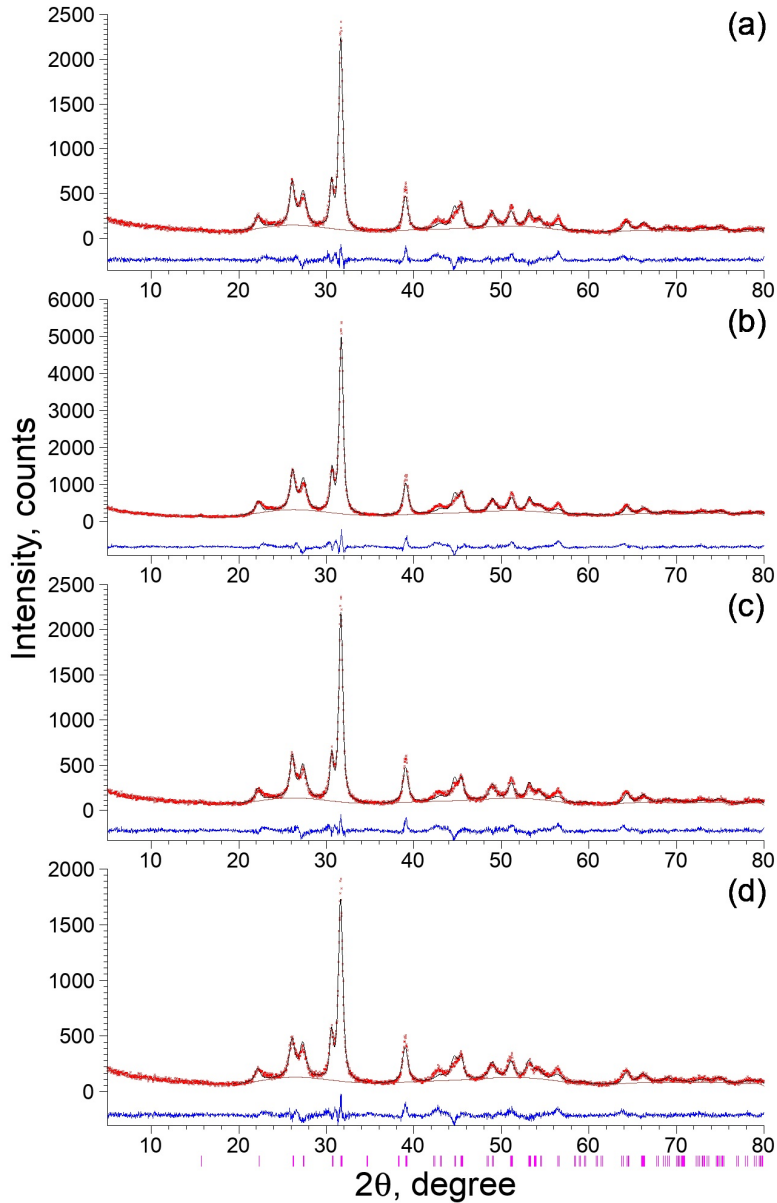


FIG. 2. The X-ray spectra of as-deposited SnS colloid particles obtained at different deposition times: (a) SnS-4 (120 min), (b) SnS-3 (90 min), (c) SnS-2 (60 min), (d) SnS-1 (30 min)

using equation (3) and then the appropriate dependences  $[F(R)h\nu]^{1/2}$  versus  $h\nu$  were plotted.

$$F(R_\infty) = \frac{(1 - R_\infty)^2}{2R_\infty} = \frac{k}{s}, \quad (3)$$

where  $F(R_\infty)$  is the diffuse reflectance of a sample relative to the reference,  $k$  is the molar absorption coefficient, and  $s$  is the scattering coefficient.

The results of the graphic determination of  $E_g$  values are presented in the inset of Fig. 4. It has been revealed that all curves have linear parts at 1.41–1.44 eV. The found  $E_g$  value is 1.34 eV for the all studied samples [20]. This value is close to  $E_g = 1.24$  eV calculated for bulk SnS and is consistent with the reported experimental values of 1.05–1.47 eV [7, 21, 24, 25]. The  $E_g$  value of SnS may depend significantly on the degree of crystallinity, particle size and the stoichiometry of the samples. In a number of studies [1, 26] the change in the optical absorption edge of SnS was attributed to the presence of other phases like SnO<sub>2</sub> ( $E_g = 2.3 - 3.5$  eV), SnS<sub>2</sub> ( $E_g = 2.44$  eV) and Sn<sub>2</sub>S<sub>3</sub> ( $E_g = 2.0$  eV). Since no regions of decreasing reflectance at these energies are observed, the possible formation of the

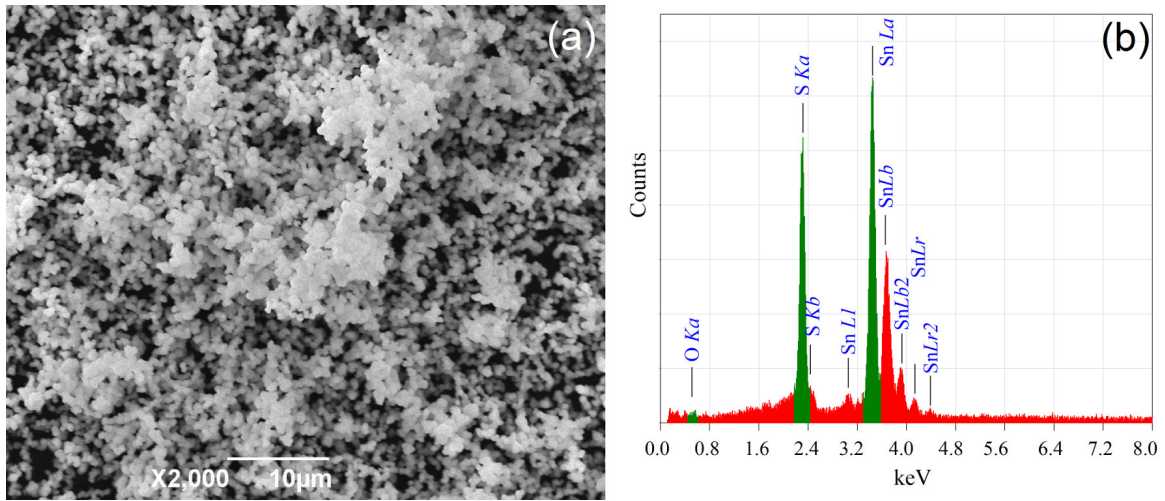


FIG. 3. The typical SEM image of  $\text{Sn}_{1+x}\text{S}$  colloid particles (a); EDX analysis (b) is presented for the SnS-1 sample synthesized during 30 min

aforementioned impurity phases may be excluded from consideration. These results are well matched with the XRPD observations.

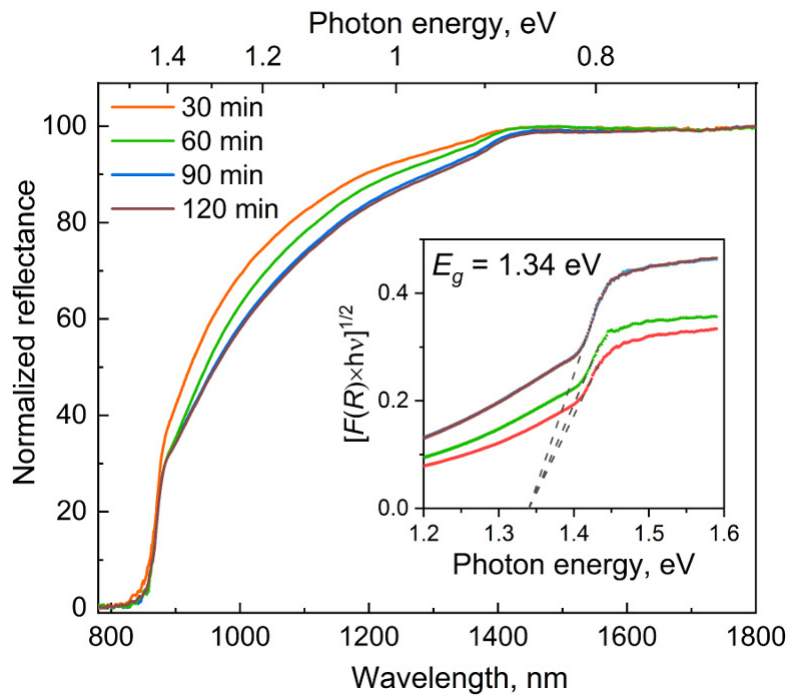


FIG. 4. Diffuse reflectance spectra for polycrystalline  $\text{Sn}_{1+x}\text{S}$  colloid particles obtained after different precipitation times. The inset shows the determination of the optical band gap energy

### 3.5. DFT computational data

A considerable 5–10% Sn-excess has been registered in our SnS samples by means of EDX analysis, which surely exceeds experimental error in the detection and to ascribe the composition as Sn-rich SnS -  $\text{Sn}_{1+x}\text{S}$ . No considerable distortion of the  $\alpha$ -SnS crystallattice has been established using XRPD method, which allows us to propose several simple scenarios for Sn surplus based on the same lattice: the most obvious S-vacancies at S-sublattice, Sn-atoms intercalated between SnS(001) layers and the non-trivial Sn-doping of S-sites.

Since the exact scenario cannot be definitively determined by means of the used characterization techniques, the DFT calculations have been employed preliminarily. The  $1 \times 2 \times 2$  and  $1 \times 3 \times 3$  supercells of  $\alpha$ -SnS were employed as

parent models of  $\text{Sn}_{1+x}\text{S}$  compounds. The lattice parameters of pristine  $\alpha$ -SnS crystal can be found in fair agreement with experimental data as  $a = 11.42 \text{ \AA}$ ,  $b = 4.05 \text{ \AA}$  and  $c = 4.33 \text{ \AA}$ . A modification of the lattice by Sn surplus in amount of  $x = 0.05$ – $0.07$  does lead to an essential modulation of the lattice parameters. The most prominent variation is observed for  $c$ -parameter: shrinking on 1.5% for  $\text{Sn}_{1+x}\text{S}$  with S-vacancies or with Sn-intercalants and expanding on 0.8 % for  $\text{Sn}_\text{S}$ -substituents. The  $a$ -parameter increases on 12.7 % for Sn-intercalated  $\text{Sn}_{1+x}\text{S}$ , where Sn-intercalants adapt atypical double coordination and the Sn-S bond length equal to  $2.78 \text{ \AA}$ . In the remaining cases, both  $a$ - and  $b$ -parameters remain insensitive to a given  $x$ .

The relative stabilities of all three types of  $\text{Sn}_{1+x}\text{S}$  compounds have been estimated using the formation enthalpy  $\Delta H$  at  $T = 0 \text{ K}$ , calculated as the difference between the DFT total energies of a  $\text{Sn}_{1+x}\text{S}$  composition and of elements as  $\beta$ -Sn and cyclo- $\text{S}_8$ . In general, the data give proof for the thermodynamic destabilization of the SnS lattice upon any Sn-overdose, though, to different extents depending on  $x$  (see Fig. 5). Namely, Sn-intercalates  $\text{Sn}_{1+x}\text{S}$  are characterized thermodynamically as the least stable, what should be an exclusion factor else in addition to the easily accessible Sn-intercalants for water solvent, hence, to enhanced reactivity of such  $\text{Sn}_{1+x}\text{S}$  in experiment. Sulfur-deficient  $\text{Sn}_{1+x}\text{S}$  compositions seem thermodynamically more stable, yet, unexpectedly losing in front of  $\text{Sn}_\text{S}$ -substituted  $\text{Sn}_{1+x}\text{S}$ . The latter compositions appear the most stable in all range of considered  $x$  up to 0.12–0.15. Probably, their stability is promoted by similarity in local environment of Sn-atom placed at S-site of SnS lattice and that within the lattice of elemental  $\beta$ -Sn: both have a distorted octahedral Sn-environment and the Sn-Sn bond lengths as  $3.09 \text{ \AA}$  and  $2.92$ – $3.22 \text{ \AA}$ , respectively. A higher resistance to water oxidation could be also expected for such Sn-doping atoms due to preserved interplane SnS(100) distances as in pristine SnS and protection from SnS layers (i.e. from both basal and lateral directions).

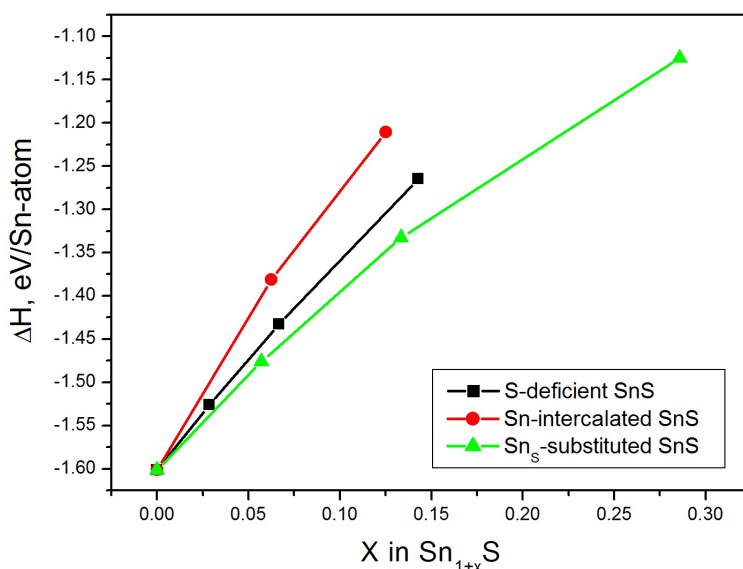


FIG. 5. Model formation enthalpies  $\Delta H$  (at  $T = 0 \text{ K}$ ) for different Sn-rich SnS compositions based on  $\alpha$ -SnS lattice: SnS with S-vacancies, SnS with intercalated Sn-atoms and SnS with Sn-doping into S-sites. DFT-GGA calculations

The calculated density of states (DOS) of pristine SnS and all types of  $\text{Sn}_{1+x}\text{S}$  are depicted in Fig. 6. Theoretically, SnS is a semiconductor with the band gap  $0.77 \text{ eV}$ . The band gaps are basically underestimated by classical DFT methods; however, this has no effect on their relative values and the character of DOS distribution. The bottom of the conduction band is dominated by  $\text{Sn}5p$ -states. The top of the valence band composed of the  $\text{S}3p$ -states with a considerable contribution of the  $\text{Sn}5s$ - and  $\text{Sn}5p$ -states. The low-lying separate band in the range from  $-6$  to  $-8 \text{ eV}$  is contributed mostly from the valence  $\text{Sn}5s$ -states. These main features of the DOS distribution are well preserved for the DOS profiles of  $\text{Sn}_{1+x}\text{S}$  compounds. However, the latter demonstrate distinct variety near the frontiers of the fundamental band gap. The least stable Sn-intercalated  $\text{Sn}_{1+x}\text{S}$  should be n-type semiconductor with the main band gap  $0.86 \text{ eV}$  and the donor impurity level at  $0.13 \text{ eV}$  below the bottom of conduction band of SnS. S-deficient  $\text{Sn}_{1+x}\text{S}$  should be also n-type semiconductor with the main band gap  $0.76 \text{ eV}$  and the deep donor level at  $0.33 \text{ eV}$  below the bottom of conduction band.  $\text{Sn}_\text{S}$ -substituted  $\text{Sn}_{1+x}\text{S}$  demonstrates a more sophisticated DOS splitting near Fermi level: the main band gap  $1.10 \text{ eV}$  hosts both donor and acceptor impurity levels at  $0.59 \text{ eV}$  and  $0.05 \text{ eV}$ , respectively, below the bottom of conduction band. Additionally, the  $\text{Sn}5s$ -band in the spectrum of this compound

possesses a distinct splitting of the Sn5s-levels at 0.23 eV deep, serving as a good indicator for the possible detection of Sn<sub>S</sub>-impurities in ongoing experimental characterization.

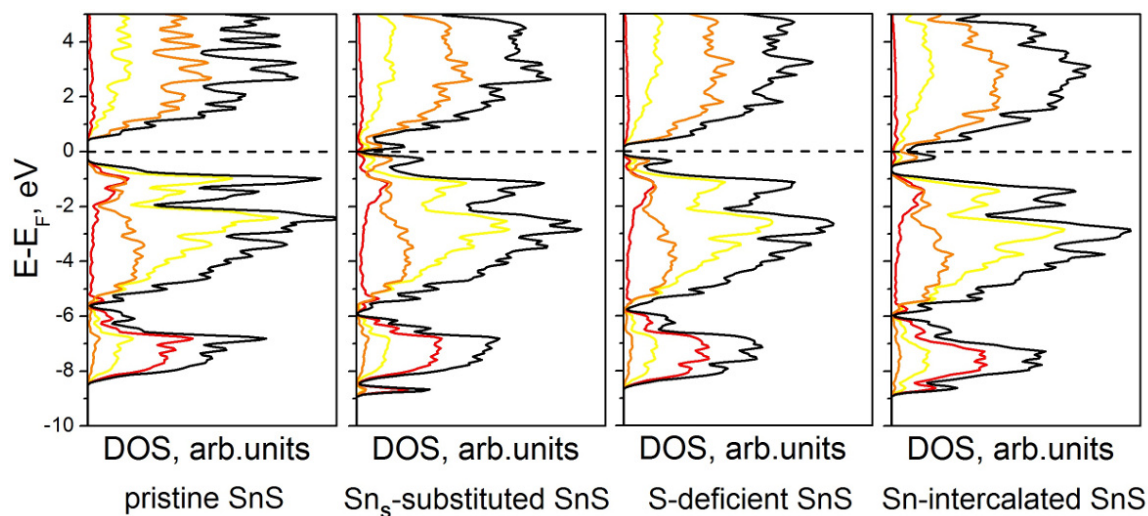


FIG. 6. Total and selected partial densities of states (DOS) for stoichiometric  $\alpha$ -SnS compound and different  $\alpha$ -S<sub>1+x</sub>S compounds. Total and partial Sn5s-, Sn5p- and S3p-DOS are drawn in black, red, orange and yellow, respectively. DFT-GGA calculations

#### 4. Conclusions

In summary, tin (II) monosulfide colloids assembled of nanoparticles were synthesized in aqueous media at low temperatures by a CBD technique. The XRPD approves the formation of orthorhombic SnS phase with the optical band gap energy of 1.34 eV. Synthesized SnS nanoparticles with crystallite size of 19–23 nm tend to cluster in aqueous solution to form larger aggregates, i.e. colloid particles, with an average size  $\sim 1\mu\text{m}$ . The composition of SnS was found to be Sn-rich due to the partial reduction of Sn<sup>2+</sup> cations by anions S<sub>2</sub>O<sub>3</sub><sup>2-</sup>. The chemical formula for the synthesized colloid particles might be written as Sn<sub>1+x</sub>S. The DFT calculations demonstrated Sn<sub>S</sub>-substituted Sn<sub>1+x</sub>S to be the most thermodynamically stable in all range of considered x up to 0.12–0.15. Based on the present experimental and theoretical study, we suggest that CBD-deposited SnS has some potential as an inexpensive, earth-abundant absorber material and photocatalyst for the degradation of organic compounds under sunlight. Furthermore, the resistivity of binary semiconductors is known to be strongly dependent on small deviations in stoichiometry. Sn-rich orthorhombic SnS may contribute to the superior electrochemical performance and may be applied for creating promising SnS-based anode materials for lithium-ion batteries [27]. Thus, our future work will focus on the electrochemical measurements with the aim of opening up a new opportunity for using CBD technique for the synthesis of SnS with regulated stoichiometry.

#### Acknowledgements

This work was performed in accordance with the scientific and research plans and state assignment of the ISSC UB RAS (theme AAAA-A19-119031890025-9) and by the Government of the Russian Federation (program 211, project No 02.A03.21.0006).

#### References

- [1] Reddy K.T.R., Reddy N.K., Miles R.W. Photovoltaic properties of SnS based solar cells. *Sol. Energy Mater. Sol. Cells*, 2006, **90**, P. 3041–3046.
- [2] Noguchi H., Setiyadi A., Tanamura H., Nagatomo T., Omoto O. Characterization of vacuum-evaporated tin sulfide film for solar-cell materials. *Sol. Energy Mater. Sol. Cells*, 1994, **35**(1-4), P. 325–331.
- [3] Mathews N.R., Anaya H.B.M., Cortes-Jacome M.A., Angeles-Chavez C., Toledo-Antonio J. A. Tin sulfide thin films by pulse electrodeposition: structural, morphological, and optical properties. *J. Electrochem. Soc.*, 2010, **157**(3), P. H337–H341.
- [4] Kabouche S., Bellal B., Louafi Y., Trari M. Synthesis and semiconducting properties of tin(II) sulfide: Application to photocatalytic degradation of Rhodamine B under sun light. *Materials Chem. Phys.*, 2017, **195**, P. 229–235.
- [5] Gao W., Wu C., Cao M., Huang J., Wang L., Shen Y. Thickness tunable SnS nanosheets for photoelectrochemical water splitting. *J. Alloys and Compounds*, 2016, **688**, P. 668–674.

- [6] Schneikart A., Schimper H.-J., Klein A., Jaegermann W. Efficiency limitations of thermally evaporated thin-film SnS solar cells. *J. Phys. D: Appl. Phys.*, 2013, **46**(30), P. 305109.
- [7] Hartman K., Johnson J.L., Bertoni M.I., Recht D., Aziz M.J., Scarpulla M.A., Buonassisi T. SnS thin-films by RF sputtering at room temperature. *Thin Solid Films*, 2011, **519**, P. 7421–7424.
- [8] Wangperawong A., Herron S.M., Runser R.R., Haagglund C., Tanskanen J.T., Lee H., Clemens B.M., Bent S.F. Vapor transport deposition and epitaxy of orthorhombic SnS on glass and NaCl substrates. *Appl. Phys. Lett.*, 2013, **103**, P. 052105.
- [9] Sinsersuksakul P., Heo J., Noh W., Hock A.S., Gordon R.G. Atomic layer deposition of tin monosulfide thin films. *Adv. Energy Mater.*, 2011, **1**, P. 1116–1125.
- [10] Ballipinar F., Rastogi A.C. Tin sulfide (SnS) semiconductor photo-absorber thin films for solar cells by vapor phase sulfurization of Sn metallic layers using organic sulfur source. *J. Alloys and Compounds*, 2017, **728**, P. 179–188.
- [11] Sajeesh T.H., Warriar A.R., Kartha C.S., Vijayakumar K.P. Optimization of parameters of chemical spray pyrolysis technique to get n and p-type layers of SnS. *Thin Solid Films*, 2010, **518**, P. 4370–4374.
- [12] Takeuchia K., Ichimuraa M., Araia E., Yamazaki Y. SnS thin films fabricated by pulsed and normal electrochemical deposition. *Sol. Energy Mater. Sol. Cells*, 2003, **75**, P. 427–432.
- [13] Pramanik P., Basu P.K., Biswas S. Preparation and characterization of chemically deposited tin(II) sulphide thin films. *Thin Solid Films*, 1987, **150**(2-3), P. 269–276.
- [14] Avellaneda D., Nair M.T.S., Nair P.K. Polymorphic tin sulfide thin films of zinc blende and orthorhombic structures by chemical deposition. *J. Electrochem. Soc.*, 2008, **155**, P. D517–D525.
- [15] Han Q., Wang M., Zhu J., Wu X., Lu L., Wang X. Great influence of a small amount of capping agents on the morphology of SnS particles using xanthate as precursor. *J. Alloys and Compounds*, 2011, **509**(5), P. 2180–2185.
- [16] Ordejon P., Artacho E., Soler J.M., Self-consistent order-N density-functional calculations for very large systems. *Phys. Rev. B*, 1996, **53**, P. R10441.
- [17] Soler J.M., Artacho E., Gale J.D., Garcia A., Junquera J., Ordejon P., Sanchez-Portal D. The SIESTA method for ab initio order-N materials simulation. *J. Phys. Condens. Matter*, 2002, **14**, P. 2745–2780.
- [18] Markov V.F., Maskaeva L.N., Ivanov P.N. *Hydrochemical deposition of metal sulfide thin solid films: modeling and experiment*. Ekaterinburg: UrB RAS, 2006, 217 p. (in Russian)
- [19] Lurie Ju.Ju. *Handbook of Analytical Chemistry*. Mir Publishers, 1975, 488 p.
- [20] Gomes L.C., Carvalho A. Phosphorene analogues: isoelectronic two-dimensional group-IV monochalcogenides with orthorhombic structure. *Phys. Rev.*, 2015, **B92**(8), P. 085406.
- [21] Titova L.V., Fregoso B.M., Grimm R.L. Chapter 5: Group-IV monochalcogenides GeS, GeSe, SnS, SnSe, in book Chalcogenide: From 3D to 2D and Beyond. *Woodhead Publishing Series in Electronic and Optical Materials*, 2020, P. 119–151.
- [22] Popov I.S., Kozhevnikova N.S., Enyashin A.N. Quantum-chemical study of structural and electronic properties of a new tin monosulfide polymorph  $\pi$ -SnS. *Doklady Physical Chemistry*, 2017, **472**(2), P. 23–26.
- [23] Kubelka P., Munk-Aussig F. Ein Beitrag zur Optik der Farbanstriche. *Z. Tech. Physik*, 1931, **12**, P. 593–601.
- [24] Reddy N.K., Hahn Y.B. Temperature-dependent structural and optical properties of SnS films. *J. Appl. Phys.*, 2007, **101**(9), P. 093522.
- [25] Parenteau M., Carlone C. Influence of temperature and pressure on the electronic transitions in SnS and SnSe semiconductors. *Phys. Rev. B*, 1990, **41**(8), P. 5227–5234.
- [26] Lopez S., Granados S., Ortiz A. Semicond. Spray pyrolysis deposition of Sn<sub>2</sub>S<sub>3</sub> thin films. *Sci. Technol.*, 1996, **11**(3), P. 433–436.
- [27] Zhang J., Cao D., Wu Y., Cheng X., Kang W., Xu J. Phase transformation and sulfur vacancy modulation of 2D layered tin sulfide nanoplates as highly durable anodes for pseudocapacitive lithium storage. *Chemical Engineering J.*, 2020, **392**, P. 123722(1-10).

## HRTEM, XPS and XRD characterization of ZnS/PbS nanorods prepared by thermal evaporation technique

B. Abadllah<sup>\*,1</sup>, B. Assfour<sup>2</sup>, M. Kakhia<sup>1</sup>, Ali Bumajdad<sup>3</sup>

<sup>1</sup>Atomic Energy Commission, Department of Physics. P. O. Box 6091, Damascus, Syria

<sup>2</sup>Atomic Energy Commission, Department of chemistry. P. O. Box 6091, Damascus, Syria

<sup>3</sup>Chemistry Department, Faculty of Science, Kuwait University, Safat 13060, Kuwait

\*pscientific27@aec.org.sy

PACS 61.46.+w

DOI 10.17586/2220-8054-2020-11-5-537-545

Zinc sulfide (ZnS) and zinc sulfide/lead sulfide (ZnS/PbS) nanorods were grown on glass substrates using a thermal evaporation method. The morphology of the prepared samples has been studied by transmission electron microscopy (TEM), field-emission scanning electron microscopy (FE-SEM) and Scanning Electron Microscopy (SEM). Both differences and similarities in morphology between the samples have been discovered. In the ZnS/PbS sample, ZnS nanorods were formed with diameter less than 50 nm and length between 2000 and 3000 nm. The pure ZnS sample has dense structure and its thickness was about 200 nm. Samples were studied in detail using energy-dispersive X-ray spectroscopy (EDX). The surface chemical compositions of the samples were confirmed by means of X-ray photoelectron spectroscopy (XPS). The determination of the crystal structure using the X-ray diffraction revealed that two phases of ZnS, blende and wurtzite, are present in the sample after adding Pb, while only blende is identified in the pure ZnS sample.

**Keywords:** nanorods, ZnS, HRTEM, XPS, thermal evaporation.

*Received:* 1 September 2020

*Revised:* 28 September 2020

### 1. Introduction

ZnS, ZnO, AlN and CN<sub>x</sub> nanotubes are envisaged to be highly promising for applications in semiconductors, photo detectors, lasers, solar cells, and -nanogenerators [1]. During the last decade zinc sulfide (ZnS) has been categorized as one of the most propitious semiconductor materials due to its wide device applications [2–8]. It is environmentally friendly, cheap and easy to prepare. The potential application of ZnS in solar cell applications is well established [9]. As is used as a buffer layer, the spectral response of the solar cell is increased. ZnS is a polymorphic solid, meaning it has the ability to exist in more than one crystal structure. It has a direct wide band gap of 3.2–3.9 eV at room temperature [10]. It appears as cubic (known zinc blende or sphalerite) or as a hexagonal wurtzite structure (Fig. 1). The blende form is the most common natural form of ZnS and it is almost identical to the Si unit cell with a band gap of 3.7 eV.

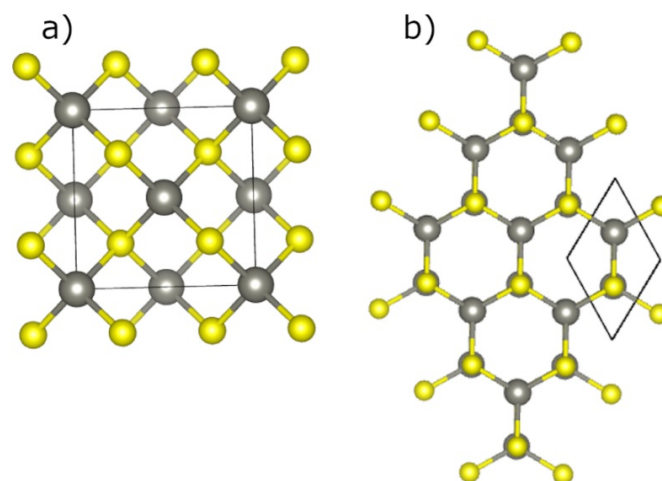


FIG. 1. The cubic unit cell of zinc blende (a) and the hexagonal unit cell of wurtzite (b). Sulfur and zinc atoms are represented as yellow and gray spheres, respectively

Several methods have been used to prepare ZnS films by different research groups [11], such as magnetron sputtering [12, 13], pulsed laser deposition, chemical bath deposition (CBD) [14], ultrasonic spray pyrolysis [15], electron gun evaporation [16] and thermal evaporation [12]. The latter is particularly interesting, due to its simplicity and cheapness. Moreover, thermal evaporation process produce polycrystalline material with a predominant cubic phase [12]. ZnS deposition on different substrates, such as silicon, glass, and titanium oxide, have been also extensively discussed in the literature [17, 18]. It is well established that the substrate plays a crucial role in determining the quality of the deposited sample. For example, depending on the crystalline quality of the AlN substrate ZnO deposited films show an epitaxial growth [19, 20]. Extensive studies have been reported on ZnS nanostructures doped with different transition metal ions (such as Co, Mn, Ni, Fe) prepared by different techniques [21–24]. Depending on the type of dopant ion, the doped materials exhibit different luminescent, electronic and magnetic properties.

In this work, we prepare a ZnS/PbS nanostructures deposited on glass substrates using a vacuum-based simple thermal evaporation method. Several characterizations techniques were applied to describe their morphology, composition and structural properties. HRTEM and SEM techniques were applied to investigate the morphology of samples. The crystallographic properties of the films were studied using X-ray diffraction method. EDX and XPS scans are used for quantification of Zn, S and Pb in the sample.

## 2. Experimental methods

ZnS/PbS thin films were prepared on glass substrates using simple thermal evaporation technique. 12 wt% PbS powder is added to 88 wt% ZnS powder (99.99% purity) in the crucible as source material, under a vacuum of  $10^{-5}$  Torr using low speed turbomolecular pump (pumping speed 25000 rpm). The chamber geometry, gas flow and the gas remaining time enhance the thin film quality [25]. The distance between the ZnS and substrate holder was about 25 cm; the substrate holder was heated before deposition to 100 °C. Thin film morphology was examined using scanning SEM, TSCAN Vega\XMU model, equipped with energy dispersive spectroscopy (EDX) to determine the chemical composition of the synthesized films. Transmission electron microscopy (TEM) images for ZnS/PbS sample were also taken to verify the film morphology. The X-ray diffraction (XRD) measurements were carried out on uncompressed powder inside steel holder by using Bruker, D8 ADVANCE diffractometer with Cu  $K\alpha$  ( $\lambda = 0.154$  nm), measurements were conducted in the range of 20–80° ( $2\theta$ ). Phase identification from powder diffraction data was performed using the QualX peaks identification software [26]. The diffraction data was further analyzed using Rietveld refinements method as implemented in GSAS-II package [27].

The XPS experiments were performed using a model VG Scientific 200 spectrometer (UK) equipped with MgK $\alpha$  radiation (1253 eV) and operated at 23 kV and 13 mA. All binding energy values (in eV) were determined with respect to the C1s line (284.6 eV).

TEM was performed with a JEM2200FS double aberration-corrected transmission electron microscope (JEOL Ltd.) which was operating at an acceleration voltage of 200 kV.

## 3. Results and dissection

The chemical composition of the film deposited on the glass substrate was explored by means of EDX and XPS techniques. Fig. 2 shows the collected EDX spectrum of the products. Spectrum analysis shows that the film is composed of Zn, Pb, S and small amount of C and O elements (Table 1). The concentration of S in the sample is almost equal to the sum of Zn and Pb concentrations ( $S/(Zn+Pb) = 0.998$ ). The C and O atoms are contaminants from the atmosphere which are extremely difficult to avoid. Hence, our product is a stoichiometric film. Films with same stoichiometry were also acquired by different techniques, such as ultrasonic spray pyrolysis [15] and electron beam evaporation [16].

TABLE 1. Atomic percentage for Zn, Pb, S, O and C elements from EDX analysis

Element	Weight %	Atomic %
C_K	1.9	7.4
O_K	0.03	0.08
S_K	31.96	46.72
Pb_M	3.25	0.74
Zn_K	62.86	45.07

For further investigation of the chemical composition of the product, XPS scan of the sample was performed (Fig. 3). In order to compensate the surface charging effects C 1s signal (284.6 eV) was used as a reference signal.

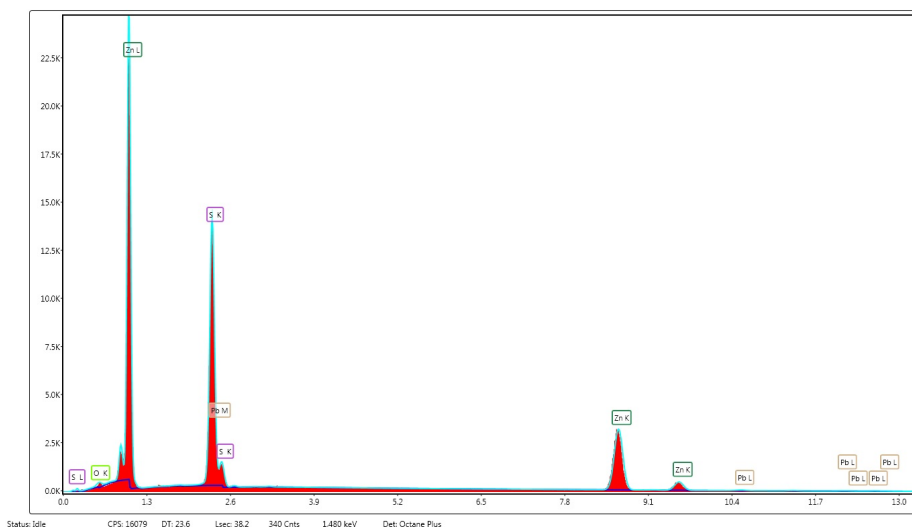


FIG. 2. EDX spectrum for ZnS/PbS nanorods films deposited on glass substrate

XPS curves were fitted (lowest curve in each spectrum) after adjusting to theoretical curves. Detailed spectra for the Zn2p, S2p, Pb4f, regions and related data are presented in Fig. 4. The results of XPS surface analyses are summarized in Table 2, which confirm the formation of ZnS and PbS compound and the stoichiometry of the film. Moreover, there was a strong indication for the presence of traces of, ZnO, PbO, CO and PbSO<sub>3</sub> on the surface of the films due to preparation and measurement conditions.

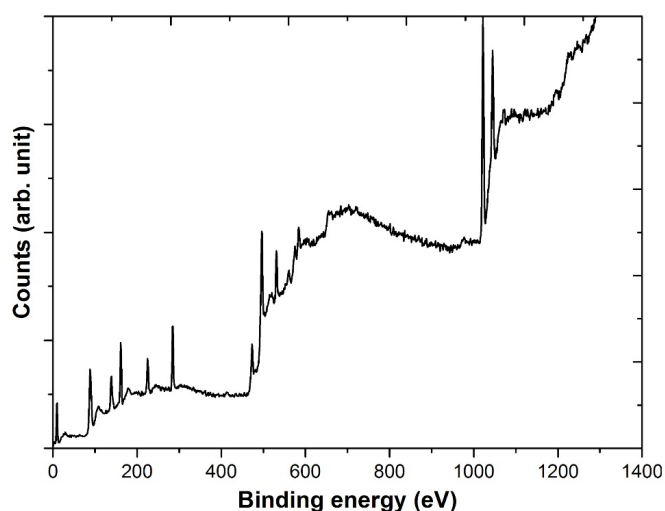


FIG. 3. XPS scans of ZnS/PbS sample on glass substrate

The X-ray diffraction pattern of the pure ZnS sample at room temperature is shown in Fig. 5. The peaks can be tied to the blend phase of ZnS. A good agreement between observed and calculated spectra was obtained; typical  $wR_p$  of the fit was  $\sim 0.09$ . For the ZnS/PbS product, the best agreement between observed and calculated pattern could only be achieved by the presence of the two phases of ZnS (blende and wurtzite) and one phase for PbS, namely galena (Fig. 6). The phase fraction for each identified phase in the product was fitted simultaneously. Indications from XRD results show that the ZnS/PbS sample contains more zinc blende (23.42%) than wurtzite (9.53%). The concentration of the PbS phase is 3.32% and the rest is SiO<sub>2</sub>. The ratio between the PbS phase and ZnS phases is about 0.1 which coincide with the XPS results. X-ray line width measurements have shown that the average particle size of ZnS is about 30 nm. The average strain value was found to be negligible for all phases. Such low value of strain is advantageous because the films have a good adhesion without high stress value. This can be attributed to the thermal evaporation technique. These results were in agreement with work of Benyahia *et al.* [11], where thermal evaporation was also

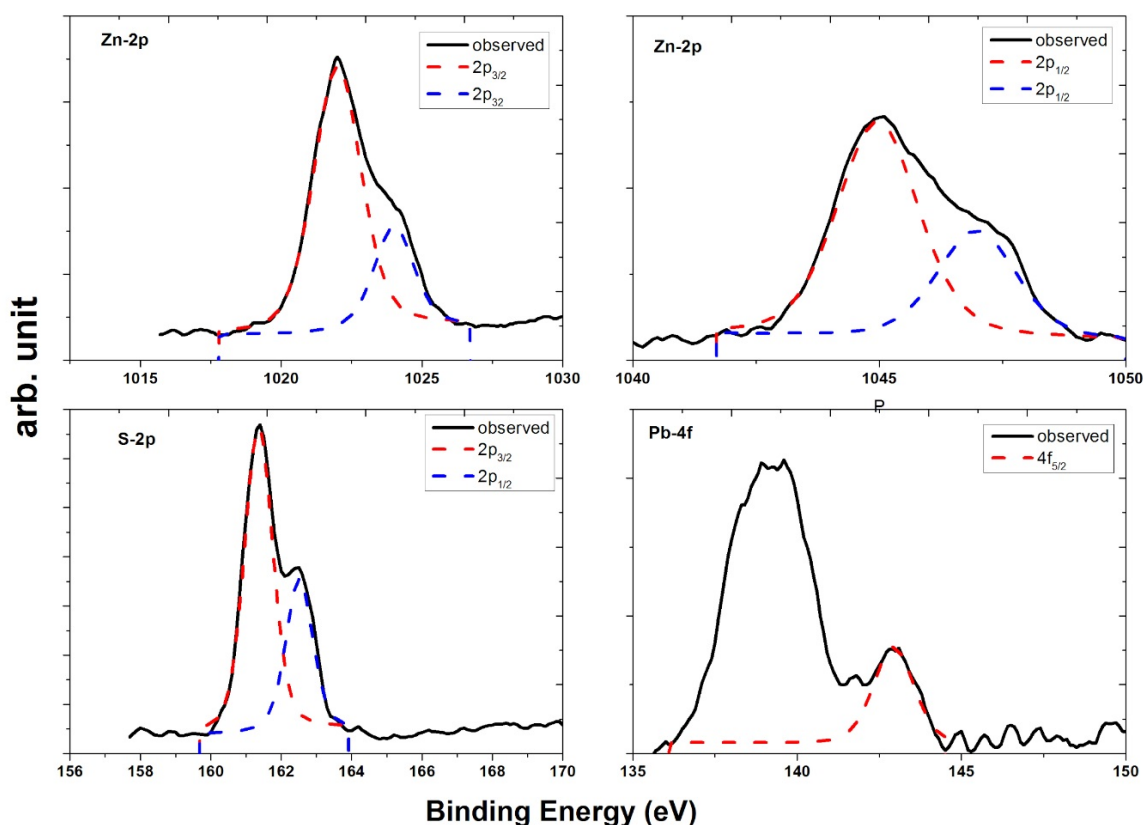


FIG. 4. Zn2p, S2p and Pb 4f XPS spectra recorded for the ZnS/PbS sample. Photon energies are 1253 eV

TABLE 2. XPS spectral features table

Name	Peak BE/eV	FWHM/eV	Area (P) CPS/eV	Atomic %	Peak assignment
C1s	284.7	1.0	1174.9	21.4	(C–C) adventitious carbon
C1s A	285.2	1.2	1216.2	22.2	(C–O–C) adventitious carbon
C1s B	288.4	1.2	127.9	2.3	(O–C=O) adventitious carbon
O1s	531.3	1.4	922.2	6.7	(Organic C=O) chemisorbed oxygen[28,29]
O1s A	532.1	1.8	793.6	5.8	(Organic C–O) chemisorbed oxygen
Pb4f, 5/2	142.9	1.5	247.8	0.2	Pb in PbS[30, 31]
Pb4f, 7/2	138.2–139.6	1.2	13038.4	0.5	Pb in Pb(OH) <sub>2</sub> / PbO/PbSO <sub>4</sub>
Zn2p, 3/2	1022.0	2.0	7296.1	10.6	Zn in ZnS/ ZnO
Zn2p, 3/2 A	1024.0	1.7	2289.3	3.3	Zn in ZnS[32, 33]
Zn2p, 1/2	1045.0	2.0	2915.9	4.3	Zn in ZnS[34, 35]
Zn2p, 1/2 A	1047.0	1.9	1408.3	2.1	Zn in ZnS
S2p, 3/2	161.4	1.0	1404.5	14.3	Sulphur in metal sulfide
S2p, 1/2	162.5	0.9	662.9	6.8	Sulphur in S–O/S–C/S–H

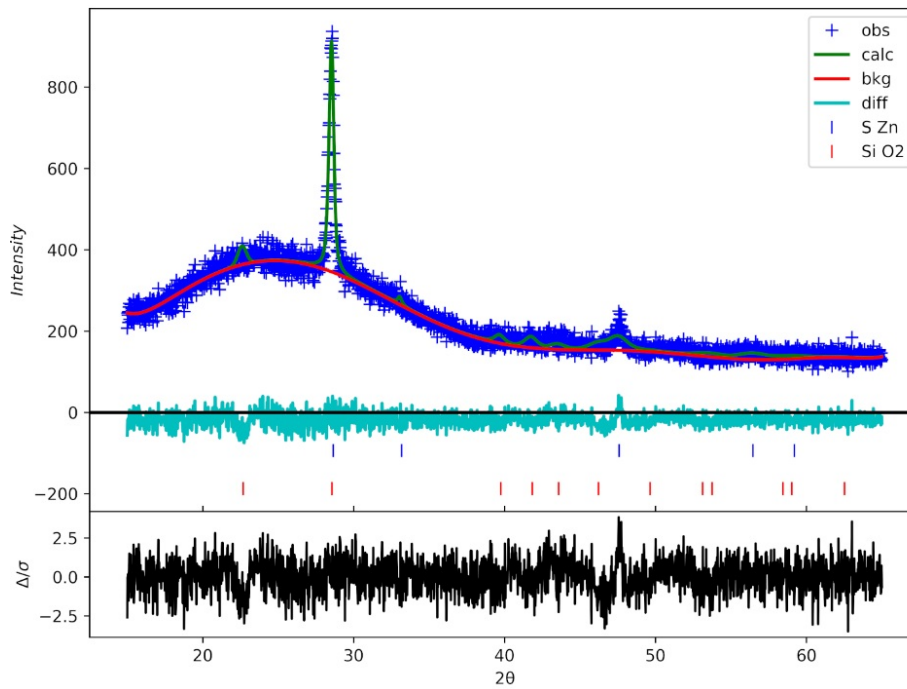


FIG. 5. X-ray diffraction data acquired from pure ZnS sample (blue +) including Rietveld refinements (green line) and background (red line). Vertical dashed lines denote  $d_{hkl}$  values associated with ZnS and SiO<sub>2</sub> phases

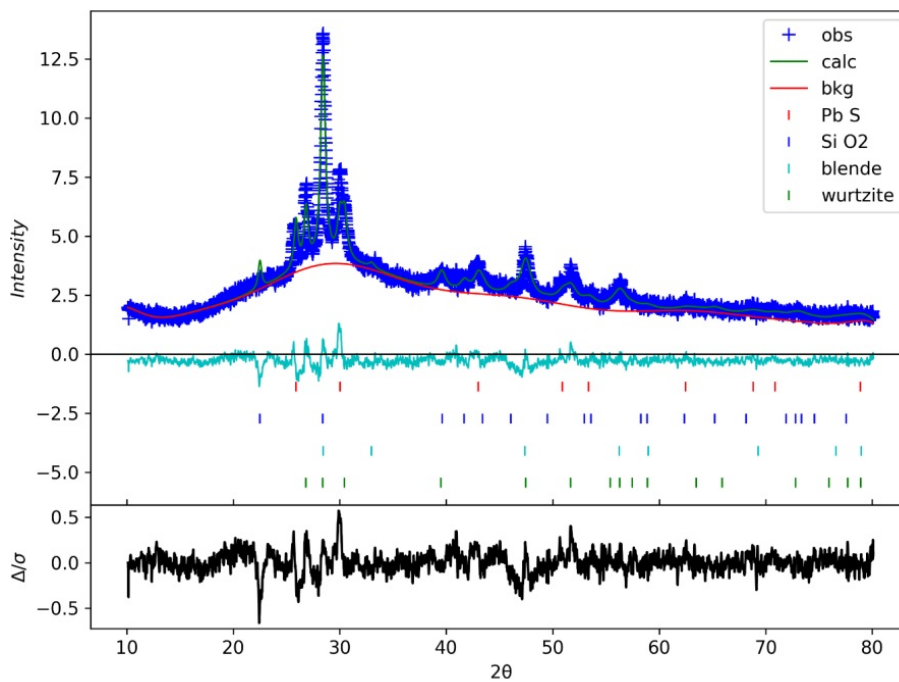


FIG. 6. X-ray diffraction data acquired from ZnS/PbS sample (blue +) including Rietveld refinements (green line) and background (red line). Vertical dashed lines denote  $d_{hkl}$  values associated with ZnS (two phases), PbS and SiO<sub>2</sub> phases. Typical  $wR_p$  of the fit is  $\sim 0.07$

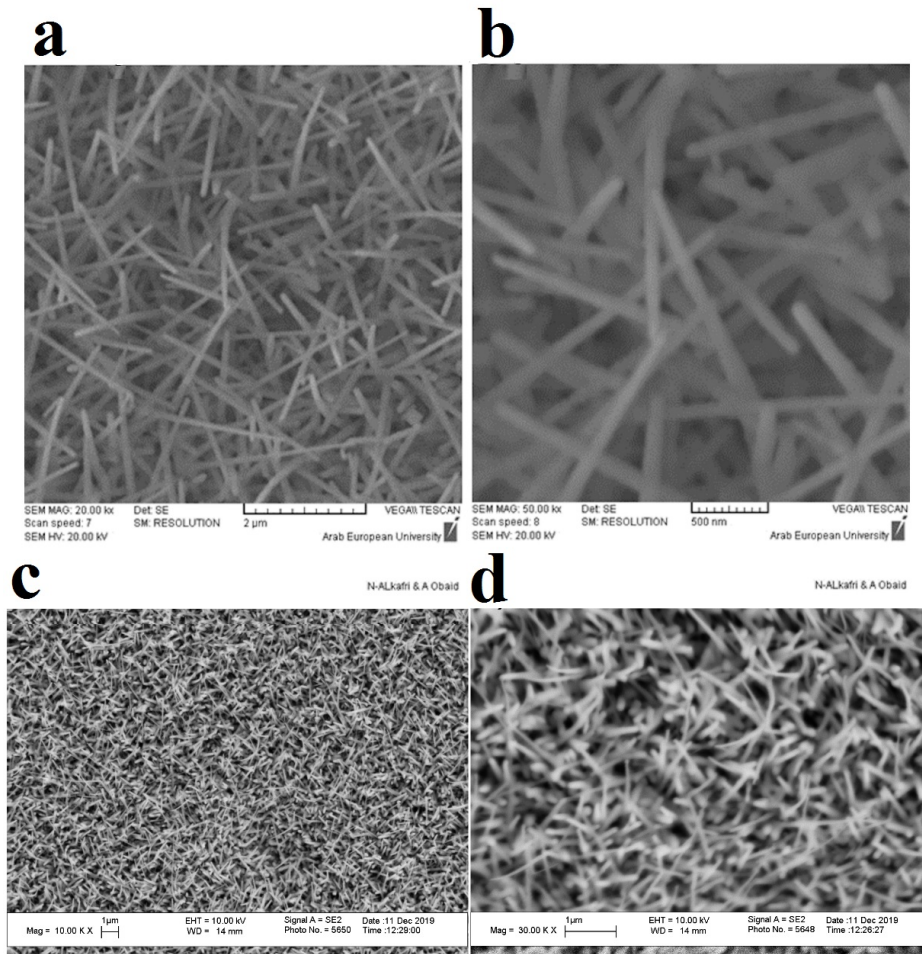


FIG. 7. SEM images in low (a) and high (b) magnification. FE-SEM in low (c) and high (d) magnification for the ZnS/PbS nanorods grown on glass templates

used for ZnS deposition and blende structure was obtained. The blende structure was also obtained in our previous work, where deposition was performed using electron gun techniques [16]. The identified PbS phase, galena, has also a cubic structure. Galena is a natural mineral of Pb, it is most abundant sulfide minerals and mostly associate with blende and calcite minerals. Therefore, the presence of the Zn blende and Pb galena together in the same thin film is not surprising. It worth mentioning that, unlike previously reported work on the growth of wurtzite ZnS nanorods [36], no phase transformation from zinc blende to wurtzite ZnS has been observed in the present product. It is clear in fact that the addition of increased amounts of lead to the compound (ZnS) of the amphoteric element (Zn) will generally result in a greater ionic character of the chemical bond between the “cation” and “anion”. It is well known, that blende (ZB) is a lattice with a less ionic bond. While, wurtzite (WZ) with a more ionic bond [37], therefore the high bond polarity favors the wurtzite structure instead of zinc-blende structure and the appearance of a wurtzite structure in our sample is in full agreement with the known general chemical concepts. A number of authors have recognized the effect of growth parameters such as substrate temperature and the ratio of dopant atoms on phase formation. For example, Karan *et al.* reported about the reversible phase transformation of platelet-shaped ZnS nanostructures between e (WZ) and (ZB) phases by reversible insertion/ejection of dopant Mn(II) ions induced by a thermocyclic process [38]. Joyce *et al.* showed that simply by tailoring the basic growth parameters of temperature and V-III ratio, pure ZB and pure WZ III-V nanowires can be obtained [39]. Amico and coworker investigated doping effects, as induced by Al and Cu, on promoting different ZnS phases using first principles simulations [40].

SEM is a versatile tool to investigate the surface topography and features of nanostructured materials. Moreover, it is useful to determine the growth mode of deposited films. Fig. 7(a,b) shows the SEM plane-view images of the ZnS/PbS sample in two different magnifications. It is clear that the template substrate covered with ZnS nanorods. This confirms the growth as nanorods for ZnS deposited on glass substrate. FESEM (Fig. 7(c,d)) scan shows similar

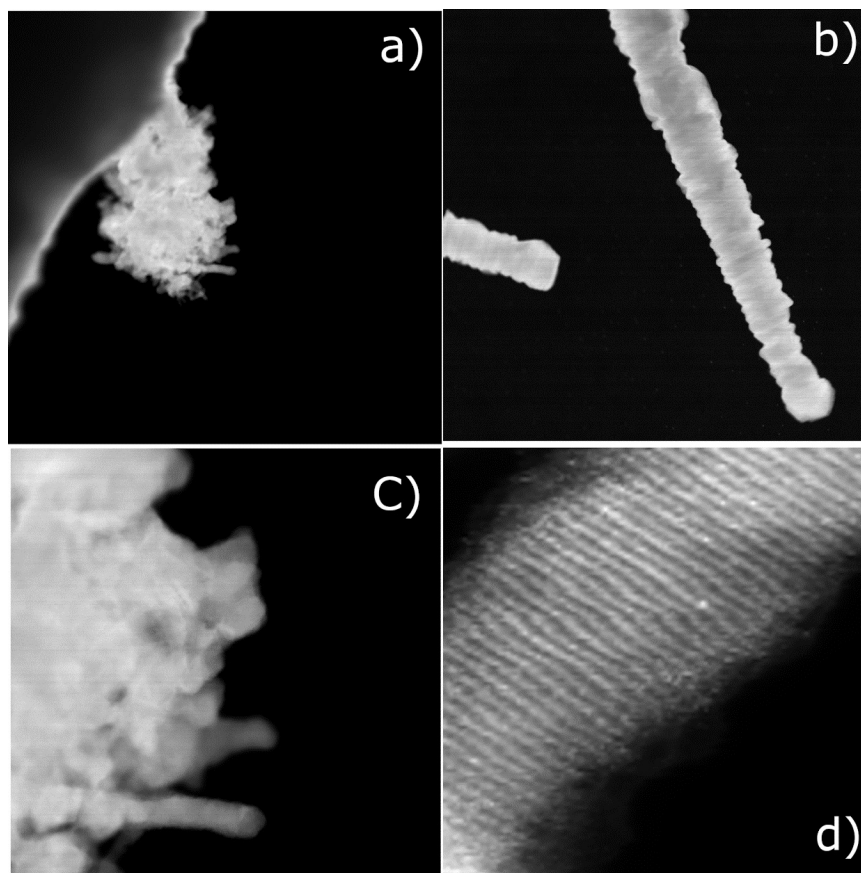


FIG. 8. (a and b) TEM morphology image of the synthesized ZnS/PbS nanorods. (c) TEM image of an individual nanorod. (d) HRTEM image of one selected nanorod

images for the surface morphology of the sample. The growth mechanism for the ZnS nanorods can be explained as following: the PbS evaporated initially because of the temperature milting (evaporation temperature of PbS is lower than of ZnS), and it formed monolayer or nucleation layer. Moreover, the growth of objects is enhanced as large lead atoms acting as dopants markedly accelerate the diffusion processes.

For further investigation of the film morphology, TEM and HRTEM characterization of the sample were performed. Although the TEM has many advantages over SEM, it has also some drawback and limitations. For example, sample preparation is much more difficult than SEM and results from TEM scan are dependent on the quality and cleanliness of the sample. Fig. 8 gives a TEM morphology image of the sample in low and high magnifications. Fig. 8(c) shows the TEM image of an individual nanorod, revealing the flat and smooth surface with uniform diameters of the nanorod. The mean value of nanorod is varying between 180 and 200 nm. Fig. 8(d) shows the HRTEM image of one nanorod in the lattice fringes.

#### 4. Conclusions

In summary, we prepared ZnS/PbS nanorods deposited on substrate of glass using thermal evaporation technique. SEM and TEM images are used for exploring morphology of the films. They confirm the formation of nanorods with a mean diameter 200 nm. Chemical composition of the product was investigated by mean of EDX and XPS. it confirms the stoichiometry of the film. XRD pattern analysis indicates the presence of two phase from ZnS (blende and wurzite) and one phase from PbS (galena).

#### Acknowledgements

The authors greatly acknowledge support to this project by Professor I. Othman, the Director General of the Atomic Energy Commission of Syria. Prof. Dr. Toma Susi for HRTEM measurement. The Kuwait University Research Administration, under Grant Number's GS 01/05 and GS 03/01 for XPS and XRD analysis. The Nanoscopy Science Center at Kuwait University for performing FESEM measurement.

## References

- [1] Huang X., Wang M., Willinger M.-G., Shao L., Su D.S., Meng X.-M. Assembly of Three-Dimensional Hetero-Epitaxial ZnO/ZnS Core/Shell Nanorod and Single Crystalline Hollow ZnS Nanotube Arrays. *ACS Nano*, 2012, **6**(8), P. 7333-9.
- [2] Leftheriotis G., Papaefthimiou S., Yianoulis P. Integrated low-emittance-electrochromic devices incorporating ZnS/Ag/ZnS coatings as transparent conductors. *Solar Energy Materials and Solar Cells*, 2000, **61**(2), P. 107-12.
- [3] Kavanagh Y., Alam M.J., Cameron D.C. The characteristics of thin film electroluminescent displays produced using sol-gel produced tantalum pentoxide and zinc sulfide. *Thin Solid Films*, 2004, **447-448**, P. 85-9.
- [4] Wan H., Xu L., Huang W.-Q., Huang G.-F., He C.-N., Zhou J.-H., et al. Band engineering of ZnS by codoping for visible-light photocatalysis. *Applied Physics A*, 2014, **116**(2), P. 741-50.
- [5] Nizamoglu S., Ozel T., Sari E., Demir H.V. White light generation using CdSe/ZnS core-shell nanocrystals hybridized with InGaN/GaN light emitting diodes. *Nanotechnology*, 2007, **18**(6), P. 065709.
- [6] Bae W.K., Kwak J., Park J.W., Char K., Lee C., Lee S. Highly Efficient Green-Light-Emitting Diodes Based on CdSe@ZnS Quantum Dots with a Chemical-Composition Gradient. *Advanced Materials*, 2009, **21**(17), P. 1690-4.
- [7] Wang L., He W., Xiao X., Meng F., Zhang Y., Yang P., et al. Hysteresis-Free Blue Phase Liquid-Crystal-Stabilized by ZnS Nanoparticles. *Small*, 2012, **8**(14), P. 2189-93.
- [8] Samadpour M. Efficient CdS/CdSe/ZnS quantum dot sensitized solar cells prepared by ZnS treatment from methanol solvent. *Solar Energy*, 2017, **144**, P. 63-70.
- [9] Diamond A.M., Corbellini L., Balasubramaniam K.R., Chen S., Wang S., Matthews T.S., et al. Copper-alloyed ZnS as a p-type transparent conducting material. *Physica status solidi(a)*, 2012, **209**(11), P. 2101-7.
- [10] Shin S.W., Pawar S.M., Park C.Y., Yun J.H., Moon J.-H., Kim J.H., et al. Studies on Cu<sub>2</sub>ZnSnS<sub>4</sub> (CZTS) absorber layer using different stacking orders in precursor thin films. *Solar Energy Materials and Solar Cells*, 2011, **95**(12), P. 3202-6.
- [11] Benyahia K., Benhaya A., Aida M.S. ZnS thin films deposition by thermal evaporation for photovoltaic applications. *Journal of Semiconductors*, 2015, **36**(10), P. 103001.
- [12] Haque F., Rahman K.S., Islam M.A., Chelvanathan P., Chowdhury T.H., Alam M.M., et al., editors. A Comparative Study on ZnS Thin Films Grown by Thermal Evaporation and Magnetron Sputtering. IEEE Student Conference on Research and Development (SCOReD), 16-17 December, 2013, Putrajaya, Malaysia.
- [13] Jazmati A.K., Abdallah B., Lahlah F., Shaker S.A. Photoluminescence and optical response of ZnO films deposited on silicon and glass substrates. 2019.
- [14] Abdallah B., Ismail A., Kashoua H., Zetoun W. Effects of Deposition Time on the Morphology, Structure, and Optical Properties of PbS Thin Films Prepared by Chemical Bath Deposition. *Journal of Nanomaterials*, 2018, **2018**, P. 8.
- [15] Alnama K., Abdallah B., Kanaan S. Deposition of ZnS thin film by ultrasonic spray pyrolysis: effect of thickness on the crystallographic and electrical properties. *Composite Interfaces*, 2017, **24**(5), P. 499-513.
- [16] Abdallah B., Alnama K., Nasrallah F. Deposition of ZnS thin films by electron beam evaporation technique, effect of thickness on the crystallographic and optical properties. *Modern Physics Letters B*, 2019, **33**(04), P. 1950034.
- [17] Basak A., Hati A., Mondal A., Singh U.P., Taheruddin S.K. Effect of substrate on the structural, optical and electrical properties of SnS thin films grown by thermal evaporation method. *Thin Solid Films*, 2018, **645**, P. 97-101.
- [18] Abdallah B., Duquenne C., Besland M.P., Gautron E., Jouan P.Y., Tessier P.Y., et al. Thickness and substrate effects on AlN thin film growth at room temperature. *The European Physical Journal – Applied Physics*, 2008, **43**(3), P. 309-13.
- [19] Rahmane S., Abdallah B., Soussou A., Gautron E., Jouan P.-Y., Le Brizoual L., et al. Epitaxial growth of ZnO thin films on AlN substrates deposited at low temperature by magnetron sputtering. *physica status solidi (a)*, 2010, **207**(7), P. 1604-8.
- [20] Abdallah B., Rihawy M.S. Ion beam measurements for the investigation of TiN thin films deposited on different substrates by vacuum arc discharge. Nuclear Instruments and Methods in Physics Research Section B: Beam Interactions with Materials and Atoms, 2019, **441**, P. 33-40.
- [21] Al-Jawad SMH, Ismail MM. Characterization of Mn, Cu, and (Mn, Cu) co-doped ZnS nanoparticles. *J Opt Technol*. 2017;84(7):495-9.
- [22] Wu M., Zhiqiang W., Zhao W., Wang X., Jiang J. Optical and Magnetic Properties of Ni Doped ZnS Diluted Magnetic Semiconductors Synthesized by Hydrothermal Method. *Journal of Nanomaterials*, 2017, **2017**, P. 1-9.
- [23] Attaf A., Derbali A., Saidi H., Benamra H., Aida M.S., Attaf N., et al. Physical properties of Pb doped ZnS thin films prepared by ultrasonic spray technique. *Physics Letters A*, 2019, P. 126199.
- [24] Dixit N., Vaghasia J.V., Soni S.S., Sarkar M., Chavda M., Agrawal N., et al. Photocatalytic activity of Fe doped ZnS nanoparticles and carrier mediated ferromagnetism. *Journal of Environmental Chemical Engineering*, 2015, **3**(3), P. 1691-701.
- [25] Ahmad Z., Abdallah B. Controllability Analysis of Reactive Magnetron Sputtering Process. *Acta Physica Polonica A*, 2013, **123**, P. 3.
- [26] Altomare A., Corriero N., Cuocci C., Falcicchio A., Moliterni A., Rizzi R. QUALX2.0: a qualitative phase analysis software using the freely available database POW\_COD. *Journal of Applied Crystallography*, 2015, **48**(2), P. 598-603.
- [27] Toby B.H., Von Dreele R.B. GSAS-II: the genesis of a modern open-source all purpose crystallography software package. *Journal of Applied Crystallography*, 2013, **46**(2), P. 544-9.
- [28] Cheon J., Talaga D.S., Zink J.I. Photochemical Deposition of ZnS from the Gas Phase and Simultaneous Luminescence Detection of Photofragments from a Single-Source Precursor, Zn(S<sub>2</sub>COCHMe<sub>2</sub>)<sub>2</sub>. *Journal of the American Chemical Society*, 1997, **119**(1), P. 163-8.
- [29] Barreca D., Gasparotto A., Maragno C., Tondello E., Spalding T.R. Analysis of nanocrystalline ZnS thin films by XPS. *Surf Sci Spectra*. 2002, **9**, P. 51-64.
- [30] Burungale V., Devan R., Pawar S., Harale N., Patil V., Rao V., et al. Chemically synthesized PbS Nano particulate thin films for a rapid NO<sub>2</sub> gas sensor. *MATERIALS SCIENCE-POLAND*, 2015, 34.
- [31] Zatsepin D.A., Boukhvalov D.W., Gavrilov N.V., Kurmaev E.Z., Zatsepin A.F., Cui L., et al. XPS-and-DFT analyses of the Pb 4f - Zn 3s and Pb 5d - O 2s overlapped ambiguity contributions to the final electronic structure of bulk and thin-film Pb-modulated zincite. *Applied Surface Science*, 2017, **405**, P. 129-36.
- [32] Langer D.W., Vesely C.J. Electronic Core Levels of Zinc Chalcogenides. *Physical Review B*, 1970, **2**(12), P. 4885-92.
- [33] Battistoni C., Paparazzo E., Dumond Y., Nogues M. X-ray photoelectron spectra of the spinel systems CdCr<sub>x</sub>In<sub>2-x</sub>S<sub>4</sub>. *Solid State Communications*, 1983, **46**(4), P. 333-6.

- [34] Barreca D., Tondello E., Lydon D., Spalding T.R., Fabrizio M. Single-Source Chemical Vapor Deposition of Zinc Sulfide-Based Thin Films from Zinc bis(O-ethylxanthate). *Chemical Vapor Deposition*, 2003, **9**(2), P. 93-8.
- [35] Briggs D. Handbook of X-ray Photoelectron Spectroscopy C.D. Wanger, W.M. Riggs, L.E. Davis, J.F. Moulder and G.E. Muilenberg Perkin-Elmer Corp., Physical Electronics Division, Eden Prairie, Minnesota, USA, 1979, **190**, P. 195. *Surface and Interface Analysis*, 1981, **3**(4).
- [36] Li Z., Liu B., Li X., Yu S., Wang L., Hou Y., et al. Synthesis of ZnS nanocrystals with controllable structure and morphology and their photoluminescence property. *Nanotechnology*, 2007, **18**(25), P. 255602.
- [37] Yao T. Zinc Oxide. In: Buschow KHJr, Cahn R.W., Flemings M.C., Ilshner B., Kramer E.J., Mahajan S., et al., editors. *Encyclopedia of Materials: Science and Technology*, 2001, P. 9883-7.
- [38] Karan N.S., Sarkar S., Sarma D.D., Kundu P., Ravishankar N., Pradhan N. Thermally Controlled Cyclic Insertion/Ejection of Dopant Ions and Reversible Zinc Blende/Wurtzite Phase Changes in ZnS Nanostructures. *Journal of the American Chemical Society*, 2011, **133**(6), P. 1666-9.
- [39] Joyce H.J., Wong-Leung J., Gao Q., Tan H.H., Jagadish C. Phase Perfection in Zinc Blende and Wurtzite III-V Nanowires Using Basic Growth Parameters. *Nano Letters*, 2010, **10**(3), P. 908-15.
- [40] D'Amico P., Calzolari A., Ruini A., Catellani A. New energy with ZnS: novel applications for a standard transparent compound. *Scientific Reports*, 2017, **7**(1), P. 16805.

## Stability and electronic properties of ZnSe nanowires: An ab initio approach

Sanjay Prakash Kaushik<sup>1</sup>, Satyendra Singh<sup>2\*</sup>, Ram-Krishna Thakur<sup>1</sup>

<sup>1</sup>School of Basic & Applied Sciences, G. D. Goenka University, Gurugram – 122103, India

<sup>2</sup>Department of Physics, Seth G. B. Podar College, Nawalgarh – 333042, India

\*satyendra7171@gmail.com

DOI 10.17586/2220-8054-2020-11-5-546-552

The presented work revolves around exploration of the structural dependence of electronic properties of zinc selenide nanowire. For this purpose the shapes under consideration are 2\_atom\_linear wire, 2\_atom\_zigzag wire, 4\_atom\_square wire and 6\_atom\_hexagonal wire for zinc selenide. ABINIT code has been used for the study. The band structure, geometrical optimization and stability of proposed structures have been studied. A 4\_atom\_square nanowire structure has come out to be comparatively more stable than other proposed structures while the findings of the study for band structure reveals that zinc selenide nanowires may have conducting, semi conducting or insulating nature which depends on the proposed geometry of the nanowire.

**Keywords:** zinc selenide nanowires, band structure, electronic properties, density function theory.

*Received: 10 July 2020*

*Revised: 25 August 2020*

### 1. Introduction

The electrical properties and study of nanowires have been interesting fields to study for the researchers since the 1980's. A drastic variation in optical as well as electrical behavior of these nanostructured substances is seen as compared to their bulk form. The miniature devices show exotic properties and this has increased the need of investigation and exploration of behavior of metallic structure of nanometer-sized dimensions for such devices. These devices seen to have significant advantages over the devices formed by photolithography. The structural dependence of electronic behavior of few nanowires with significant technical importance with implication of local density approximation is the outcome of this proposed work. Extensive experimental work on germanium and silicon nanowires has been already performed by researchers [1–3]. From the family of II–VI group ZnSe semiconductor has its unique application as light emitting diodes [4], photo detector [5] and scintillator [6]. Sufficient experimental work is reported on synthesis of zinc selenide nanowires. Ye et al. [7] synthesized ZnSe nanowire of thickness 20 to 120 nanometer and tens of micrometers in length under an Ar atmosphere by vapor transport. Panda et al. [8] reported that alignment and confinement play a major role in optical properties of synthesized ZnSe nanorods and nanowires. Singh et al. [9] reported the structural dependence for ZnO. ZnSe nanowires with the length of few micrometers and 80 – 150 nanometers in diameter were fabricated and current-voltage characteristics were being studied by Philipos et al. [10]. ZnSe nanowire were being synthesized on the zinc foil by Cheng et al. [11]. Archana et al. [12] used edamine as surface capping ligand and synthesized ZnSe nanowire by wet chemical method. First principles study of optical, magnetic and electronic properties of ZnSe was performed by Benstali et al. [13]. Arya et al. [14] in their work, fabricated ZnSe nanowire via template-assisted electro deposition method. Nasioka et al. [15] studied the doping effect of Er on ZnSe and studied structural properties and found that varying the dopant concentration led to disorder in initial structure. Eitan et al. [16] have performed the guided growth of horizontal zinc selenide nanowires in controlled manner. Zhang et al. [17] studied the first-principles calculations on the basis of DFT investigated the electronic structures and optical properties of Cr<sup>2+</sup> zinc selenide. Dong et al. [18] synthesized ZnSe nanowire via a heat-triggered precursor route. Wisniewski et al. [19] used low temperature spectroscopy to identify the recombination mechanisms for ZnSe nanowire.

The proposed work deals with comparative study of electronic properties, band structure and density of state curve study for four different shapes 2-atom\_linear nanowire, 2-atom\_zigzag nanowire, 4-atom\_square nanowire and 6-atom\_hexagonal nanowire, which has not been explored by anyone so far.

### 2. Computational details

The structure of zinc selenide nanowires using DFT calculations [20,21] was explored. This pseudopotential technique is found to be very dynamic tool for studying the electronic and structural properties of different materials [22]. The present study has been performed by ABINIT code [23]. Exchange correlation of Troullier, Martins and Perdew et al. [24, 25] has also helped in calculations. The pseudopotential has been obtained from ABINIT Webpage. To test the potentials the calculations were performed on bulk zinc selenide material. The results showed close agreement

to already existing experimental results. The structures were optimized for Hellmann–Feynman forces up to value of  $10^{-3}$  eV/Å on each atom. The cut off energy for the calculations has been taken as 30 Hartree. The positioning of nanowire has been done on a super cell along x-y direction with side 20 a.u. The z axis is considered as the axis of the wire. The integration of Brillouin zone has been done and 15k – points sampling in z direction has been done with the help of Monkhorst-pack technique [26]. In order to allow atoms to relax no constraints were imposed. The optimized value of lattice parameter for bulk ZnSe has been obtained. The lowest energy was obtained after due optimization of all the structures.

### 3. Results and discussion

The paper explores the investigation of four completely unmatched geometric structures of ZnSe nanowires. The details of proposed structures have been explored in our already published work [27–35]. The proposed structures of ZnSe nanowires have been shown in Fig. 1. To get the desired stability the requirement is to get the configuration which belongs to least energy amongst the all proposed structures. The energy variation with inter atomic distance for all geometries is mentioned in Table 1 shows the energy variation with distance for all proposed structures. Table 2 highlights the optimized energy and corresponding distance. The calculation of energy, for infinite linear wire, as a function of  $x = a$  has been obtained, wherever  $a$  is the zinc selenide distance up to 0.01 nanometers and thereafter the effective total energy is determined. The 2-atom\_linear nanowire indicates minimum energy at the 0.64 nm and acquires stability at  $-985.12$  eV, whereas the 2-atom\_zigzag nanowire shows least energy of  $-985.29$  eV at 0.26 nm distance. For 4-atom\_square nanowire, the energy is least at 0.80 nm with value of  $-985.88$  eV. The minimum configuration for the 6-atom hexagonally shaped nanowire at the inter atomic distance of 0.38 nm has lowest total energy, which is found to be  $-985.64$  eV. The overall findings of study show that the 4-atom square nanowire has the least energy configuration as compared other proposed structures under study and this is proposed to be the most stable structure amongst the all. The graph showing the variation between distance and energy, for all the structures, is shown in Fig. 2.

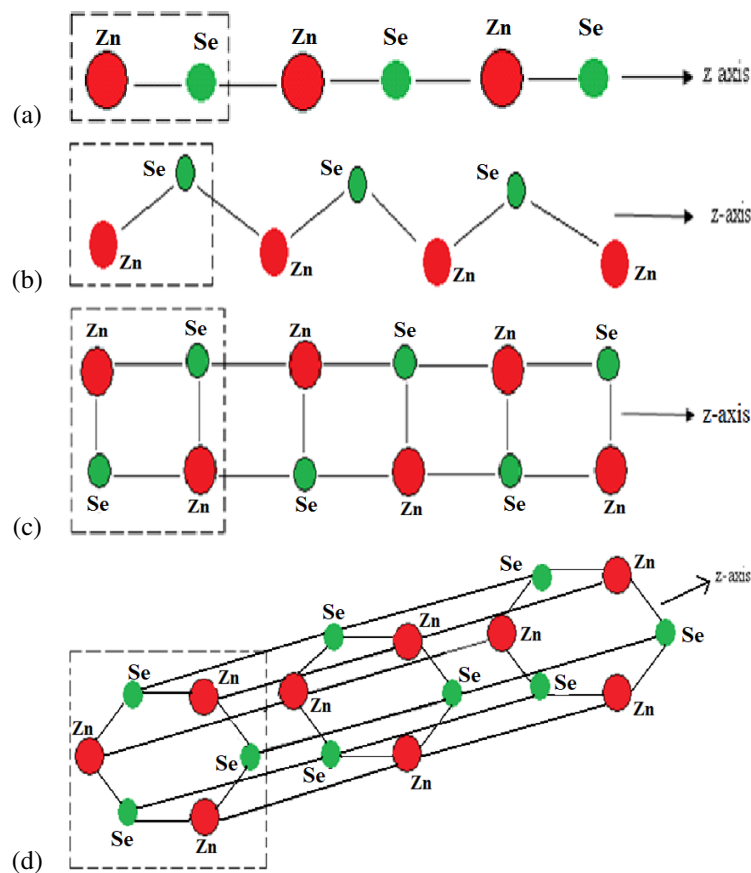


FIG. 1. Structures of ZnSe nanowires: (a) 2-atom ZnSe linear nanowire; (b) 2-atom ZnSe zigzag nanowire; (c) 4-atom ZnSe square nanowire; (d) 6-atom ZnSe hexagonal nanowire

TABLE 1. The variation between  $X$  (interatomic distance in nanometer) vs energy (eV/atom). The bold faced ones are most stable structures

X = Zn – Se distance(nm)	Total Energy (eV/atom)			
	2-atom linear nanowire	2-atom zigzag nanowire	4-atom square nanowire	6-atom hexagonal nanowire
0.06	–558.56	–707.49	–288.62	–277.18
0.10	–943.30	–930.12	–929.22	–817.48
0.16	–981.71	–975.71	–980.68	–941.08
0.22	–983.55	–983.72	–985.23	–972.50
0.26	–984.61	<b>–985.29</b>	–984.89	–982.16
0.32	–985.07	–985.00	–985.31	–985.14
0.38	–979.18	–983.79	–984.99	<b>–985.64</b>
0.42	–972.23	–984.43	–983.94	–985.49
0.48	–967.21	–983.78	–984.34	–983.57
0.52	–977.33	–985.15	–984.63	–974.30
0.58	–970.18	–980.43	–984.29	–984.13
0.64	<b>–985.12</b>	–985.12	–984.91	–981.84
0.68	–979.21	–977.76	–985.05	–878.83
0.74	–985.06	–985.08	–985.49	–984.01
0.80	–982.18	–985.16	<b>–985.88</b>	–982.87

TABLE 2. The total energy and inter atomic distances of various structures

Structures	Zn – Se distance (nanometer)	Zn – Zn distance (nanometer)	Total Energy (eV/atom)
2-atom linear wire	0.64	1.28	–985.12
2-atom zigzag wire	0.26	0.52	–985.29
4-atom square wire	0.80	1.60	<b>–985.88</b>
6-atom hexagonal wire	0.38	7.6	–985.64

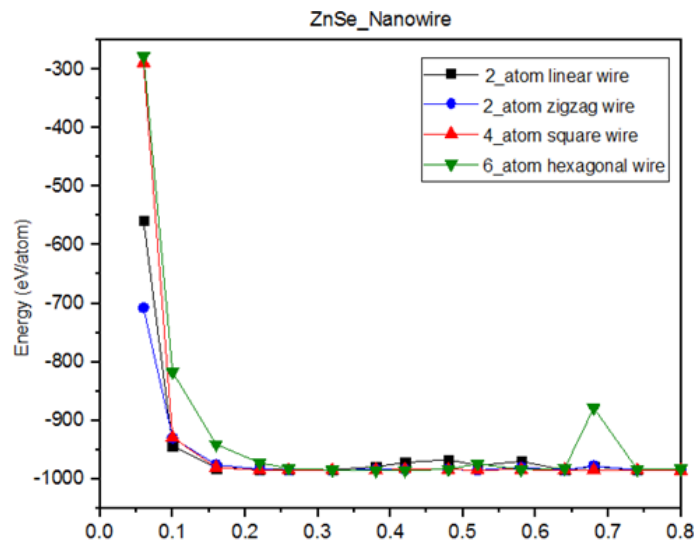


FIG. 2. Variation between interatomic distance  $X$  (nanometer) versus energy (eV/atom) for different NWs

The energy versus density of state variation is shown in Fig. 3. The nature DOS for optimized inter atomic distance was under analysis and it shows that the density of state is greater for the 6-atom hexagonal wire near the Fermi level, whereas it is less for the 4-atom squared wire near the Fermi level, and hence, the 4-atom squared shape is the most stable structure amongst those under consideration here.

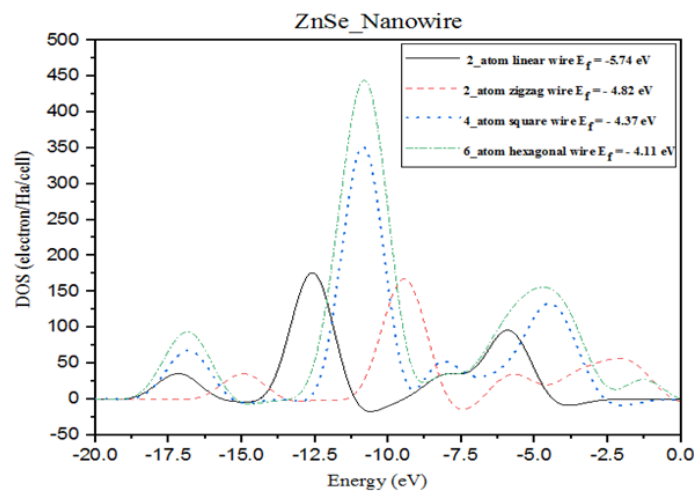


FIG. 3. The variation between DOS versus Energy (eV) with for all structures

The band structures for all the shapes of ZnSe nanowire has been shown in Figs. 4 – 7. Fig. 4 shows that one of the bands crosses the Fermi level for 2-atom linear nanowire, indicating its metallic behavior, whereas for 2-atom zigzag nanowire, one of the bands is lying close to Fermi level as shown by Fig. 5, and thus this structure may be semi conducting in nature. The studies of the band structures for 6-atom hexagonal nanowire and 4-atom square nanowire in Figs. 6 and 7 respectively indicate that all bands are seen to be lesser than the Fermi level, and thus both structures are possibly insulating in nature.

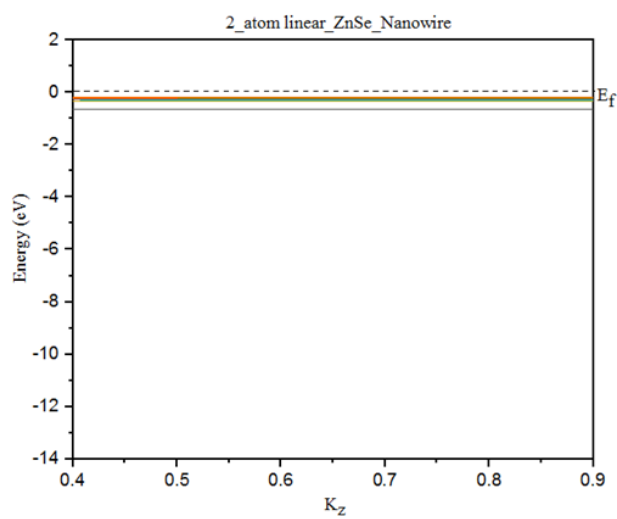


FIG. 4. Band structure for 2-atom linear nanowire

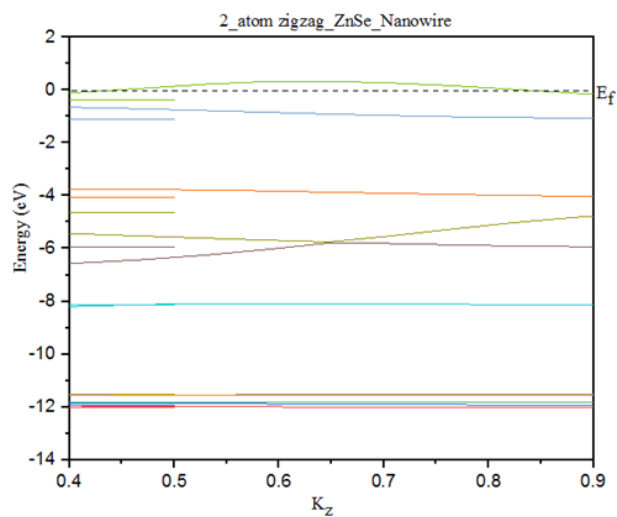


FIG. 5. Band structure for 2-atom zigzag nanowire

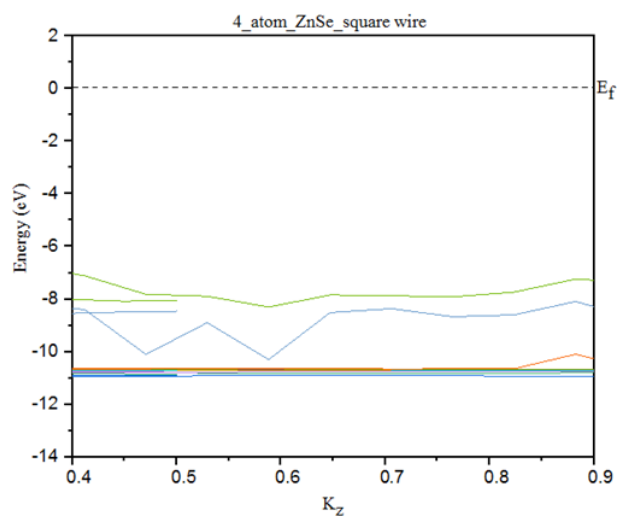


FIG. 6. Band structure for 4-atom square nanowire

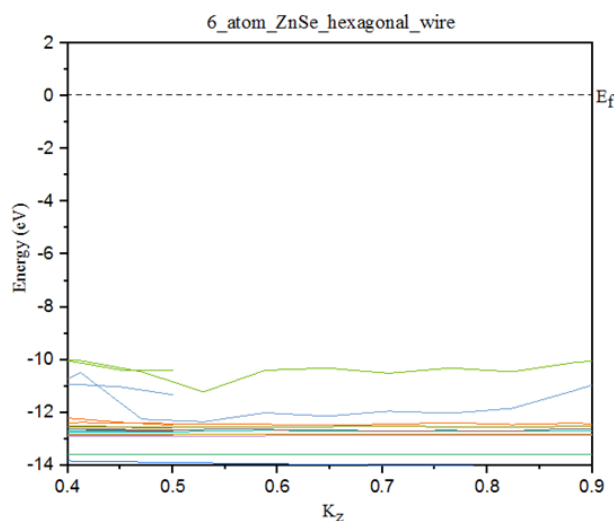


FIG. 7. Band structure for 6-atom hexagonal nanowire

#### 4. Conclusions

We have performed an investigation of four different shapes for ZnSe nanowires with ab initio DFT calculations and have analyzed the interatomic distance versus energy, DOS versus energy curve as well the band structure for all the proposed geometries to have better understanding of electronic behavior and stability for the various proposed shapes. The finding establishes that 4-atom square nanowire shape is more stable as compared to other shapes. The bulk ZnSe is semiconducting in nature, whereas our study for proposed shapes reveals that the 2-atom linear nanowire may be semiconducting in nature. The 2-atom zigzag nanowire seems to be conducting in nature while the 4-atom square nanowire and the 6-atom hexagonal nanowire is insulating in nature.

#### Acknowledgements

We express our gratitude to G. D. Goenka University, Gurugram (Haryana) and Seth G. B. Podar College, Nawalgarh (Rajasthan) for all the help.

#### References

- [1] Li D., Wu Y., et al. Thermal Conductivity of individual silicon nanowires. *Applied Physics Letter*, 2003, **83** (14), P. 2934–2936.
- [2] Tian B., Zheng X., et al. Coaxial silicon nanowires as solar cells and nanoelectronic power sources. *Nature*, 2007, **449** (7164), P. 885–889.
- [3] Andrew B.G., Lincoln J.L., Mark S.G., Charles M.L. Growth and transport properties of complementary germanium nanowire field-effect transistors. *Applied Physics Letter*, 2004, **84** (21), P. 4176–4178.
- [4] Chen S.H., Wang S.J.J., Lo C.J., Chi J.Y. White-light emission from organics-capped ZnSe quantum dots and application in white-light-emitting diodes. *Applied Physics Letter*, 2005, **86** (13), 131905.
- [5] Vigue F., Tournie E., Faurie J.P. ZnSe-based Schottky barrier photodetectors. *Electronic Letters*, 2000, **36** (4), 352.
- [6] Nasioka I., Boyko M., et al. Optical characterization of Er-doped ZnSe for scintillation applications. *Optical Materials*, 2014, **38**, P. 272–277.
- [7] Ye C., Fang X., et al. Structural characterization of long ZnSe nanowires. *Applied Physics A*, 2004, **79** (1), P. 113–115.
- [8] Panda A.B., Acharya S., Efrima S. Ultranarrow ZnSe Nanorods and Nanowires: Structure, Spectroscopy, and One-Dimensional Properties. *Advanced Material*, 2005, **17** (20), P. 2471–2474.
- [9] Singh S., Srivastva P. Ab-initio Study of the Structural Stability and Electronic Properties of ZnO Nanowires. *Proceedings of fifth international conference "Communication systems and network technologies"*, 2015, Gwalior, India, April 4–6, 2015, P. 1279–1283.
- [10] Philipose U., Ruda H.E., et al. Conductivity and photoconductivity in undoped ZnSe array. *Journal of Applied Physics*, 2006, **99** (6), 066106.
- [11] Cheng C.L., Chen Y.F. Low temperature synthesis of ZnSe nanowires by self-catalytic liquid-solid growth. *Material Chemistry and Physics*, 2009, **115** (1), P. 158–160.
- [12] Archana J., Navaneethan M., et al. Chemical synthesis of monodispersed ZnSe nanowire and its functional properties. *Material Letters*, 2012, **81**, P. 59–61.
- [13] Benstaali W., Bentala S., Abbad A., Belaidi A. Ab-initio study of magnetic, electronic and optical properties of ZnSe doped transition metals. *Material Science in Semiconductor Processing*, 2013, **16** (2), P. 231–237.
- [14] Arya S., Khan S., et al. Electrical properties of electrodeposited zinc selenide (ZnSe) nanowires. *Journal of Material Science*, 2014, **25** (9), P. 4150–4155.
- [15] Nasioka I., Bokyo M., et al. Optical characterization of Er doped ZnSe for scintillation application. *Optical Materials*, 2014, **38**, P. 272–277.
- [16] Oksenberg E., Popovitz-Biro R., Rechav K., Joselevich E. Guided growth of Horizontal ZnSe Nanowires and their integration into high performance blue-UV Photodetectors. *Advanced Material*, 2015, **27** (27), P. 3999–4005.

- [17] Zhang Y., Feng G., et al. First principles study of the electronic structures and optical properties of Cr<sup>2+</sup> doped ZnSe as a function of impurity concentration. *Physica Status Solidi (b)*, 2016, **253** (6), P. 1133–1137.
- [18] Li D., Xing G., et al. Ultrathin ZnSe nanowires: one pot synthesis via a heat triggered precursor slow releasing route, controllable Mn doping and application in UV and near visible light detection. *Nanoscale*, 2017, **9**, P. 15044–15055.
- [19] Wisniewski D., Byrne K., et al. Fingerprinting Electronic Structure in Nanomaterials: A Methodology Illustrated by ZnSe Nanowires. *Nano Letters*, 2019, **19** (4), P. 2259–2266.
- [20] Hohenberg P., Kohn W. Inhomogeneous Electron Gas. *Physical Review B*, 1964, **136**, P. 864–866.
- [21] Kohn W., Sham L.J. Self-Consistent Equations Including Exchange and Correlation Effects. *Physical Review A*, 1965, **140** (4), A1133–A1138.
- [22] Martin R.M. *Electronic Structure*, Cambridge University Press, Cambridge, 2009.
- [23] Gonze X., Beuken J.M., et al. First-principles computation of material properties: the ABINIT software project. *Computational Material Science*, 2002, **25**, 478.
- [24] Perdew J.P., Burke K., Ernzerhof M. Generalized Gradient Approximation Made Simple. *Physical Review Letter*, 1996, **77** (18), P. 3865–3868.
- [25] Troullier N., Martins J.L. Efficient pseudopotentials for plane-wave calculations. *Physical Review B*, 1991, **43** (3), P. 1993–2006.
- [26] Monkhorstand H.J., Pack J.D. Special points for Brillouin-zone integrations. *Physical Review B*, 1976, **13** (12), P. 5188–5192.
- [27] Srivastava P., Singh S., Mishra A. Stability and Electronic Properties of GaN Nanowires – An *Ab-Initio* Approach. *Journal of Computational & Theoretical Nanoscience*, 2008, **5** (4), P. 635–638.
- [28] Srivastava P., Singh S. Linear & Second-order optical response of different GaN Nanowires. *Physica E*, 2008, **40** (8), P. 2742–2746.
- [29] Singh S., Srivastava P., Mishra A. Ab-initio study of Gallium Arsenide Nanowires. *Journal of Computational & Theoretical Nanoscience*, 2009, **6** (7), P. 1556–1560.
- [30] Singh S.S., Srivastava P., Mishra A. Structural Stability and Electronic Properties of GaSb nanowires. *Physica E*, 2009, **42** (1), P. 46–50.
- [31] Srivastava P., Singh S., Mishra A. Electronic Properties of GaP Nanowires of Different Shapes. *Journal of Nanoscience and Nanotechnology*, 2011, **11** (12), P. 10464–10469.
- [32] Srivastava P., Singh S. Stability Analysis of AlN Nanowire. *Journal of Computational & Theoretical Nanoscience*, 2011, **8** (9), P. 1764–1768.
- [33] Singh S., Srivastava P. Optical properties of gallium phosphide (GaP) Nanowires. *Applied Nanoscience*, 2013, **3** (2), P. 89–94.
- [34] Singh S., Srivastava P. Linear and Nonlinear optical properties of GaAs Nanowires. *Applied Nanoscience*, 2015, **5** (3), P. 273–279.
- [35] Singh S., Kaushik S.P., Supreet. Ab initio study of Electronic Properties of Cadmium Sulphide Nanowires. *J. Comput. Theor. Nanosci.*, 2020, **17** (2/3), P. 546–551.

## Nanotexture effect of the fiber surface on the sorption capacity of nonwoven fabrics

Yu. V. Rudyak<sup>1</sup>, F. A. Doronin<sup>1</sup>, G. O. Rytikov<sup>1,2</sup>, E. K. Filyugina<sup>3</sup>, V. G. Nazarov<sup>1</sup>

<sup>1</sup>Moscow Polytechnic University, 38 B. Semenovskaya str., Moscow 107023, Russia

<sup>2</sup>State University of Management, 99 Ryazansky pr., Moscow 109542, Russia

<sup>3</sup>National Research University Higher School of Economics, 20, Myasnitskaya Street, Moscow 101000, Russia

rudyak@mail.ru, f.a.doronin@mospolytech.ru, gr-yandex@yandex.ru,  
ekaterina.filyugina@mail.ru, 110505n@gmail.com

DOI 10.17586/2220-8054-2020-11-5-553-564

An approach to structural and functional modelling of the oxyfluorinated nonwovens based composite materials has been developed. The structural component of the model is presented in the form of integral and differential characteristic functions of the planar heterogeneity. The correlation analysis methods revealed the existence of links between the latex sorption capacities and the nanostructural characteristics of the experimental samples' SEM-images. The obtained functional-structural model allows us to quantify the expected values of sorption capacities of the nonwoven fiber materials under the certain restrictions on the chemical compositions of the impregnating mixtures.

**Keywords:** oxyfluorination, surface modification, fiber, modification, sorption capacity.

*Received: 4 September 2020*

*Revised: 15 September 2020*

### 1. Introduction

Woven and nonwoven fabrics are well-known and widespread options for implementing materials based on polymer fibers [1–3]. Unlike fabrics consisting of regularly ordered forming threads, nonwoven fabrics have a chaotic and fundamentally multi-layered structure, because, otherwise, they do not provide the necessary level of mechanical strength of finished products for practical operation [4–8]. A significant influence of finish treatment on the physico-chemical and as a result, functional and operational properties (wettability, sorption capacity, permeability, radioparadise, etc.) nonwoven fabric [9–11] can be used for solving a wide range of tasks (provide heat and moisture insulation, filtration from different different-scale admixtures in water and fuel, emergency spill response of fuel and lubricants, etc.) [12–14]. At the same time, the optical characteristics of different-scale visualizations of nonwoven fabric surfaces can significantly change under the influence of various finishing methods, which makes it possible to identify correlations between the functional and morphological characteristics of fibrous materials based on the analysis of their macro-, micro- and nanoscale images [15–17]. The study of the relationships between the set of parameters of manufacturing modes, structural and functional characteristics of the original and modified samples allows one to predict and control the properties of products used in various natural conditions, made on the basis and/or using fibrous materials. The identification of correlations between the structural and functional characteristics of the corresponding experimental samples makes it possible to clarify the mechanisms by which changes in functional properties are provided by the control program for the production of new materials based on nonwoven fabrics.

### 2. Experimental samples

Test non-woven fabrics were made on the basis of two-component mixtures of polyester fibers of various linear densities (0.33 and 1.7 Tex) using the technology described in [18]. Thermomechanical processing of experimental samples was performed at a temperature of 130°C and the speed of broaching non-woven fabrics between the heated shafts 12 m/min. Chemical treatment of samples was carried out by oxychlorination with a gas mixture of 7.5%F<sub>2</sub>+10%O<sub>2</sub>+82.5%He with processing times of 0.5, 1, 1.5 and 2 hours.

The latex-sorption capacity of the experimental samples was subjected to a direct gravimetric measurement (Table 1). The latter was chosen as a simulation model of liquid-phase functional additives applied to the surface and staining non-woven fabrics in volume during final pre-operational processing.

Latex treatment was performed in four different modes, hereafter referred to as L1, L2, L3 and L4. Modified cloths were impregnated with latex copolymer of vinylidene chloride and butadiene (DVCB-70, 70% butadiene and 30% vinylidene chloride) with a rubber content of 26% (GOST 9501-60 synthetic Latex DVCB-70, TU 38.303-04-03-90) at a temperature of 22°C. To regulate the degree of impregnation, water-diluted latex with a rubber content of 3.5 (L 1), 4.4 (L2), 6.0 (L 3) and 13 % (L4) was used. Samples immersed in latex were rolled with a roller for

TABLE 1. The latex-sorption capacity SC for oxyfluorinated bicomponent polyester fiber materials under various modes of gas-phase modification and liquid-phase processing

Duration of oxyfluorination, h	The impregnation mode			
	L1	L2	L3	L4
0.5	3.8 ± 0.4	4.1 ± 0.4	4.9 ± 0.5	5.1 ± 0.5
1.0	3.6 ± 0.4	3.3 ± 0.3	4.5 ± 0.5	4.2 ± 0.4
1.5	3.6 ± 0.4	2.9 ± 0.3	3.8 ± 0.4	4.7 ± 0.5
2.0	4.4 ± 0.4	2.5 ± 0.3	3.7 ± 0.4	4.5 ± 0.5

2 minutes. Latex-impregnated non-woven fabrics were passed through pressing rollers and, when blown with air at a temperature of 120 °C, dried until constant values of sample weights were reached.

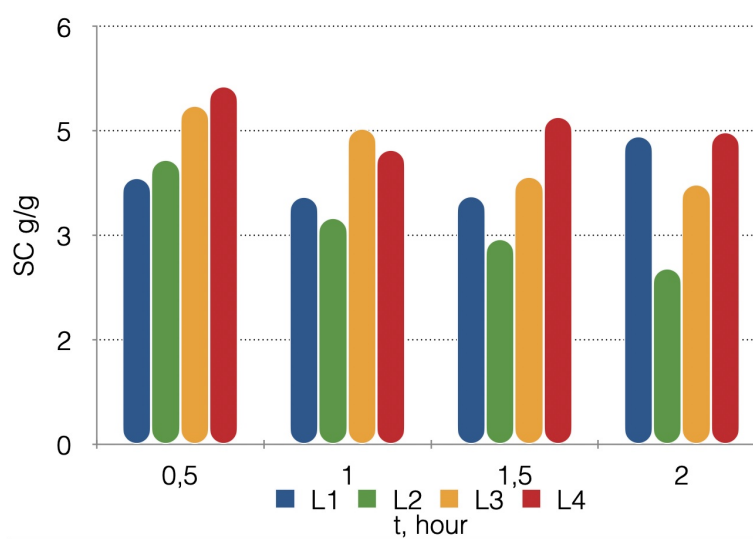


FIG. 1. Values of the SC sorption capacity for latex of experimental samples treated in L1, L2, L3 and L4 modes at different durations of oxyfluorination with a gas mixture of 7.5%F<sub>2</sub>+10%O<sub>2</sub>+82.5%He

It is seen (Table 1, Fig. 1) that the different modes of impregnation with latex sorption capacity of samples in most cases decreases with increasing length  $t$  of gas-phase chemical modification, but trends are not absolute in nature, which is probably related to the increase in the hydrophilicity of polyester fibers during the oxyfluorination and the dependence of sediment stabilities latex on the concentration of rubber in water.

### 3. The average sorption capacity dependence on the duration of oxyfluorination

Figure 2 shows the dependence of the average values of sorption capacities of experimental samples (regardless of the mode of latex impregnation) on the duration of oxyfluorination with a gas mixture of 7.5% F<sub>2</sub>+10% O<sub>2</sub>+82.5% He for 0.5, 1, 1.5 and 2 hours. The average value of the sorption capacity of the initial samples is represented by a point corresponding to the zero duration of gas-phase modification.

The dependence of the average value of the sorption capacity on the duration of oxyfluorination is well described by the equation:

$$SC = SC_0 \cdot e^{-t^2} + SC_\infty, \quad (1)$$

where  $SC_0$  is the sorption capacity of the initial samples,  $SC_\infty$  – is the conditional expected sorption capacity of samples oxyfluorinated over an infinitely long time, and  $t$  is the dimensionless time.

The values of parameters of the functional-dynamic model (1) obtained by the generalized method of least squares (OLS), intended for predicting the average sorption capacity of bicomponent nonwovens when the duration of oxyfluorination changes, are presented in Table 2.

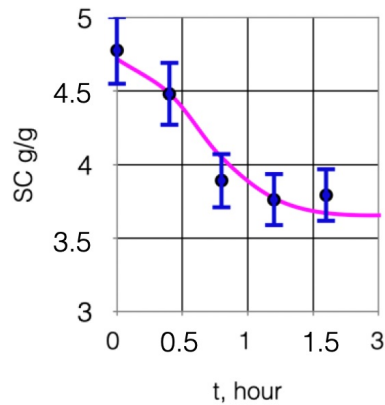


FIG. 2. Dependence of the average values of sorption capacities of experimental samples on the duration of oxyfluorination with a gas mixture of 7.5% F<sub>2</sub> +10% O<sub>2</sub>+82.5% He for 0.5, 1, 1.5 and 2 hours

TABLE 2. Values of parameters of the functional-dynamic model obtained by the GLS (generalized least squares) method (1)

Parameter	$SC_0 \pm \delta SC_0, \text{g/g}$	$SC_\infty \pm \delta SC_\infty, \text{g/g}$	$R^2$
Value	$1.1 \pm 0.1$	$3.7 \pm 0.4$	0.95

Thus, the dependence of the average sorption capacity of the sample on the duration of oxyfluorination shows the principal possibility of controlling the functional characteristics of composite materials based on non-woven fabrics using gas-phase chemical modification.

#### 4. The concept of structural model

In order to ensure the efficiency of impregnation of non-woven fabrics, the highest for some and the lowest for other latex compositions (simulating various liquid-phase functional compounds applied), it is necessary to develop a technique for monitoring and predicting the properties of composite fiber materials based on the analysis of the corresponding optical images. For example, Fig. 3 shows enlarged optical front and profile images of one of the experimental samples after oxyfluorination.

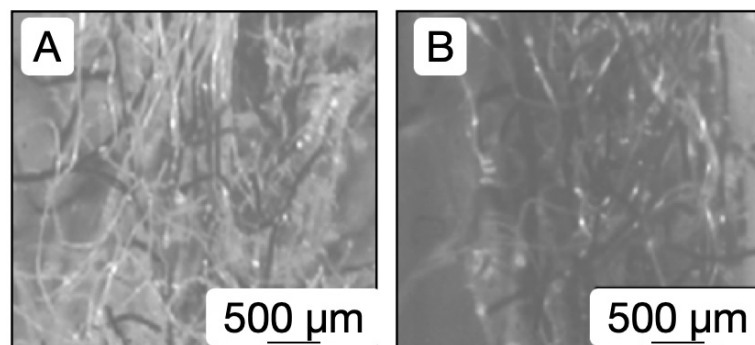


FIG. 3. Optical front (A) and profile (B) images of the experimental sample after oxyfluorination

A significant disadvantage of direct adaptation of the previously developed original approach to the formation of structural models in the form of decompositions into two-dimensional Fourier series is a large number of parameters, the specification of which is necessary to achieve high-quality approximation of digital images of optical images of analyzed objects. Mathematically strict verification of such models requires a large amount of experimental data, and its visualization involves the use of pseudo-three-dimensional images, which makes it difficult for researchers and engineers to perceive and qualitatively analyze the structural characteristics of the studied materials.

To solve the above problem, an original approach to the quantitative description of images of experimental samples was developed, consisting in the formation of characteristic functions of planar digital heterogeneity, which formalize the dependence on the threshold values of pixel  $B$  brightness of the normalized total area  $S/S_0(B)$  of shapes formed by pixels of the analyzed images, the brightness of which does not exceed  $B$ . Each image of an experimental sample can be compared with an integral and differential characteristic function, determining the latter using a difference scheme  $\Delta(S/S_0(B+1) - S/S_0(B))$ . The visual models of front-facing (A) and profile (B) images corresponding to different pixel brightness thresholds (Fig. 3) are shown in Table 3.

TABLE 3. Values of parameters of the functional-dynamic model for predicting the values of the average sorption capacity when changing the duration of oxyfluorination

Threshold value $B$ the brightness of pixels of the images	16	48	80	112	144	176	208	240
Octile of image pixel brightness distribution	I	II	III	IV	V	VI	VII	VIII
Visual models of the front image								
$S/S_0 _{front}$	0.16	0.69	0.89	0.98	0.997	0.9998	1	1
$\Delta(S/S_0) _{front}$	6.8	6.4	3.7	1.4	0.27	0.03	0	0
Visual models of the profile image								
$S/S_0 _{profile}$	< 0.01	0.09	0.42	0.69	0.85	0.94	0.98	> 0.99
$\Delta(S/S_0) _{profile}$	< 0.01	2.7	6.6	7.5	5.5	3.4	1.4	0.3

Thus, the functional dependences of the integral  $S/S_0(B)$  and differential  $\Delta S/S_0(B)$  functions of planar heterogeneity can be considered as unified quantitative structural characteristics of the samples under consideration.

The characteristic functions  $S/S_0(B)$  and  $\Delta S/S_0(B)$  describing the front and profile images of experimental samples oxyfluorinated with a mixture of 7.5%  $F_2$ +10%  $O_2$ + 82.5% He for 0.5, 1, 1.5 and 2 hours are shown in Fig. 4 and Fig. 5, respectively.

## 5. Correlation and regression analysis of functional and structural relationships

A quantitative assessment of the possibility of establishing in a certain sense “universal” (common to all optical images obtained under the same conditions of observation) threshold values  $B$  of pixel brightness, at which the relationship between the values of characteristic functions  $S/S_0(B)$  and  $\Delta(S/S_0(B))$  and the values of sorption capacities ( $SC$ ) of experimental samples is statistically significant, was performed using data correlation analysis methods.

The results of the correlation analysis (correlogram) of the structural and functional relationships of the sorption capacity with the parameters of the functions of integral and differential planar digital heterogeneity of frontal and profile images of experimental samples are shown in Fig. 6. The obtained values of Pearson correlation coefficients are stored on the ordinate axes; the threshold values of pixel brightness are stored on the abscissa axes.

It can be seen that the prediction of sorption properties of oxyfluorinated non-woven material by quantitative analysis of the front image of the corresponding sample is to some extent possible based on data from the first octile (0..32) of the corresponding correlograms. In cases (a), (c), (e) and (g) in this range of pixel brightness, the maximum value of the correlation coefficient of the sorption capacity of experimental samples  $SC$  and the values of the characteristic function  $\Delta(S/S_0(B))$  of the corresponding images is observed. However, since the correlation coefficient in the case of (c) takes a value  $\cong 0,5$ , and in the cases of (e) and (g) –  $\cong 0,75$ , the formation of the corresponding regression model is not appropriate due to the obviously poor quality of approximation of the model curve data.

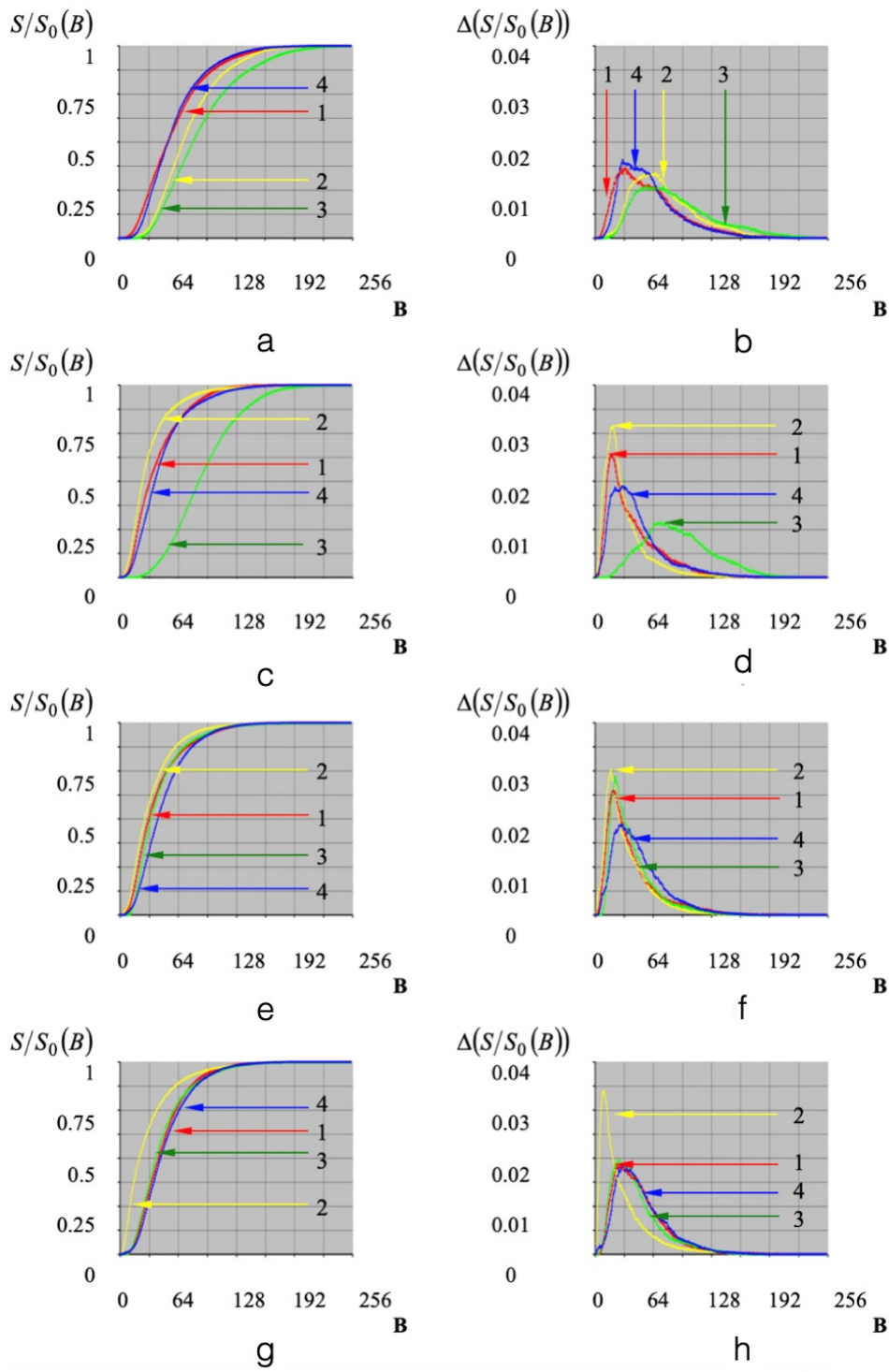


FIG. 4. The characteristic functions  $S/S_0(B)$  (a,c,e,g) and  $\Delta(S/S_0(B))$  (b,d,f,h) of the front images of the experimental samples L1(a,b), L2(c,d), L3(e,f) and L4(g,h). Curves 1–4 characterize the samples oxyfluorinated with a mixture of 7.5%  $F_2$ +10%  $O_2$ +82.5% He for 0.5, 1, 1.5 and 2 hours, respectively

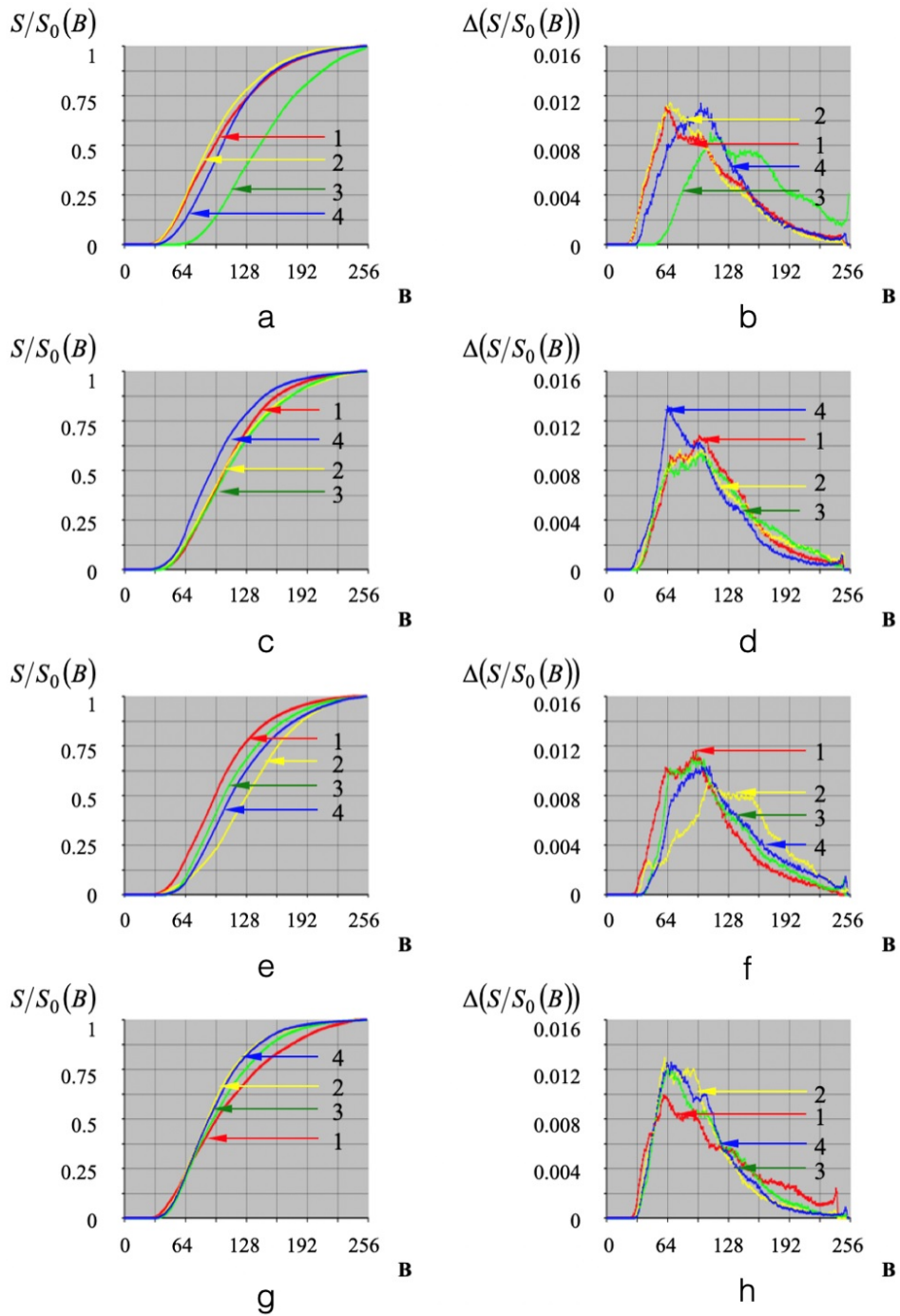


FIG. 5. The characteristic functions  $S/S_0(B)$  (a,c,e,g) and  $\Delta S/S_0(B)$  (b,d,f,h) of the profile images of the experimental samples L1(a,b), L2(c,d), L3(e,f) and L4(g,h). Curves 1–4 characterize samples oxyfluorinated with a mixture of 7.5%  $F_2$ + 10%  $O_2$ + 82.5% He for 0.5, 1, 1.5 and 2 hours, respectively

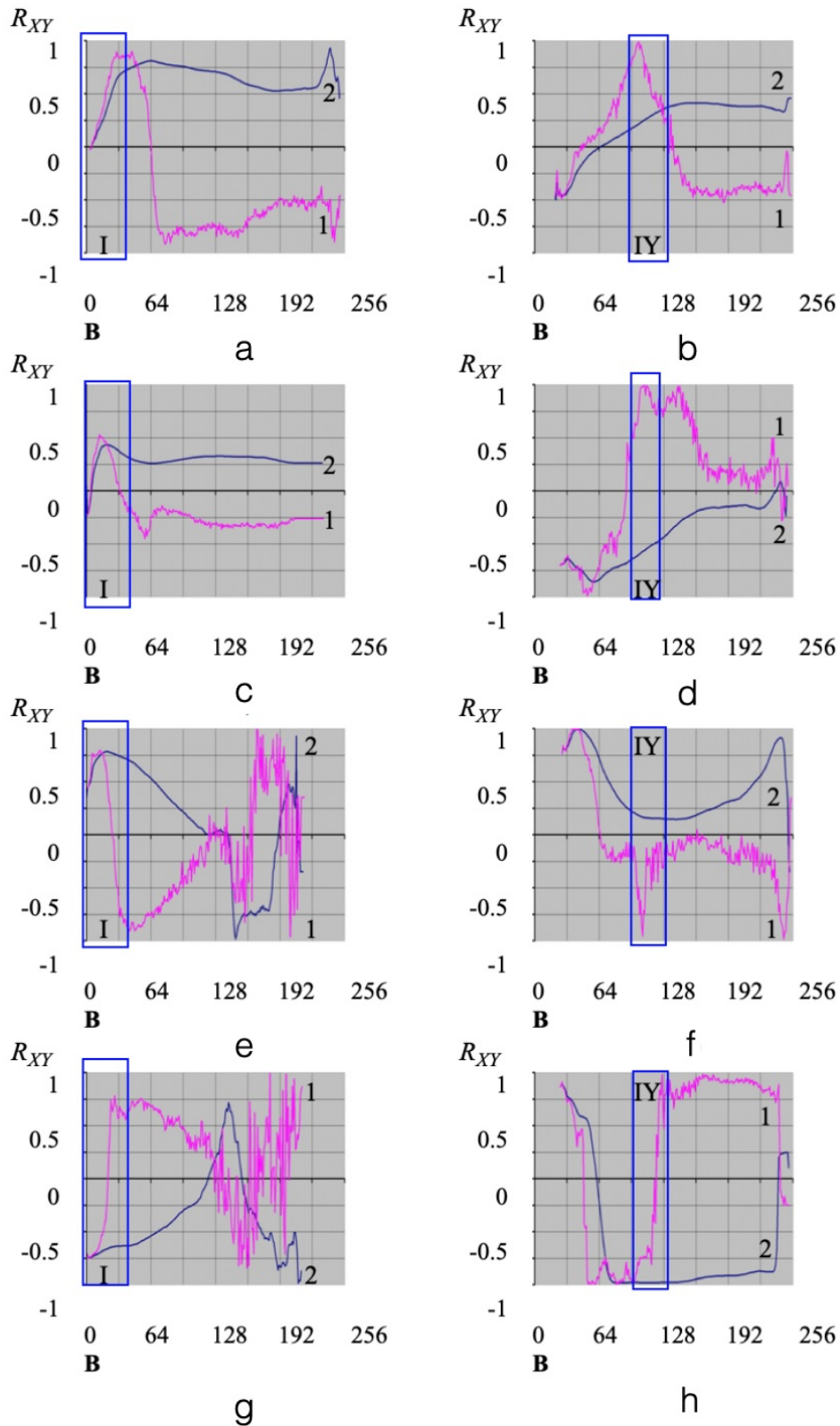


FIG. 6. The correlograms of the sorption capacity and the characteristic functions of digital planar heterogeneities for frontal (a,c,e,g) and profile (b,d,f,h) images of the experimental samples L1 (a,b), L2 (c,d), L3 (e,f) and L4 (g,h). Curves 1 and 2 correspond to the dependencies of the Pearson correlation coefficients  $R_{SC;S/S_0}(B)$  and  $R_{SC;\Delta(S/S_0)}(B)$  on the brightness threshold  $B$ . The first and fourth octiles are highlighted as rectangles

In the quantitative analysis of profile sections of experimental samples, the highest modulo values of the correlation coefficients  $R_{SC;\Delta(S/S_0)}(B)$  observed in the first half of the fourth octiles (96..112) (highlighted by rectangles in Fig. 6(b,d,f,h) of the obtained correlograms reach values close to the maximum possible for the considered parameters ( $\cong 1$  and  $\cong -1$ ). In other words, in cases (b) and (d), the maximum correlation is observed, and in cases (f) and (h), the maximum anticorrelation of the characteristic function  $\Delta(S/S_0(B))$  and sorption capacities of experimental samples  $SC$  are observed.

Thus, for statistically reliable structural and functional forecasting, it is necessary to form a quantitative assessment of sorption capacity  $SC$  mainly based on the analysis of differential planar heterogeneity functions  $\Delta(S/S_0(B))$  for profile images of experimental samples.

Based on a set of linear regression models describing possible partial dependences of sorption capacities of experimental samples (impregnated with latex in the modes L1, L2, L3 and L4) on the corresponding values of functions  $\Delta(S/S_0(B))$  for all  $B$  belonging to the interval [96; 112] (the first half of the fourth octile of correlograms), four models of the form visualized in Fig. 7 and specified in Table 4 were formed:

$$SC_l = \sum_{k=96}^{112} p_k \cdot (a_k \cdot \Delta_l(S/S_0(B_k)) + b_k) = \alpha_l \cdot \overline{\Delta_l(S/S_0)} + \beta_l, \tag{2}$$

in which  $p_k = \frac{R_k^2}{\sum_{k=96}^{112} R_k^2}$ ;  $R_k^2 = 1 - \frac{\sum_{l=1}^4 (SC_l - SC_{l,k})^2}{\sum_{l=1}^4 (SC_l - SC_{l,k})^2}$ ;  $\{SC_l\}_4$  – values of the sorption capacities of samples

impregnated in the modes L1, L2, L3 and L4;  $SC_{l,k}$  – the value of the sorption capacity of the  $l$ -sample calculated by the  $k$ -model;  $\overline{SC}_l$  – the average value of the sorption capacity of all samples of the  $l$ -series;  $\alpha_l$  and  $\beta_l$  – parameters of the  $l$ -functional and structural model.

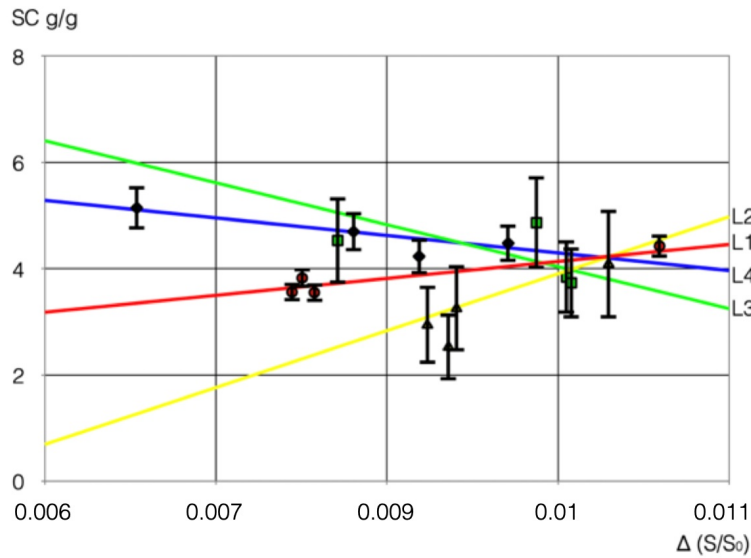


FIG. 7. The dependences of the experimental samples' sorption capacities on the values of the digital differential planar heterogeneity functions

TABLE 4. Values of parameters of functional and structural models (2) obtained by the weighted least squares (WLS) method

Parameter	L1	L2	L3	L4
$\alpha_l \pm \delta\alpha_l$	260±30	860±90	-630±30	-260±30
$\beta_l \pm \delta\beta_l$	1.7±0.2	-4.5±0.5	10.2±1	6.9±0.7
$R_l^2$	0.88±0.09	0.61±0.09	0.01±0,01	0.73±0.07

It can be seen that the sorption capacity slightly depends on the structural characteristics of the modified nonwoven fabric at low (L1) and high (L4) concentrations of rubber in latex and strongly depends on the structural characteristics at concentrations of rubber close to a certain "threshold" value. If the proportion of rubber in the impregnating latex is less than this value, the sorption capacity increases with increasing differential planar heterogeneity. Otherwise, the larger the value  $\Delta(S/S_0)$  becomes, the smaller the sorption capacity for latex will characterize the sample.

Thus, to ensure relatively stable values of the sorption capacity for the oxyfluorinated nonwoven fabric over its entire "effective" surface, functional covering materials similar to latexes with a percentage of rubber or less than 4 or more than 12% should be used. If it is necessary to synthesize stochastic sorption maps formed during impregnation of bicomponent polyester fiber materials, it is necessary to use mixtures similar to latex with an approximately 6% rubber content as functional ones.

The presence of the above "extreme" value is probably associated not only with the limited sedimentation stability of rubber in water, but also significantly depends on the relative position, total area, and degree of oxyfluorination of the surfaces of latex-wetted fibers.

### 5.1. Multi-scale structural analysis of nonwoven fabrics

Macroscopic optical images of the original and oxyfluorinated nonwoven fabrics fragments with dimensions of  $800 \times 1000$  microns are shown in Fig. 8.

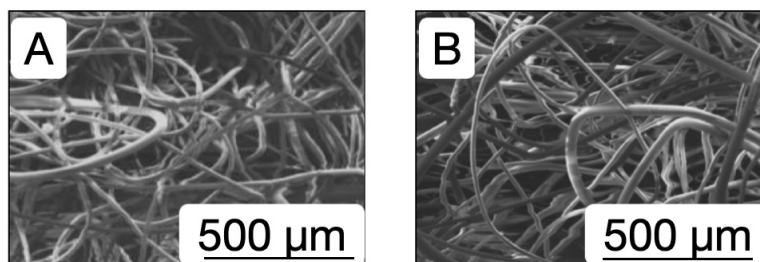


FIG. 8. SEM-images of nonwoven fabrics surfaces made of polyester fibers based on PET initial (A) and oxyfluorinated (B) with a gas mixture of 7.5%  $F_2$ +10%  $O_2$ +82.5% He

Neither visual nor quantitative analysis of these fibrous materials images made it possible to statistically reliably establish the presence and degree of the oxyfluorination influence on the material macroscopic structure.

When analyzing SEM-images (with dimensions of  $250 \times 350$  microns) of the same samples' fragments at the microscopic level (at the lowest magnification available for the Jeol7500F microscope (Japan)) differences in the observed textural heterogeneity degrees of the initial and oxyfluorinated fibers surfaces become noticeable (Fig. 9), but a quantitative description of the corresponding nanoscale inhomogeneities is still impossible (due to the fact that at a low resolution of the electron microscope, the characteristic size for one pixel of the generated image exceeds 1 micron).

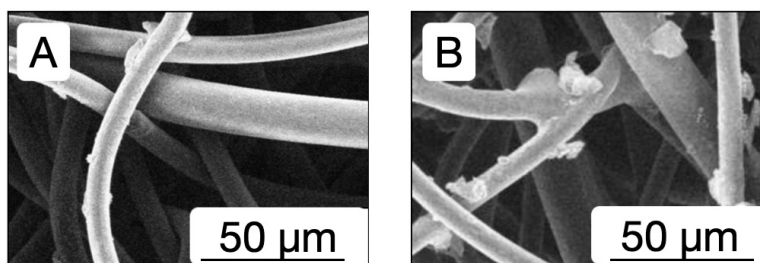


FIG. 9. SEM-images of polymer fiber groups for initial (A) and oxyfluorinated (B) with a gas mixture of 7.5%  $F_2$ + 10%  $O_2$ + 82.5% He

Finally, at the maximum magnification for the Jeol7500F (Fig. 10), it is possible to fix and then model the nanotextures of the original and oxyfluorinated nonwoven fibers using the original method of the quantitative SEM-images analysis developed earlier [19–21]. The characteristic size for one pixel in this case is  $\sim 1$  nm.

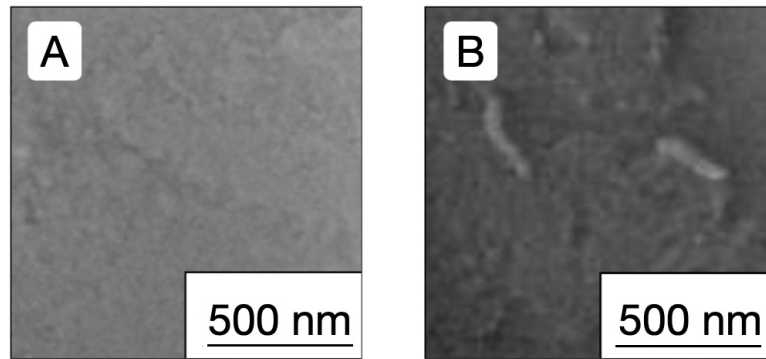


FIG. 10. SEM-images of polymer fiber surfaces: initial (A) and oxyfluorinated (B) with a gas mixture of 7.5%  $F_2$ +10%  $O_2$ + 82.5% He

## 5.2. Dependence of the fiber surfaces' nanotexture on the duration of modification

SEM-images (with dimensions of  $1.2 \times 1.2$  microns) of the surfaces' fragments for the original and treated with a gas mixture of 7.5%  $F_2$ + 10%  $O_2$ + 82.5% He fibers (with modification durations of 0.5, 1, 1.5 and 2 hours) are shown in Fig. 11.

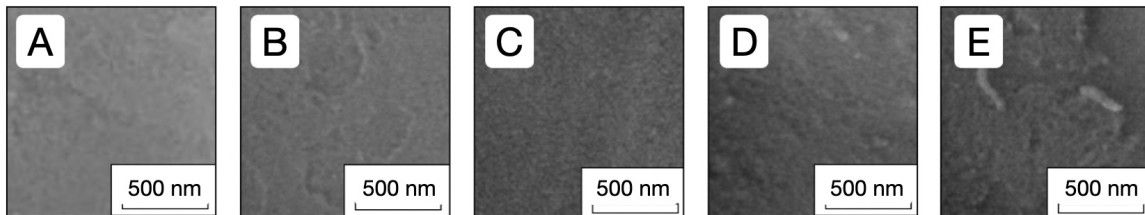


FIG. 11. SEM-images of the PET fiber surfaces: initial (A) and oxyfluorinated with a gas mixture of 7.5%  $F_2$ + 10%  $O_2$ +82.5% He for 0.5 (B), 1 (C), 1.5 (D), and 2 (E) hours

The study of the nanostructural transformations dynamics of fiber surfaces showed that the localization region of the morphological spectrum (Fig. 12), which characterizes the sample's SEM-image, increases with increasing the oxyfluorination duration, probably reaches the maximum value, and then decreases. (Fig. 13). The dynamics of the morphological spectrum expressed in dimensionless units of the radius of the localization region and the derivative of the model (1) are anticorrelated at the level of  $0.78 \pm 0.08$ .

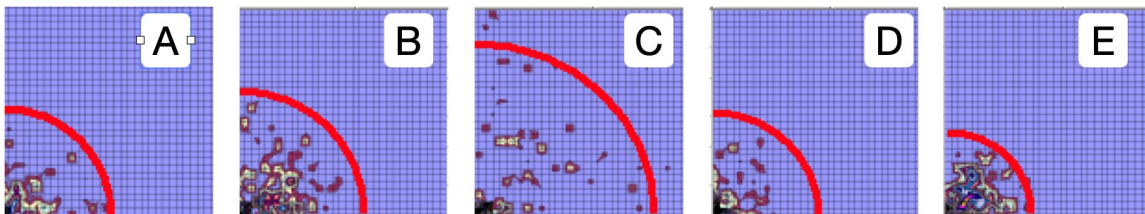


FIG. 12. Morphological spectra of the surfaces SEM-images for material-forming PET fibers: initial (A) and oxyfluorinated with a gas mixture of 7.5%  $F_2$ + 10%  $O_2$ + 82.5% He for 0.5 (B), 1 (C), 1.5 (D) and 2 (E) hours. The line indicates the radius of localization of the morphological spectrum

Since it is known [22] that the PET surface hydrophilicity increases sharply during gas-phase treatment with mixtures whose active reagents are fluorine and oxygen, when latex hits the effective surface of a nonwoven fabric, the processes of diffusion of latex as a colloidal solution into the thickness of the nonwoven material and intensive water sorption by the PET fibers surface, hydrophilized by oxyfluorination begin to compete. This phenomenon increases the uncertainty in predicting the sorption capacity at close to critical values of the rubber concentration in latex.

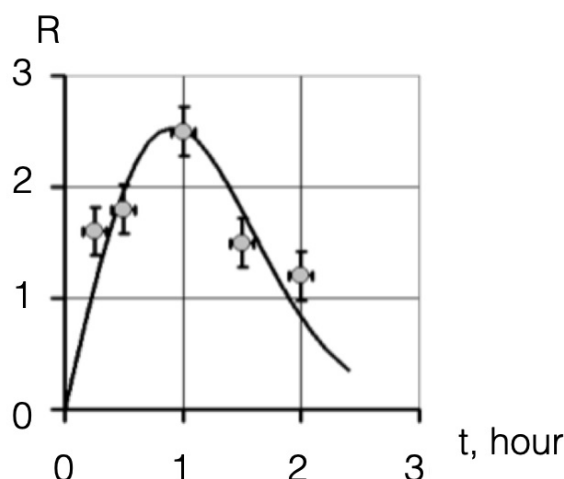


FIG. 13. Dependence of the morphological spectrum localization radius of the polymer fiber surface SEM-image on the duration of its oxyfluorination

However, the relationship between the latex-sorption capacity increment of the material, and the values of the regions radii for the morphological spectra localization, which characterize the nanoscale SEM-images of fibers surfaces, describes the mechanism by which changes in setting of the modification mode (the duration of the gas-phase oxyfluorination) manages the functional material properties (e.g., sorption capacity).

## 6. Conclusion

An approach to structural and functional modeling of composite materials based on oxyfluorinated nonwovens has been developed. The structural component of the model can be represented in the form of integral or differential characteristic functions of planar heterogeneity  $S/S_0(B)$  and  $\Delta S/S_0(B)$  and in the form of expansion into a two-dimensional Fourier series with a morphological spectrum  $\{A_{kl}\}_{N \times N}$ .

The presence of correlations between the sorption capacities (for latex) and the structural characteristics of the optical image of experimental samples was established using classical methods of correlation analysis of data. The obtained functional and structural model allows us to quantify the expected values of the sorption capacity of bicomponent polyester fiber materials under certain restrictions on the chemical composition of the impregnating liquid-phase mixtures. It was found that the uncertainty in the predicted values of the sorption capacity increases sharply with the  $\cong 6\%$  content of rubber in latex, which indicates the determining influence of the particular structure of a particular sample on its sorption properties relative to the above-mentioned impregnating mixture. Since it is impossible to form structurally identical non-woven fabrics (due to the peculiarities of manufacturing technology), it is recommended to use compositions similar to latex with a far from extreme percentage of rubber ( $<4$  or  $>12\%$ ) when finishing oxyfluorinated fiber materials with covering compounds.

## Acknowledgments

This work was funded by Ministry of Science and Higher Education of the Russian Federation (State assignment "Structure and properties of the polymer materials produced using system of chemically, thermally and / or mechanically induced both surface and bulk modification techniques", topic number FZRR-2020-0024, code 0699-2020-0024).

## References

- [1] Li Y., Ma T., Yang S.T., Kniss D.A. Thermal compression and characterization of three-dimensional nonwoven PET matrices as tissue engineering scaffolds. *Biomaterials*, 2001, **22**(6), P. 609–618.
- [2] Hyde G.K., Scarel G., Peng Q., Lee K., Gong B., Roberts K.G., Roth K.M., Hanson C.A., Devine C.K., Stewart S.M., Hojo D., Na J.-S., Jur J.S., Parsons G.N., Spagnola J.C. Atomic layer deposition and abrupt wetting transitions on nonwoven polypropylene and woven cotton fabrics. *Langmuir: the ACS journal of surfaces and colloids*, 2010, **26**(4), P. 2550–2558.
- [3] Du D., Li P., Ouyang J. Graphene coated nonwoven fabrics as wearable sensors. *Journal of Materials Chemistry C*, 2016, **4**(15), P. 3224–3230.
- [4] Smirnov A.V., Genis A.V. Effect of process parameters on the structure and physicommechanical properties of nonwoven materials manufactured by aerodynamic spinning from polymer solution. *Fibre Chemistry*, 2002, **34**(6), P. 400–406.
- [5] Kumar A., Gaurav, Malik A.K., Tewary D.K., Singh B. A review on development of solid phase microextraction fibers by sol-gel methods and their applications. *Analytica Chimica Acta*, 2008, **610**(1), P. 1–14.

- [6] Bolbasov E.N., Stankevich K.S., Sudarev E.A., Kudryavtseva V.L., Tverdokhlebov S.I., Bouznic V.M., Antonova L.V., Matveeva V.G., Anisimov Y.G. The investigation of the production method influence on the structure and properties of the ferroelectric nonwoven materials based on vinylidene fluoride - tetrafluoroethylene copolymer. *Materials Chemistry and Physics*, 2016, **182**, P. 338–346.
- [7] Moheman A., Alam M.S., Mohammad A. Recent trends in electrospinning of polymer nanofibers and their applications in ultra thin layer chromatography. *Advances in Colloid and Interface Science*, 2016, **229**, P. 1–24.
- [8] Bao L., Wang Y., Wakatsuki K., Morikawa H., Baba T., Fukuda Y. Development of a high-density nonwoven structure to improve the stab resistance of protective clothing material. *Industrial Health*, 2017, **55**(6), P. 513–520.
- [9] Lipinski C.A., Lombardo F., Dominy B.W., Feeney P.J. Experimental and computational approaches to estimate solubility and permeability in drug discovery and development settings. *Advanced Drug Delivery Reviews*, 1997, **23**(1-3), P. 3–25.
- [10] Ng E.P., Mintova S. Nanoporous materials with enhanced hydrophilicity and high water sorption capacity. *Microporous and Mesoporous Materials*, 2008, **114**(1-3), P. 1–26.
- [11] Liu K., Jiang L., Yao X. Recent developments in bio-inspired special wettability. *Chemical Society Reviews*, 2010, **39**(8), P. 3240–3255.
- [12] Hes L., de Araujo M., Djulay V.V. Effect of mutual bonding of textile layers on thermal insulation and thermal contact properties of fabric assemblies. *Textile Research Journal*, 1996, **66**(4), P. 245–250.
- [13] Tovmash A.V., Polevov V.N., Mamagulashvili V.G., Chernyaeva G.A., Shepelev A.D. Fabrication of sorption-filtering nonwoven material from ultrafine polyvinyl alcohol carbonized fibres by electrospinning. *Fibre Chemistry*, 2005, **37**(3), P. 187–191.
- [14] Radetic M.M., Jovic D.M., Jovancic P.M., Petrovic Z.Lj., Thomas H.F. Recycled wool-based nonwoven material as an oil sorbent. *Environmental Science and Technology*, 2003, **37**(5), P. 1008.
- [15] Prorokova N.P., Istratkin V.A., Kumeeva T.Y., Vavilova S.Y., Kharitonov A.P., Bouznic V.M. Improvement of polypropylene nonwoven fabric antibacterial properties by the direct fluorination. *RSC Advances*, 2015, **5**(55), P. 44545–44549.
- [16] Bondar Y.V., Kim H.J., Lim Y.J. Sulfonation of (glycidyl methacrylate) chains grafted onto nonwoven polypropylene fabric. *Journal of Applied Polymer Science*, 2007, **104**(5), P. 3256–3260.
- [17] Poncin-Epaillard F., Brosse J.C., Falher T. Cold plasma treatment: surface or bulk modification of polymer films. *Macromolecules*, 1997, **30**(15), P. 4415–4420.
- [18] Dedov A.V., Nazarov V.G. Processed nonwoven needlepunched materials with increased strength. *Fibre Chemistry*, 2015, **47**(2), P. 121–125.
- [19] Isaev E.A., Pervukhin D.V., Kornilov V.V., Tarasov P.A., Grigoriev A.A., Rudyak Yu.V., Rytikov G.O., Nazarov V.G. Platelet adhesion quantification to fluorinated polyethylene from the structural characteristics of its surface. *Mathematical biology and bioinformatics*, 2019, **14**(2), P. 420–429.
- [20] Drozdov S.A., Nazarov V.G., Nozdrachev S.A., Rudyak Yu.V., Rytikov G.O. The polymer composites morphological structure simulation. *Nanosystems: Physics, Chemistry, Mathematics*, 2017, **8**(1), P. 137–145.
- [21] Petrushin V.N., Rudyak Y.V., Rytikov G.O. The holistic method of the surface structure characterization. Proceedings of “2016 14th International Baltic Conference on Atomic Layer Deposition (BALD 2016)”. St. Petersburg, Russia, 2–4 October 2016, P. 15–19.
- [22] Nazarov V.G., Doronin F.A., Evdokimov A.G., Rytikov G.O., Stolyarov V.P. Oxyfluorination-Controlled Variations in the Wettability of Polymer Film Surfaces. *Colloid Journal*, 2019, **81**, P. 146–157.

## Spin-glass transition in porous spheres BiFeO<sub>3</sub>

A. V. Dmitriev<sup>1\*</sup>, E. V. Vladimirova<sup>1</sup>, M. A. Semkin<sup>2</sup>, A. V. Korolev<sup>3</sup>

<sup>1</sup>Institute of Solid State Chemistry, UB RAS, 91, Pervomaiskaya Str., Ekaterinburg, 620990, Russia

<sup>2</sup>Ural Federal University, Department of Magnetism, 48, Kuibyshev Str., Ekaterinburg, Russia

<sup>3</sup>M. N. Mikheev Institute of Metal Physics UB RAS, 18, S. Kovalevskaya Str., Ekaterinburg, 620108, Russia

\*dmitriev@ihim.uran.ru

DOI 10.17586/2220-8054-2020-11-5-565-571

Magnetic properties of porous spheres BiFeO<sub>3</sub> have been studied at temperatures ranging from 2 to 300 K. A transition to cluster spin glass state has been detected in the region of about 100 K. The presence of the transition is confirmed by nonlinear variation of coercive force and the appearance of exchange displacement of magnetic hysteresis loops at temperature below 100 K. Temperature dependence of magnetization for zero-field cooled regime exhibit a maximum at some temperature  $T_m$ . The function  $T_m(H)$  ( $H$  is magnetic field) changes in accordance with Almeida–Thouless line. The performed measurements of the frequency dependence of AC susceptibility confirm the behavior of spin glass with spin freezing temperature  $T_f = 116$  K. The critical index  $z\nu = 2.5$  agrees well with the mean-field theory  $z\nu = 2.0$ .

**Keywords:** bismuth ferrite, magnetic properties, porous spheres, Almeida–Thouless line, spin cluster glass.

*Received: 19 August 2020*

*Revised: 14 September 2020*

### 1. Introduction

It is known that the bismuth ferrite BiFeO<sub>3</sub> (BFO) is one of few materials exhibiting multiferroic properties at room temperature. However, bulk BFO is not suitable for application because of a spin cycloid with period length of 62 nm in its magnetic structure [1] that reduces weak ferromagnetism to zero, thus preventing the appearance of a linear magnetoelectric effect [2]. Reduction to nanodimension is an effective method of ferromagnetic order formation in BFO system due to an increase of the fraction of uncompensated spins and suppression of spiral order as a result of reduction of crystallite sizes [3, 4]. Both in thin BFO films and nanocrystals, magnetic switching can be induced by electric field [5, 6], which opens up prospects for practical application of BFO in magnetic sensors, spintronics and data storage devices [1].

Recently, the study of magnetic properties was focused on BFO films and nanopowders. Different experiments, including direct magnetic measurements, suggest several magnetic transitions in the temperature range from 5 to 250 K [7–9]. The nature of these transitions is not entirely understood. They can be related either to spin orientation variation or to transition to spin glass state. The results of neutron diffraction studies and investigations of Raman spectra and dielectric properties revealed the presence of a phase transition connected with spin reorientation at 150 K [10–12]. Spin reorientation transition facilitates transition to spin glass state at further decrease of temperature [12]. The majority of researchers of nanocrystalline powders believe that magnetic properties can be explained in the model of antiferromagnetic nucleus with ferromagnetic shell. At the same time, some questions remain undetermined. Unusual effects of exchange displacement of hysteresis loop above transition temperature to spin glass state and nonmonotonic variation of coercive force require further research [9, 13]. Park et al. [3] inferred that the anomalous magnetization behavior in BFO nanoparticles arises from a complex interplay between the finite size effects, interparticle interaction, and a random distribution of anisotropy axis in nanoparticle assemblies. The systems of interacting magnetic nanoparticles may demonstrate a large variety of phenomena, which are of interest both for fundamental scientific studies and future practical applications of magnetic nanoparticles [14].

Examples of nanoparticles assembling are such materials as nanofibers [15], nanotubes [16], hollow spheres [17, 18] etc. consisting of randomly oriented nanocrystals [15, 18]. Earlier we showed that spherical agglomerates of about 1  $\mu\text{m}$  in size possess at room temperature weak ferromagnetism typical of nanoparticles making up spheres [18]. At the same time, there are no available data on the presence of low-temperature phase transitions typical of nanoparticles. At present, almost no experimental studies of low-temperature magnetic properties of nanostructured BFO are available.

In this work, the magnetic properties of spherical porous BFO agglomerates produced by ultrasonic spray pyrolysis are comprehensively studied in the temperature range 2 – 300 K. Based on the results of field and temperature dependences of magnetization, magnetic AC susceptibility measurements we have established the existence of a phase transition to spin glass state in the examined materials.

## 2. Experimental

Spherical BFO agglomerates were synthesized by ultrasonic spray pyrolysis (USP) from a solution of iron and bismuth nitrates with addition of 6 moles of tartaric acid (TA) per 1 mole of  $\text{BiFeO}_3$ . The synthesis procedure is described in detail in works [18, 19].

X-ray powder diffraction (XRPD) analysis was carried out using an XRD-7000 (SHIMADZU) diffractometer with a secondary monochromator with  $\text{Cu K}\alpha$  radiation in the  $2\theta$  range from 20 to  $80^\circ$  with a step of  $0.03^\circ$ . Structural investigations were performed in transmission geometry using an automatic STOE STADI-P diffractometer equipped with a linear mini-PSD detector using  $\text{Cu K}\alpha_1$  radiation in the  $2\theta$  range from 5 to  $120^\circ$  with a step of  $0.02^\circ$ . Polycrystalline silicon ( $a = 5.43075(5) \text{ \AA}$ ) was used as an external reference.

The morphology of the samples and 3D FIB-SEM tomography study were carried out using a TESCAN LYRA 3 dual beam system.

Magnetic measurements were carried out using setups of Quantum Design – MPMS-XL-7 (UFU) as well as PPMS-9 of the Collaborative Access Center “Testing Center of Nanotechnology and Advanced Materials” of the Institute of Metal Physics.

## 3. Results and discussion

The X-ray diffraction patterns of BFO sample are presented in Fig. 1(a). All the basic reflections correspond to ferrite  $\text{BiFeO}_3$  with perovskite structure and space group  $R3c$  (ICSD Collection Code 15299). The lattice parameters are calculated by way of full-profile analysis of X-ray diffraction patterns with the use of structural models of the corresponding compounds ( $a_{hex} = 5.58851$ ,  $c_{hex} = 13.7852$ ). The sizes of coherent scattering regions (CSR) were found by the Le Bail method using the Klug & Alexander approach [20], allowing the contribution of size effects to FWHM to be determined. The value of CSR, calculated from the X-ray diffraction patterns, is proportional to the sizes of nanocrystallites composing the agglomerates (CSR = 26.2 nm). Therefore, hereafter, we shall consider that the CSR value is equal to nanocrystallite size. For the analysis of lattice distortions we used the rhombohedral cell parameters  $a = a_{hex}/\sqrt{2}$  and  $c = c_{hex}/2\sqrt{3}$  ( $c/a = 1.0070$ ). The obtained nanocrystal sizes and the lattice distortion parameter coincide with the results of structural studies of nanopowders reported in work [21]. Earlier, we showed [18] that the samples synthesized by USP technology contain no oxygen vacancies, and all Fe ions have valence 3+.

The electron microscopy study of the powders reveals that all the samples produced from solutions with TA concentration 6 mol TA/mol BFO represent porous agglomerates of spherical shape. The mean diameter of the agglomerates determined from the results of 300 – 400 measurements amounted to about 1.2 microns (Fig. 1(b)). The internal structure of agglomerates was studied by the SEM method with focused gallium ion beam polishing (FIB). Fig. 1(c) displays a SEM image of an agglomerate after cross-section with preliminary application of a platinum mask with the use of a gas injecting system (GIS). The platinum mask is a heat sink and it also protects particle from melting and mechanical failure during ion beam etching. The image of particle after polishing (Fig. 1(c)) proves that the agglomerates have a porous cellular structure throughout.

Figure 2(a) demonstrates magnetic hysteresis loops of the examined powder. Note that the loops shape and the magnetization values practically coincide with the field dependences of magnetization of BFO nanopowders of size smaller than 40 nm reported in work [3]. The coercive force values at room temperature are also similar. The temperature dependence  $H_C(T)$  exhibits a minimum near 100 K. An analogous  $H_C(T)$  dependence is observed in nanocrystals [9] with a minimum at 50 – 60 K. The authors of work [8] attribute the  $H_C(T)$  minimum to the transition of iron ions on the surface of nanoparticles to spin cluster glass state, which is confirmed by the exchange displacement of hysteresis loops. It is interesting to study the exchange displacement in porous spheres BFO. The inset in Fig. 2(a) shows  $M(H)$  loops for ZFC and FC sample ( $H_{FC} = 70 \text{ kOe}$ ) at 2 K (the sample was field cooled from 300 to 2 K). It can be seen that the FC hysteresis loop is displaced towards negative field and positive magnetization, whereas in ZFC process the loop is centered around the origin of coordinates.

Note that the process of field cooling adopted in this study is not a traditional FC, since  $T_N$  of BFO is much higher than 300 K. Thus, the exchange anisotropy established in this system without usual FC can be related to spontaneous effect of exchange displacement [7]. The dependence of  $H_E(T)$  on cooling field of 70 kOe is presented in Fig. 2(b). As the temperature is raised,  $H_E$  decreases abruptly and becomes equal to zero at  $T > 100 \text{ K}$ .

If the minimum on the temperature dependence of  $H_C(T)$  in the region of 100 K is related to the transition to spin glass state, then near this temperature there should be a temperature-dependent anomaly in the magnetization variation in ZFC mode.

Figure 3(a) demonstrates ZFC and FC magnetization curves of spherical agglomerates of BFO in 500 Oe field. As seen from Fig. 3(a), there is a divergence of ZFC and FC curves, which begins at 300 K and increases gradually with decreasing temperature. The observed splitting of the ZFC and FC curves at low temperatures is a distinctive feature

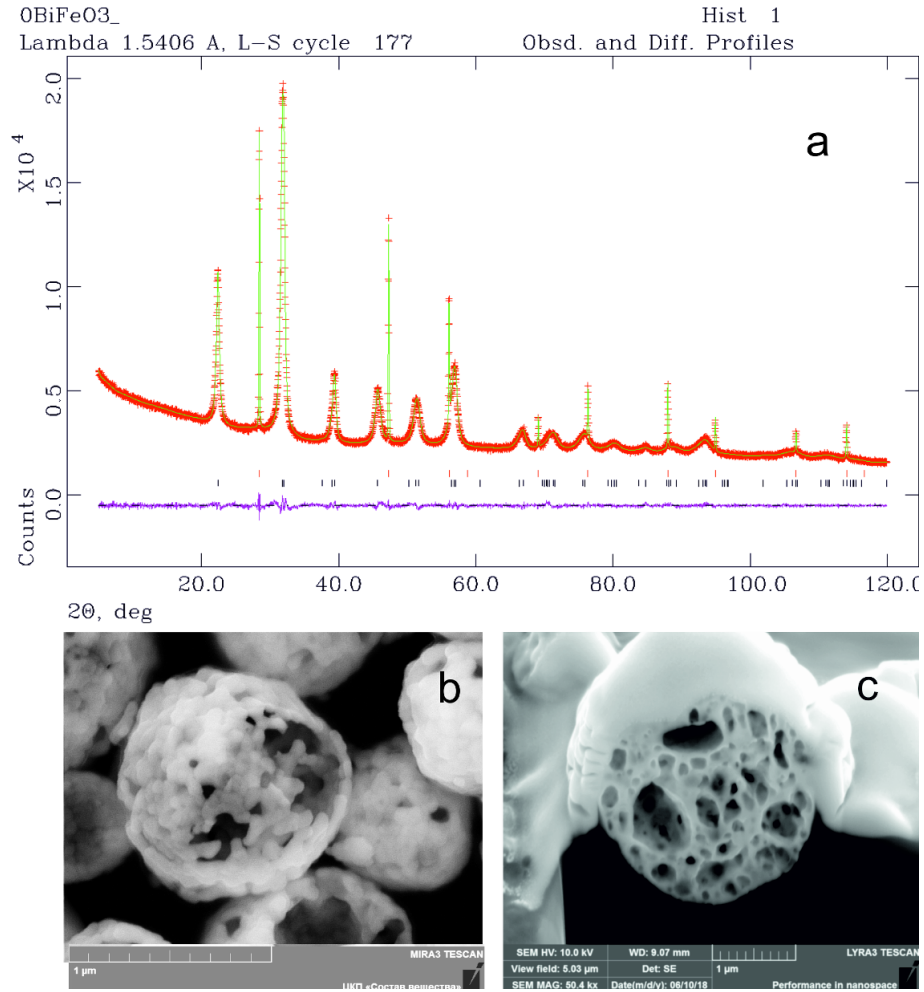


FIG. 1. a – Experimental (crosses), calculated (solid line), and difference (bottom line) XRPD patterns for  $\text{BiFeO}_3$  and Si used as internal standard. Series of tick marks correspond to the Bragg reflections. b – SEM image of BFO agglomerates. c – SEM image of agglomerate after gallium ion beam polishing for 15 min. A platinum mask is applied on top

of spin glass-like state and can be due to local spin clusterization [22]. In addition, we observe a sharp inflection on the ZFC curve at about 120 K, which can be ascribed to a typical blocking process of superparamagnetic spin moments assembly [23]. On the contrary, these moments are arranged parallel to the applied field during FC measurement, which leads to a large divergence of FC and ZFC curves below the freezing temperature. Similar changes in FC and ZFC are observed in BFO nanopowders [7–9]. A distinctive feature is that the maximum on the ZFC curve in nanoparticles is observed as a rule at a temperature of about 50 K.

The ZFC and FC magnetization characteristics of spherical BFO agglomerates were additionally studied by applying displacement magnetic field of different strength from 0.1 to 30 kOe. The splitting temperature  $T_{irr}(H)$  (irreversibility in ZFC) in all fields was observed in the temperature range 250 – 300 K. We could not establish the field dependence of  $T_{irr}(H)$  because of gradual divergence (perhaps this is due to the absence of heating above 300 K). The temperature dependences of ZFC magnetization in different fields are presented in Fig. 3(b).

The temperature ( $T_m$ ) of ZFC plot,  $M(T)$ , is displaced towards lower temperatures when the magnetic field  $H$  increases. For fields smaller than 10 – 20 kOe this displacement is described by Almeida–Thouless dependence (AT line):

$$H = A[1 - T_m(H)/T(0)]^3, \quad (1)$$

where  $T_m(H)$  and  $T(0)$  are the field dependence and the maximum temperature at  $H = 0$ , respectively. Eq. (1) establishes the boundary of transition to superparamagnetic state or the appearance of spin glass (AT line). As seen from Fig. 3(c), the  $T_{max}(H)$  dependence can be divided into 2 parts: the first – in the interval 3 – 20 kOe; the second – in the interval 0 – 3 kOe. Data fitting by AT equation yields  $T_1(0) = 97$  K for magnetic fields 3 – 20 kOe and

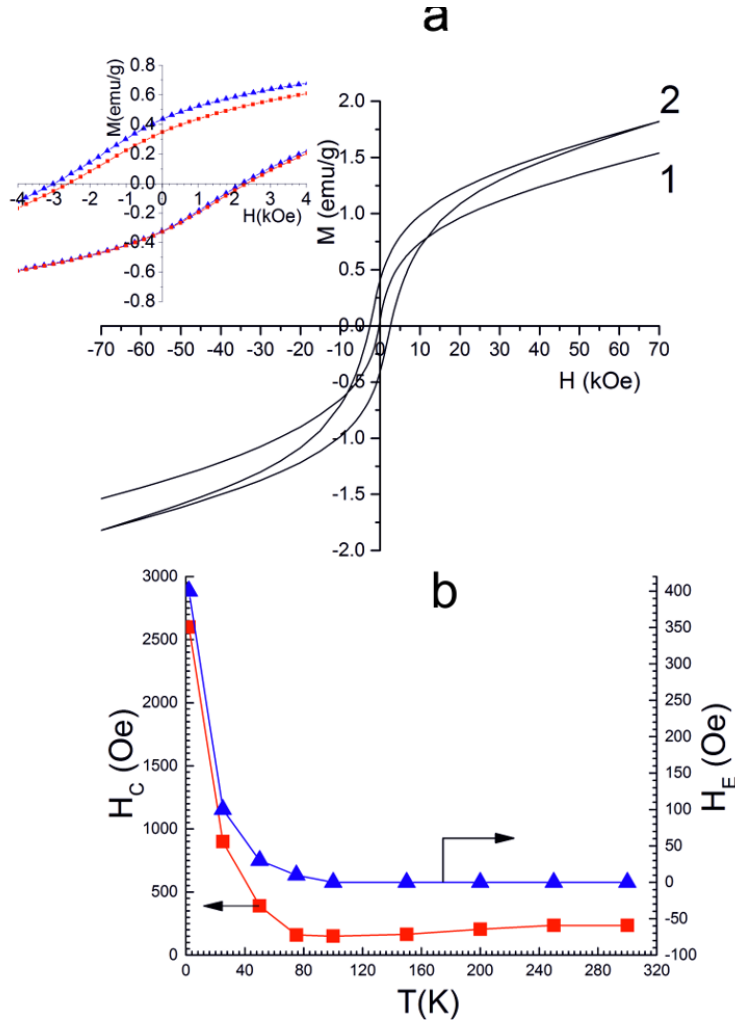


FIG. 2. a – Field dependences of magnetization. 1 – 300 K; 2 – 2 K. Inset: loops obtained in ZFC and FC regimes in field of 70 kOe. b – Temperature dependences of coercive force  $H_C$  and displacement fields  $H_E$

$T_2(0) = 140$  K for fields 0 – 3 kOe. An analogous inflection on the AT line in the region of 1 – 2 kOe is observed in films and nanocrystals [8, 24].

In order to find out, to which state the low-temperature phase corresponds, we measured the frequency-dependent variable of magnetic AC susceptibility  $[\chi(\omega, T)]$  in zero DC field.

Figure 4(a) shows the temperature dependences of the real part  $\chi^1$  of susceptibility to alternating field for porous spheres BFO at different frequencies at  $H = \text{const} \approx 0$ . It is seen that the position of the  $\chi^1(T)$  peak, corresponding to the freezing temperature  $T_f$ , is displaced towards higher temperatures with increasing frequency. The shift of the peak temperature  $\chi^1(\omega, T)$  was analyzed in terms of the empirical parameter of frequency-dependent sensitivity  $K = \Delta T_f / (T_f \Delta \ln \omega)$  (so-called Mydosh parameter), lying in the range 0.001 – 0.01 and 0.01 – 0.1 [25] for spin glass freezing and SPM blocking, respectively. In case of BFO, the  $K$  parameter turns out to be equal to 0.06, which is higher than in usual spin glass system and fits better SPM blocking. From Fig. 3(a) it is possible to obtain the temperature dependences of relaxation time  $\tau = 1/2\pi f$  (Fig. 4(b)). Since the Mydosh parameter corresponds to SPM, then in accordance with the Neel superparamagnetic model the relaxation process should follow the Arrhenius equation [26]:

$$\tau = \tau_0 \exp(E_a/k_B T_f), \quad (2)$$

where  $\tau_0$  is the relaxation time constant,  $E_a$  is the anisotropy energy, and  $k_B$  is the Boltzmann constant. The results of fitting with  $E_a/k_B = 3249 \pm 6$  K and  $\tau_0 = 2.3 \cdot 10^{-15}$  are presented in Fig. 4(b). From the obtained values it follows that BFO spheres are not Neel SPM system [27], since for superparamagnetic relaxation  $\tau_0$  should be  $10^{-10} - 10^{-13}$  s. The temperature dependence of relaxation time can be also approximated with the use of Vogel–Fulcher or

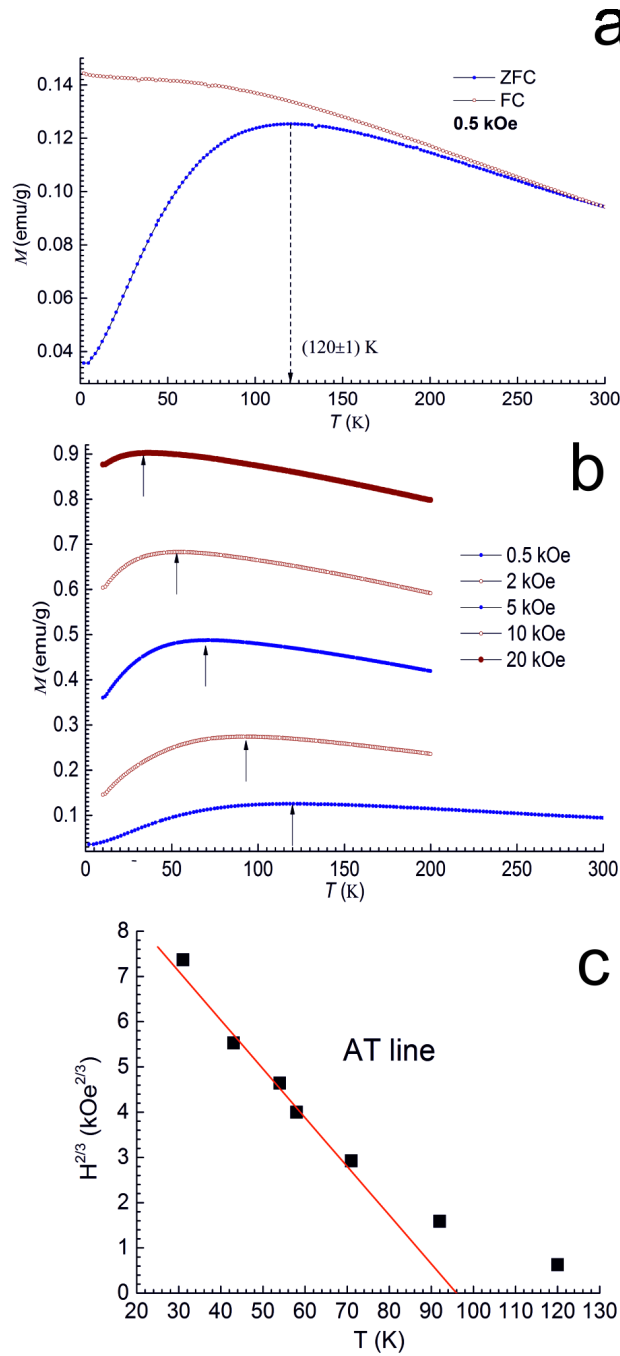


FIG. 3. Almeida–Thouless line is shown by dotted line. a – Temperature dependences of FC and ZFC magnetization at values of magnetic field strength 0.5 KOe; b – Temperature dependences of ZFC magnetization at different values of magnetic field strength; c – Almeida–Thouless line (AT)

power laws. For the Vogel–Fulcher law [28]:

$$\tau = \tau_0 \exp[E_a/k_B(T_f - T_{VF})], \quad (3)$$

where  $T_{VF}$  is the representative Vogel–Fulcher temperature. The best fit between  $\tau(T)$  data and eq. (3) yields  $E_a/k_B = 86 \pm 6$  K,  $T_{VF} = 109 \pm 0.2$  K and  $\tau_0 = (2.7 \pm 0.06) \times 10^{-5}$  s. For the power law [29]:

$$\tau = \tau_0(T_f/T_g - 1)^{z\nu}, \quad (4)$$

where  $T_g$  is the glass transition temperature (static freezing temperature),  $\nu$  is the critical index describing the correlation distance growth, and  $z$  is the dynamic index describing the relaxation retardation. The power law is observed

at  $T_g = 116 \pm 11$  K,  $\tau_0 = (6.7 \pm 0.13) \times 10^{-6}$  s and  $z\nu = 2.5 \pm 1$ . The values of  $\tau_{01}$  and  $\tau_{02}$  for both power and VF laws fall in the typical category of cluster glass (CG) ( $\tau = 10^{-5} - 10^{-10}$  s) for concentrated systems [30], rather than in canonical spin glasses in diluted systems. Thus, both the power law and V-F dynamics prove that the frequency-dependent anomaly in  $\chi(\omega, T)$  of spherical samples BFO is related to the transition to cluster spin glass state.

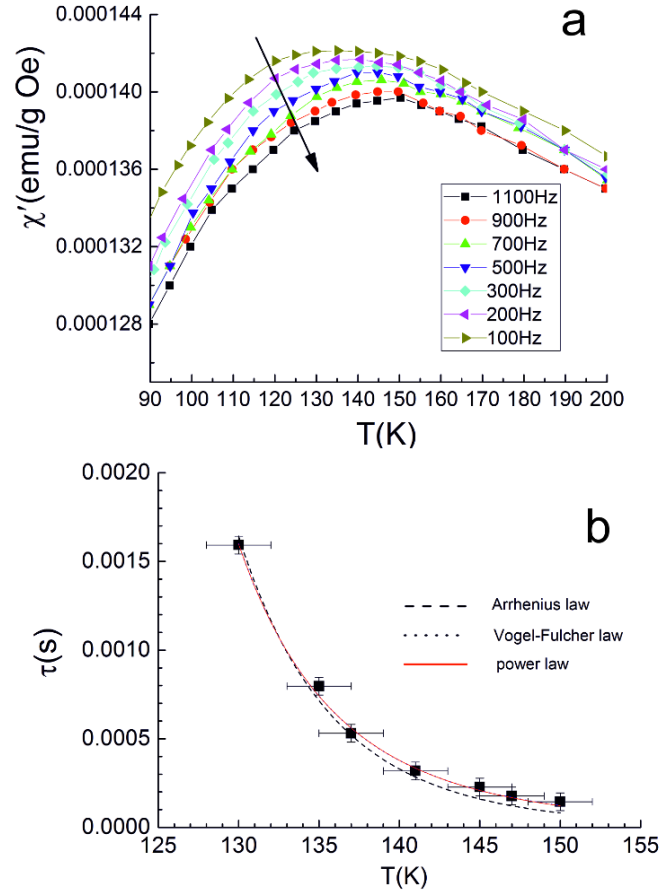


FIG. 4. a – The temperature dependence of the real part of AC magnetic susceptibility at different frequencies. The arrow shows the direction of frequency enhancement and the shift of the maximum. b – The temperature dependence of relaxation time

#### 4. Conclusion

As a result of the research, it was established: (i) the presence of a minimum in the temperature dependence of  $H_s(T)$  at 100 K and the appearance of an exchange bias increasing with decreasing temperature; (ii) FC and ZFC magnetizations differ greatly below 250 – 300 K; (iii) a maximum is observed in the temperature dependence of the magnetization ZFC at a certain value of  $T_m$ , and with an increase in intensity  $H$ , the value of  $T_m$  decreases; (iv) a maximum near 120 K is observed on the temperature dependence of AC magnetic susceptibility, which shifts towards low temperatures when the frequency decreases. The intensity of the maximum of susceptibility lowers if frequency increases, which is typical of glass-like state that becomes less sensitive with enhancement of frequency.

The experimental data obtained in this work prove that in the temperature region of about 100 K there takes place a transition to spin glass state (or at least nonergodic behavior) in porous spheres  $\text{BiFeO}_3$ . The high values of relaxation time  $\tau_0$  of the order of  $10^{-6} - 10^{-5}$  s allow one to draw a conclusion about the formation of cluster spin glass. The critical index describing the retardation of vitreous solid dynamics is  $z\nu \approx 2.5$ , which is much closer to the value obtained in the medium field system (where  $z\nu \approx 2.0$ ) than in the classical Ising short-range model ( $z\nu \approx 7 - 10$ ).

Note the presence of a knee on the  $T_m(H)$  dependence in the region of fields 1 – 2 kOe. An analogous inflection is observed in nanopowders and films. The reasons of this inflection are not clear and require further studies.

As distinct from nanocrystals, porous spheres BiFeO<sub>3</sub> have a higher temperature of transition to spin glass state and at temperatures above the glass transition temperature there is no exchange displacement of hysteresis loops. There is also no phase transition to the ferromagnetic state at 5 K.

### Acknowledgements

This work was supported by a research program at the Institute of Solid State Chemistry. The authors are grateful to Dr. Maria V. Lukashova (OOO “Tescan”, Saint Petersburg, Russia) for scanning microscopy and 3D FIB-SEM tomography.

### References

- [1] Catalan G., Scott J.F. Physics and applications of bismuth ferrite. *Adv. Materials*, 2009, **21**, P. 2463–2485.
- [2] Pyatakov A.P., Zvezdin A.K. Magnetolectric and multiferroic media. *Uspekhi fizicheskikh nauk*, 2012, **182**, P. 593–620. (in Russian)
- [3] Tae-Jin Park, Papaefthymiou G.C., et al. Size-dependent magnetic properties of single-crystalline multiferroic BiFeO<sub>3</sub> nanoparticles. *Nano Lett.*, 2007, **7** (3), P. 766–772.
- [4] Ederer C., Spaldin N.A. Weak ferromagnetism and magnetoelectric coupling in bismuth ferrite. *Phys. Rev. B*, 2005, **71**, 060401.
- [5] Carranza-Celis D., Cardona-Rodríguez A., et al. Control of Multiferroic properties in BiFeO<sub>3</sub> nanoparticles. *Scientific Reports*, 2019, **9**, 3182.
- [6] Sando D., Barthélémy A., Bibes M. BiFeO<sub>3</sub> epitaxial thin films and devices: past, present and future. *J. Phys.: Condens. Matter*, 2014, **26**, 473201.
- [7] Sining Dong, Yiping Yao, et al. Dynamic properties of spin cluster glass and the exchange bias effect in BiFeO<sub>3</sub> nanocrystals. *Nanotechnology*, 2011, **22**, 385701.
- [8] Manoj Singh K., Prellier W., et al. Spin-glass transition in single-crystal BiFeO<sub>3</sub>. *Phys. Rev. B*, 2008, **77**, 144403.
- [9] Fengzhen Huang, Xingyu Xu, et al. The exchange bias behavior of BiFeO<sub>3</sub> nanoparticles with natural core-shell structure. *Scientific Reports*, 2018, **8**, 2311.
- [10] Cazayous M., Gallais Y., et al. Possible Observation of Cycloidal Electromagnons in BiFeO<sub>3</sub>. *Phys. Rev. Lett.*, 2008, **101**, 037601.
- [11] Jarrier R., Marti X., et al. Surface phase transitions in BiFeO<sub>3</sub> below room temperature. *Phys. Rev. B*, 2012, **85**, 184104.
- [12] Goswami S., Bhattacharya D. Magnetic transition at ~150 K in nanoscale BiFeO<sub>3</sub>. *Journal of Alloys and Compounds*, 2018, **783**, P. 277–282.
- [13] Lomanova N.A., Tomkovich M.V., et al. Magnetic properties of Bi<sub>1-x</sub>Ca<sub>x</sub>FeO<sub>3-δ</sub> nanocrystals. *J. Nanopart. Res.*, 2018, **20** (17), P. 12–17.
- [14] Komogortsev S.V., Fel’k V.A., Li O.A. The magnetic dipole–dipole interaction effect on the magnetic hysteresis at zero temperature in nanoparticles randomly dispersed within a plane. *Journal of Magnetism and Magnetic Materials*, 2019, **473** (1), P. 410–415.
- [15] Guilherme H.F. Melo, Joro P.F. Santos, et al. Correlation between electrospinning parameters and magnetic properties of BiFeO<sub>3</sub> nanofibers. *Electrospinning*, 2017, **1**, P. 73–86.
- [16] Lei Wu, Wenbo Sui, et al. One-dimensional BiFeO<sub>3</sub> Nanotubes: Preparation, Characterization, Improved Magnetic Behaviors, and Prospects. *Applied Surface Science*, 2016, 384, P. 368–375.
- [17] Dmitriev A.V., Vladimirova A.V., et al. Hollow spheres of BiFeO<sub>3</sub>: Synthesis and properties. *Journal of Alloys and Compounds*, 2018, **743**, P. 654–657.
- [18] Dmitriev A.V., Vladimirova A.V., et al. Synthesis of hollow spheres of BiFeO<sub>3</sub> from nitrate solutions with tartaric acid: Morphology and magnetic properties. *Journal of Alloys and Compounds*, 2019, **777**, P. 586–592.
- [19] Dmitriev A.V., Vladimirova A.V., et al. Self-Assembly of Hollow Bismuth Ferrite Spheres from Nitrate Solutions. *Journal of Electronic Materials*, 2019, **48** (8), P. 4959–4969.
- [20] Klug H.P., Alexander L.E. X-ray Diffraction Procedures for Polycrystalline and Amorphous Materials. Wiley-Interscience, New York, 1974, 992 p.
- [21] Selbach S.M., Tybell T., Mari-Ann Einarsrud, Tor Grande. Size-Dependent Properties of Multiferroic BiFeO<sub>3</sub> Nanoparticles. *Chem. Mater.*, 2007, **19**, P. 6478–6484.
- [22] Nakamura S., Soeya S., Ikeda N., Tanaka M. Spin-glass behavior in amorphous BiFeO<sub>3</sub>. *J. Appl. Phys.*, 1993, **74**, P. 5652–5657.
- [23] Martínez B., Obradors X., et al. Low Temperature Surface Spin-Glass Transition in  $\gamma$ -Fe<sub>2</sub>O<sub>3</sub> Nanoparticles. *Phys. Rev. Lett.*, 1998, **80**, P. 181–183.
- [24] Manoj K. Singh, Ram S. Katiyar, Prellier W., Scott J.F. The Almeida–Thouless line in BiFeO<sub>3</sub>: is bismuth ferrite a mean field spin glass? *J. Phys.: Condens. Matter*, 2009, **21**, 042202.
- [25] Mydosh J.A. Disordered magnetism and spin glasses. *J. Magn. Magn. Mater.*, 1996, **158**, P. 606–610.
- [26] Bedanta S., Kleemann W. Supermagnetism. *J. Phys. D: Appl. Phys.*, 2009, **42**, 013001.
- [27] Mukadam M.D., Yusuf S.M., et al. Dynamics of spin clusters in amorphous Fe<sub>2</sub>O<sub>3</sub>. *Phys. Rev. B*, 2005, **72**, 174408.
- [28] Tholence J.L. On the frequency dependence of the transition temperature in spin glasses. *Solid State Commun.*, 1993, **88**, P. 917–921.
- [29] Hohenberg P.C., Halperin B.I. Theory of Dynamic Critical Phenomena. *Rev. Mod. Phys.*, 1977, **49**, P. 435–479.
- [30] Pimenov A., Mukhin A.A., et al. Possible evidence for electromagnons in multiferroic manganites. *Nat. Phys.*, 2006, **2**, P. 97–100.

## Synthesis of nanostructured hollow microspheres of vanadium (III, V) oxides

E. V. Vladimirova, O. I. Gyrdasova, A. V. Dmitriev

Institute of Solid State Chemistry, Ural Branch, Russian Academy of Sciences,  
Pervomayskaya, 91, Yekaterinburg, 620990 Russia

Vladimirova@ihim.uran.ru, gyrdasova@ihim.uran.ru, av.dmit.10.10@gmail.com

DOI 10.17586/2220-8054-2020-11-5-572-577

Vanadium oxides  $V_2O_5$  and  $V_2O_3$  have been synthesized by ultrasonic spray pyrolysis in the form of nanostructured spherical agglomerates with an average diameter of 0.5–1.5  $\mu\text{m}$ . By changing the synthesis conditions, the vanadium oxidation state and microspheres surface morphology can be varied. The microspheres of  $V_2O_5$  are formed during aerobic synthesis, while  $V_2O_3$  microspheres are produced under an atmosphere of argon. An increase in the concentration of the initial solution leads to an increase in both size of  $V_2O_5$  nanoparticles and the diameters of the  $V_2O_5$  microspheres. Long-term storage of  $V_2O_3$  in air results in morphological degradation of the microspheres.

**Keywords:** nanostructured microspheres, ultrasonic spray pyrolysis, solutions, vanadium oxides.

*Received:* 9 September 2020

### 1. Introduction

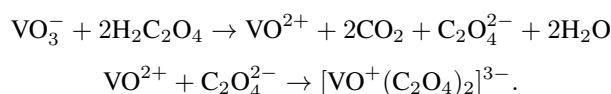
It is known [1] that a number of oxides of 3d-, 4d- and 5f- elements, including vanadium, are capable for metal-dielectric phase transition (MDPT) under the influence of temperature and pressure. This phase transition leads to changes in the structural, thermophysical, optical, magnetic and electrical properties of the compound and finds wide practical application. Thus, for  $V_2O_3$ , a phase transition at 150–160 K is observed from a low-temperature monoclinic (space group I2/a) to a rhombohedral (space group R3c) modification, which is accompanied by an increase in the electrical conductivity by seven orders of magnitude and a change in magnetic behavior from antiferromagnetic to paramagnetic [2, 3]. Therefore, materials based on vanadium (III) oxide are widely used for the manufacture of thermistors with a sharp change in resistance [4], which are used in electronic and electrical devices as breakers and inrush current limiters. In order to control the temperature of the  $V_2O_3$  phase transition, the influence of deformation, pressure and doping is studied [5–9]. Several vanadium oxides and vanadium oxide-based compounds have a layered or tunnel type of crystal structure of V-O polyhedra, which provides significant mobility of metal cations embedded in crystallographic lattice [10]. This property makes these compounds a promising material for use as sensor materials and electrodes for intercalation batteries. Therefore, vanadium oxides with mixed valence and their derivatives have recently attracted attention as chemical sensors, nanoscale magnets, and electrical and optical devices [11–13]. The specific interest is the practical application of  $V_2O_5$ -based solid solutions as highly efficient cathode materials for metal-ion batteries, which demonstrates a high energy density (with charging capacity up to 650 mAh/g) and significant cycle stability [14–16]. The nanostructured  $V_2O_5$ -based materials obtained in the last decade demonstrate a high rate of the intercalation and deintercalation of  $M^{n+}$  ions compared to commercial ones [17]. A large amount of experimental results has been accumulated on the hierarchical structures of nanocrystalline vanadium (V) oxide [18]. Information on the features of the formation of  $V_2O_3$  in the nanocrystalline state is scarce and contradictory. Significant differences in the character of MDPT in nanodispersed  $V_2O_3$  in comparison with bulk crystalline samples were found [19]. Due to the synergetic effect, three-dimensional (3D) hierarchical nanostructures have a stable structure, a developed surface, and a large number of active centers. Such structures are intensively studied and applied in the field of optics, catalysis, and energy conservation [20]. The morphological features of nanocrystalline samples are varied by the preparation conditions. There are several ways to synthesize vanadium oxides in the 3-D state: hydrothermal method [17], thermal decomposition of complexes with an organic ligand [21], and spray pyrolysis method [22–25]. The production of oxide materials in the form of hollow microspheres is a challenging task, since these objects combine the advantages of 3-D structures and thin films. This work describes the most promising method of ultrasonic spray pyrolysis (USP). Previously, using the USP method, hollow microspheres of multiferroics  $\text{BiFe}_{1-x}\text{Mn}_x\text{O}_3$  were obtained and studied [26, 27]. The USP method makes it possible to control the conditions for the formation of a single-phase oxide from an aqueous aerosol with a radial distribution of dissolved components in the droplet volume, which subsequently determines the formation of spherical agglomerates of a given diameter [26]. By varying the intensity of ultrasonic exposure, the temperature and atmosphere of aerosol thermolysis, it seems possible to obtain vanadium oxide in the expected valence and morphological state.

The aim of this study is to obtain vanadium (III and V) oxides in the form of nanostructured hollow microspheres using the USP method in a controlled gas atmosphere.

## 2. Experimental

Ammonium metavanadate  $\text{NH}_4\text{VO}_3$  was used as a vanadium-containing precursor. Oxalic  $\text{C}_2\text{H}_2\text{O}_4$  acid was added to an aqueous solution of  $\text{NH}_4\text{VO}_3$  in a molar ratio of ammonium metavanadate:acid equal to 1:2. The vanadyl ions  $\text{VO}^{2+}$  solution with concentration of 0.10–0.30 mol/l was subjected to ultrasonic spraying in a vertical tube furnace at a temperature of 550–800°C. Air or argon was used as a carrier gas at a rate of 0.10–0.20 m/s. The resulting oxide was collected by an electrostatic precipitator.

The use of the  $\text{V}^{4+}$  precursor for the synthesis of vanadium oxides in different oxidation states excludes the stage of reduction of the formed  $\text{V}_2\text{O}_5$  by hydrogen. It is known that the addition of carboxylic acids to the ammonium metavanadate solution ensures the reduction of  $\text{VO}_3^-$  ions to  $\text{VO}^{2+}$  and stabilizes the vanadyl ion in an aqueous medium in the form of a complex [19]:



USP synthesis was carried out using gas carrier: air or Ar. The synthesis temperature in both cases was 600°C. Aerosol was fed into the reaction zone at a rate of 0.2 m/s, corresponding to a synthesis time of 5 sec. A schematic diagram of the of vanadium oxide (III or V) synthesis is shown in Fig. 1.

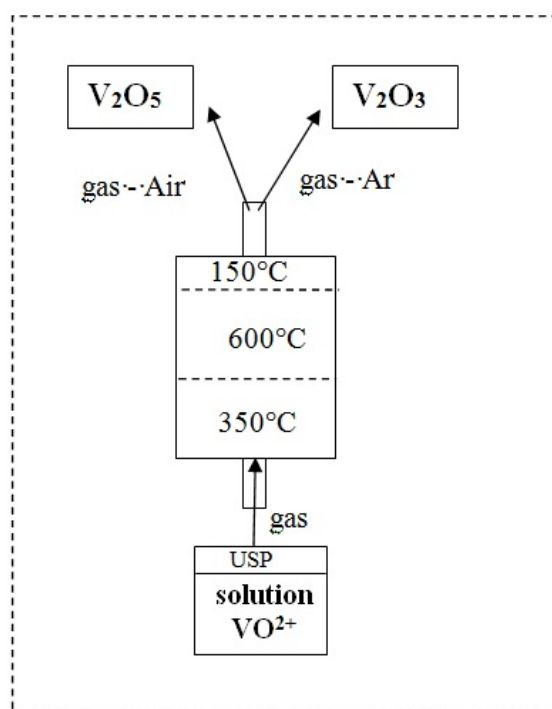


FIG. 1. A schematic diagram of the  $\text{V}_2\text{O}_n$  synthesis

X-ray phase analysis was carried out on an XRD-7000 diffractometer (SHIMADZU) with a secondary monochromator in  $\text{CuK}\alpha$  radiation in the  $2\theta$  angle range from 20° to 80° with a step of 0.03°. X-ray diffraction analysis was performed using the PowderCell software. The morphology of the samples, their chemical composition and the uniformity of the distribution of chemical elements were studied using a JEOL JSM-6390LA scanning electron microscope (SEM) equipped with an EDS Inca Energy 250 X-ray spectrometer.

## 3. Results and discussion

Under the described conditions, the single-phase samples of vanadium oxides were obtained. When carrying out the USP process in air the only product was  $\text{V}_2\text{O}_5$ . And using Ar as a gas carrier the final product was  $\text{V}_2\text{O}_3$ .

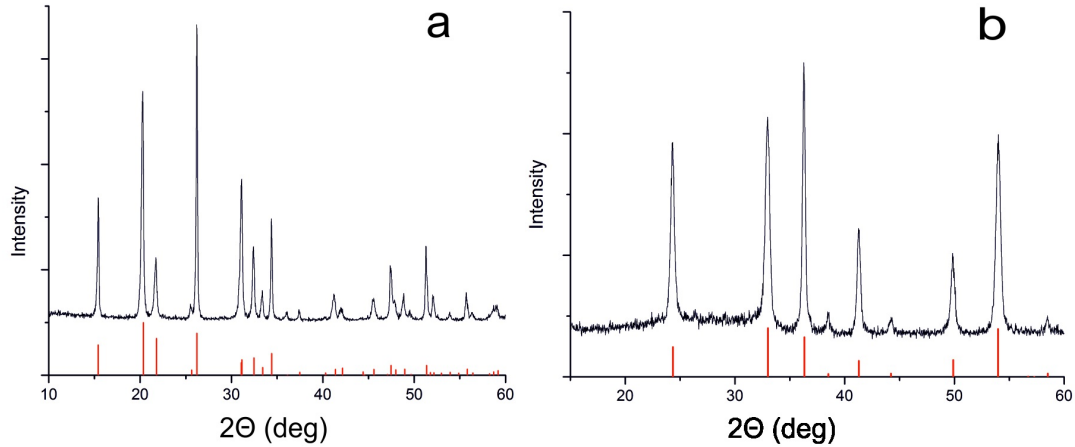


FIG. 2. X-ray diffraction patterns of samples obtained by USP  $\text{VO}^{2+}$  solution: in air (a), in Ar (b)

The diffraction patterns of the samples have a profile characteristic of the corresponding vanadium oxide (ICSD Collection Code 15299) (Fig. 2). During the USP the aerosol particles get directly into the drying zone with a temperature of 250–350 °C, and then into the calcination zone with a temperature of 600 °C (Fig. 1). The parameters and conditions of USP, i.e. the concentration of vanadyl ion  $\text{C}_{\text{VO}^{2+}}^{2+}$  and the supplying rate of solution to the drying zone. These parameters ensure the production of hollow microspheres observed experimentally. The Table 1 shows the effect of the synthesis conditions of  $\text{V}_2\text{O}_n$  ( $\text{C}_{\text{VO}^{2+}}^{2+}$ ) on the parameters of unit cells and the size of coherent scattering regions D (Table 1).

TABLE 1. Characteristics of samples obtained from solution

Sample	Synthesis conditions	Oxide composition	Unit cell parameters	D, $\mu\text{m}$	CSR, nm
I	air $\text{C}_{\text{VO}^{2+}}=0.04$ mol/l	$\text{V}_2\text{O}_5$	$a = 11.4807$ $c = 3.5636$ $b = 4.3989$	0.45	50
II	air $\text{C}_{\text{VO}^{2+}}=0.3$ mol/l	$\text{V}_2\text{O}_5$	$a = 11.4863$ $c = 3.5561$ $b = 4.3792$	0.65	62
III	Ar $\text{C}_{\text{VO}^{2+}}=0.3$ mol/l	$\text{V}_2\text{O}_3$	$a = 4.94498$ $b = 14.0123$	0.45	36

The complex mechanisms of aerosol droplet formation, drying, and thermolysis in a dynamic mode were studied in detail in [26]. It was shown that the morphology of particles when using the USP process is formed during drying and is retained during the subsequent calcination.

It has been experimentally established that the diameter of a spherical particle formed by USP process  $d_g$  can be expressed by the following theoretical relationship:

$$d_g = d_D = \sqrt{\frac{C_V}{\rho_p}},$$

where  $C_V$  is the vanadium concentration,  $\rho_p$  is the vanadium oxide density,  $d_D$  is the average aerosol droplet size.

The droplet size is inversely proportional to the frequency of ultrasonic action on the solution during spraying. The intensity of US-vibrations is determined by the viscosity and surface tension of the liquid used as a precursor.

According to SEM and X-ray phase analysis the average diameter of the regular  $\text{V}_2\text{O}_5$  microspheres obtained from dilute solutions of vanadium in air is 0.45  $\mu\text{m}$  of (Fig. 3a). The surface of the spheres is dense, without pores and faults. With an increase in the vanadium concentration in the solution up to 0.3 mol/l, the average diameter of the resulting spheres grows insignificantly (Table 1, Fig. 2b), and the lattice parameters do not undergo noticeable changes.

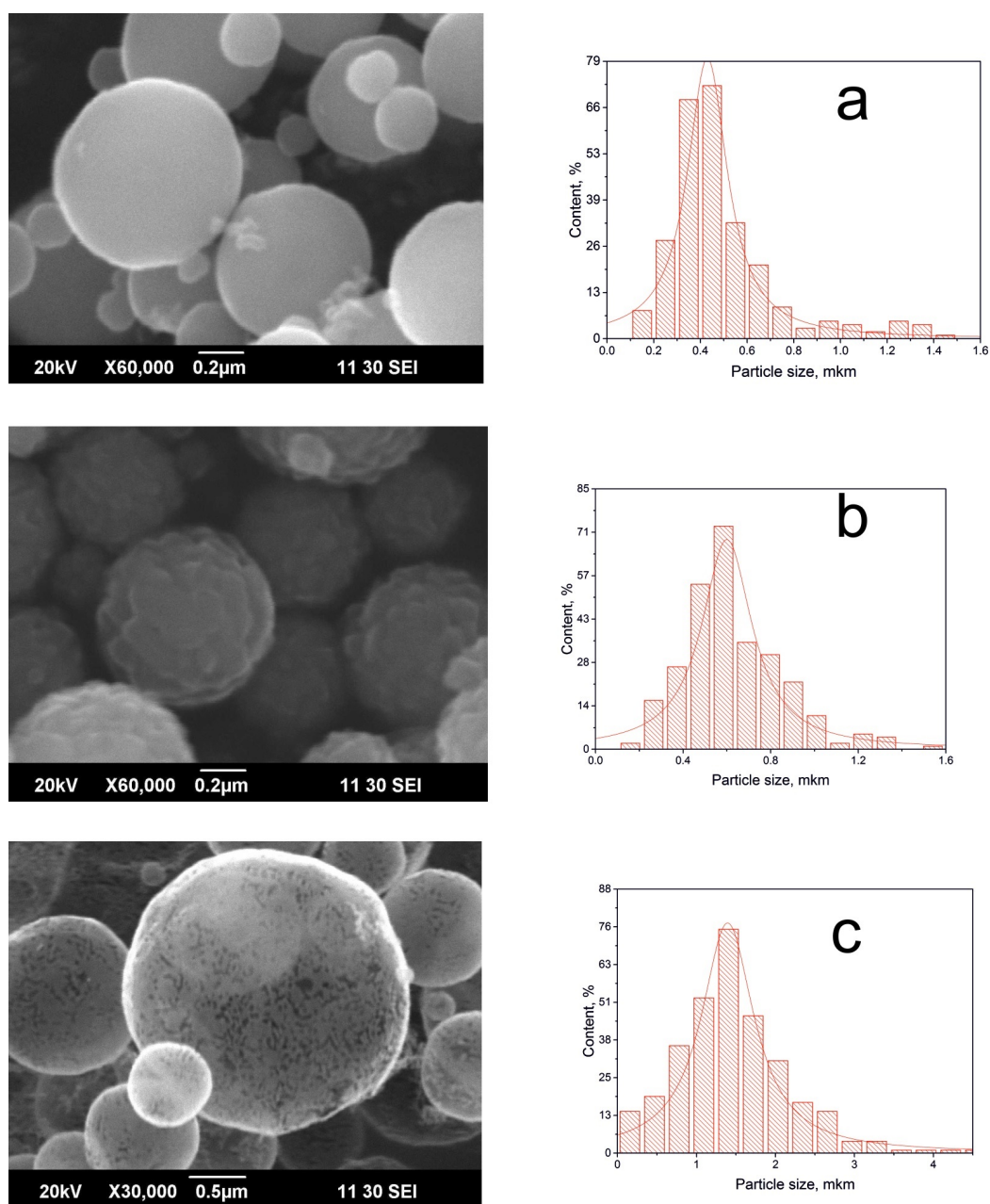


FIG. 3. SEM image and particle size distribution of  $V_2O_5$  samples obtained from a solution with a concentration of 0.04 mol/l (a) and 0.3 mol/l (b) and  $V_2O_3$  (c)

The main difference between obtained  $V_2O_5$  microspheres is the surface type morphology. The surface of  $V_2O_5$  microspheres obtained from concentrated solution is formed by flat scaly crystals closely adjacent to each other (Fig. 3b). In the case of USP under an Ar atmosphere, the  $V_2O_3$  microspheres with an average diameter of 1.5 μm were obtained (Fig. 3c). The surface of the spheres is loose, formed from one layer of nanosized crystallites. It is known that vanadium (III) oxide is metastable and over time it undergoes spontaneous oxidation to  $V_2O_5$  [27, 28]. The process of partial morphological and structural degradation characteristic of  $V_2O_3$  was observed after 12 months of storage of the sample in air (Fig. 4).

The so-called “aging” of spherical samples is observed in a significant broadening of diffraction peaks characteristic to the  $V_2O_3$  structure (Fig. 4). At the same time, no peaks of the  $V_2O_5$  impurity were found in the diffraction patterns. According to SEM data (Fig. 4), the surface of the aged  $V_2O_3$  samples is formed by lamellar aggregates connected weakly to each other. Therefore, the shell was easily destroyed and the spheres were completely degraded.

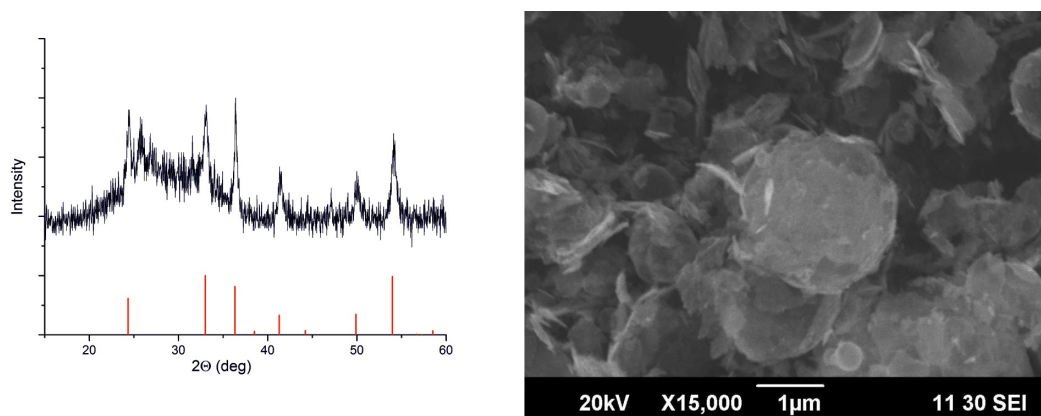


FIG. 4.  $V_2O_3$  sample after storage in air: diffraction pattern and SEM image

#### 4. Conclusion

Vanadium oxide (III or V), in the form of hollow microspheres, was obtained by the method of ultrasonic spray pyrolysis (USP) in the controlled gas atmosphere at one stage. The size of the microspheres and the main properties of their surface are established to be dependent on the concentration of the precursor in an aqueous solution and thermolysis atmosphere. Thus, the average diameter of microspheres can be experimentally varied in the range 0.45–1.5  $\mu\text{m}$ . The surface of  $V_2O_3$  spheres obtained in an Ar atmosphere is formed by one layer of crystallites with an average size of 36 nm. Spontaneous oxidation of spherical  $V_2O_3$  leads to complete degradation of its surface.

#### Acknowledgments

This work was carried out in accordance with the state assignment and research plans of the Institute of Solid State Chemistry of the Ural Branch of the Russian Academy of Sciences (grant No AAAA-A19-119031890026-6, No AAAA-A19-119031890025-9).

#### References

- [1] Mott N.F. Metal-insulator transitions. Taylor&Francis, London, 1990, 294 p.
- [2] Goodenough J.B. Magnetism and the Chemical Bond. *J. Appl. Phys.*, 1968, **39**, P. 403.
- [3] Carter S.A., Rosenbaum T.F., Honig J.M., and Spalek J. New phase boundary in highly correlated, barely metallic  $V_2O_3$ . *Phys. Rev. Lett.*, 1991, **67**, P. 3440.
- [4] Zhang Y., Fan ., Liu X. et al. Beltlike  $V_2O_3$ @C core-shell-structured composite: design, preparation, characterization, phase transition, and improvement of electrochemical properties of  $V_2O_3$ . *Eur. J. Inorg. Chem.*, 2012, **10**, P. 1650–1659.
- [5] Metcalf P.A. et al. Electrical, structural, and optical properties of Cr-doped and non-stoichiometric  $V_2O_3$  thin films. *Thin Solid Films*. 2007, **515**(7-8), P. 3421–3425.
- [6] Weber D. et al. Bixbyite-Type  $V_2O_3$  - A Metastable Polymorph of Vanadium Sesquioxide. *Inorganic Chemistry*, 2011, **50**(14), P. 6762–6766.
- [7] Populoh S. et al. The power factor of Cr-doped  $V_2O_3$  near the Mott transition. *Appl. Phys. Lett.*, 2011, **99**(17), P. 3–7.
- [8] Panaccione G. et al. Bulk electronic properties of  $V_2O_3$  probed by hard X-ray photoelectron spectroscopy. *J. of Electron Spectroscopy and Related Phenomena*, 2007, **156-158**, P. 64–67
- [9] Laad M.S., Craco L., Müller E. Orbital-selective insulator-metal transition in  $V_2O_3$  under external pressure. *Phys. Rev. B.*, 2006, **73**(4), P. 15–21.
- [10] Zavalij P.Y. and Whittingham M.S. Whittingham. Structure chemistry of vanadium oxides with open frameworks. *Acta Cryst.*, 1999, **B55**, P. 627–630.
- [11] Strelcov E., Lilach Y. and Kolmakov A. Gas Sensor Based on Metal–Insulator Transition in  $VO_2$  Nanowire Thermistor. *Nano Lett.*, 2009, **9**, P. 2322–2326.
- [12] Krusin-Elbaum L., Newns D. M., Zeng H., Derycke V., Sun J.Z. and Sandstrom R. Room-temperature ferromagnetic nanotubes controlled by electron or hole doping. *Nature*, 2004, **431**, P. 672–676.
- [13] Vavilova E., Hellmann I., Kataev V., Täschner C., Büchner B. and Klingeler R. Magnetic properties of vanadium oxide nanotubes probed by static magnetization and 51V NMR. *Phys. Rev. B*, 2006, **73**, P. 144417(1-7).
- [14] Chen Zh., Augustyn V., Wen J., Zhang Yu., Shen M., Dunn B. and Lu Yu. M. Shen, B. Dunn and Yu. Lu. High Performance Supercapacitors Based on Intertwined CNT/ $V_2O_5$  Nanowire Nanocomposites *Adv. Mater.*, 2011, **23**, P. 791–799.
- [15] Dong W., Sakamoto J. and Dunn B. Electrochemical Properties of Vanadium Oxide Aerogel/Aerogel Nanocomposites. *J. Sol-Gel Sci. Technol.*, 2003, **26**, P. 641–644.
- [16] Yan M., He P., Chen Y., Wang S., Wei Q., Zhao K., Xu X., An Q., Shuang Y., Shao Y., Mueller K.T., Mai L., Liu J., Yang J. Water-lubricated intercalation in  $V_2O_5 \cdot nH_2O$  for high-capacity and high-rate aqueous rechargeable zinc batteries. *Adv. Mater.* 2018, **30**, P. 1703725.
- [17] Pan J., Li M., Luo Y.Y., Wu H., Zhong L., Wang Q., Li G.H. Synthesis and SERS activity of  $V_2O_5$  nanoparticles. *Appl. Surf. Sci.*, 2015, **333**, P. 34–38.

- [18] Liu X., Zeng J., Yang H., Zhou K., Pan D.  $V_2O_5$ -based nanomaterials: synthesis and their applications. *RSC Adv.*, 2018, **8**(8), P. 4014–4031.
- [19] Blagojevic V.A., Carlo J.P., Brus L.E., Steigerwald M.L., Uemura Y.J., J.L. Billinge, G. M Luke. Magnetic phase transition in  $V_2O_3$  nanocrystals. *Physical Review B*, 2010, **82**(9), P. 094453.
- [20] Mai L.Q., Tian X.C., Xu X., Chang L., Xu L. Nanowire Electrodes for Electrochemical Energy Storage Devices. *Chem.Rev.*, 2014, **114**, P. 11828–11862.
- [21] Asim N., Radiman S., Yarmo M.A., BanayeGolriz M.S. Vanadium pentoxide: Synthesis and characterization of nanorod and nanoparticle  $V_2O_5$  using CTAB micelle solution. *Microporous Mesoporous Mater.*, 2009, **120**, P. 397–401.
- [22] Abd-Alghafour N.M., Ahmed N.M., Hassan Z., Mohammad S.M., Bououdina M., Ali M.K.M. Characterization of  $V_2O_5$  nanorods grown by spray pyrolysis technique. *J. Mater. Sci. - Mater. Electron*, 2016, **27**, P. 4613–4621.
- [23] Zhendong Yin, Jie Xu, Yali Ge et al. Synthesis of  $V_2O_5$  microspheres by spray pyrolysis as cathode material for supercapacitors. *Mater. Res. Express*, 2018, **5**(3), P. 036306.
- [24] Zhang X.Y., Wang J.G., Liu H.Y., Liu H.Z. and Wei B.Q. Facile Synthesis of  $V_2O_5$  Hollow Spheres as Advanced Cathodes for High-Performance Lithium-Ion Batteries. *Materials*, 2017, **10**, P. 77–85.
- [25] Yue Q., Jiang H., Hu Y., Jia G., Li C. Mesoporous single-crystalline  $V_2O_5$  nanorods assembled into hollow microspheres as cathodematerials for high-rate and long-life lithium-ion batteries. *Chem. Commun.*, 2014, **50**, P. 13362–13369.
- [26] Dmitriev A.V., Vladimirova E.V., Kandaurov M.V., Chufarov, A.Yu., Kellerman D.G. Magnetic properties of powders  $BiFe_{0.93}Mn_{0.07}O_3$  powders obtained by ultrasonic spray pyrolysis. *Phys. Solid State*, 2017, **59**, P. 2360–2364.
- [27] Dmitriev A.V., Vladimirova E.V., Kandaurov M.V., Kellerman D.G., Chufarov A.Yu., Tyutyunnik A.P. Hollow spheres of  $BiFeO_3$ : Synthesis and properties. *Journal of Alloys and Compounds*, 2018, **743**, P. 654–657.
- [28] Lyakh O.V., Eismont N.G., Surikov Wad. I., Surikov Val. I. Physical aspects of aging of vanadium (III) oxide. *Omsk Scientific Bulletin*, 2013, **120**(2), P. 8–11.
- [29] Przesniak-Welenc M., Karczewski J., Smalc-Koziorowska J., Łapinski M., Sadowskia W, and Koscielska B. The influence of nanostructure size on  $V_2O_5$  electrochemical properties as cathode materials for lithium ion batteries. *RSC Adv.*, 2016, **6**(61), P. 55689–55697.

## High sensitive room temperature ammonia sensor based on dopant free m-WO<sub>3</sub> nanoparticles: Effect of calcination temperature

M. S. Duraisami\*, K. Parasuraman

PG & Research Department of Physics, Poompuhar College (Autonomous), Melaiyur – 609107, Tamilnadu, India  
Affiliated to Bharathidasan University, Tiruchirappalli

\*tharmamithran@gmail.com

PACS 07.07.Df, 81.07.b, 61.46-w, 61.46.Hk, 61.72Uj, 61.82.Rx      DOI 10.17586/2220-8054-2020-11-5-578-589

In this article, monoclinic tungsten tri-oxide (m-WO<sub>3</sub>) nanoparticles (hereafter NPs) were prepared by facile precipitation method and they were successfully examined as gas sensing materials for monitoring gaseous ammonia at room temperature have been reported. The effect of calcination temperature on structural and morphological properties of the prepared samples were also investigated. Physicochemical properties of the samples were characterized by XRD, SEM, XPS, UV-Vis and PL analysis. XRD studies confirmed the monoclinic structure of the prepared NPs. Optical studies disclosed that the obtained samples were having wider optical band gaps ranging from 2.48 to 2.76 eV. Sensing signatures such as selectivity, transient response along with performance indicators like repeatability and stability have also been investigated. Invitingly, the sample calcined at 823 K exhibited highly improved sensing response of 142 towards 200 ppm of ammonia with rapid response/recovery time of 26 / 79 s.

**Keywords:** ammonia sensor, tungsten trioxide, nanoparticles, calcination, precipitation.

*Received: 11 June 2020*

*Revised: 13 September 2020*

*Final revision: 23 September 2020*

### 1. Introduction

One of the serious challenges we face in recent times is that living environment is losing its stability as a result of the toxic gases released from several industries. According to the statistic survey of WHO, 4 out of 10 most common causes of death are due to respiratory related ailments [WHO, World Health Statistic, 2011]. Toxic gases may often contribute to adverse effects in humans and also their occurrence in environment poses severe threats. Therefore, if the living environment is to be maintained well, it is necessary to detect the leakage of harmful gases at lower concentrations. Among the toxic gases, ammonia is highly reactive and soluble alkaline gas which is present in the environment at ppb levels [1]. The permissible long (8 hour) and short (10 minutes) term exposure limits for ammonia in human are 25 and 35 ppm [2–4]. Due to the demand for fertilizers, ammonia be the second largest chemical product manufactured in the world. Despite its uses, sensing ammonia is an essential process owing to its lethal behavior at higher concentrations [5]. Significantly, ammonia sensors attracted more attention for realizing their applications in various fields like petrochemicals, food and beverage, agriculture, automotive industry, fertilizers and medical applications [6].

One of the most appropriate candidates in the field of toxic gas detection is chemiresistive sensor. In which semi-conducting metal oxide (SMO) nanostructures have been investigated extensively in the fabrication of distinctive gas sensors due to their tunable transport properties [7]. Among the SMOs, WO<sub>3</sub> is a notable well known n-type semiconductor with a wide range of band gap varies from 2.2 to 2.8 eV [8]. Llobet et al. [9] have studied WO<sub>3</sub> nanostructures as an excellent gas sensing material towards reducing gases like ammonia. Moreover, WO<sub>3</sub> nanostructures play a key role in the preparation of colloidal quantum dot LEDs [10], bio sensing electrodes [11] and used in the fields of mechanochemical [12], field emission devices, electrochromic and photocatalysts [13]. Wang et al. [14] have studied WO<sub>3</sub> nanofibers for ammonia gas detection at an operating temperature of 623 K. Wu et al. [15] reported an ammonia sensor based on graphene/PANI nanocomposite with a response of about 11 for 100 ppm. Liu et al. [16] have studied the Ag-decorated Titanium oxide quantum dot clusters for ammonia detection at room temperature. Recently Wang et al. [17] have investigated the gas sensing performance of closely packed WO<sub>3</sub> microspheres for ammonia detection with a response of 3.2 towards 100 ppm ammonia. Tai et al. [18] used PANI/Titanium oxide nanocomposite to detect 117 ppm of ammonia gas at 298 K. Li et al. [19] reported the ZnO thin film as ammonia sensor with a maximum response of 57.5 towards 600 ppm at 423 K.

However, various interpretations were reported for sensing ammonia, still high sensitive ammonia sensors based on undoped SMO at room temperature is rare. For this objective, the present study is primarily aimed to explore the improved gas sensing performances of undoped WO<sub>3</sub> NPs synthesized by a facile precipitation process. The

precipitation method is a well facilitated and self-styled technique as well as envisioned to be one of the most reliable methods for the preparation of nano sized WO<sub>x</sub> particles with different morphologies [20]. We are considering the effect of calcination temperature on crystal structure and morphology of the NPs as one of the key factors to improve sensing performance. On these grounds, we prepared WO<sub>3</sub> NPs under various calcination temperatures such as 623, 723, 823 and 923 K. Thus the prepared NPs were used as redox sensors to monitor ammonia gas.

## 2. Materials and methods

### 2.1. Synthesis of WO<sub>3</sub> NPs

All the analytical grade chemicals were procured from Sigma–Aldrich and used without further purification. In a typical precipitation procedure, 1.2 millimole of sodium tungstate dihydrate (Na<sub>2</sub>WO<sub>4</sub>·2H<sub>2</sub>O, 99.9 %) and 2 millimole of calcium chloride dihydrate (CaCl<sub>2</sub>·2H<sub>2</sub>O, 99.9 %) were prepared separately using 100 ml of de-ionized water (DI). Then these two solutions were mixed under vigorous magnetic stirring (900 rpm) for 45 minutes at room temperature. Thereafter, the resulting white precipitate was collected, washed many times with ethanol, acetone and DI, and dried at 333 K for 16 hours using hot air oven. Then, the dried material was soaked in 50 ml of concentrated nitric acid (HNO<sub>3</sub>, ≥99 %) for 48 hours resulting yellow precipitates were obtained. These yellow precipitates were cleansed several times with ethanol, acetone and DI. Finally the substance was placed in muffle furnace and calcined at 623 K for 2 hours to improve crystallinity. After the completion of thermal treatment the sample has been ground to acquire fine WO<sub>3</sub> NPs. The similar procedure is followed to the remaining three different calcination temperatures (723, 823 and 923 K).

### 2.2. Reaction scheme

Figure 1 depicts the schematic representation of WO<sub>3</sub> NPs synthesis procedure. An intermediate substance CaWO<sub>4</sub> was first formed by vigorous stirring of the precursor mixture (Na<sub>2</sub>WO<sub>4</sub> and CaCl<sub>2</sub>). The Ca<sup>2+</sup> cations (Lewis acid-electron-pair acceptor) might interact with the WO<sub>4</sub><sup>2-</sup> anions (Lewis base-electron-pair donor), resulting in the formation of white CaWO<sub>4</sub> precipitates. Then, CaWO<sub>4</sub> was decomposed slowly upon solution acidification to form yellow tungstite (WO<sub>3</sub>·H<sub>2</sub>O) precipitates. The liberated H<sup>+</sup> ions from the strong oxidizing agent HNO<sub>3</sub> serve as one of the reactants for the formation of WO<sub>3</sub>·H<sub>2</sub>O. Remnants were removed by further cleansing process. On the post calcination treatment, WO<sub>3</sub>·H<sub>2</sub>O gets transformed to WO<sub>3</sub> nanostructures.

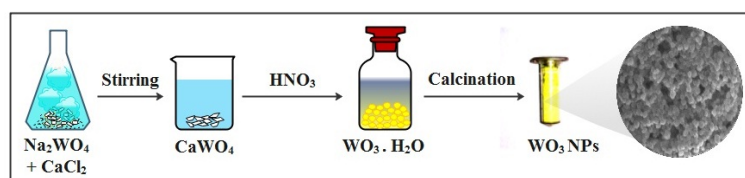
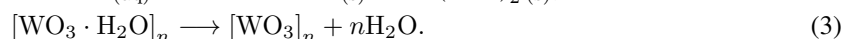
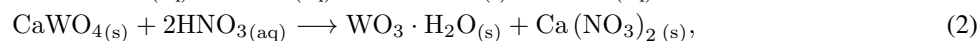
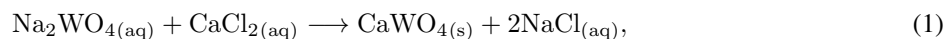


FIG. 1. Schematic representation of WO<sub>3</sub> NPs synthesis procedure

This can be explained as follows; the removal of internal water molecules and W=O double bonds permit the layers to connect through the oxygen atoms to stack together and turn to more compact structure [21]. The possible formation process of WO<sub>3</sub> NPs can be explained as given in Eq. (1), (2) and (3).



### 2.3. Characterization techniques

The Crystalline structure of the prepared samples was employed using the XRD patterns obtained from Panalytical Xpert-pro Diffractometer with a source of CuK $\alpha_1$  ( $\lambda = 1.5406 \text{ \AA}$ ). The surface morphology of the obtained NPs was analysed using Scanning Electron Microscope (ZEISS-SEM) and Transmission Electron Microscopy (TEM-Hitachi H-9500). EDS (Bruker) analysis was performed to identify the elemental composition of the sample. Electronic state of the elements within the samples was identified using X-ray Photoelectron Spectrometer (Thermo Fisher Scientific Inc., K Alpha, USA). The spectral observations from Fourier Transform Infrared Spectroscopy (Perkin-Elmer Spectrum Two, USA) and Ultraviolet-Visible spectrophotometer (Perkin-Elmer Lambda 35 Spectrophotometer, USA) have given the interpretations about the presence of functional groups and the optical characteristics of the NPs respectively.

The Photo Luminescence spectra of the prepared NPs were recorded at room temperature using Varian Cary Eclipse Spectrophotometer with the scan rate of 600 nm/min.

## 2.4. Fabrication of gas sensing setup and measurements

All the sensing measurements have been taken at room temperature using a high resistance electrometer (Keithley 6517A, USA) with an integrated gas measurement setup as depicted in Fig. 2. Initially the prepared NPs were dispersed in an appropriate amount of isopropyl alcohol and drop casted on the surface of a glass plate, hence a widespread layer was formed and acts as a sensing material. In it, two copper electrodes have been attached with an applied DC voltage of 10 V. The entire gas sensing process was carried out in the customized evaporation chamber of 1 L capacity. When a liquefied analyte like ammonia was injected in to the evaporation chamber using a micropipette, which swiftly turned in to vapor state and made a contact with the sample. The steady-state baseline resistance ( $R_a$ ) in air ambience and the variation of electrical resistance from  $R_a$  to  $R_g$  (resistance under the exposure of target gas) were measured by a highly efficient electrometer (Keithley 6517B, USA) controlled by a personal computer. The concentrations of the analytes to be injected were calculated using static liquid-gas distribution method (Eq. (4)) [22]:

$$C_{(p p m)} = \frac{\delta V_{\Gamma} R T}{M P_b V_b} \times 10^6, \quad (4)$$

where  $C$  is the concentration of test vapor (ppm),  $\delta$  is the density of test vapor ( $gmL^{-1}$ ),  $V_{\Gamma}$  is the volume of injected vapor ( $\mu L$ ),  $R$  is the universal gas constant ( $8.3145 J \cdot mol^{-1} K^{-1}$ ),  $T$  is the absolute temperature (K),  $M$  is the molecular weight,  $P_b$  is the chamber pressure (atm) and  $V_b$  is the volume of the chamber (L). Generally, for reducing gases, the sensing responses were calculated by the given relation (Eq. (5)) [22]:

$$S = \frac{R_a}{R_g}, \quad (R_a \gg R_g) \quad (5)$$

where  $R_a$  and  $R_g$  are the resistances of the sample in dry air and target gas.

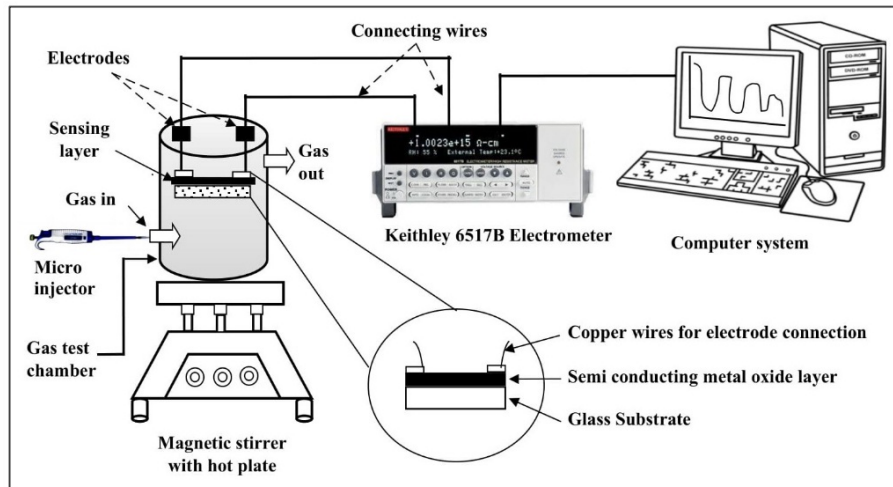


FIG. 2. Illustration of an integrated gas measurement setup

## 3. Results and discussion

### 3.1. Structural, morphological and functional groups

Figure 3 shows the XRD pattern of all the synthesized  $WO_3$  NPs. As the calcination temperature increases from 623 to 823 K, the crystallinity comes up gradually and the emergence of different peaks have been observed. Three characteristic diffraction peaks (triplet) for  $WO_3$  were observed from the crystal planes (002), (020) and (200). These peaks are matched well with the observed XRD patterns (standard JCPDS data card no. 43-1035). The samples were crystallized with the polycrystalline monoclinic phase with the lattice parameters  $a = 7.297$ ,  $b = 7.539$ ,  $c = 7.688$  Å. The well-known Debye–Scherrer formula is used to determine the average crystallite size ( $D$ ) of the samples as given in Eq. (6):

$$D = \frac{K\lambda}{\beta \cos \theta}, \quad (6)$$

where  $K$  is Scherrer constant (0.89),  $\beta$  – full width at half maximum of the high intensity peak (FWHM in radians),  $\theta$  – Bragg angle,  $\lambda$  is wavelength of the X-rays (1.5406 Å for CuK $\alpha_1$ ). It is observed that, the predominant facet was varied as a function of calcination temperature, therefore the average crystallite size was calculated from triplet peaks, however, which is inappropriate for 623 K sample due to its partial crystalline nature. The mean crystallite size found to be increase in the range of 17 to 39 nm with increased calcination temperature. This trend implies that higher temperature provided adequate energy for smaller particles to coalesce into larger ones. It is clearly known from XRD studies that there is no influence of any other characteristic peaks of impurities were observed, hence WO<sub>3</sub> NPs were formed without any impurities.

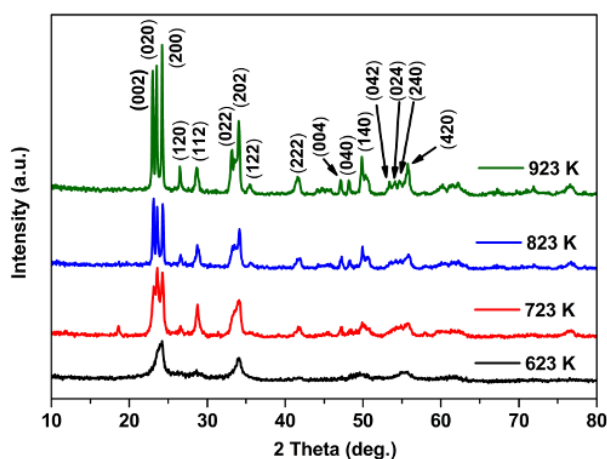


FIG. 3. X-ray diffraction patterns of the synthesised WO<sub>3</sub> samples

The SEM images and size distribution histograms for the prepared samples are shown in Fig. 4. Invitingly, the morphology was improved with increased calcination temperature from 623 to 823 K. Uniformly distributed fine cluster like nanogranular morphology has been observed at 823 K. While increasing the calcination temperature beyond 723 K, the precursor complexes may have adequate thermal energy to reorient themselves resulting lesser chance of agglomeration. In which the inorganic compounds decomposed completely and free from impurities in-turn a notable effect on the final morphology. Beyond 823 K, the morphology undergoes a transition from nanoclusters to macro grains. This may be ascribed to the subsequent growth of interconnected crystallites among the grain network, which favors the formation of larger micrometer-sized particles [23]. SEM studies are in good agreement with XRD results.

The crystallite size estimated from XRD studies is compared with the grain size obtained from SEM analysis and are listed in Table 1. The grain size obtained from the SEM images was found to be larger than the average crystallite size estimated from the XRD patterns because SEM visualizes the surface of NPs, which may contain more than one crystallite. Increase in the calcination temperature increased the crystallinity of the NPs, ultimately resulting in the increase in the grain size and the surface became smoother. Therefore the effect of calcination temperature and the specific route chosen for the synthesis have influenced the morphology. The 823 K sample was then chosen for TEM studies, because the grain growth was less enhanced than at 923 K. The TEM images disclosed that the formation of highly dispersed NPs (Fig. 5(a,b)) with arbitrary size and shape. Selective Area Electron Diffraction pattern (SAED) confirmed the polycrystalline nature of the system as shown in Fig. 5(c). To identify the elemental composition, EDS analyses was employed. Fig. 6(a) clearly showed that the sample was only composed of tungsten and oxygen and no other impurities were observed, which also supports the XRD results. The inset of Fig. 6(a) displays the atomic and weight percent of oxygen and tungsten.

FTIR spectra clearly identified the various mode of vibrations of the samples in the infrared regime (Fig. 6(b)). O-Lattice group was observed at 502 cm<sup>-1</sup>. The typical band at 610 cm<sup>-1</sup> was due to the  $\gamma$  (W–O–W) signal. The presence of stretching vibrations (W=O, W–O) of WO<sub>3</sub> NPs identified at 955 cm<sup>-1</sup>. The vibration at 1401 cm<sup>-1</sup> can be attributed to the presence of W–O functional group. The 1625 cm<sup>-1</sup> band is assigned to the H–O–H bending vibration. Especially from the peak sited at 3449 cm<sup>-1</sup> indicates the emergence of intercalated water molecules (W–OH ··· H<sub>2</sub>O). These assignments found evidence for the formation of WO<sub>3</sub> NPs [24].

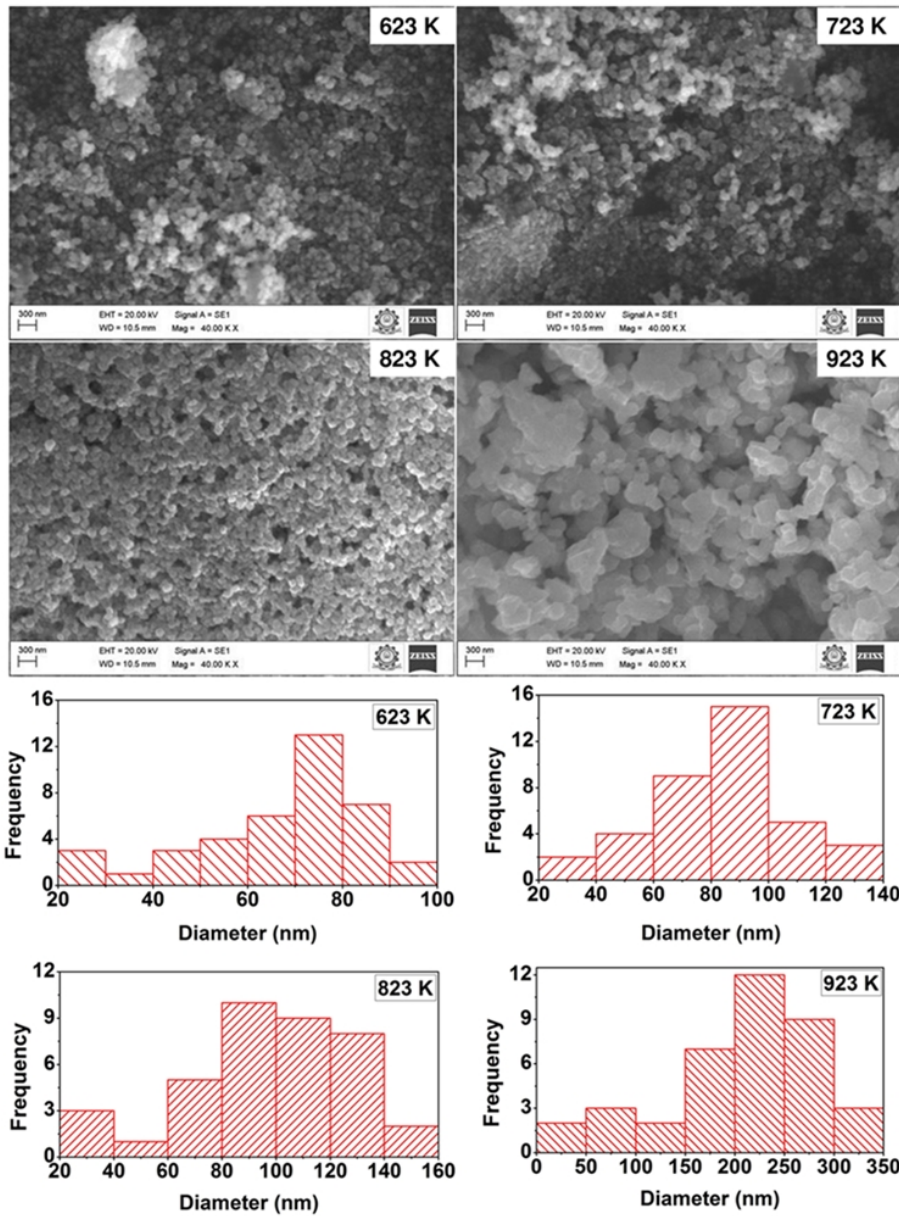


FIG. 4. SEM images and size distribution histograms of  $\text{WO}_3$  NPs calcined at various temperatures

TABLE 1. Structural, morphological and optical parameters of the prepared  $\text{WO}_3$  NPs

Samples	$2\theta$ (deg.)	FWHM ( $\beta$ ) (deg.)	Crystallite size ( $D$ ) (nm)	Grain size obtained from SEM (nm)	Optical band gap energy (eV)
623 K	–	–	–	75	2.76
723 K	23.6730	0.4783	17	86	2.65
823 K	23.7088	0.2292	35	104	2.55
923 K	23.5897	0.2080	39	233	2.48

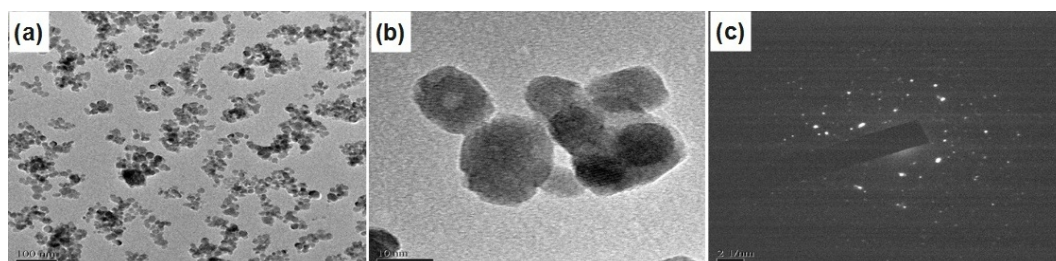
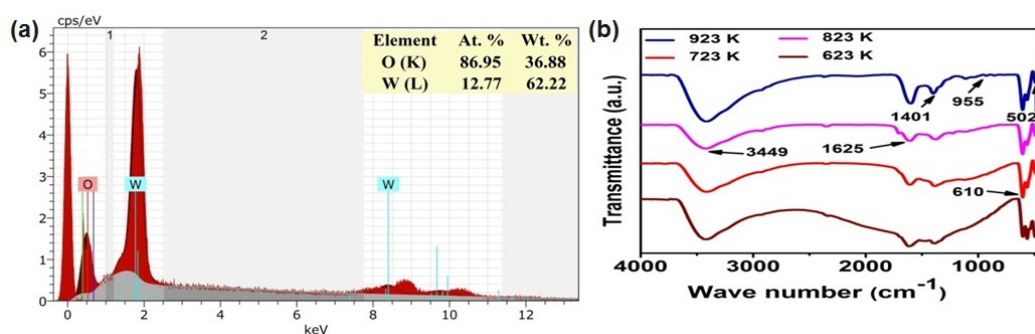


FIG. 5. (a,b) TEM images and (c) SAED pattern of the sample calcined at 823 K

FIG. 6. (a) EDS spectra of  $\text{WO}_3$  NPs calcined at 823 K and (b) FTIR spectra of the prepared nanostructures

### 3.2. XPS analysis

Figure 7 shows the XPS spectra of pristine  $\text{WO}_3$  samples calcined at various temperatures. The high resolution spectra of W4f- and O1s-levels have been acquired. The peak couples located at  $\sim 35.8$  and  $37.8$  eV corresponding to  $\text{W}4f_{7/2}$  and  $\text{W}4f_{5/2}$  respectively, which are characteristic for  $\text{W}^{6+}$  oxidation state as shown in Fig. 7(a). It should be mentioned that these doublet peaks were typical for all specimens and that there were relative small changes in values.

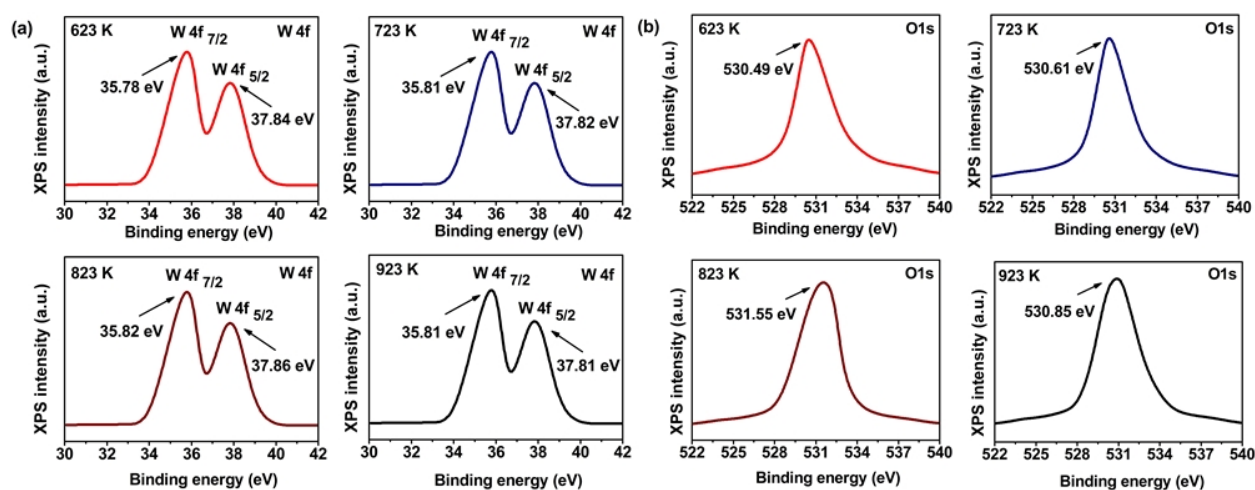


FIG. 7. (a) W4f and (b) O1s XPS spectra of the samples calcined at various temperatures (623–923 K)

The O1s peaks located at 530.49, 530.61 and 530.85 eV were attributed to lattice oxygen ( $\text{O}^{2-}$ ) in  $\text{WO}_3$  (Fig. 7(b)). While the peak at 531.55 eV (O1s of 823 K) is associated with  $\text{O}^{2-}$  of  $\text{OH}^-$  in the oxygen deficient regions within the matrix of  $\text{WO}_3$  [25]. These oxygen vacancies are crucial for improving surface conductivity. In  $m\text{-WO}_3$ , the valence and conduction bands are comprised primarily of O 2p and W 5d states. The oxygen vacancies lead to outward motion of W atoms surrounding the vacancy i.e., relax away from the vacancy. On relaxation of internal coordinates,

the doubly occupied vacancy-induced states tend to move into the conduction band. As a result, two electrons then occupy the extended conduction-band states [26]. These investigations confirmed the successful formation of WO<sub>3</sub> NPs.

### 3.3. Optical studies

**3.3.1. Evaluation of optical band gap.** To explore the optical performance of the resulting NPs, UV-Vis spectroscopy was studied. As the calcination temperature increases, the absorption intensity in the visible region also increases as shown in Fig. 8(a). The sample calcined at 923 K showed absorption maximum at ~365 nm. Optical band gap of the prepared NPs was estimated from the Tauc's relation as shown in Eq. (7):

$$\alpha hv = k (hv - E_g)^{n/2}, \quad (7)$$

where  $\alpha$  is the absorption coefficient,  $h$  is the Planck's constant,  $\nu$  is the light frequency;  $k$  is a constant,  $E_g$  is the optical band gap, and  $n = 1$  for direct transition and is 4 for allowed indirect transition. The band gap was calculated by extrapolating the linear portion of the plot of  $hv$  versus  $(\alpha hv)^2$  curve to X-axis as shown in Fig. 8(a) (inset). A wide range of band gap from 2.48 to 2.76 eV has been observed, indicating that the samples were having tunable band gap (Table 1). Due to quantum confinement effect the band gap decreases with increasing particle size. The obtained band gap values were agreed well with WO<sub>3</sub> NPs reported in the literature [8].

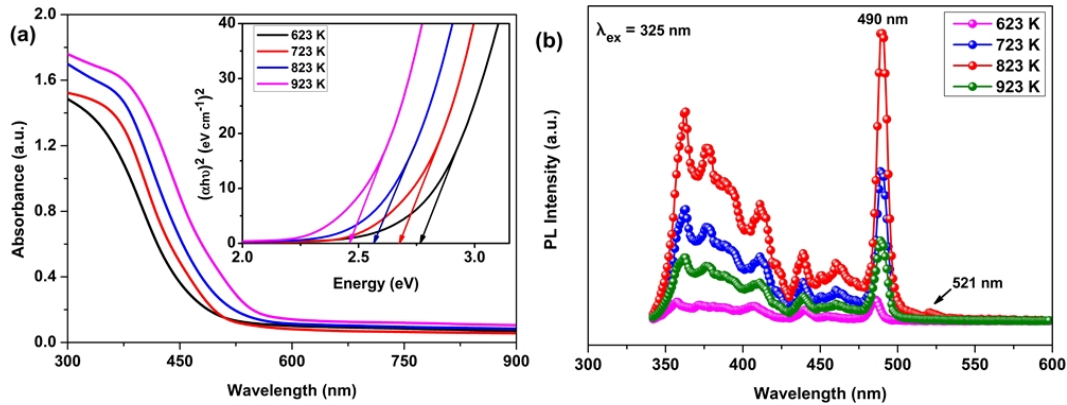


FIG. 8. (a) Absorbance spectra and Tauc's plot (inset) and (b) PL spectra of the prepared WO<sub>3</sub> samples

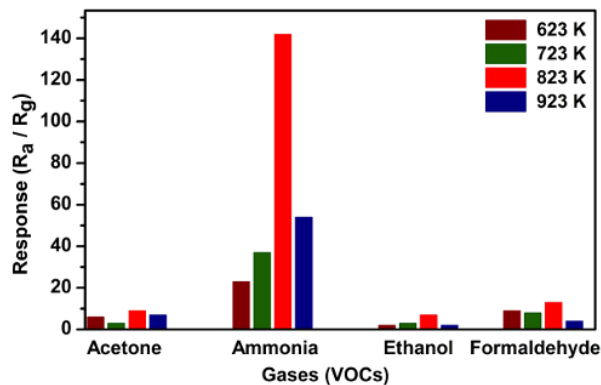


FIG. 9. Selectivity studies of the synthesised WO<sub>3</sub> samples (623 – 923 K)

**3.3.2. Defect states.** Figure 8(b) shows the PL signatures of the prepared samples at room temperature with the excitation wavelength of 325 nm. The peak found at 378 nm corresponds to NUV emission and is attributed to the recombination between the electron occupying the resonant defect state in conduction band and a hole in the valence band [27]. The emission at 412 nm may be allocated to the recombination of free excitons and is denoted as near band edge emission. The peak located at 459 nm suggesting that the electron hole pair separation rapidly, which may facilitate the electron transfer efficiency [28]. The blue emission at 490 nm can be assigned to oxygen vacancies

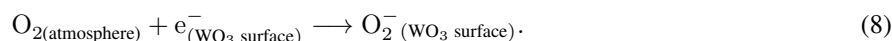
associated with defect level in the band gap for its electron transition [29]. As the calcination temperature of WO<sub>3</sub> NPs increases up to 823 K, the intensity of the oxygen vacancies related PL peak (490 nm) is found to increase and the further increase in calcination temperature is accompanied by a decrease in oxygen vacancies, while the relevant crystalline performance is improved by a decrease in bulk defects. Unambiguously, the WO<sub>3</sub> NPs calcined at 823 K has a significantly higher PL intensity compared to other samples, which suggests the higher recombination rate of photo-induced electron-hole pair. In addition, a green emission peak at 521 nm was observed in 823 K sample, which is related to doubly charged oxygen vacancy centers ( $v_0^{++}$ ) located at the surface of the NPs. This emission may be associated with various luminescent centers, such as defect energy states due to oxygen vacancies as well as dangling bonds into NPs. On the other hand, no signal corresponds to green emission occur in the 623, 723 and 923 K samples. Furthermore, all other peaks are due to the defects from bulk WO<sub>3</sub> formation. The obtained PL results are in good agreement with XRD and XPS studies.

### 3.4. Gas sensing studies

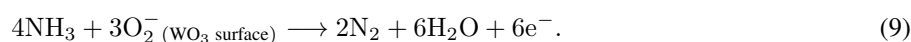
In order to find highly selective behavior, all the samples were tested as sensing materials in the presence of 200 ppm of various injected analytes like acetone, ammonia, ethanol and formaldehyde. All the samples show highly selective behavior to ammonia at room temperature while less sensitive to other gases, which purports pleasantly enough selective behavior of the prepared NPs as depicted in Fig. 9. Interestingly, the 823 K sample was highly selective ( $S = 142$ ) towards 200 ppm ammonia. This behavior may be explained as follows. (i) Higher reducing capability of ammonia and lower kinetic diameter (0.326 nm) than that of other target gases promotes the diffusion process appreciably [30]. (ii) Lower ionization energy (10.18 eV), and also the dissociation of bond occurs at N–H with the significant dissociation energy of 314 kJ/mol [31], which are comparatively lower than other test gases in-turn the enhanced surface interactions [32]. (iii) Gas-solid interaction might be enhanced due to the lone pair of electrons in ammonia when the occurrence of H–N bond dissociation [5]. (iv) The diffusion of ammonia vapor within the Debye length has been excellently monitored by the cluster-like nanograin morphology of the NPs. (v) Good crystallinity associated with uniformly assembled surface morphology may acts as a percolation path for vapor diffusion. (vi) The presence of oxygen vacancies (as identified from the O1s spectra of 823 K) might have enhanced the reactive oxygen sites on the surface of WO<sub>3</sub> NPs and in turn improved gas–solid interaction. (vii) It is well known that oxygen vacancies had an obvious effect on improving the sensitivity. These vacancies act as electron donors, i.e., which introduce carriers in the conduction band of WO<sub>3</sub> thereby increasing the conductivity (as discussed in Section 3.2). (viii) The presence of green emission peak due to perturbed oxygen defect centers and larger surface defects (as observed through PL spectra of 823 K sample) might have improved the surface catalytic behavior and thereby resulting enhanced gas response. These intrinsic defects introduce more mid-gap states and largely enhance the transition probability of the valence electrons to its conduction band.

These notions supported explaining the significant ammonia response values reported in this literature, despite the large crystallite size resulting from the thermal treatment at 823 K.

When WO<sub>3</sub> is exposed to air ambience, the atmospheric oxygen species interact with the surface and chemisorbed as O<sub>2</sub><sup>−</sup> on the surface by capturing the electrons from the conduction band of WO<sub>3</sub> (Eq. (8)). It causes further increment in the surface resistance and this value could be fixed as the baseline resistance ( $R_a$ ). This increased resistance would also develop a depletion region between the grain boundaries of the sample [33].



When the sensing material is exposed under the influence of reducing gas like ammonia, which interacts with adsorbed O<sub>2</sub><sup>−</sup> ions, this results in the liberation of electrons (Eq. (9)). Those released electrons have retained in the conduction band of the sensing material. As the width of the space charge region was decreased and leads to a decrease in surface resistance thereby attaining the steady state ammonia resistance ( $R_g$ ). According to [34], the feasible interaction mechanism of WO<sub>3</sub> sensing surface towards atmospheric oxygen molecules and ammonia vapor at room temperature is as demonstrated in Eq. (9):



In case of recovery cycle, interacted ammonia gets desorbed and the sensor reached its baseline resistance. It accomplishes one proper cycle of response and recovery profile of the sensor.

The possible reasons for the low sensitive behavior of other samples (calcined at 623, 723 and 923 K) may be ascribed to various factors as follows: (i) the reduction in crystallinity would affect the gas diffusion and electron transport among the grain network, which would also have lowered the sensitivity of 623 and 723 K samples; (ii) beyond 823 K, the sensing response was found to be decrease, and it could be attributed to the agglomerated morphology of the NPs, however, higher calcination causes crystal grain growth in the sample, which would effectively modify

the microstructural properties of the NPs [35]. This might be affect the electron transfer during gas-solid interaction, resulting in a significant change (decrease) in the sensing response. (iii) Besides, the lack of oxygen vacancies (as observed from the O1s spectra of 623, 723 and 923 K) and poor oxygen defect centers (as identified from PL spectra) reduce the reactive oxygen adsorption sites on the sensing surface thereby lowering the sensor kinetics. The transient resistance response characteristics of the 823 K NPs were investigated towards ammonia in the range of 5 – 200 ppm as shown in Fig. 10. Inventingly, the sensing response was found to be 7 for 10 ppm of ammonia. Thus, it could be possible to detect ammonia even at low concentration levels under room temperature ambience and thus chiefly desired. The 823 K NPs also showed a high response of 18 towards 25 ppm ammonia while it increased to 142 in the presence of 200 ppm ammonia. When the concentration of ammonia vapor was increased from 5 to 1000 ppm, a very steep increase was observed in sensing response as depicted in Fig. 11(a). This trend is paramount factor for designing readout signal circuits and also applied in the construction of low-power gas sensing devices. Beyond 1000 ppm, the sensing response was found to be saturated, which may be due to the formation of multilayers of ammonia. These layers might affect the further gas – solid interaction by decreasing the active sites present in the sensor surface [36]. The lowest detection limit of the sensor towards ammonia gas was experimentally found to be 5 ppm. The saturation in sensor resistance is illustrated using a step change plot as shown in Fig. 11(b).

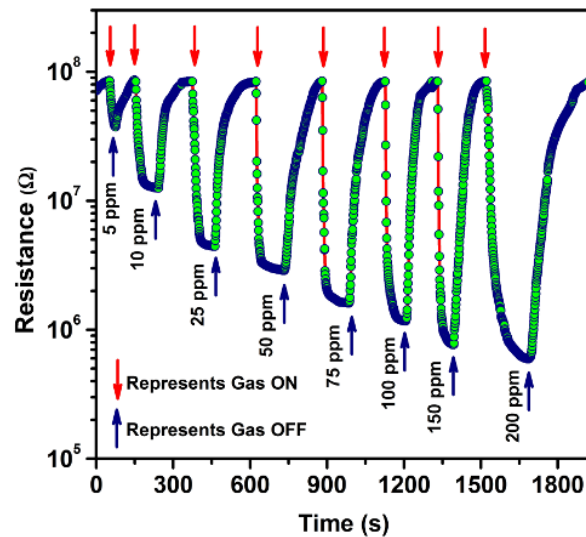


FIG. 10. Transient resistance response of 823 K sample towards different ammonia concentrations (5 – 200 ppm)

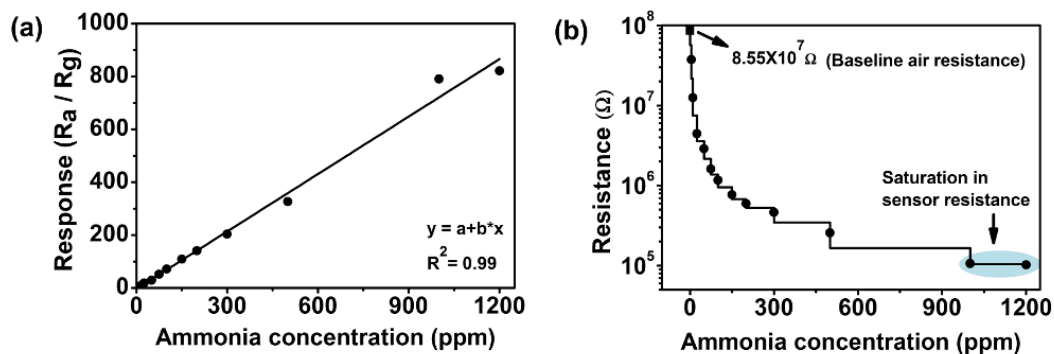


FIG. 11. (a) Response trend of 823 K sample towards various concentrations (5 – 1200 ppm) of ammonia at room temperature and (b) Change in electrical resistance as a function of ammonia concentration from its initial baseline resistance

The 823 K NPs exhibited quick response and recovery profile towards 200 ppm of ammonia as shown in Fig. 12. The response and recovery times were found to be 26 and 79 s respectively. Repeatable behavior of the 823 K sample

was investigated towards 200 ppm ammonia for three cycles. The repeatability was found to be excellent over the three evaluation cycles and displayed in Fig. 13(a). The sample also exhibited better stability towards 200 ppm of ammonia for a period of 50 days in the interval of 10 days as illustrated in Fig. 13(b) and showed only 4.22 % change (decrease) in sensitivity over 50 days.

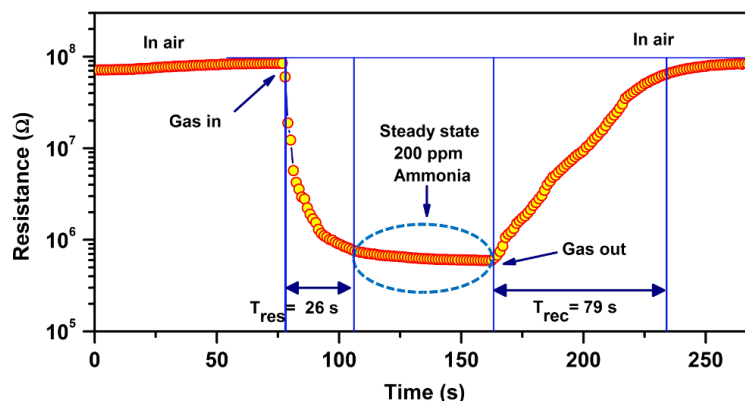


FIG. 12. Response-recovery profile of 823 K sample towards 200 ppm of ammonia

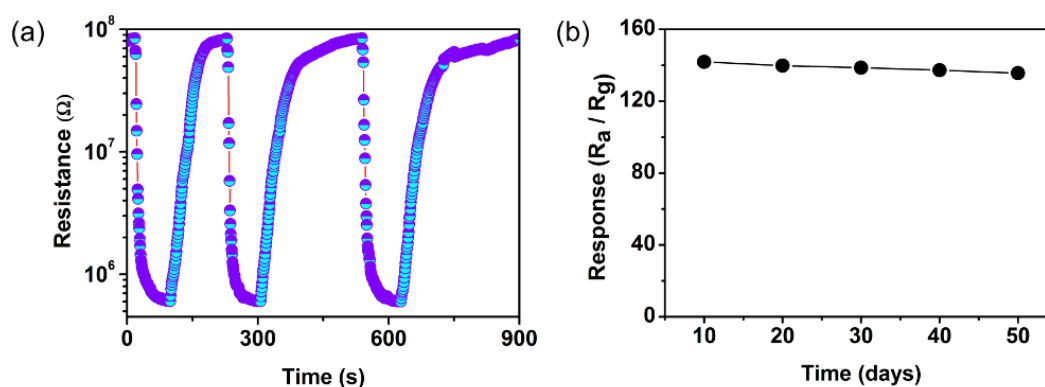


FIG. 13. (a) Repeatability and (b) Stability of 823 K sample towards 200 ppm of ammonia

To highlight the feature of the present study, the ammonia sensing performance of the NPs reported in this literature is compared with the available reports in Table 2.

#### 4. Conclusion

The following conclusions can be drawn from the study results.

(1) Polycrystalline m-WO<sub>3</sub> NPs were synthesized by precipitation method and are employed as an effective sensing material in the fabrication of gas sensor towards different analytes, particularly ammonia. (2) Targeting ammonia vapor and operation at room temperature, the optimum calcination temperature was determined to be 823 K and the sensor based on 823 K sample showed a high response of 7 towards 10 ppm of ammonia, while it increased to 142 towards 200 ppm of ammonia with rapid response and recovery times of 26 and 79 s respectively. (3) Satisfying active detection range (5 – 1200 ppm), repeatability and long-term stability were ensured. (4) Improved crystallinity, well-ordered nanocluster like morphology, enhanced electron transfer efficiency due to intrinsic defects, presence of oxygen vacancies and the perturbed oxygen defect centers would effectively support the enhanced sensing behavior of the 823 K sample. (5) This study disclosed that the thermal treatment has to be altered to change the crystallinity and morphology of the pristine WO<sub>3</sub> NPs resulting in improved sensitivity.

The most noteworthy aspect is that all the excellent gas sensing performance of the WO<sub>3</sub> gas sensor was achieved at room temperature. This innovation disclosed the following significant possibilities: (i) the reported sensor can be used as an eminent gas sensing tool to contribute in many real-time applications such as diagnosis breath analysis systems, food and beverage sectors owing to its excellent figure of merits; (ii) the present work is completely free from the requirements of stabilizing agents and inbuilt micro heaters.

TABLE 2. Comparison of ammonia sensing performances of the present work with other reports

Material	Response	Concentration (ppm)	Response time (s)	Recovery time (s)	Temperature (K)	Ref.
WO <sub>3</sub>	5.5 <sup>a</sup>	100	18.3	91.2	648	[37]
WO <sub>3</sub>	9.7 <sup>a</sup>	1500	7	8	523	[38]
WO <sub>3</sub>	5.5 <sup>d</sup>	100	1	5	473	[39]
PANI	2.3 <sup>d</sup>	100	120	300	298	[40]
ZnO/ native-graphite	12 <sup>c</sup>	40–45	510	420	303	[41]
ZnO	1.43 <sup>a</sup>	5	30	450	503	[42]
ZnO	17 % <sup>b</sup>	100	51	160	303	[43]
ZnO	10 % <sup>b</sup>	25	49	19	303	[44]
WO <sub>3</sub>	142 <sup>a</sup>	200	27	77	303	This work

$${}^a S = \frac{R_a}{R_g}, \quad {}^b S = \frac{(R_0 - R_g)}{R_0} \times 100 \%, \quad {}^c S = \frac{R_a - R_g}{R_a}, \quad {}^d S = \frac{R_g}{R_a}.$$

## References

- [1] Agency for toxic substances and disease (ASTDR) Registry, Public Heal. Statement Ammon. 2004, CAS# 7664–41–7, **1** (n.d.).
- [2] Erisman J.W., Sutton M.A., et al. How a century of ammonia synthesis changed the world. *Nat. Geosci.*, 2008, **1**, P. 636–639.
- [3] Malins C., Doyle A., et al. Personal ammonia sensor for industrial environments. *J. Environ. Monit.*, 1999, **1**, P. 417–422.
- [4] Alarie Y. Dose–response analysis in animal studies: prediction of human responses. *Environ. Health Perspect.*, 1981, **42**, P. 9–13.
- [5] Mani G.K., Rayappan J.B.B. A highly selective room temperature ammonia sensor using spray deposited zinc oxide thin film. *Sens. Actuators B Chem.*, 2013, **183**, P. 459–466.
- [6] Timmer B., Olthuis W., Berg A.V.D. Ammonia sensors and their applications – A review. *Sens. Actuators B. Chem.*, 2005, **107** (2), P. 666–677.
- [7] Parthasarathy Srinivasan, Madeshwari Ezhilan, et al. Room temperature chemiresistive gas sensors: challenges and strategies – a mini review. *Journal of Materials Science: Materials in Electronics*, 2019, **30**, P. 15825–15847.
- [8] Reza Abazari, Ali Reza Mahjoub, et al. Characterization and optical properties of spherical WO<sub>3</sub> nanoparticles synthesized via the reverse microemulsion process and their photocatalytic behavior. *Materials letters*, 2014, **133**, P. 208–211.
- [9] Llobet E., Molas G., et al. Fabrication of Highly Selective Tungsten Oxide Ammonia Sensors. *Journal of The Electrochemical Society*, 2000, **147** (2), P. 776–779.
- [10] Wood V., Panzer M.J., et al. Selection of Metal Oxide Charge Transport Layers for Colloidal Quantum Dot LEDs. *ACS Nano*, 2009, **3** (11), P. 3581–3586.
- [11] Lidia Santos, Celia Silveira, et al. Synthesis of WO<sub>3</sub> Nanoparticles for Biosensing Applications. *Sensors and Actuators B Chemical*, 2015, **223**, P. 186–194.
- [12] Jinhui Wang, Liu G., Youwei Du. Mechanochemical synthesis of sodium tungsten bronze nanocrystalline powders. *Materials Letters*, 2003, **57** (22–23), P. 3648–3652.
- [13] Haidong Zheng, Jian Zhen Ou, et al. Nanostructured Tungsten Oxide-Properties, Synthesis, and Applications. *Adv. Funct. Mater.*, 2011, **21**, P. 2175–2196.
- [14] Guan Wang, Yuan Ji, et al. Fabrication and Characterization of Polycrystalline WO<sub>3</sub> Nanofibers and Their Application for Ammonia Sensing. *J. Phys. Chem. B*, 2006, **110**, P. 23777–23782.
- [15] Zuquan Wu, Xiangdong Chen, et al. Enhanced sensitivity of ammonia sensor using graphene/polyaniline nanocomposite. *Sensors and Actuators B*, 2013, **178**, P. 485–493.
- [16] Liu H., Shen W., Chen X. A room temperature operated ammonia gas sensor based on Ag-decorated TiO<sub>2</sub> quantum dot clusters. *RSC Adv.*, 2019, **9**, P. 24519–24526.
- [17] Wang C.-Y., Zhang X., et al. Ammonia sensing by closely packed WO<sub>3</sub> microspheres with oxygen vacancies. *Chemosphere*, 2018, **204**, P. 202–209.
- [18] Tai H., Jiang Y., et al. Fabrication and gas sensitivity of polyaniline–titanium dioxide nanocomposite thin film. *Sensors and Actuators B: Chemical*, 2007, **125**, P. 644–923.
- [19] Li C.F., Hsu C.Y., Li Y.Y. NH<sub>3</sub> sensing properties of ZnO thin films prepared via sol–gel method. *J. Alloys Compd.*, 2014, **606**, P. 27–31.
- [20] Martinez-de la Cruz A., Sanchez Martinez D., Lopez Cuellar E. Synthesis and characterization of WO<sub>3</sub> nanoparticles prepared by the precipitation method: Evaluation of photocatalytic activity under vis–irradiation. *Solid State Sciences*, 2010, **12**, P. 88–94.
- [21] Ahmadi M., Sahoo S., et al. WO<sub>3</sub> nano-ribbons: Their phase transformation from tungstite (WO<sub>3</sub>·H<sub>2</sub>O) to tungsten oxide (WO<sub>3</sub>). *J. Mater. Sci.*, 2014, **49** (17), P. 5899–5909.
- [22] Parthasarathy Srinivasan, John Bosco Balaguru Rayappan. Growth of Eshelby twisted ZnO nanowires through nanoflakes & nanoflowers: A room temperature ammonia sensor. *Sensors & Actuators: B. Chemical*, 2018, **277**, P. 129–143.

- [23] Chen D., Sugahara Y. Tungstate-Based Inorganic-Organic Hybrid Nanobelts/Nanotubes with Lamellar Mesostructures: Synthesis, Characterization, and Formation Mechanism, *Chem. Mater.*, 2007, **19**, P. 1808–1815.
- [24] Diaz-Reyes J., Dorantes-García V., Perez-Benítez A., Balderas-Lopez J.A. Obtaining of films of tungsten trioxide (WO<sub>3</sub>) by resistive heating of a tungsten filament. *Superficies y Vacío.*, 2008, **21** (2), P. 12–17.
- [25] Jie Li, Yuan Liu, et al. A full-sunlight-driven photocatalyst with super long-persistent energy storage ability. *Sci. Rep.*, 2013, **3** (2409), P. 1–6.
- [26] Wang W., Janotti A., Van de Walle C.G. Role of oxygen vacancies in crystalline WO<sub>3</sub>. *J. Mater. Chem. C*, 2016, **4**, P. 6641–6648.
- [27] Kriti, Puneet Kaur, et al. Influence of defect structure on colour tenability and magneto optical behaviour of WO<sub>3</sub> nanoforms. *RSC Adv.*, 2019, **9**, P. 20536–20548.
- [28] Jeyapaul T., Prakash K., et al. Synthesis of WO<sub>3</sub> nanorods and their photocatalytic degradation of organic contaminants. *Rasayan J. Chem.*, 2018, **11** (4), P. 1405–1414.
- [29] Mohammed Harshulkhan S., Janaki K., et al. Structural and optical properties of Ag doped tungsten oxide (WO<sub>3</sub>) by microwave-assisted chemical route. *J. Mater Sci: Mater. Electron.*, 2016, **27**, P. 3158–3163.
- [30] Arockia Jayalatha Kulandaisamy, Jonnala Rakesh Reddy, et al. Room temperature ammonia sensing properties of ZnO thin films grown by spray pyrolysis: Effect of Mg doping. *Journal of Alloys and Compounds*, 2016, **688**, P. 422–429.
- [31] Dill J.D., Allen L.C., Topp W.C., Pople J.A. Systematic study of the nine hydrogen-bonded dimers involving ammonia, water, and hydrofluoric acid. *J. Am. Chem. Soc.*, 1975, **97**, P. 7220–7226.
- [32] Nayak A.K., Ghosh R., et al. Hierarchical nanostructured WO<sub>3</sub>-SnO<sub>2</sub> for selective sensing of volatile organic compounds. *Nanoscale*, 2015, **7**, P. 12460–12473.
- [33] Barsan N., Weimar U. Conduction Model of Metal Oxide Gas Sensors. *J. Electroceramics*, 2001, **7**, P. 143–167.
- [34] Jeevitha G., Abhinaya R., et al. Porous reduced graphene oxide rGO/WO<sub>3</sub> nanocomposites for the enhanced detection of NH<sub>3</sub> at room temperature. *Nanoscale Adv.*, 2019, **1**, P. 1799–1811.
- [35] Wang H., Quan X., Zhang Y., Chen S. Direct growth and photoelectrochemical properties of tungsten oxide nanobelt arrays, *Nanotechnology*, 2008, **19** (065704), P. 1–6.
- [36] Patil D.R., Patil L.A., Amalnerkar D.P. Ethanol gas sensing properties of Al<sub>2</sub>O<sub>3</sub>-doped ZnO thick film resistors. *Bulletin of Materials Science*, 2007, **30**, P. 553–559.
- [37] Yan A., Xie C., et al. Synthesis, formation mechanism and sensing properties of WO<sub>3</sub> hydrate nanowire netted-spheres. *Materials Research Bulletin*, 2010, **45** (10), P. 1541–1547.
- [38] Nguyen Van Hieu, Vu Van Quang, Nguyen Duc Hoa, Dojin Kim. Preparing large-scale WO<sub>3</sub> nanowire-like structure for high sensitivity NH<sub>3</sub> gas sensor through a simple route. *Curr. Appl. Phys.*, 2011, **11**, P. 657–661.
- [39] Ji-yan Leng, Xiu-juan Xu, et al. Synthesis and gas-sensing characteristics of WO<sub>3</sub> nanofibers via electrospinning. *Journal of Colloid and Interface Science*, 2011, **356**, P. 54–57.
- [40] Sengupta P.P., Kar P., Adhikari B. Influence of dopant in the synthesis, characteristics and ammonia sensing behavior of processable polyaniline. *Thin Solid Films*, 2009, **517**, P. 3770–3775.
- [41] Tulliani J.M., Cavalieri A., et al. Room temperature ammonia sensors based on zinc oxide and functionalized graphite and multi-walled carbon nanotubes. *Sensors and Actuators B*, 2011, **152**, P. 144–154.
- [42] Siril V.S., Madhusoodanan K.N., Rajan S.K., Louis G. Study on ammonia gas sensing property of hydrothermally synthesized pure ZnO nanorods. *AIP Conf. Proc.*, 2017, **1849**, 020033.
- [43] Andre R., Kwak D., et al. Sensitive and Selective NH<sub>3</sub> Monitoring at Room Temperature Using ZnO Ceramic Nanofibers Decorated with Poly(styrene sulfonate). *Sensors*, 2018, **18** (1058), P. 1–13.
- [44] Venkatesh P.S., Dharmaraj P., et al. Point defects assisted NH<sub>3</sub> gas sensing properties in ZnO nanostructures. *Sens. Actuators B Chem.*, 2015, **212**, P. 10–17.

## Photocatalytic properties of persistent luminescent rare earth doped SrAl<sub>2</sub>O<sub>4</sub> phosphor under solar radiation

Deepika Pal<sup>1</sup>, Anil Kumar Choubey<sup>2</sup>

<sup>1</sup>Department of Nanotechnology, Christian College of Engineering & Technology,  
Kailash Nagar Bhilai, Chhattisgarh, India

<sup>2</sup>Department of Physics, M. J. College, Junwani-Kohka Road, Bhilai, Chhattisgarh, India  
deepikapal664@gmail.com, anil.choubey@hotmail.com

PACS 52.70.Kz, 81.16.Hc, 87.15.Mi

DOI 10.17586/2220-8054-2020-11-5-590-594

This paper aims to study the photocatalytic properties of strontium aluminate phosphors. The rare earth doped strontium aluminate was synthesized by combustion method. The photocatalytic property was studied by absorption of methylene orange in aqueous solution under solar radiation. Eu:Dy codoped SrAl<sub>2</sub>O<sub>4</sub> shows better photocatalytic properties than Eu or Dy doped or Eu, Dy, Ho codoped SrAl<sub>2</sub>O<sub>4</sub>. Structural and morphological characterization was done by X-ray diffraction, SEM, EDX techniques.

**Keywords:** photocatalysis, strontium aluminate, combustion method, persistence luminescence.

*Received: 10 May 2020*

*Revised: 26 August 2020*

*Final revision: 16 September 2020*

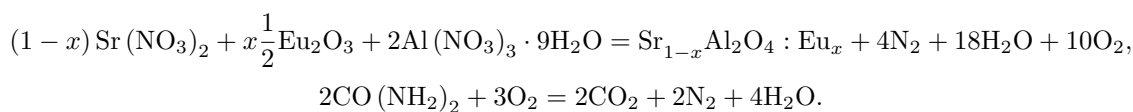
### 1. Introduction

Today, environmental pollution is major concern, especially resulting from volatile organic compounds like benzene or textile dyes, like Methylene blue, Congo red, etc.; these volatile organic compounds are known to be toxic and carcinogenic. It is required to develop photo-catalysts for the degradation of these toxic materials to reduce air pollution and to develop better wastewater cleaning process. Advanced oxidation is a process which produces reactive oxygen groups to react with different chemicals which in turn help in degradation of these chemicals. Photocatalysis is also a kind of advanced oxidation process to remove organic pollutants from water [1, 2]. When photocatalysts are dispersed in water, they absorb UV or sun light to produce electron-hole pairs which in turn generate free radicals (e.g. hydroxyl radicals OH<sup>-</sup> and O<sup>2-</sup>) that take part in secondary reactions which removes organic pollutants from water [3]. Photocatalysts are semiconductors or insulators such as Al<sub>2</sub>O<sub>3</sub> [4], ZnO [5], Fe<sub>2</sub>O<sub>3</sub> [6]. TiO<sub>2</sub> has been widely used for decolorizing of organic contaminants, dyes and phenols. The problem with TiO<sub>2</sub> is that it is toxic for living organisms [7, 8] like fish and other aquatic animals, as it can penetrate their skin to produce oxidative stress and impaired liver function. Hence, the search for new environmentally friendly photocatalysts is required that could be easily removed from water. It has been found that long-lasting phosphors show photocatalytic properties [9]. Rare earth doped alkaline earth aluminates are a very important class of luminescent materials due to their higher quantum efficiency and persistent luminescence [10]. They are good host materials and have wide band gaps, thus, they have been suggested for possible application such as development of white LED'S, gamma ray dosimeter, pressure sensor, stress sensor, environmental radiation dosimetry, luminescent paint, emergency exit lamps, radiation detection [11, 12] etc. There are few papers which report persistent luminescent phosphors prepared by combustion method as photocatalytic materials.

In this paper, we have reported the synthesis of SrAl<sub>2</sub>O<sub>4</sub> doped with Eu/Dy/Ho by combustion method and their photocatalytic properties.

### 2. Experimental

The combustion method involves a highly exothermic reaction between an organic fuel and metal nitrates. The reaction is initiated at low temperatures (around 610 °C) and proceeds to completion in a few minutes. The exothermic chemical reaction between the metal nitrates and fuel provides the required heat for synthesis of nano-phosphor. Research grade strontium nitrate Sr(NO<sub>3</sub>)<sub>2</sub>, aluminum nitrate Al(NO<sub>3</sub>)<sub>3</sub> · 9H<sub>2</sub>O, europium oxide Eu<sub>2</sub>O<sub>3</sub>, dysprosium oxide Dy<sub>2</sub>O<sub>3</sub>, holmium oxide Ho<sub>2</sub>O<sub>3</sub> were used as the starting materials and urea CO(NH<sub>2</sub>)<sub>2</sub> was used as a fuel. The Stoichiometric composition to prepare Sr<sub>1-x</sub>Al<sub>2</sub>O<sub>4</sub>:Eu<sub>x</sub> phosphor, the chemical reaction used for the combustion reaction is as follows:



The stoichiometric composition of the metal nitrates (oxidizers) and urea (fuel) were calculated using the total oxidizing and reducing valences of the components, which serve as the numerical coefficients so that the equivalence ratio is unity and the heat liberated during combustion is at a maximum. For the calculation of oxidizer to fuel ratio, the elements were assigned formal valences as follows: Sr = +2, Al = +3, Eu/Dy/Ho = +3, C = +4, N = 0, O = -2 and H = +1. Nitrogen had a valence of zero because N<sub>2</sub> was assumed to be liberated during the combustion process. The rare earth oxides were dissolved in minimum amount of HNO<sub>3</sub>. The stoichiometric quantities of metal nitrate and urea were mixed for crushing in a mortar; then the nitrates of rare earth were mixed. The composition was stirred for 1 hour at 80 °C to form a thick paste. The paste was transferred to a crucible and put into a vertical cylindrical muffle furnace maintained at 610 °C. The mixture went decomposition with the evolution of large amount of gases (oxides of carbon, nitrogen and ammonia). The exothermic reaction continues and the spontaneous ignition occurs. The solution underwent smoldering combustion with enormous swelling, producing white foamy and voluminous ash. The whole process completed in ~30 seconds. The foamy product was milled to obtain the precursor powder. Sample annealing was done at 1050 °C for 3 hours in reducing atmosphere. The structural characterization XRD was done with a PANalytical 3kW X'pert powder- Multifunctional X-ray diffractometer available at NIT, Raipur in the range 10° < 2θ < 80° with a step of 0.02°. The morphology of the sample powders was done with ZEISS EVO 18 Scanning Electron Microscope (SEM), 30 kV of acceleration voltage with Quorum SC7620 sputter gold coater. The Energy Dispersive X-ray (EDX) of the phosphor was done with INCA 250 EDS with X-MAX 20 nm detector at NIT, Raipur. The absorbance spectra of powders were taken using ELICO-SL210 UV Spectrometer in 200 – 700 nm range. Photocatalytic properties were studied after dissolving 0.1 gm of photocatalysts powder in the solution of methylene orange. The mixture was stirred in the dark for 30 minutes and then placed in direct sunlight for different intervals and absorbance studies were performed subsequently.

### 3. Results and discussions

#### 3.1. Structural and morphological characterization

Figure 1 shows the XRD patterns of the SrAl<sub>2</sub>O<sub>4</sub> powders doped and codoped with Eu/Dy/Ho which matches well with the monoclinic phase of SrAl<sub>2</sub>O<sub>4</sub>, JCPDS card number 34-0379. The main peak corresponds to 220, 031, -211, 211 planes. The doping of rare earth ions does not affect the crystal structure due similar ionic radii of Sr<sup>2+</sup> (0.114 nm), Eu<sup>2+</sup> (0.112 nm), Dy<sup>3+</sup> (0.117 nm), Ho<sup>3+</sup> (0.115 nm). The average crystallite sizes calculated by Scherrer method for Eu, Dy, EuDy, EuDyHo doped samples were found to be 17.12, 20.54, 17.78 and 18.34 nm respectively.

The SEM micrograph of Eu, Dy, Eu:Ho, Eu:Dy:Ho doped SrAl<sub>2</sub>O<sub>4</sub> is shown in Fig. 2(A), 2(B), 2(C) and 2(D) respectively. Each sample were coated with gold by gold sputter before SEM. The samples show flower like structure with flakes randomly oriented.

The EDX spectral studies provide the elemental contents qualitatively and quantitatively. The EDX studies of Eu, Dy, Eu:Ho, Eu:Dy:Ho doped SrAl<sub>2</sub>O<sub>4</sub> is shown in Fig. 3(A), 3(B), 3(C) and 3(D) respectively. Clearly the spectra show sharp peaks corresponding to Sr, Al, O and Eu/Dy/Ho elements respectively and show no other impurities presence of the samples. The elemental contents are shown in Table 1.

#### 3.2. Photocatalytic activity under solar irradiation

Photocatalytic activity was observed by the percentage degradation of methylene orange (MO) in aqueous solution. MO shows an absorbance band at 465 nm and absorption intensity of this peak as a function of time was observed. Decrease in absorbance intensity indicate the decrement of MO concentration. The percentage degradation was calculated as:

$$\text{Degradation (\%)} = \frac{I_t - I_0}{I_0} \times 100 \%, \quad (1)$$

where I<sub>0</sub> – absorbance before solar radiation, I<sub>t</sub> – absorbance after time *t* of solar radiation.

Aqueous solutions of Methylene Orange (0.0025 gm/100 mL) were prepared in a beaker subsequently, 0.1 gm of photocatalysts powder were added to 100 ml aliquots of these solutions. The mixture was stirred in the dark for half hour. Later, the solutions of dye photocatalyst were directly exposed to sunlight for regular intervals. Fig. 4 shows the percentage degradation of MO as a function of time. The percentage degradation of undoped samples were

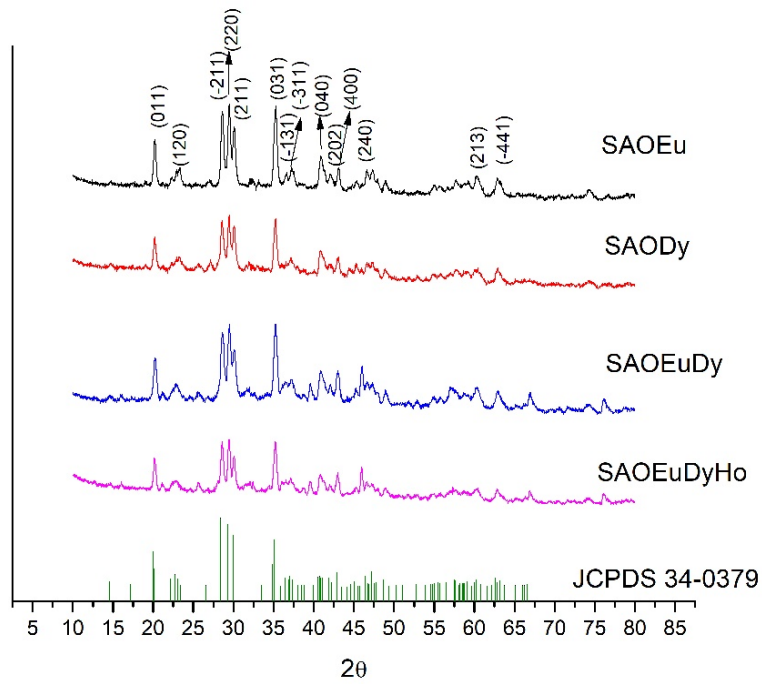


FIG. 1. The XRD image of rare earth doped and codoped  $\text{SrAl}_2\text{O}_4$

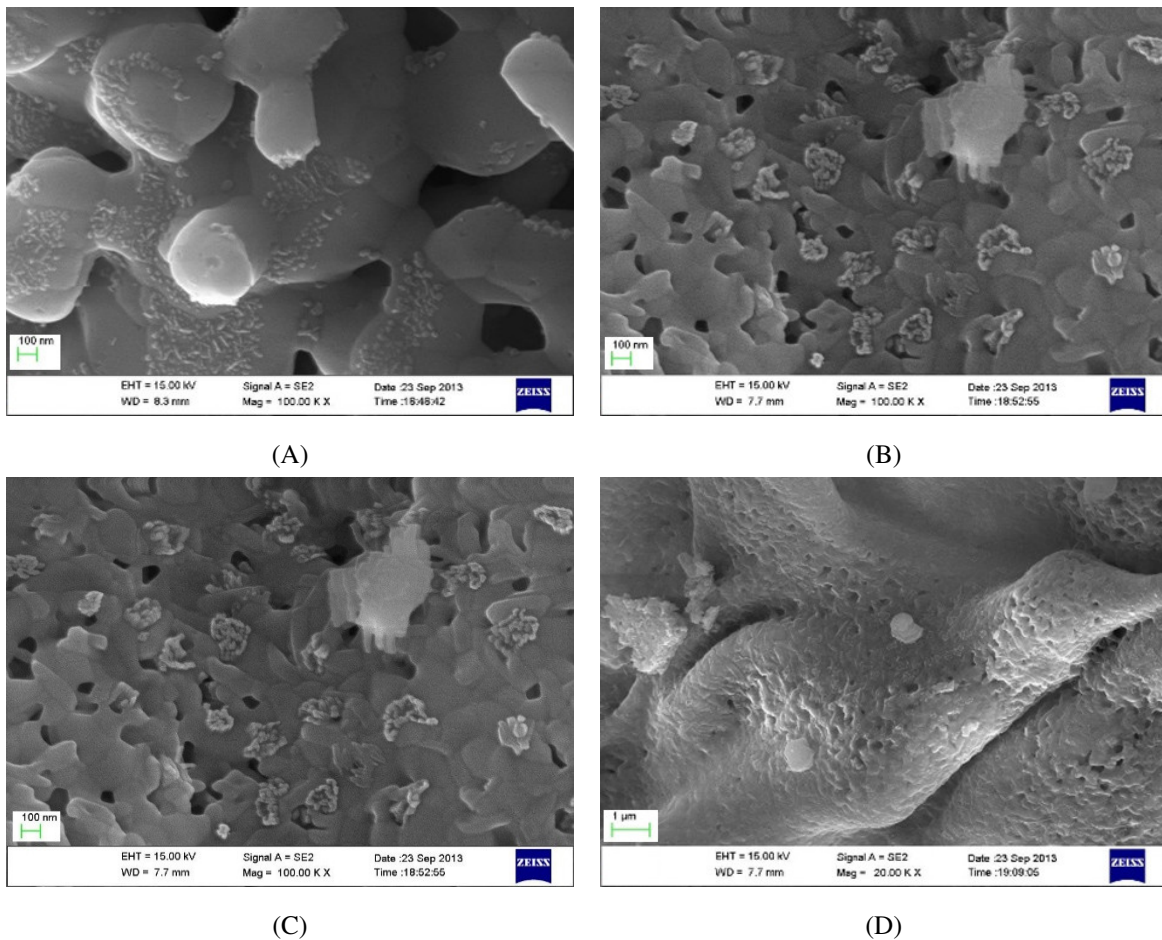


FIG. 2. SEM micrograph of  $\text{SrAl}_2\text{O}_4$  doped with A)  $\text{Eu}_{0.05}$ ; B)  $\text{Dy}_{0.1}$ ; C)  $\text{Eu}_{0.05}\text{Ho}_{0.01}$ ; D)  $\text{Eu}_{0.05}\text{Dy}_{0.1}\text{Ho}_{0.01}$

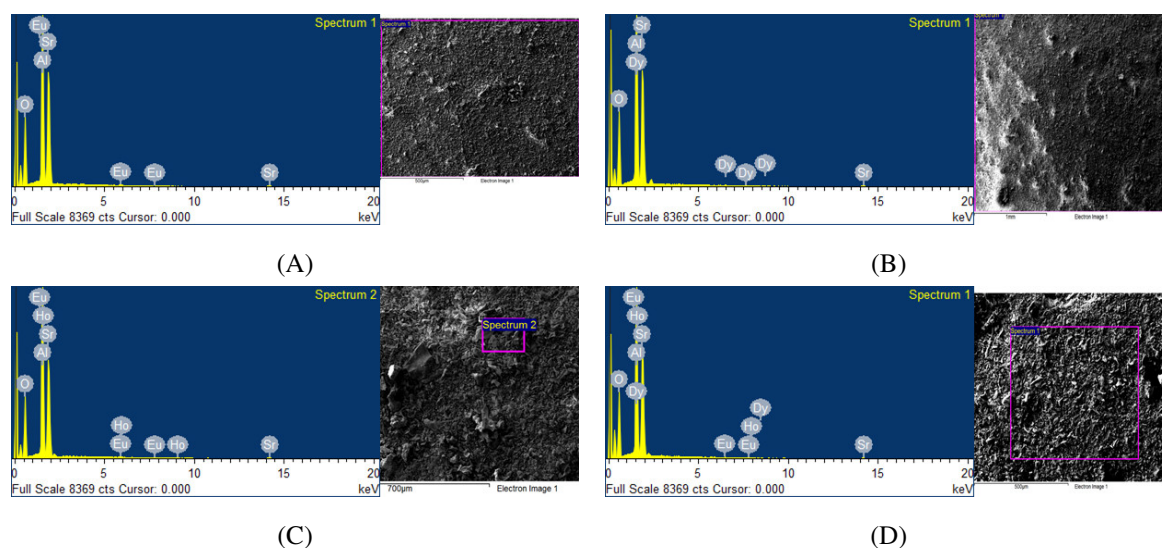


FIG. 3. EDX spectra of SrAl<sub>2</sub>O<sub>4</sub> doped with A) Eu<sub>0.05</sub>; B) Dy<sub>0.1</sub>; C) Eu<sub>0.05</sub>Ho<sub>0.01</sub>; D) Eu<sub>0.05</sub>Dy<sub>0.1</sub>Ho<sub>0.01</sub>

TABLE 1. Element contents of SrAl<sub>2</sub>O<sub>4</sub>

Elements	SrAl <sub>2</sub> O <sub>4</sub> :Eu <sub>0.05</sub> %		SrAl <sub>2</sub> O <sub>4</sub> :Dy <sub>0.1</sub> %		SrAl <sub>2</sub> O <sub>4</sub> :Eu <sub>0.05</sub> Ho <sub>0.1</sub> %		SrAl <sub>2</sub> O <sub>4</sub> : Eu <sub>0.05</sub> Dy <sub>0.1</sub> Ho <sub>0.01</sub> %	
	weight %	Atomic %	weight %	Atomic %	weight %	Atomic %	weight %	Atomic %
Sr	36.11	10.73	34.66	10.19	34.96	10.48	35.93	10.73
Al	20.95	20.21	22.05	21.06	23.71	23.08	21.39	20.73
O	42.4	68.97	42.61	68.64	40.37	66.28	41.84	68.4
Eu	0.54	0.09	–	–	0.41	0.07	0.21	0.04
Dy	–	–	0.68	0.11	–	–	0.46	0.07
Ho	–	–	–	–	0.57	0.09	0.17	0.03
Total	100	100	100	100	100	100	100	100

negligible and not reported here. The percentage degradation of Eu, Dy, Eu:Dy, and Eu:Dy:Ho doped samples after 240 minutes were 20.8%, 15.7%, 22.8%, and 13.2% respectively. The highest percentage degradation was obtained for Eu:Dy codoped SrAl<sub>2</sub>O<sub>4</sub>. It has been reported earlier [13] that Eu:Dy codoped SrAl<sub>2</sub>O<sub>4</sub> was known to be more persistent luminescent material than that of the doped alone, though its luminescence intensity decreased. Since the photocatalytic activity depends upon the generation of free carriers, the long persistent luminescent materials allow more time for the free carriers for catalytic action, in comparison to the high luminescent but less persistent materials. With codoping of Ho and Dy in SrAl<sub>2</sub>O<sub>4</sub>:Eu,Dy, the luminescence intensity increases but the persistence time is decreased [14] which results in less photocatalytic activity in Ho:Dy codoped phosphor.

#### 4. Conclusions

SrAl<sub>2</sub>O<sub>4</sub> doped and codoped with Eu, Dy and Ho were synthesized by combustion method. The XRD analysis shows monoclinic structure of SrAl<sub>2</sub>O<sub>4</sub> without any considerable effect on structure due to doping. The photocatalytic properties under solar radiation were observed. The undoped samples showed negligible photocatalytic effect with respect to the doped samples. The Eu:Dy codoped samples showed better photocatalytic properties than Eu/Dy doped or Eu:Dy:Ho codoped samples. The photocatalytic response of strontium aluminate phosphors were less than TiO<sub>2</sub> but they are more environmental friendly as they are activated by solar radiation and they can be removed from water by simple precipitation method.

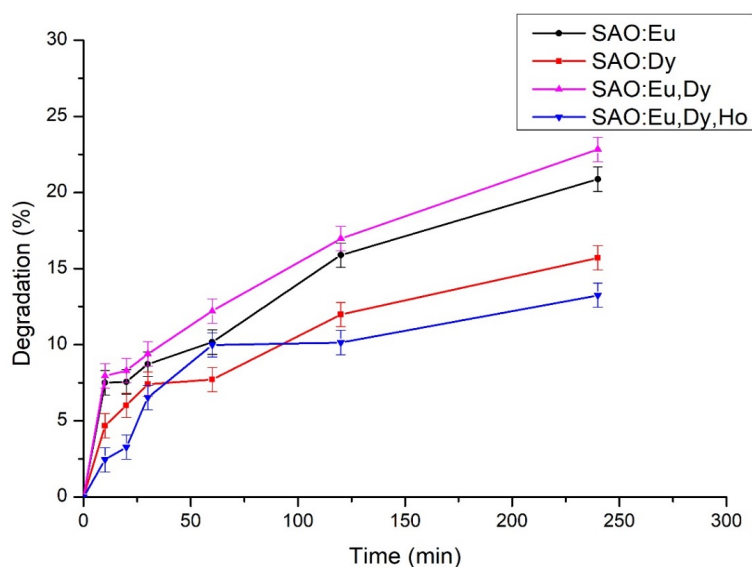


FIG. 4. The percentage degradation of MO under solar radiation as a function of time

## References

- [1] Berlanga A., Garcia-Diaz R., et al. Photocatalytic Activity of  $\text{SrAl}_2\text{O}_4:\alpha\text{Cu}$  powders under Solar Irradiation. *Nano Hybrid and Composites*, 2017, **16**, P. 63–66.
- [2] Sang Y., Liu H., Umar A. Photocatalysis from UV/Vis to near-infrared light: Towards full solar-light spectrum activity. *Chem. Cat. Chem.*, 2015, **7**, P. 559–573.
- [3] Ibhaddon A., Fitzpatrick P. Heterogeneous Photocatalysis: Recent Advances and Applications. *Catalysts*, 2013, **3**, P. 189–218.
- [4] Tzompantzi F., Piña Y., et al. Hydroxylated sol-gel  $\text{Al}_2\text{O}_3$  as photocatalyst for the degradation of phenolic compounds in presence of UV light. *Catalysis Today*, 2014, **220–222**, P. 49–55.
- [5] Behnjady M.A., Modirshahla N., Hamzavi R. Kinetic study on photocatalytic degradation of C.I. Acid Yellow 23 by ZnO photocatalyst. *Journal of Hazardous Materials*, 2006, **133** (1–3), P. 226–232.
- [6] Karunakaran C., Senthilvelan S.  $\text{Fe}_2\text{O}_3$ -photocatalysis with sunlight and UV light: Oxidation of aniline. *Electrochemistry Communications*, 2006, **8** (1), P. 95–101.
- [7] Wu J., Liu W., et al. Toxicity and penetration of  $\text{TiO}_2$  nanoparticles in hairless mice and porcine skin after sub chronic dermal exposure. *Toxicology Letters*, 2009, **191**, P. 1–8.
- [8] Dong H., Zeng G., et al. An overview on limitations of  $\text{TiO}_2$ -based particles for photocatalytic degradation of organic pollutants and the corresponding countermeasures. *Water Research*, 2015, **79**, P. 128–146.
- [9] Zhong J.B., Ma D., et al. Sol-gel preparation and photocatalytic performance of  $\text{TiO}_2/\text{SrAl}_2\text{O}_4: \text{Eu}^{2+}, \text{Dy}^{3+}$  toward the oxidation of gaseous benzene. *Journal of Sol-Gel Science and Technology*, 2009, **52** (1), P. 140–145.
- [10] Liu B., Gu M., et al. Theoretical Study of Structural, Electronic, lattice dynamical and dielectric properties of  $\text{SrAl}_2\text{O}_4$ . *Journals of Alloys and Compounds*, 2011, **509**, P. 4300–4303.
- [11] Choubey A.K., Brahme N., et al. Thermoluminescence characterization of  $\gamma$ -ray irradiated  $\text{Dy}^{3+}$  activated  $\text{SrAl}_4\text{O}_7$  nanophosphor. *Advanced Materials Letters*, 2014, **5** (7), P. 396–399.
- [12] Fu Z., Zhou S., Pan T., Zhang S. Band structure calculations on the monoclinic bulk and nano-  $\text{SrAl}_2\text{O}_4$  crystals. *Journals of Solid state Chemistry*, 2005, **178**, P. 230–233.
- [13] Lü X., Shu W. et al. Roles of Doping Ions in Persistent Luminescence of  $\text{SrAl}_2\text{O}_4: \text{Eu}^{2+}, \text{RE}^{3+}$  Phosphors. *Glass Physics and Chemistry*, 2007, **33** (1), P. 62–67.
- [14] Györi Z., Havasi V., et al. Luminescence properties of  $\text{Ho}^{3+}$  co-doped  $\text{SrAl}_2\text{O}_4: \text{Eu}^{2+}, \text{Dy}^{3+}$  long-persistent phosphors synthesized with a solid-state method. *Journal of Molecular Structure*, 2013, **1044**, P. 87–93.

## Synthesis of $\text{Ni}_{0.4}\text{Zn}_{0.6}\text{Fe}_2\text{O}_4$ spinel ferrite and microwave adsorption of related polymer composite

K. D. Martinson<sup>1</sup>, D. D. Sakhno<sup>2</sup>, V. E. Belyak<sup>2</sup>, I. B. Panteleev<sup>2</sup>, I. V. Kochurov<sup>3</sup>, Yu. E. Zevatskiy<sup>3,4</sup>, V. I. Popkov<sup>1</sup>

<sup>1</sup>Ioffe Institute, Saint Petersburg, 194021, Russia

<sup>2</sup>Saint Petersburg State Institute of Technology, Saint Petersburg, 190013, Russia

<sup>3</sup>AO “NovBytChim”, Saint Petersburg, 199026, Russia

<sup>4</sup>Saint Petersburg Electrotechnical University “LETI”, Saint Petersburg, 197376, Russia

martinsonkirill@mail.ru

PACS 61.46.+w, 75.50.Bb, 75.60.-d

DOI 10.17586/2220-8054-2020-11-5-595-600

Nickel-zinc ferrites are important industrial materials in the production of various types of microwave devices; therefore, studies of new methods of obtaining functional ceramic on their basis are of great interest at present. In this work, soft magnetic ceramics based on  $\text{Ni}_{0.4}\text{Zn}_{0.6}\text{Fe}_2\text{O}_4$  spinel ferrite with low values of the coercive force were successfully obtained under various sintering modes (1000 and 1100 °C, holding time – 16 hours) based on nanostructured pre-ceramic ferrite powder synthesized by the solution combustion method. The initial powder and sintered ceramics were investigated by EDX, SEM and PXR methods. The electromagnetic parameters of the final product were investigated by vibration magnetometry and using the method of rectangular waveguide transmissions in the X-band. It was shown that, depending on the selected sintering mode, it is possible to obtain magnetic ceramics with an average grain size in the range from 1 to 3  $\mu\text{m}$  and with values of the coercive force ( $H_c$ ) from 16.32 to 19.41 Oe, remanent magnetization ( $M_r$ ) from 3.39 to 4.31 emu/g and saturation magnetization ( $M_s$ ) from 67.90 to 78.42 emu/g. After the preparation of a ferrite-polymer composite with different content of  $\text{Ni}_{0.4}\text{Zn}_{0.6}\text{Fe}_2\text{O}_4$  (0–50 wt%), it was found that the highest absorption characteristics of electromagnetic waves were observed for the sample with 40 wt% of spinel ferrite obtained at 1100 °C, 16 hours sintering mode.

**Keywords:** solution combustion synthesis, spinel, ferrites, soft magnets, microwave adsorption.

Received: 7 October 2020

### 1. Introduction

Ferrites-spinels and orthoferrites of rare earth elements remain relevant objects of research for many decades due to their wide application in many areas of modern science and technology [1–3]. In addition to the well-known classical areas of their application, such as the production of hard and soft magnets [4], magnetic fluids [5], sensors [6], microwave devices [7], etc., in recent years, new opportunities have been opening up with the use of nanostructured ferrites as materials with high antibacterial activity [8], MRI contrast agents [9], photocatalysts [10], materials for wastewater treatment [11], magnetically recoverable catalysts [12] and many others. Interest in nanocrystalline ferrites is primarily due to their high chemical and thermal stability and improved electromagnetic parameters in comparison with classical micron systems of a similar composition [13–16]. Besides, obtaining multicomponent ferrites is much easier if they are in a nanostructured form [17].

One of the most interesting representatives of spinel ferrites from an industrial point of view is the multicomponent Ni-Zn ferrite of the composition  $\text{Ni}_x\text{Zn}_{1-x}\text{Fe}_2\text{O}_4$ , which is widely used in the production of various microwave devices and as radio-absorbing materials (RAW) absorbing electromagnetic waves during which the incident energy is converted into thermal due to the interaction of waves and matter [18]. Radio-absorbing materials are the most important dual-use products widely used in both the military and civilian sectors [19]. For example, for electromagnetic shielding of aircraft and submarines, to eliminate interference and absorb secondary radiation from various electronic devices, microwave ovens, aircraft devices, etc. [20]. There are a large number of materials that, by their conductive and magnetic characteristics, can act as absorbers of electromagnetic waves. For example, polymers are not subject to corrosion and are much lighter than oxide systems, but they have much higher insulation and low stability of electromagnetic parameters [21]. This problem can be solved by adding magnetic particles to conducting polymers [22]. One of the possible variants of such magnetic particles is nickel-zinc ferrite with the composition  $\text{Ni}_{0.4}\text{Zn}_{0.6}\text{Fe}_2\text{O}_4$ , which has shown its effectiveness as a radio-absorbing material [23].

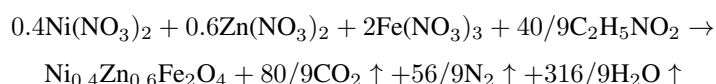
However, the use of ferrites as a radio-absorbing material places high demands on the stability of the magnetic and electromagnetic characteristics of the final product, which is difficult to achieve when using classical methods of production [24]. One of the promising methods for obtaining nanostructured complex oxide systems is the solution combustion method, which has shown its efficiency in the production of spinel ferrites and orthoferrites of various compositions [25–28]. Its main advantages are the ability to finely control the particle size, structure, morphology,

magnetic and electromagnetic characteristics by varying the composition of the initial reaction medium, which was shown in detail in our previous works [29–31].

In this work, the solution combustion method was used to obtain an initial nanostructured pre-ceramic powder  $\text{Ni}_{0.4}\text{Zn}_{0.6}\text{Fe}_2\text{O}_4$  with a high degree of crystallinity. The resulting powder was sintered according to classical ceramic technology, ground and dispersed into a varnish based on an acrylic copolymer in various weight percentages (0,10,....,50 wt%). The resulting product was tested using a rectangular waveguide transmission line method in the X-band (8.5–13 GHz).

## 2. Experimental

The initial nanostructured nickel-zinc ferrite of composition  $\text{Ni}_{0.4}\text{Zn}_{0.6}\text{Fe}_2\text{O}_4$  was obtained by the solution combustion method using glycine as a fuel and a chelating agent. Nickel nitrate ( $\text{Ni}(\text{NO}_3)_2 \cdot 6\text{H}_2\text{O}$ , pur., 99.9%), zinc nitrate ( $\text{Zn}(\text{NO}_3)_2 \cdot 6\text{H}_2\text{O}$ , pur., 99.9%), iron nitrate ( $\text{Fe}(\text{NO}_3)_3 \cdot 9\text{H}_2\text{O}$ , pur., 98.0%) and glycine ( $\text{C}_5\text{H}_5\text{NO}_2$ , pur., 98.0%) were used. Glycine was taken in a stoichiometric ratio according to the reaction of formation of nickel-zinc ferrite:



The initial reagents were taken in a stoichiometric amount and dissolved in 50 ml of distilled water with constant stirring for 30 min and a temperature of 50 °C. Then, the initial solution was heated to the autoignition temperature, during which a brown-colored ferrite powder was formed. The combustion product thus obtained was thermally treated in the air at a temperature of 600 °C for 3 hours to remove unreacted organic matter and mechanically processed in a vibrating mill (balls diameter = 2 cm) for 4 hours. Then the milled powder was pressed using polyethylene glycol as a binder and sintered at two temperature conditions – 1000 and 1100 °C for 16 hours. The resulting ceramics were analyzed and re-ground in a planetary mill (ball diameter = 1 cm) for 12 hours to obtain a submicron powder. The final composite was obtained by mixing nickel-zinc ferrite powders with a varnish based on an acrylic copolymer in various weight percentages (0, 10, ..., 50%) and passed electromagnetic characterization.

The morphology and chemical composition of the resulting powder and ceramics were studied by scanning electron microscopy (SEM) and energy dispersive analysis (EDX) using a Tescan Vega 3 scanning electron microscope and an Oxford Instruments X-act EDX microprobe analyzer. powder X-ray diffractometry on a Rigaku SmartLab 3 diffractometer ( $\text{CuK}\alpha = 0.15406 \text{ nm}$ ). Magnetic hysteresis loops were obtained using a LakeShore 7410 vibratory magnetometer. EMI absorption analysis was performed using a linear X-band method using a standard rectangular waveguide and a VectorStar MS4640B vector network analyzer.

## 3. Results and discussion

The phase composition of the obtained samples of nickel-zinc ferrite was studied by powder X-ray diffractometry (PXRD), the results of which are shown in Fig. 1. The data obtained indicate that the initial pre-ceramic powder and the ceramics obtained on its basis are single-phase samples of  $\text{Ni}_{0.4}\text{Zn}_{0.6}\text{Fe}_2\text{O}_4$  (JCPDS # 08-0234) without impurities. The most intense reflections are observed in the sample sintered at a temperature of 1100 °C for 16 hours, while the intensity of the peaks of the sample obtained at 1000 °C is slightly lower. The crystallite size of the initial powder was found using the Scherrer formula and was  $47 \pm 5 \text{ nm}$ . Besides, using the internal standard (Si) according to the Rietveld method, the degree of crystallinity of the initial sample was estimated to be 94%.

Figure 2 shows the SEM micrographs of the initial nanostructured powder and sintered ceramic. According to the data obtained, the morphology of the initial sample of nickel-zinc ferrite is a typical picture of the products of glycine-nitrate combustion at a stoichiometric ratio of glycine to nitrate-groups. Such porous agglomerates with a large number of micron and submicron pores formed during abundant gas evolution during the combustion process are often observed during the formation of other complex oxide systems [12, 17]. It should be noted that such a morphology complicates the process of pressing and sintering the powder, which is solved by grinding the starting material in a vibrating mill, as a result of which the formed agglomerates are broken into smaller components. The data obtained show that the microstructure of the obtained ceramics significantly depends on the selected sintering temperature regimes. In the case of a sample sintered at a temperature of 1000 °C, a large number of voids between grains are observed, the size of which is in the submicron range (the average size is in the range from 0.8 to 1.3 microns). Despite the small grain size, the presence of voids significantly worsens both the magnetic and electromagnetic parameters of ceramics, which means that this temperature regime cannot be considered as optimal for sintering pre-ceramic powders obtained under conditions of solution combustion. Nevertheless, the sample sintered at a temperature of 1100 °C demonstrates a completely different microstructure from the first sample. Despite a significant increase in the grain

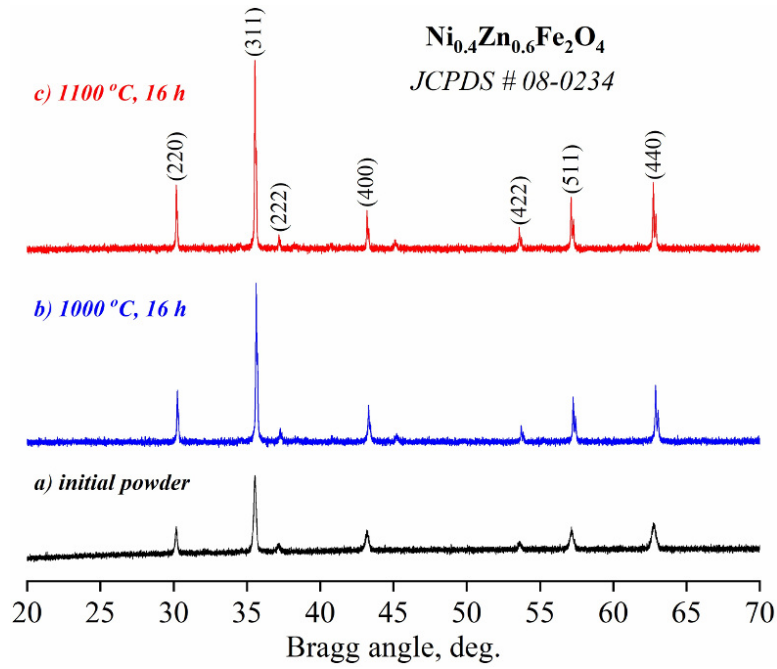


FIG. 1. PXRD patterns of the initial powder and sintered ceramics of nickel-zinc ferrite

size, which lies in the range from 1 to 3.5  $\mu m$ , there is also a significant decrease in the number of voids between the grains, which in turn affects the quality and stability of the magnetic and electromagnetic characteristics.

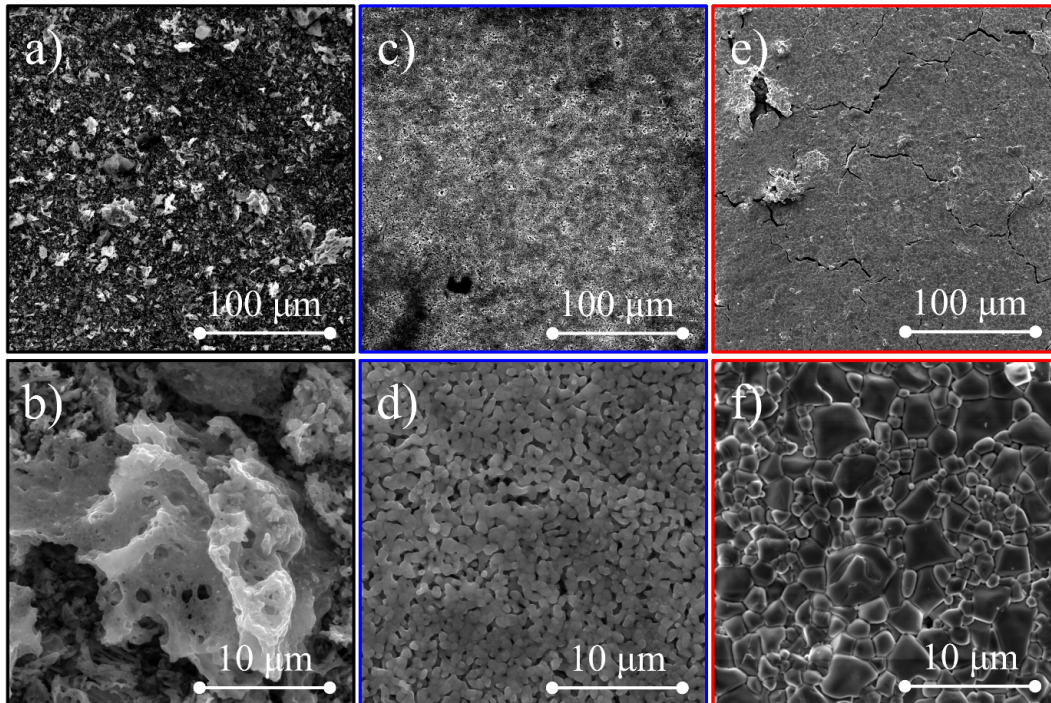


FIG. 2. SEM images of initial nickel-zinc ferrite powder obtained via glycine-nitrate combustion method (a,b) and ceramics based on them sintered at 1000 °C (c,d) and 1100 °C (e,f)

The hysteresis loops of samples of the initial powder and sintered  $Ni_{0.4}Zn_{0.6}Fe_2O_4$  ceramics are shown in Fig. 3. It follows from the data obtained that the highest values of the magnetic parameters ( $H_c = 16.32$  Oe,  $M_s = 78.42$  emu/g,  $M_r = 3.39$  emu/g) are observed in the sample sintered at a temperature of 1100°, which is due to

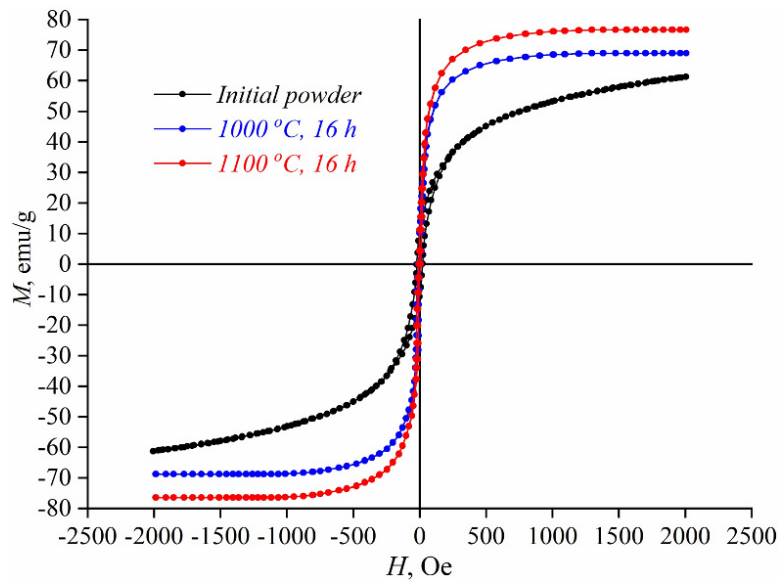


FIG. 3. Hysteresis loops of  $\text{Ni}_{0.4}\text{Zn}_{0.6}\text{Fe}_2\text{O}_4$  initial powder and sintered ceramics

the peculiarity of its microstructure. It should be noted that the appearance of the loops is similar for both sintered specimens and differs in the values of saturation magnetization, remanent magnetization and coercive force (Fig. 4).

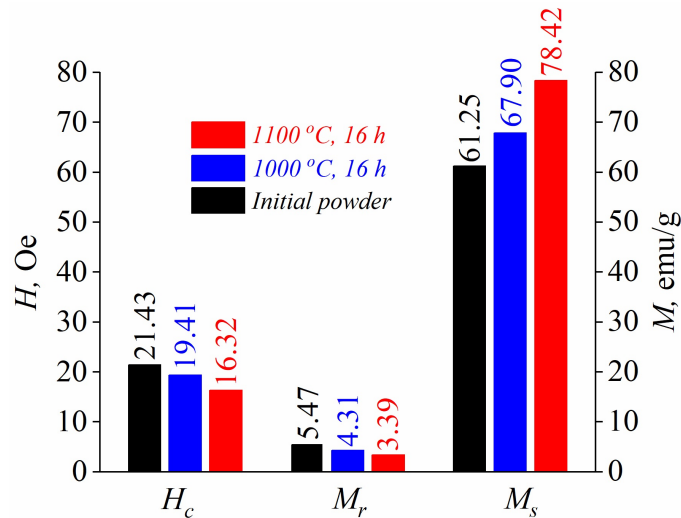


FIG. 4. Magnetic characteristics of obtained nickel-zinc ferrite samples

Figure 5 shows the curves of electromagnetic absorption for two sintered samples of nickel-zinc ferrite. The measurement was carried out on a composite obtained by dispersing the crushed ceramic in an acrylic copolymer varnish. The black curves in both figures are air measurements and were used as a reference. It is shown that with an increase in the proportion of ferrite in the polymer matrix, a significant increase in the values of electromagnetic absorption is observed. Both samples demonstrate approximately the same absorption values, with the only exception that the sample sintered at a temperature of 1100 °C demonstrates slightly better electromagnetic characteristics. This is due to the larger grain size and fewer voids, which in turn made the grinding process more difficult. Further increase in the mass fraction of nickel-zinc ferrite was not possible due to the limits of dispersion into the initial copolymer matrix.

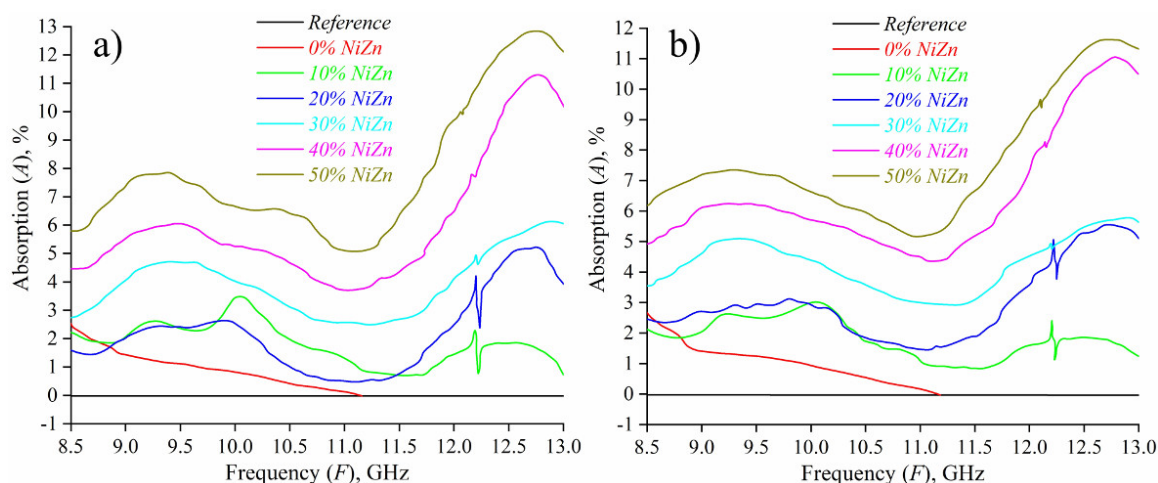


FIG. 5. Microwave absorption of Ni<sub>0.4</sub>Zn<sub>0.6</sub>Fe<sub>2</sub>O<sub>4</sub>-based polymer composites: nickel-zinc ferrite sintered at 1000 °C (a) and 1100 °C (b)

#### 4. Conclusion

Thus, a simple method was proposed for obtaining electromagnetic absorbing materials based on a copolymer matrix and ceramics of the composition Ni<sub>0.4</sub>Zn<sub>0.6</sub>Fe<sub>2</sub>O<sub>4</sub> sintered from a nanostructured pre-ceramic powder synthesized by the method of solution combustion. This approach makes it possible to disperse up to 50 weight percent of spinel ferrite into the copolymer matrix and achieve high values of electromagnetic absorption. It has been shown that the most optimal sintering mode is a temperature of 1100 °C and a holding time of 16 hours at which it is possible to obtain soft magnetic ceramics with values of coercive force, saturation magnetization and remanent magnetization equal to 16.32 Oe, 3.39 emu/g and 78.42 emu/g, respectively.

#### Acknowledgments

The reported study was funded by RFBR, project number 20-03-00976.

#### References

- [1] Wang X., Cao S., Wang Y., Yuan S., Kang B., Wu A., Zhang J. Crystal growth and characterization of the rare earth orthoferrite PrFeO<sub>3</sub>. *Journal of Crystal Growth*, 2013, **362**, P. 216–219.
- [2] Martinson K.D., Ivanov V.A., Chebanenko M.I., Panchuk V.V., Semenov V.G., Popkov V.I. Facile combustion synthesis of TbFeO<sub>3</sub> nanocrystals with hexagonal and orthorhombic structure. *Nanosystems: Physics, Chemistry, Mathematics*, 2019, **10**, P. 694–700.
- [3] Valenzuela R. Novel applications of ferrites. *Physics Research International*, 2012, **2012**, P. 2090–2220.
- [4] Namai A., Yoshikiyo M., Yamada K., Sakurai S., Goto T., Yoshida T., Miyazaki M., Nakajima M., Suemoto T., Tokoro H., Ohsoshi S. Hard magnetic ferrite with a gigantic coercivity and high-frequency millimeter-wave rotation. *Nature communications*, 2012, **3**, P. 1035.
- [5] Dyachenko S.V., Vaseshenkova M.A., Martinson K.D., Cherepkova I.A., Zhernovoi A.I. Synthesis and properties of magnetic fluids produced on the basis of magnetite particles. *Russian Journal of Applied Chemistry*, 2016, **89**, P. 690–696.
- [6] Sutka A., Gross K.A. Spinel ferrite oxide semiconductor gas sensors. *Sensors and Actuators B: Chemical*, 2016, **222**, P. 95–105.
- [7] Martinson K.D., Kozyritskaya S.S., Pantelev I.B., Popkov V.I. Low coercivity microwave ceramics based on LiZnMn ferrite synthesized via glycine-nitrate combustion. *Nanosystems: Physics, Chemistry, Mathematics*, 2019, **10**, P. 313–317.
- [8] Camacho-Gonzalez M.A., Quezada-Cruz M., Ceron-Montes G.I., Ramirez-Ayala M.F., Hernandez-Cruz L.E., Garrido-Hernandez A. Synthesis and characterization of magnetic zinc-copper ferrites: antibacterial activity, photodegradation study and heavy metals removal evaluation. *Materials Chemistry and Physics*, 2019, **236**, P. 121808.
- [9] Hankiewicz J.H., Stoll J.A., Stroud J., Davidson J., Livesey K.L., Tvrđy K., Roshko A., Russek S.E., Stupic K., Bilski P., Campley R.E., Celinski Z.J. Nano-sized ferrite particles for magnetic resonance imaging thermometry. *Journal of Magnetism and Magnetic Materials*, 2019, **469**, P. 550–557.
- [10] Kondrashkova I.S., Martinson K.D., Zakharova N.V., Popkov V.I. Synthesis of nanocrystalline HoFeO<sub>3</sub> photocatalyst via heat treatment of products of glycine-nitrate combustion. *Russian Journal of General Chemistry*, 2018, **88**, P. 2465–2471.
- [11] Kefeni K.K., Mamba B.B., Msagati T.A.M. Application of spinel ferrite nanoparticles in water and wastewater treatment: a review. *Separation and Purification Technology*, 2017, **188**, P. 399–422.
- [12] Martinson K.D., Kondrashkova I.S., Omarov S.O., Sladkovskiy D.A., Kiselev A.S., Kiseleva T.Yu., Popkov V.I. Magnetically recoverable catalyst based on porous nanocrystalline HoFeO<sub>3</sub> for process of n-hexane conversion. *Advanced Powder Technology*, 2020, **31**, P. 402–408.
- [13] Albuquerque A.S., Tolentino M.V.C., Ardisson J.D., Moura F.C.C., Mendonca R., Macebo W.A.A. Nanostructured ferrites: structural analysis and catalytic activity. *Ceramics International*, 2012, **38**, P. 2225–2231.
- [14] Trif L., Molnar-Voros N., Tolnai G., Sajo I., Meszaros S., Kalman E. Preparation and characterization of nanostructured ferrite materials by a nitrate-citrate self-combustion sol-gel synthesis. *Materials Science Forum*, 2008, **589**, P. 167–172.

- [15] Nam J.-H., Park S. J., Kim W.K. Microstructure and magnetic properties of nanostructured NiZnCu ferrite powders synthesized by sol-gel process. *IEEE Transactions on Magnetics*, 2003, **39**, P. 3139–3141.
- [16] Fantauzzi M., Secci F., Angotzi M.S., Passiu C., Cannas C., Rossi A. Nanostructured spinel cobalt ferrites: Fe and Co chemical state, cation distribution and size effects by X-ray photoelectron spectroscopy. *RSC Advances*, 2019, **9**, P. 19171.
- [17] Martinson K.D., Ivanov A.A., Pantelev I.B., Popkov V.I. Pre-ceramic nanostructured LiZnMn-ferrite powders: synthesis, structure, and electromagnetic properties. *Glass and Ceramics*, 2020, **77**, P. 215–220.
- [18] Monteiro E.S., Kasal R.B., Moraes N.C., Melo J.C.A. Santos J.C.A., Figueiredo A. B.-H. S., Nanoparticles of  $Ni_{1-x}Zn_xFe_2O_4$  used as microwave absorbers in the x-band. *Materials Research*, 2019, **22**, P. 20190188.
- [19] Yusoff A.N., Abdullah M.H. Microwave electromagnetic and absorption properties of some LiZn ferrites. *Journal of Magnetism and Magnetic Materials*, 2004, **269**, P. 271–280.
- [20] Dosoudil R., Usakova M., Franek J., Slama J., Olah V. RF electromagnetic wave adsorbing properties of ferrite polymer composite materials. *Journal of Magnetism and Magnetic Materials*, 2006, **304**, P. 755–757.
- [21] Zhao T., Hou C., Zhang H., Zhu R., She S., Wang J., Li T., Liu Z., Wei B. Electromagnetic wave absorbing properties of amorphous carbon nanotubes. *Scientific Reports*, 2014, **4**, P. 5619.
- [22] Biswas S., Arief I., Panja S.S., Bose S. Absorption-dominated electromagnetic wave suppressor derived from ferrite-doped cross-linked graphene framework and conducting carbon. *ACS Applied Materials and Interfaces*, 2017, **9**, P. 3030–3039.
- [23] Priyadharsini P., Pradeep A., Rao P.S., Chandrasekaran G. Structural, spectroscopic and magnetic study of nanocrystalline Ni-Zn ferrites. *Materials Chemistry and Physics*, 2009, **116**, P. 207–213.
- [24] Oka H., Tanaka K., Osada H., Kubota K., Dawson F.P. Study of electromagnetic wave absorption characteristics and component parameters of laminated-type magnetic wood with stainless steel and ferrite powder for use as building materials. *Journal of Applied Physics*, 2009, **105**, P. 07E701.
- [25] Martinson K.D., Cherepkova I.A., Pantelev I.B., Popkov V.I. Single-step solution combustion synthesis of magnetically soft  $NiFe_2O_4$  nanopowders with controllable parameters. *International Journal of Self-Propagating High-Temperature Synthesis*, 2019, **28**, P. 266–270.
- [26] Bharati V.A., Patade S.R., Bajaj S., Parlikar R., Keche A.P. Sondur V.V. Structural and magnetic properties of nickel ferrite nanoparticles prepared by solution combustion method. *Journal of Physics: Conference Series*, 2020, **1644**, P. 012005.
- [27] Ortiz-Quinonez J.-L., Pal U., Villanueva M.S. Structural, magnetic, and catalytic evaluation of spinel Co, Ni, and Co-Ni ferrite nanoparticles fabricated by low-temperature solution combustion process. *ACS Omega*, 2018, **3**, P. 14986–15001.
- [28] Minin R.V., Zhuravlev V.A., Lapshin O.V., Itin V.I. Svetlichnyi V.A. Nanocrystalline cobalt ferrite powders by spray solution combustion synthesis. *International Journal of Self-Propagating High-Temperature Synthesis*, 2020, **29**, P. 1–9.
- [29] Martinson K.D., Pantelev I.B., Shevchik A.P., Popkov V.I. Effect of Red/Ox ratio on the structure and magnetic behavior of  $Li_{0.5}Fe_{2.5}O_4$  nanocrystals synthesized by solution combustion approach. *Letters on Materials*, 2019, **4**, P. 475–479.
- [30] Popkov V.I., Almjashaeva O.V., Gusarov V.V. The Investigation of the Structure Control Possibility of Nanocrystalline Yttrium Orthoferrite in Its Synthesis from Amorphous Powders. *Russian Journal of Applied Chemistry*, 2014, **87**(10), P. 1417–1421.
- [31] Popkov V.I., Almjashaeva O.V., Schmidt M.P., Izotova S.G., Gusarov V.V. Features of Nanosized  $YFeO_3$  Formation under Heat Treatment of Glycine-Nitrate Combustion Products. *Russian Journal of Inorganic Chemistry*, 2015, **60**(10), P. 1193–1198.

## Synthesis and comparative photocatalytic activity of CuO layers on SiO<sub>2</sub> substrates

E. V. Polyakov, R. R. Tzukanov, I. V. Volkov, L. Yu. Buldakova, I. V. Baklanova, O. A. Lipina, V. P. Zhukov, Yu. V. Kuznetsova, A. P. Tutunnik, M. A. Maximova

Institute of Solid State Chemistry UB RAS, 91, Pervomaiskaya str.,  
Ekaterinburg, 620990, Russian Federation  
polyakov@ihim.uran.ru

PACS 81.15.-z; 78.20.-e

DOI 10.17586/2220-8054-2020-11-5-601-607

Using the thermodynamic and kinetic approaches, it was found that  $\text{Cu}(\text{NH}_3)_4^{2+}$  complex predominating at 23°C spontaneously decomposes at elevated temperatures, forming CuO precipitate in a bulk solution and a layer (CuO|SiO<sub>2</sub>) on the surface of silica glass. The rates of these heterogeneous processes are fairly well described by the 1st-order reaction of decay of the  $\text{Cu}(\text{NH}_3)_4^{2+}$  complex. The formation of the CuO precipitate and layer is a two-step kinetic process. The rate of precipitate formation dominates above 65 °C while the rate of the layer formation prevails below this value. The CuO|SiO<sub>2</sub> material synthesized below 65° possesses an optical bandgap of (1.25±0.05) eV, which is smaller compared to the crystals of commercial CuO. The CuO|SiO<sub>2</sub> material displays a photocatalytic activity in the reaction of UV-decomposition of benzoquinone-hydroquinone. It was discovered that the photocatalytic activity depends on the thickness of the photocatalyst layer.

**Keywords:** Copper(II), oxide, layer, glass, surface, kinetics, photocatalyst.

*Received: 18 September 2020*

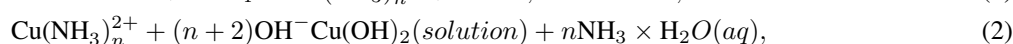
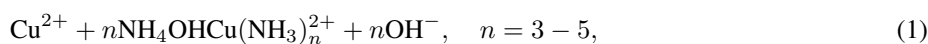
### 1. Introduction

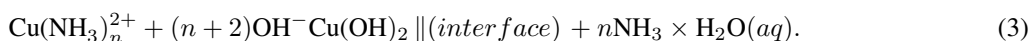
A low efficiency of applied light utilization is considered to be the main drawback of powder photocatalysts. It can be improved by fixing micro- and nanoparticles of active material on substrates in the form of films and layers [1–3]. The properties of film photocatalysts depend on the accessibility of their surface for radiation, the morphology and size of surface particles and, consequently, on the conditions of synthesis. Among promising photocatalysts, CuO stands out as a *p*-type semiconductor with an optical gap width 1.21–1.51 eV that makes it active in the UV and visible spectral regions [4, 5]. CuO films allow utilization of up to 30% of incident light energy, which is much more compared to Cu<sub>2</sub>O [6]. Synthesis of CuO layers in solutions [6–8] is a multistage process with the use of a solid-phase precursor Cu(OH)<sub>2</sub>. The more simple and convenient method is the thermal decomposition of ammonia complexes of Cu(II) [9]. This unites the formation of primary CuO particles, their isolation and growth at the interface. The application of this method for the synthesis of photomaterials is restrained by the lack of information concerning synthesis conditions and the photocatalytic activity of produced CuO layers. The aim of present study was to invent a single-stage hydrochemical method for the production of CuO photocatalyst layers with optimal mass (thickness) on glass substrates by the thermal decomposition of ammonia complexes of Cu(II) in the conditions excluding the formation of Cu<sub>2</sub>O.

### 2. Experimental work

Layer formation was studied by Dynamic Light Scattering (DLS) and Laser Doppler Electrophoresis measurements carried out on a Zetasizer Nano ZS particle analyzer (Malvern Panalytical Ltd.). The Raman spectral analysis of the samples was performed at room temperature using an inVia Reflex Renishaw spectrometer ( $\lambda = 532$  nm, P=25 mW). The phase analysis of the products was fulfilled on a STADI-P X-ray powder automatic diffractometer (STOE) with  $\text{CuK}\alpha 1$  radiation using the library of X-ray diffraction data PDF-2 (ICDD Release 2009). The morphology of the layers on substrate was studied using the scanning electron microscopy (SEM) and EDX elemental analysis on a JSM JEOL 6390LA facility. UV-visible absorption spectroscopy was performed using a Shimadzu UV-3101PC UV/Vis/Near-IR Spectrophotometer. The diffuse reflectance spectra of the layers were recorded in the interval of 220–800 nm by means of a Shimadzu UV-3600 UV-vis-NIR spectrophotometer using BaSO<sub>4</sub> crystals as a reference.

The thermodynamic study of the temperature evolution of CuO-Cu(OH)<sub>2</sub> phases in pH – Eh – temperature coordinates was carried out to choose the conditions of CuO formation in the bulk of electrolytic solution. The study was made for all known to date valence forms of copper. The HSC Chemistry v.8 program was used for the following equations (1–3):



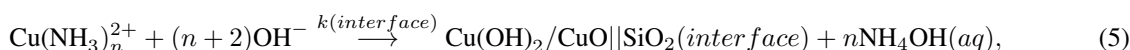


The symbol “ $\parallel(\text{interface})$ ” denotes the “solution – solid” interface. The pH-fields of predominance of 29 components including  $\text{Cu}^0$ ,  $\text{CuO}$ ,  $\text{Cu}_2\text{O}$ ,  $\text{Cu}(\text{OH})_2$  phases,  $\text{Cu}(\text{I,II,III})$  aqua-ions, their hydroxo-, mono- and dimeric ammonia complexes were determined as the function of a temperature. This allowed us to find the conditions for the spontaneous decomposition of  $\text{Cu}(\text{NH}_3)_n^{2+}$  complexes which predominate in the reaction mixture at 23°. Thus, the complexes decompose at the temperature from 35 to 95° and pH from 11.0 to 12.0 with the generation of  $\text{Cu}(\text{OH})_2$  and  $\text{CuO}$  phases.

### 3. Results and discussion

#### 3.1. Kinetics of CuO layers growth

According to the thermodynamic estimation by means of HSC Chemistry 8,  $\text{Cu}(\text{OH})_2$  to  $\text{CuO}$  transition in an  $\text{Ar}(\text{g})$  atmosphere occurs at 150°. Under aerobic conditions, this decomposition takes place at 40–80° [8]. Hence, it is possible to control the solid phase precipitation rate in the bulk of solution and at the solution $\parallel$  solid interface by choosing the synthesis conditions (temperature, solution chemistry and rate of solid phase formation) [9]. The search for synthesis conditions of  $\text{CuO}\parallel\text{SiO}_2$  layers on the inner surface of the quartz reactor ( $\text{SiO}_2$ ) was carried out in 50 ml quartz vials filled with 25 ml 0.02–0.3 M copper(II) amine solution,  $C(\text{Cu})$ , with free ammonia concentration in the range of 0.4–4.0 M at thermostat temperature up to 95°. The synthesis took place according to reactions:



$$\frac{dC(\text{Cu})}{dt} = -k(\text{bulk}, \text{interface})C(\text{Cu}). \quad (6)$$

According to SEM, the produced  $\text{CuO}\parallel\text{SiO}_2$  layers consist of bundles of elongated particles having a form of nano-sheets. They first partially fill the surface of the glass and then grow normally to the surface. Fig. 1 shows that  $\text{CuO}$  particles anchored on the glass surface form an openwork layer in which particles alternate with uncovered glass “windows”. The DLS data show that the colloidal  $\text{CuO}$  particles growing in the solution maintain a  $\xi$ -potential of  $-18.2 \pm 26.3$  mV throughout the synthesis, which indicates non-stable colloid solutions. In the initial 3–5 min period, the colloid particles have the hydrodynamic diameter of 90–100 nm and predominate in the solution. At the same time, the mean size of  $\text{CuO}$  particles anchored to the  $\text{CuO}\parallel\text{SiO}_2$  interphase keeps at the level of 280–290 nm. When the initial period ends, the size of  $\text{CuO}$  particles rises dramatically reaching the value of 1200 nm in the solution and 700–750 nm in the layer after 10–15 min synthesis, Fig. 2. The kinetic coefficients of direct reactions (4–6) were determined experimentally. For this purpose, the variation with time of the copper content in solution (I), on the inner surface of vial (II) and in the precipitate after removal of copper by filtration (III) was analyzed using the mass spectrometry method (Elan 9000), Fig. 3. The characteristics of the compositions were fairly well confirmed by means of spectroscopy and X-ray diffraction analysis (XDA). The Raman spectrum of composition (II) contains vibrational modes of  $\text{CuO}$ :  $282 \text{ cm}^{-1}$  ( $A_g$ ),  $332 \text{ cm}^{-1}$  and  $616 \text{ cm}^{-1}$  ( $B_g$ ) [4]. For composition (III), the vibrational modes of  $\text{CuO}$  are shifted relative to (II):  $303 \text{ cm}^{-1}$  ( $A_g$ ),  $350 \text{ cm}^{-1}$  and  $636 \text{ cm}^{-1}$  ( $B_g$ ) [11]. The XDA reflections of compositions (II) and (III) are identical to those of  $\text{CuO}$  phase: space group  $C12/c1$ , lattice parameters  $a = 4.6804$ ,  $b = 3.4337$ ,  $c = 5.1164$ ,  $\alpha = 90.0000$ ,  $\beta = 99.1329$ ,  $\gamma = 90.0000$ . The X-ray density of  $\text{CuO}$  in the layer is  $6.490 \text{ g/cm}^3$  and the mean crystallite size, calculated using the Scherrer equation, is 27.1–27.9 nm.

The least squares method was applied to estimate the coefficients of formation rate (6) in the bulk,  $k(\text{bulk})$ , and at the solution-glass interface,  $k(\text{interface})$ , at 23–85°. The data obtained allowed us to identify the temperature region (below 65°), in which the reaction (4) of the layer growth predominates (Fig. 3, marked by arrow). Thus, the series of  $\text{CuO}\parallel\text{SiO}_2$  materials with different  $\text{CuO}$  layer thickness were synthesized on the surface of glass and used in further photocatalytic measurements. The synthesis conditions to achieve optimal degree (60–80%) of copper(II) ions transformed into oxide were chosen as follows: 35–65° temperature interval, 15–60 min synthesis time. The photocatalytic effectiveness of studied materials is demonstrated by the UV-visible diffuse reflectance spectroscopy data. The results show that the optical bandgap  $E(\text{eV})$  calculated by means of the Kubelka-Munk equation for a direct transition in  $\text{CuO}$  crystals (see [10–12]) is equal to  $1.25 \pm 0.05 \text{ eV}$  for the  $\text{CuO}\parallel\text{SiO}_2$  materials, whereas for commercial  $\text{CuO}$  it is around  $1.50 \pm 0.05 \text{ eV}$  [13]. The absence of the  $\text{Cu}_2\text{O}$  phase in the layers was additionally confirmed by the voltammetry method [14] using the discussed copper(II) oxide layer deposited on the surface of Ni-foil electrode.

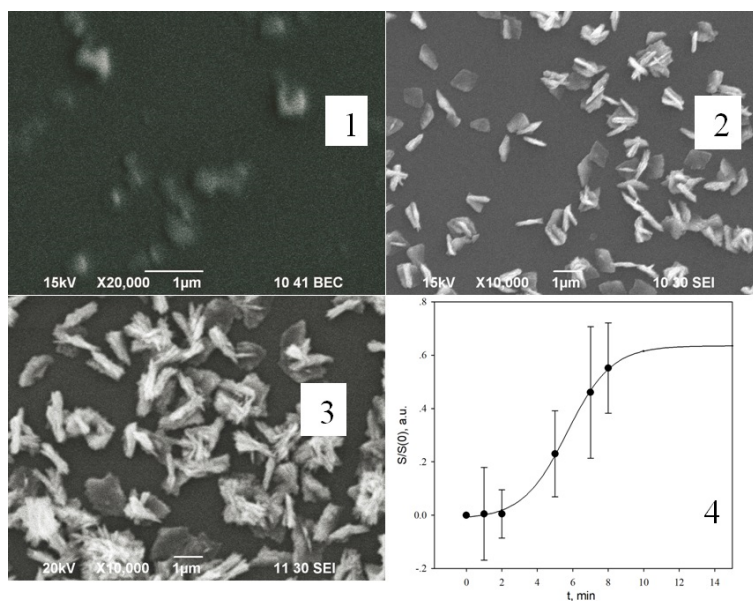


FIG. 1. Size and morphology of CuO particles forming a layer on the surface of quartz vial ( $\text{CuO}||\text{SiO}_2$ ) at different times of synthesis: 1 – 0.5 min; 2 – 3 min; 3 – 5 min. Panel 4: variation of relative coverage  $S/S(0)$  of  $\text{SiO}_2$  surface with CuO particles as a function of reaction time  $t$ .  $S$  – surface of SEM image of quartz vial covered with CuO particles ( $\mu\text{m}^2$ ),  $S(0)$  – total surface of the same image ( $\mu\text{m}^2$ ). Temperature of synthesis is  $85^\circ\text{C}$

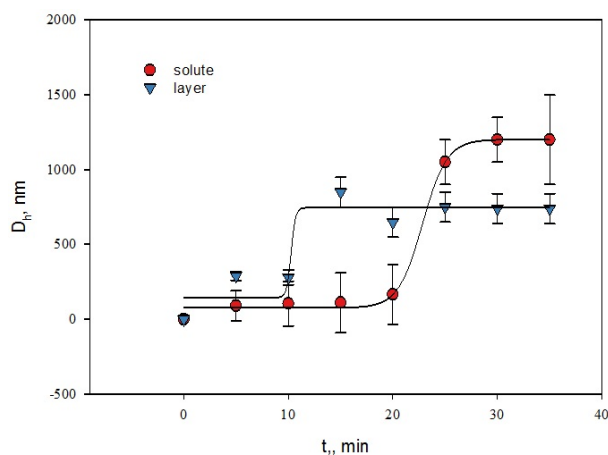


FIG. 2. Variation of CuO particles diameter ( $D_h$ ) in bulk solution (solute) and in the interface solution||layer (layer) during  $\text{Cu}(\text{NH}_3)_4^{2+}$  ion particles deposition acquired with the help of dynamic light scattering and laser Doppler electrophoresis measurements.  $85^\circ\text{C}$

### 3.2. Photocatalytic activity of CuO layers on the silica glass

The photocatalytic activity of synthesized CuO layers of different thickness on the inner surface of quartz reactor walls was analyzed under the UV irradiation in the reaction of the decomposition of the electrochemically reversible pair of benzoquinone–hydroquinone, BQ-HQ. For this purpose, 25 ml BQ-HQ solution with initial concentration  $C_s^0 = 0.1 \text{ mM}$  at  $\text{pH} = 6.8$ ,  $22^\circ$  was poured into quartz vials lined with CuO. A UV lamp was mounted above the reactor so that the UV-irradiation propagated from top to the bottom of reactor both through the “solution-air” interface (UV-light flow F1) and through the “ $\text{CuO}||\text{SiO}_2$  – solution” interface (UV-light flow F2) [15]. The scheme of the interaction of UV-light flows F1, F2 with thin (A) and thick (B) layers of CuO is depicted in Fig. 4a,b. Before each experiment, the BQ-HQ solution was contacting with CuO layer for a time needed to reach equilibrium absorption of BQ-HQ on the surface of the photocatalyst. The experiments have shown that adsorption equilibrium state was reached in 25–30 minutes. After that each of the quartz reactors was irradiated with UV light of the wavelength  $\lambda(\text{max}) = 253 \text{ nm}$

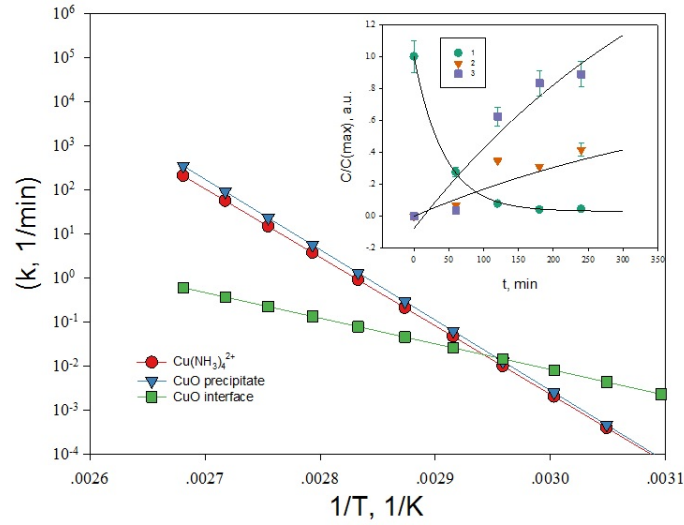


FIG. 3. Temperature dependence of kinetic coefficients of eq. 6 which describe solid phase formation according to 1st order reactions (4–5), calculated from experimental data (inset).  $T$  is the temperature of thermo-decay. On the inset the examples are shown of the kinetics of  $\text{Cu}(\text{NH}_3)_4^{2+}$  thermo-decay in  $\text{NH}_4\text{OH}$  solution as a functions of contacting time. Initial  $\text{Cu}(\text{II})$  concentration in the solution  $C(\text{max}) = 0.02$  M,  $\text{pH} = 11.3$ ,  $70^\circ\text{C}$ , volume of solution = 25 ml. Concentration in the phases (M units) is calculated as a ratio of Cu mass in the phase to the volume of solution; 1 – in solution, 2 – in precipitate, 3 – in vial coating. Solid lines represent the least square curve fit of the data in accordance with simple 1st-order decay/formation model. An arrow points out the temperature  $65^\circ$

(4.9 eV) using the technique described elsewhere [15]. The substrate concentration variation ( $C_s$ ) with irradiation time ( $t$ ) in the series of experiments with the CuO layers of a different thickness is found (see Fig. 4c) to obey the 1st-order decay reaction equation (6):

$$\begin{aligned} (BQ - HQ) + h\nu &\xrightarrow{k} \text{products}, \\ dC_s/dt &= -k_s C_s \end{aligned} \quad (7)$$

In eq. (7),  $k_s$  is the rate constant, which depends on the quantum yield of the photocatalytic reaction. The geometric thickness of the layers ( $L$ , nm) was determined by EDX analysis of  $\text{CuO}||\text{SiO}_2$  composites on a JSM JEOL 6390LA facility. The experimental correlation between the relative rate constant  $k_s/k_s(\text{max})$  and  $L$ , where  $k_s(\text{max})$  is the maximal value of constant ( $k_s$ ) in the series of layered photocatalysts, is shown in Fig. 5. It is seen that  $k_s/k_s(\text{max})$  keeps the maximal value in the series of rather thin CuO layers with  $L < 1000$  nm. This conforms to the results of quantum-chemical simulation of UV radiation absorption by monocrystalline CuO, which we performed with the use of the VASP program [16], Fig. 6. The calculated variation in the relative light transmission  $I(L_c)/I(0)$  of UV radiation as a function of the light path length in the catalyst crystal ( $L_c$ ) strongly depends on the radiation energy ( $E$ ). The calculated data show that 99% of UV-radiation with  $E > 3.5$  eV are absorbed within the thin CuO crystal layer with  $L_c \sim 80\text{--}100$  nm. Since the thickness of sheet-like bundles of CuO particles is  $\sim 200\text{--}250$  nm, Fig. 1, one can conclude that all photon energy of UV-light are absorbed by CuO sheet-like particles of the  $\text{CuO}||\text{SiO}_2$  photocatalyst independently of its thickness. Nevertheless, when the experimental layer thickness  $L$  increases, the  $k_s/k_s(\text{max})$  value decreases to a constant level, which is characteristic of micro-sized particles of CuO. To understand this phenomenon, the UV-light flow geometry and the morphology of CuO layers growing on the glass support were taken into consideration. In accordance with experimental conditions, there were two components of general UV irradiation flow, Fig. 4a,b. Fraction F1 of the flow kept a constant intensity since it passed through air/solution interface which was free of the colloid particles and CuO layer. Fraction F2 of the flow passed through the side walls of the quartz vial. As a result, its intensity depended on the thickness and transparency of the growing layer. Fig. 1 shows that the layers of CuO photocatalyst have openwork morphology. This implies that the rather small thickness of layer leads to the formation of “windows” in the silica glass. These regions of the substrate are not covered with CuO particles and freely transmit UV irradiation which scatters on and interact with the CuO nano-sheets surface. When the thickness of photocatalyst layer reaches a rather large value  $L(\text{max})$ , the surface of “windows” diminishes and the

UV-light flow F2 attains its minimal (or zero) value. In the framework of this interpretation, the value of  $L(\max)$  is about  $10^4$  nm. The frontier divided these two regions is shown in Fig. 5.

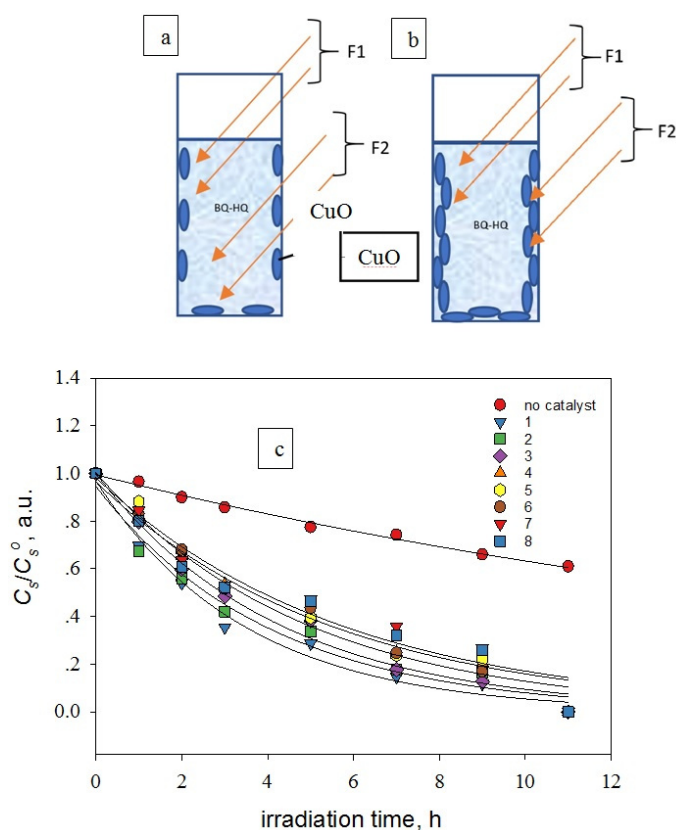


FIG. 4. Photocatalytic decomposition of 0.1 mM solution of BQ-HQ on the layers of catalyst CuO deposited on the vials inner surface as a function of irradiation time. (a, b) – the schemes of UV-irradiation of CuO on the surface of vials in the case of thin (a) and thick (b) layers. (c) – Decomposition of substrate under UV light as a function of irradiation time. Numbers near the pointers are for the catalyst layers thickness (nm): 1 – 1500, 2 – 1650, 3 – 6020, 4 – 9400, 5 – 12700, 6 – 14600, 7 – 17900, 8 – 24800. Volume of substrate solution is 25 ml, measurements at 22 °C, UV light energy – 4.90 eV. Solid lines are the best fit approximation of the substrate decomposition in accordance with eq. (6). The surface area of the glass support in each sample was constant and equal to 4.2 cm<sup>2</sup>

#### 4. Conclusion

Thus, using thermodynamic and kinetic approaches, it was found that the  $\text{Cu}(\text{NH}_3)_4^{2+}$  complex predominating at 23° spontaneously decomposes at elevated temperature with the deposition of CuO phase in the form of the precipitate in a bulk solution and layer on the surface of silica glass ( $\text{CuO}||\text{SiO}_2$ ). The rates of these heterogeneous processes are described by the 1st-order reaction of the decay of the  $\text{Cu}(\text{NH}_3)_4^{2+}$  complex. It was found that the formation of CuO precipitate and a layer is a two-step kinetic process. The rate of precipitate formation predominates above 65° while the rate of CuO layer formation prevails below 65°.  $\text{CuO}||\text{SiO}_2$  synthesized below 65° possesses an optical bandgap of  $(1.25 \pm 0.05)$  eV which is smaller in comparison with commercially-available CuO crystals. The samples of  $\text{CuO}||\text{SiO}_2$  material display the photocatalytic activity in the reaction of UV-decomposition of benzoquinone-hydroquinone. Wherein, the activity depends on the thickness and morphology of the photocatalyst layer.

#### Acknowledgements

This study has been performed in the framework of the State research program. The calculations were carried out on the URAN cluster at the Institute of Mathematics and Mechanics of the Ural Branch of the Russian Academy of Sciences.

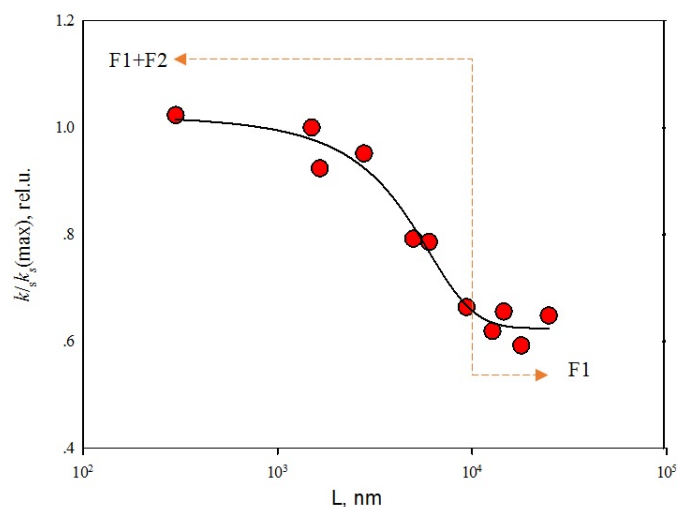


FIG. 5. Correlation between experimentally estimated rate constant of photo-degradation of substrate ( $k_s$ ) according to eq. (6) and thickness of photocatalyst CuO layer ( $L$ ) in the series of composites CuO||SiO<sub>2</sub>.  $k_s(\text{max}) = 8.20 \cdot 10^{-5}$  1/c, 22 °C. Vertical dotted line separate areas of thickness  $L$  within which the whole incident UV light flow is active ( $L < 104$  nm) or only its F1 component ( $L > 104$  nm) can penetrate through the CuO layer (see Fig. 4)

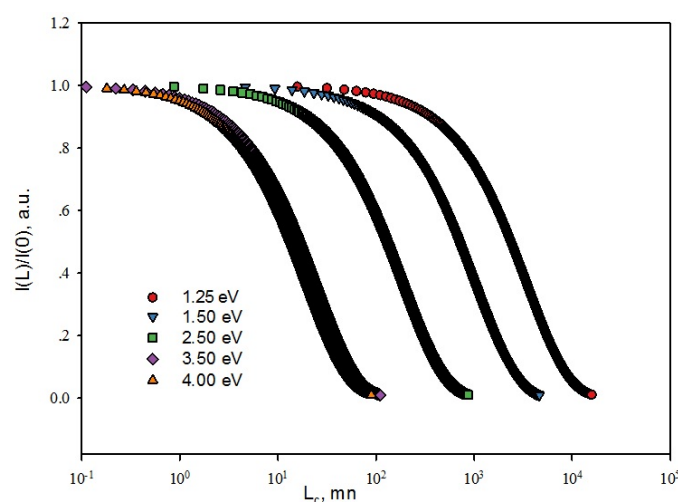


FIG. 6. The relative intensity  $I(L)/I(0)$  of light transmitted to the depth  $L_c$  in CuO with respect to the intensity at the surface  $I(0)$ , as determined by means of the VASP computer code [16]

## References

- [1] Ochiai T., Fujishima A., J. Photoelectrochemical properties of TiO<sub>2</sub> photocatalyst and its applications for environmental purification. *Journal of Photochemistry and Photobiology C: Photochemistry Reviews*, 2012, **13**, P. 247–262.
- [2] Varshney G., Kanel S.R., Kempisty D.M., Varshney V., Agrawale A., Sahle-Demessie E., Varmac R.S., Nadagouda M.N. Nanoscale TiO<sub>2</sub> films and their application in remediation of organic pollutants. *Coordination Chemistry Reviews*, 2016, **306**, P. 43–64.
- [3] Lai Ch.W., Lee K.M., Juan J.Ch. Chapter 7. Polymeric Nanocomposites for Visible-Light-Induced Photocatalysis. M.M. Khan et al. (eds.). *Nanocomposites for Visible Light-induced Photocatalysis*. Springer Series on Polymer and Composite Materials. Springer International Publishing AG, 2017.
- [4] Cheng G. Synthesis and characterisation of CuO nanorods via a hydrothermal method. *Micro and Nano Letters*, 2011, **6**, P. 774.
- [5] Tuerdi A., Abdukayum A., Chen P. Synthesis of composite photocatalyst based on the ordered mesoporous carbon-CuO nanocomplex. *Materials Letters*, 2017, **209**, P. 235–239.
- [6] Chuantian Z., Ding, Liming L. Solution-Processed Cu<sub>2</sub>O and CuO as Hole Transport Materials for Efficient Perovskite Solar Cells. *Small*, 2015, **11**, P. 5528–5532.
- [7] Kakhki R.M., Ahsani F., Mir N. Enhanced photocatalytic activity of CuO-SiO<sub>2</sub> nanocomposite based on a new Cu nanocomplex. *Journal of Materials Science: Materials in Electronics*, 2016, **27**, P. 11509–11517.

- [8] Lim Y.-F., Choi J.J., Hanrath T. Synthesis of Colloidal CuO Nanocrystals for Light-Harvesting Applications. *Journal of Nanomaterials*, 2012, **2012**, P. 1–6.
- [9] Mokrushin S.G., Kitaev G.A. Experimental investigation into laminar systems. *Kolloidnyi Zhurnal*, 1957, **19**, P. 93.
- [10] Brodie-Linder N., Audonnet F., Deschamps J., Alba-Simionesco C., Besse R., LeCaer S., Impéror-Clerc M. The key to control Cu II loading in silica based mesoporous materials. *Microporous and Mesoporous Materials*, 2010, **132**, P. 518–525.
- [11] Irwin J.C., Chzhanovski J., Wei T., Lockwood D.J., Wold A. Raman scattering from single crystals of cupric oxide. *Physica C*, 1990, **166**, P. 456–464.
- [12] Kubelka P., Munk F. An article on optics of paint layers. *Zeitschrift für technische Physik*, 1931, **12**, P. 593–609.
- [13] West A. R. *Solid State Chemistry and Its Applications*. New Jersey, Wiley, 1987, 742 p.
- [14] Polyakov E.V., Denisova T.A., Maksimova L.G., Zhuravlev N.A., Buldakova L.Yu. Hydrogen and salt forms of tin ferrocyanide as precursors of mixed ferrocyanides. *Russian Journal of Inorganic Chemistry*, 2000, **45**, P. 276–282.
- [15] Polyakov E.V., Krasilnikov V.N., Gyrdasova O.I., Buldakova L.Yu., Yanchenko M.Yu. Synthesis and photocatalytic activity of quasi-one-dimensional (1-D) solid solutions  $Ti_{1-X}MXO_{2-2X/2}$  (M(III)= Fe(III), Ce(III), Er(III), Tb(III), Eu(III), Nd(III) and Sm(III),  $0 \leq X \leq 0.1$ ). *Nanosystems: Physics, Chemistry, Mathematics*, 2014, **5**, P. 553–563.
- [16] G. Kresse, J. Furthmuller. Vasp the guide. Vasp the guide. Homepage. 2011. (<http://cms.mpi.univie.ac.at/vasp/guide/vasp.html>).

## Synthesis Ni-doped CuO nanorods via Successive Ionic Layer Deposition method and their capacitive performance

A. A. Lobinsky, M. V. Kaneva

Saint Petersburg State University, Peterhof, 198504 Saint Petersburg, Russia

lobinsky.a@gmail.com

PACS 81.07.Bc

DOI 10.17586/2220-8054-2020-11-5-608-614

In this work first described the new relatively simple approach to the synthesis of nanolayers of Ni-doped CuO via of Successive Ionic Layer Deposition (SILD) method. The study of Ni-doped CuO nanolayers, synthesized of SILD, has been carried out by HRTEM, XRD, FTIR and XPS spectroscopy methods; it was demonstrated that they had been formed of nanorods with dimensions of about 10–15 nm and tenorite crystal structure CuO were formed. The research electrochemical properties of nanolayers were carried out in 1 KOH solution by using techniques of cyclic voltammetry and galvanostatic curves method. The electrochemical study of nickel foam electrodes modified by Ni-doped CuO nanolayer prepared by 30 SILD cycles demonstrates that specific capacitance is 154 mAh/g (1240 F/g) at current density 1 A/g. Repeated cycling after 1000 charge-discharge cycles demonstrates 8% capacitance fade from the initial value, so such electrodes may be used as effective electroactive materials for alkaline battery and pseudocapacitors.

**Keywords:** copper oxide, nanocrystal, nanorods, successive ionic layer deposition, electrode materials, alkaline battery.

*Received: 10 October 2020*

### 1. Introduction

As is known, the key role of increase the effectiveness of energy storage devices consist is to create new electrode materials with high energy density and long cycle life [1, 2]. From that point of view are of great interest use available oxides and oxyhydroxides of transition metals. These oxides and oxyhydroxides compete with noble metals ( $\text{RuO}_2$ ), used by electroactive materials in pseudocapacitor. Such materials are environmentally friendly, low cost and at the same time have high specific energy values. Usually, among all oxides and oxyhydroxides, cobalt oxides [3], nickel oxides [4], manganese oxides [5] and iron oxides [6] are used most frequently. However, recent research shows that the most effective electroactive capacity materials should have high intrinsic conductivity and must have a developed morphology of specific shape, which should provide, on the one hand, high specific surface area and, on the other, provide fast diffusion of ions on the surface of the electrode [7].

Recently, copper oxide nanoparticles have been studied as electroactive materials for energy storage devices, as this is one of the oxides with high conductivity and unique morphology [8–11]. In those papers, methods of chemical and electrochemical deposition from solutions have been used for the synthesis of such nanoparticles. It is worth noticing that previously CuO nanolayers on the metal surface have been obtained via the SILD method (also called SILAR [12]) to form effective electrodes for supercapacitors. This method is based on the successive and repeated adsorption on the surface of the cations and anions substrate, which interact and give a nanolayer of an insoluble compound. The SILD method has great potential for practical use to form nanolayers on the surface of the products of complex shapes and has been used earlier, for example, for the synthesis of  $\text{NiO}_{1+x} \cdot n\text{H}_2\text{O}$  [13],  $\text{MnOOH}$  [14],  $\text{CoOOH}$  [15],  $\text{AgMnO}_2$  [16], Co-doped  $\text{Cu}(\text{OH})_2$  [17], CoO-NiO solid solution [18], and also Zn-Fe layered double hydroxysulfate [19, 20] which can be used as materials for electrocatalytic reforming of ethanol.

In the present paper, we report a new simple route of synthesis of Ni-doped CuO nanolayers via the SILD method. The obtained nanolayers consist of CuO, including nickel atoms, with nanorods morphology, oriented mainly perpendicular to the substrate surface. We also describe their properties as electroactive materials for the electrode of alkaline batteries and pseudocapacitors.

### 2. Experimental

As a substrate for the synthesis of CuO nanolayers  $0.3 \times 5 \times 25$  mm polycrystalline Ni plates were used, on which electrochemical experiments were performed, and also  $0.35 \times 10 \times 25$  mm single-crystal Si plates with  $\langle 100 \rangle$  orientation, were used for physical characterization. Extra pure water (Milli-Q) was used in all experiments. Si substrates were cleaned in an ultrasonic bath filled with acetone for 10 min. Then plates of Si were sequentially treated for 10 min in concentrated HF, water, 70%  $\text{HNO}_3$ , water, 0.1 M KOH and then flushed out by water. Ni plates

were treated according to the technique described in [21] for 15 min in 6 M HCl solution, then several times rinsed by water and dried on air at 120 °C for 30 min.

A solution of mixed  $\text{Cu}(\text{NH}_3)_4(\text{CH}_3\text{COO})_2$  and  $\text{Ni}(\text{NH}_3)_4(\text{CH}_3\text{COO})_2$  was prepared by dissolving dry analytical grade salts  $\text{Cu}(\text{CH}_3\text{COO})_2 \cdot n\text{H}_2\text{O}$  and  $\text{Ni}(\text{CH}_3\text{COO})_2 \cdot n\text{H}_2\text{O}$  ( $C = 0.01 \text{ M}$ ) and  $\text{NH}_4\text{CH}_3\text{COO}$  ( $C = 0.1 \text{ M}$ ) in deionized water. The pH of the solution was 9.4 and adjusted by the addition of the  $\text{NH}_4\text{OH}$  solution. The time between the preparation of solutions and synthesis was 0.5 h. For the synthesis of Ni-doped CuO nanolayers substrate plates were fixed in a holder of special home-made automatic setup and sequentially immersed for 30 s into a solution of mixed copper and nickel ammonia, then washed from excess reagent in distilled water. On the second step, plates were immersed in a solution of  $\text{H}_2\text{O}_2$  (3%, pH 9.5 adjusted by addition of KOH solution) and again washed in water (Fig. 1). This sequence corresponds to one SILD cycle, which is repeated 30 times to obtain the desired nanolayer thickness. Finished the sample was calcined on argon atmosphere at 200 °C for 30 minutes at a heating rate of 5 °C/min.

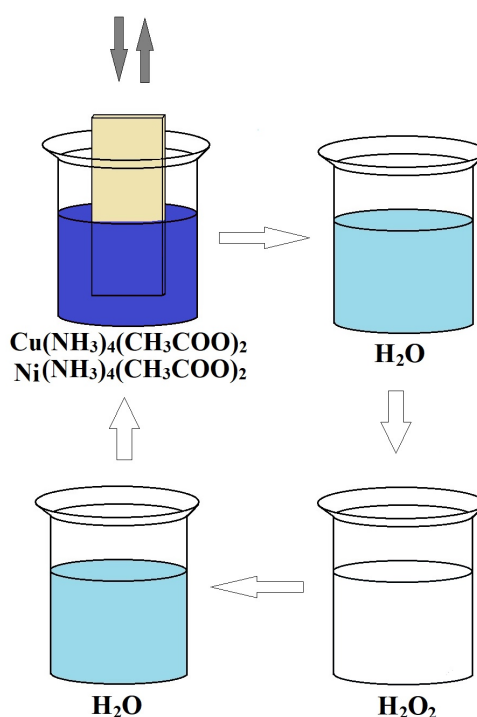


FIG. 1. Scheme of synthesis Ni-doped CuO nanolayers by SILD method

The obtained samples were characterized by HRTEM, FTIR, XPS and XRD methods. The morphology of synthesized films was investigated by HRTEM (ZeissLibra 200FE, 200 kV). FTIR transmission spectra of synthesized films on the Si surface were registered by Infracpec FSM 2201 spectrophotometer using a differential technique with respect to spectra of bare silicon plate. XRD patterns were obtained using a Bruker D8 DISCOVER X-ray diffractometer with  $\text{CuK}\alpha$  radiation in grazing incidence diffraction geometry ( $\theta = 0.3^\circ$ ). The compositional analyses of the samples were characterized by XPS (ESCALAB 250Xi electron spectrometer, with  $\text{Al K}\alpha$  radiation 14 866 eV). Hydro-chemical equilibria in solutions were estimated using the simulation program Hydra-Medusa.

The electrochemical measurements of NF electrodes with the synthesized nanolayers were carried out in a three-electrode electrochemical cell using Elins P-45X potentiostat. The working electrode was prepared by the deposition of Ni-doped CuO nanolayers on the Ni foam surface as a result of 30 treatment cycles by the SILD method. Platinum foil serves as the counter electrode and  $\text{Ag}/\text{AgCl}$  (aq. KCl sat.) as the reference electrode. Electrochemical characterization of the films was made by cyclic voltammetry (CV) and galvanostatic charge-discharge (CD) techniques.

The specific capacitance  $C$  (mAh/g) as an electrode for alkaline battery at different current densities can be calculated via eq (1):

$$C = \int \frac{I dt}{m}, \quad (1)$$

where  $I$  (mA) is a galvanostatic current,  $dt$  (h) is the discharge time of a cycle and  $m$  (g) is the mass of the active material in the film electrode [22].

Specific capacitance  $C$  (F/g) as pseudocapacitor were calculated using the following eq (2):

$$C = \frac{I\Delta t}{\Delta V m}, \quad (2)$$

where  $I$  (mA) is a galvanostatic current,  $\Delta V$  (mV) is the potential window,  $\Delta t$  (s) is the discharge time of a cycle and  $m$  (g) is the mass of the active material in the film electrode [23]. The electroactive mass of Ni-doped CuO for the working electrode was measured using an OHAUS Pioneer<sup>TM</sup> PA54C microbalance.

### 3. Result and discussion

The results of the synthesized nanolayers study via the HRTEM method (Fig. 2) demonstrate that nanolayers are formed on the surface after 30 SILD cycles. The nanolayers consist of nanocrystals with nanorods morphology and dimension about 10–15 nm.

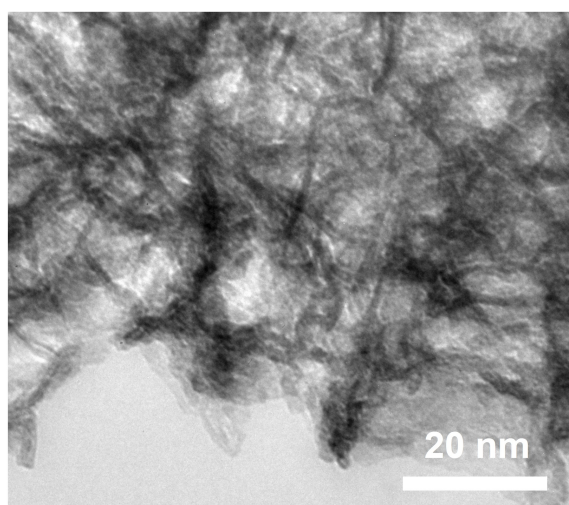


FIG. 2. HRTEM image of copper contained nanolayers

Figure 3 shows the XRD pattern of the synthesized copper contained nanolayers. The latter is in line with crystallographic planes with the orientation of (-111), (111), (-202), (020), (202), (-113) and (311), which are related to a monoclinic crystal lattice of tenorite structure CuO (JCPDS 80-1916) [24].

On the FTIR spectrum (Fig. 4) of the original sample, the broad bands at  $3400\text{ cm}^{-1}$  and  $1645\text{ cm}^{-1}$  are attributed to valence vibrations and deformation vibrations of the hydroxyl groups from  $\text{H}_2\text{O}$ , respectively [25]. The bands with peaks at  $1540\text{ cm}^{-1}$  and  $1100\text{ cm}^{-1}$  correspond to the valence vibrations of the carbonyl group of acetate contained in precursor salt [26]. The bands observed at  $530\text{ cm}^{-1}$  and  $450\text{ cm}^{-1}$  can be corresponding to Cu–O vibrations in CuO [27].

The XPS spectrum shown in Fig. 5 indicates the presence of Cu and Ni elements with the atomic ration 1.0/0.38. As shown in Fig. 5(a), two major peaks with binding energy 934.1 eV and 954.1 eV are corresponding to Cu  $2p_{3/2}$  and Cu  $2p_{1/2}$ , indicating that element Cu is the chemical state of 2+ in the sample [28]. The Ni 2p spectra (Fig. 5b) reveal the presence peaks with binding energy 855.4 eV and 872.9 eV are corresponding to Ni  $2p_{3/2}$  and Ni  $2p_{1/2}$ , and also satellites peaks, which indicate of Ni is the chemical state of 2+ and 3+ [29].

Comparison of research results, conducted via XRD, XPS and FTIR methods, allows us to conclude: obtained nanolayers consist of copper oxide, doped nickel atoms, which are likely to be included in the crystal structure CuO.

We assume that such a structure can possess interesting and practical electrochemical performance, in particular as electrode materials for power sources in the alkaline electrolyte (1M KOH). The cyclic voltammograms of the nickel foam (NF) electrode with Ni-doped CuO nanolayers were recorded in a potential window from 0 to 550 mV vs. Ag/AgCl electrode at scanning rates of 5, 10, 15 and 20 mV/s (Fig. 6). At a scan rate of 5 mV/s, two redox processes on anodic curve take place in the layer, including the  $\text{Cu}^+ \rightarrow \text{Cu}^{2+}$  transformation at 310 mV and the  $\text{Ni}^{2+} \rightarrow \text{Ni}^{3+}$  at 390 mV. The proportionality of currents to scan rate provides information that the film is thick enough, and the charge transfer rate is limited by diffusion of charge carriers in the film.

The specific capacitance of the Ni-doped CuO NF electrode is calculated from charge-discharge curves (Fig. 7) by eq (1) and eq (2) to be 154 mAh/g (1240 F/g), 69 mAh/g (1063 F/g) and 25 mAh/g (960 F/g) at the current densities

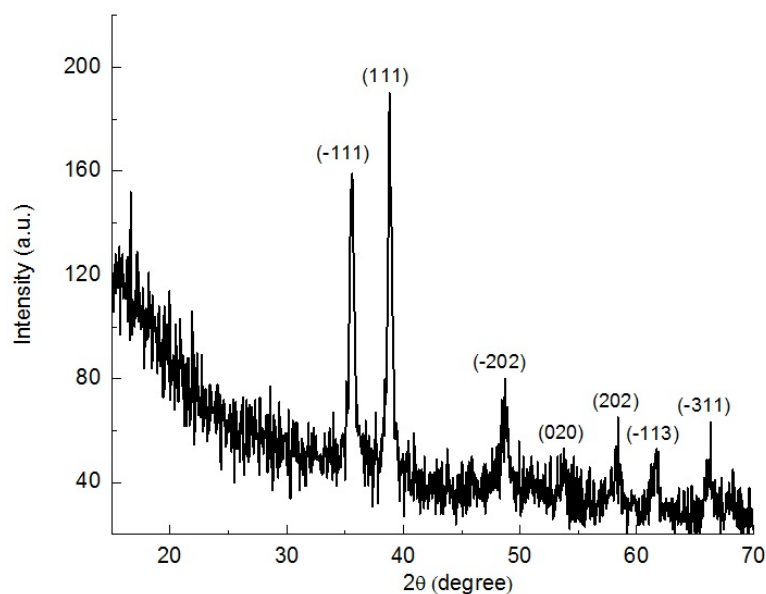


FIG. 3. XRD pattern of copper contained nanolayers

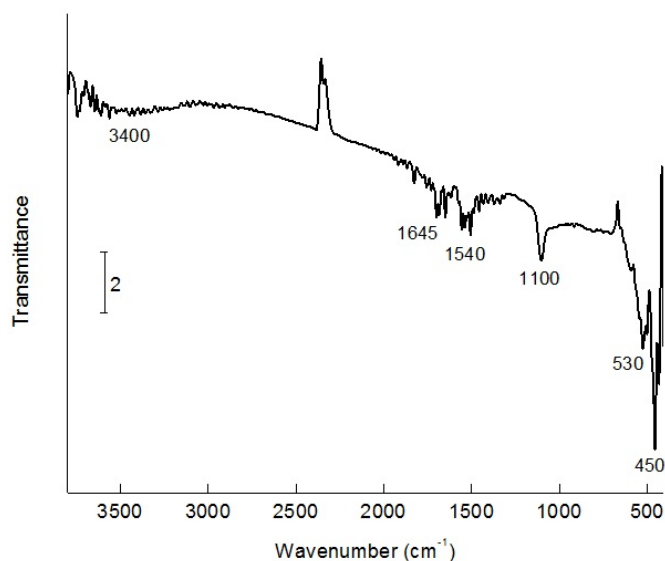


FIG. 4. FTIR transmission spectrum of copper contained nanolayers on silicon

of 1, 2 and 5 A/g, respectively. The high value of specific capacity can be explaining to good conductivity of CuO and also the significant contribution of nickel atoms in pseudocapacity for this sample.

Cyclic stability is also an important property for electroactive materials. The capacity retention of the NF electrode with Ni-doped CuO nanolayers after 1000 charge-discharge cycles at current density 2 A/g was kept 92% of its initial capacity (Fig. 8) that shows good cycling stability of this material. High cycling stability can be explained by the feature morphology of ultrathin nanocrystals of CuO which provide fast diffusion of ions on the electrode surface and while not being destroyed in discharge process.

We believe that these electrochemical capacity characteristics for electrodes of alkaline battery and pseudocapacitor based on Ni-doped CuO nanorods, synthesized via the SILD method, can be improved using a new scheme of their synthesis, including nanocomposite with carbon materials (CNT, graphene), the formation of which has been obtained after a new sequence of reagent treatment. However, these experiments fall outside the scope of the present paper. Undoubtedly, the synthesized nanolayers can also form a basis for effective electrodes of electrocatalysts and electrochemical sensors, etc.

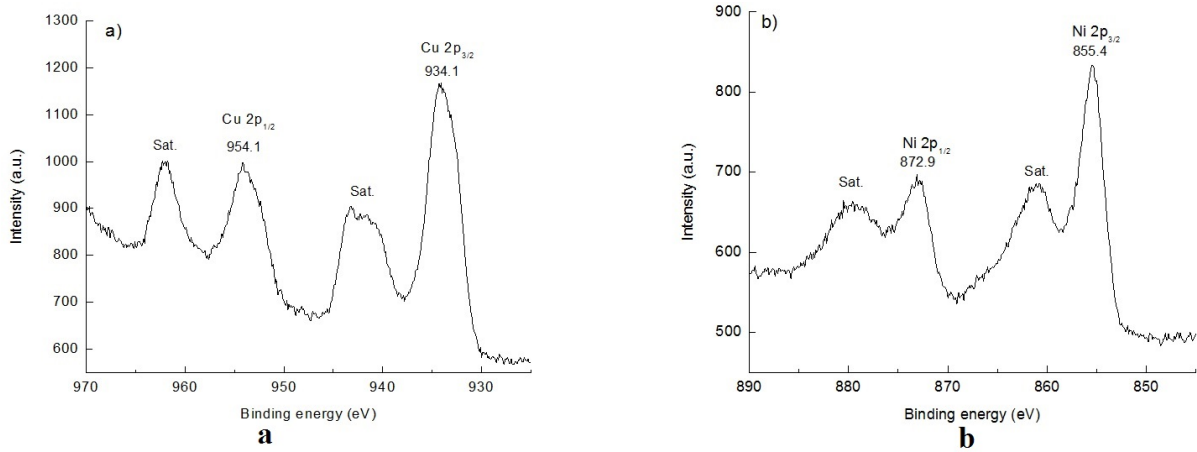


FIG. 5. XPS spectra Cu2p (a) and Ni2p (b) of copper contained nanolayers on the silicon surface

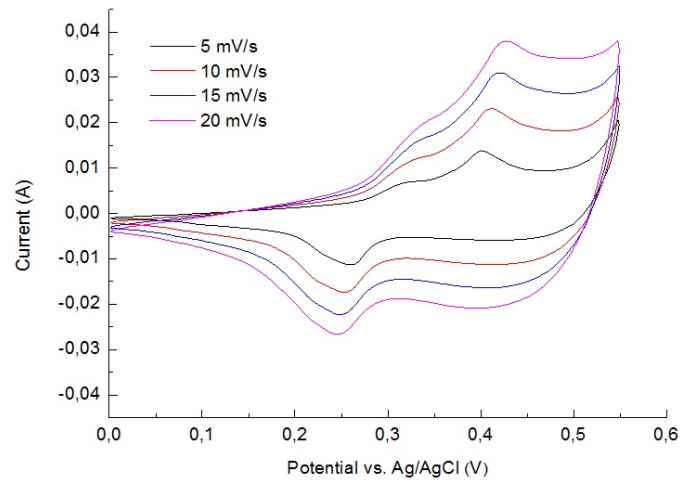


FIG. 6. CVA curves for NF electrode with Ni-doped CuO nanolayers at a scan rate of 5, 10, 15 and 20 mV/s

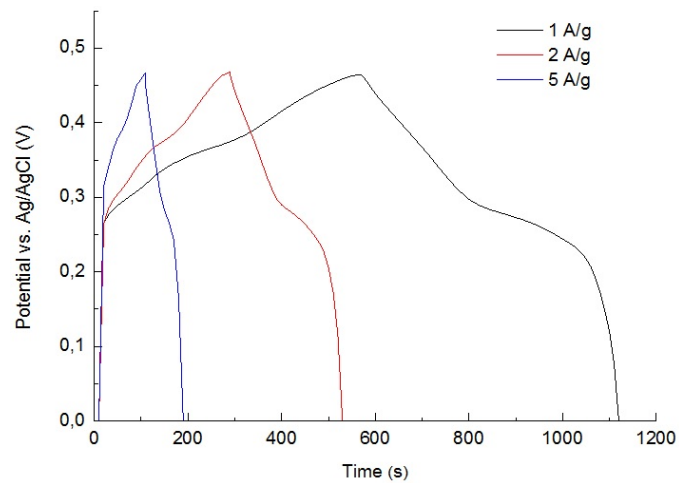


FIG. 7. Galvanostatic charge-discharge curves of the electrode with Ni-doped CuO nanolayers

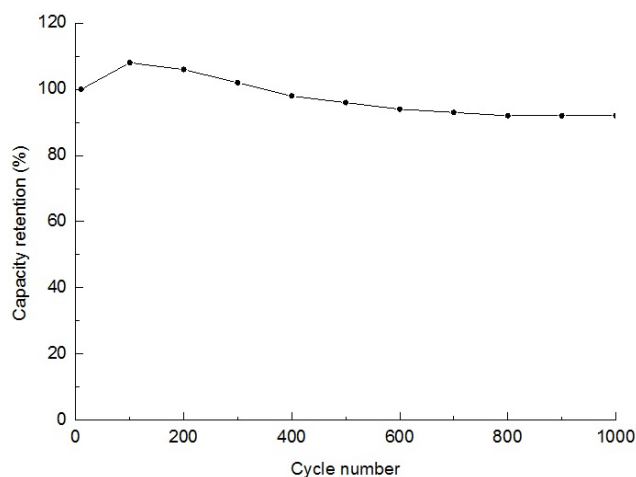


FIG. 8. The cycling stability for the NF electrode with Ni-doped CuO nanolayers at 2 A/g

#### 4. Conclusion

In summary, the possibility of obtaining Ni-doped CuO nanolayers via the SILD method using mixed copper and nickel ammonia aqueous solution and hydrogen peroxide solution was shown. The results show the synthesized nanolayers were formed nanocrystals of Ni-doped CuO the thickness of about 10–15 nm with nanorod morphology and the monoclinic tenorite crystal structure of CuO. The electrochemical study of Ni-doped CuO nanolayers-modified nickel foam electrodes, prepared by 30 SLID cycles, demonstrates that the specific capacitance is 154 mAh/g (1240 F/g) at a current density of 1 A/g. Repeated cycling for 1000 charge-discharge cycles demonstrates a relatively small 8% capacitance fade. The electrode based on Ni-doped CuO nanolayers had shown high energy density and the long-term electrochemical cycling stability. Thus this material can be a potential application as electroactive materials for alkaline battery and pseudocapacitors.

#### 5. Acknowledgments

This research was financial supported by the Grant of President of Russian Federation MK-2860.2019.3. The authors are grateful to the Centers for X-ray diffraction studies and Nanotechnology of Saint-Petersburg State University.

#### References

- [1] Zhong C., Deng Y., Hu W., Qiao J., Zhang L., Zhang J. A review of electrolyte materials and compositions for electrochemical supercapacitors. *Chem. Soc. Rev.*, 2015, **44**, P. 7484–7539.
- [2] Wang F., Wu X., Yuan X. et al. Latest advances in supercapacitors: from new electrode materials to novel device designs. *Chem. Soc. Rev.*, 2017, **46**, P. 6816–6854.
- [3] Meher S.K., Rao G.R. Ultralayered Co<sub>3</sub>O<sub>4</sub> for high-performance supercapacitor applications. *J. Phys. Chem. C*, 2011, **115**, P. 15646–15654.
- [4] Zhiyi Zhang, Qiuyue Gao, Haibo Gao, Zhenyu Shi, Junwei Wu, Mingjia Zhi, Zhanglian Hong. Nickel oxide aerogel for high-performance supercapacitor electrode. *RSC Adv.*, 2016, **6**, P. 112620–112624.
- [5] Zhu G., He Z., Chen J. et al. Highly conductive three-dimensional MnO<sub>2</sub>-carbon nanotube-graphene-Ni hybrid foam as a binder-free supercapacitor electrode. *Nanoscale*, 2014, **6**, P. 1079–1085.
- [6] Yang P., Ding Y., Lin Z. et al. Low-cost high-performance solid-state asymmetric supercapacitors based on MnO<sub>2</sub> nanowires and Fe<sub>2</sub>O<sub>3</sub> nanotubes. *Nano Lett.*, 2014, **14**, P. 731–736.
- [7] Choi C, Ashby D.S., Butts D.M. et al. Achieving high energy density and high power density with pseudocapacitive materials. *Nat. Rev. Mater.*, 2020, **5**, P. 5–19.
- [8] Liu Y., Cao X., Jiang D., Jia D., Liu J. Hierarchical CuO nanorod arrays in situ generated on three-dimensional copper foam via cyclic voltammetry oxidation for high-performance supercapacitors. *J. Mater. Chem. A*, 2018, **6**, P. 10474–10483.
- [9] Deepak P. Dubal, Girish S. Gund, Chandrakant D. Lokhande, Rudolf Holze. CuO cauliflower for supercapacitor application: Novel potentiodynamic deposition. *Materials Research Bulletin*, 2013, **48**, P. 923–928.
- [10] Mohammad Bagher Gholivand, HamidHeydari, Abbas Abdolmaleki, Hamid Hosseini. Nanostructured CuO/PANI composite as supercapacitor electrode material. *Materials Science in Semiconductor Processing*, 2015, **30**, P. 157–161.
- [11] Seyyed E Moosavifard, Maher F El-Kady, Mohammad S Rahmanifar, Richard B Kaner, Mir F Mousavi. Designing 3D highly ordered nanoporous CuO electrodes for high-performance asymmetric supercapacitors. *ACS Appl. Mater. Interfaces*, 2015, **7**(8), P. 4851–60.
- [12] Tolstoy V.P., Kodintsev I.A., Reshanova K.S., Lobinsky A.A. A brief review of metal oxide (hydroxide)-graphene nanocomposites synthesis by layer-by-layer deposition from solutions and synthesis. *Reviews on advanced materials science*, 2017, **49**(1), P. 28–37.
- [13] Lobinsky A.A., Tolstoy V.P., Gulina L.B. A novel oxidation-reduction route for successive ionic layer deposition of NiO<sub>1+x</sub>·nH<sub>2</sub>O nanolayers and their capacitive performance. *Materials Research Bulletin*, 2016, **76**, P. 229–234.

- [14] Lobinsky A.A., Tolstoy V.P. Synthesis of  $\gamma$ -MnOOH nanorods by successive ionic layer deposition method and their capacitive performance. *Journal of Energy Chemistry*, 2017, **26**, P. 336–339.
- [15] Lobinsky A.A., Tolstoy V.P. Red-ox reactions in aqueous solutions of  $\text{Co}(\text{OAc})_2$  and  $\text{K}_2\text{S}_2\text{O}_8$  and synthesis of CoOOH nanolayers by the SILD method. *Nanosystems: Physics, Chemistry, Mathematics*, 2015, **6**(6), P. 843–849.
- [16] Kodintsev I.A., Tolstoy V.P. Lobinsky A.A. Room temperature synthesis of composite nanolayer consisting of  $\text{AgMnO}_2$  delafossite nanosheets and Ag nanoparticles by successive ionic layer deposition and their electrochemical properties. *Materials Letters*, 2017, **196**, P. 54–56.
- [17] Kodintsev I.A., Martinson K.D., Lobinsky A.A., Popkov V.I. Successive ionic layer deposition of Co-doped  $\text{Cu}(\text{OH})_2$  nanorods as electrode material for electrocatalytic reforming of ethanol. *Nanosystems: Physics, Chemistry, Mathematics*, 2019, **10**(5), P. 573–578.
- [18] Kodintsev I.A., Martinson K.D., Lobinsky A.A., Popkov V.I. SILD synthesis of the efficient and stable electrocatalyst based on CoO-NiO solid solution toward hydrogen production. *Nanosystems: Physics, Chemistry, Mathematics*, 2019, **10**(6), P. 681–685.
- [19] Dmitriev D.S., Popkov V.I., Layer by layer synthesis of zinc-iron layered hydroxy sulfate for electrocatalytic hydrogen evolution from ethanol in alkali media. *Nanosystems: Physics, Chemistry, Mathematics*, 2019, **10**(4), P. 480–487.
- [20] Popkov V.I., Tolstoy V.P., Semenov V.G., Synthesis of phase-pure superparamagnetic nanoparticles of  $\text{ZnFe}_2\text{O}_4$  via thermal decomposition of zinc-iron layered double hydroxysulphate. *Journal of Alloys and Compounds*, 2020, **813**, P. 152179.
- [21] Tolstoy V.P., Lobinsky A.A., Levin O.V., Kuklo L.I. Direct synthesis of  $\text{Ni}_2\text{Al}(\text{OH})_{7-x}(\text{NO}_3)_x \cdot n\text{H}_2\text{O}$  layered double hydroxide nanolayers by SILD and their capacitive performance. *Materials Letters*, 2015, **139**, P. 4–6.
- [22] Tolstoy V.P., Lobinsky A.A. Synthesis of 2D Zn-Co LDH nanosheets by a successive ionic layer deposition method as a material for electrodes of high-performance alkaline battery-supercapacitor hybrid devices. *RSC Advances*, 2018, **8**, P. 29607–29612.
- [23] Liu Y., Cao X., Jiang D., Jia D., Liu J. Hierarchical CuO nanorod arrays in situ generated on three-dimensional copper foam via cyclic voltammetry oxidation for high-performance supercapacitors. *J. Mater. Chem. A*, 2018, **6**, P. 10474–10483.
- [24] Zhao H., Zhou X.X., Pan L.Y., Wang M., Chen H.R., Shi J.L. Facile synthesis of spinel  $\text{Cu}_{1.5}\text{Mn}_{1.5}\text{O}_4$  microspheres with high activity for the catalytic combustion of diesel soot. *RSC Adv.*, 2017, **7**, P. 20451–20459.
- [25] Xie J., Cao H., Jiang H., Chen Y., Shi W., Zheng H., Huang Y.  $\text{Co}_3\text{O}_4$ -reduced graphene oxide nanocomposite as an effective peroxidase mimetic and its application in visual biosensing of glucose. *Anal. Chim. Acta*, 2013, **796**, P. 92.
- [26] Zhangpeng Li, Jinqing Wang, Lengyuan Niu, Jinfeng Sun, Peiwei Gong, Wei Hong, Limin Ma, Shen-grong Yang Rapid. Synthesis of graphene/cobalt hydroxide composite with enhanced electrochemical performance for supercapacitors. *Journal of Power Sources*, 2014, **245**, P. 224–231.
- [27] Ethiraj A.S., Kang D.J., Synthesis and characterization of CuO nanowires by a simple wet chemical method. *Nanoscale Research Letters*, 2012, **7**(1), P. 70.
- [28] Xu L., Zhang H., Li J. at all. Designing core-shell  $\text{Ni}(\text{OH})_2$ @CuO nanowire arrays on 3D copper foams for high-performance asymmetric supercapacitors. *Chem. Electro Chem.*, 2019, **6**, P. 5462–5468.
- [29] Gui Chen, Lingjing Chen, Siu-Mui Ng, Tai-Chu Lau. Efficient chemical and visible-light-driven water oxidation using nickel complexes and salts as precatalysts. *Chem. Sus. Chem.*, 2014, **7**, P. 127–134.



# **NANOSYSTEMS:**

**PHYSICS, CHEMISTRY, MATHEMATICS**

## **INFORMATION FOR AUTHORS**

The journal publishes research articles and reviews, and also short scientific papers (letters) which are unpublished and have not been accepted for publication in other magazines. Articles should be submitted in English. All articles are reviewed, then if necessary come back to the author to completion.

The journal is indexed in Web of Science Core Collection (Emerging Sources Citation Index), Chemical Abstract Service of the American Chemical Society, Zentralblatt MATH and in Russian Scientific Citation Index.

### **Author should submit the following materials:**

1. Article file in English, containing article title, the initials and the surname of the authors, Institute (University), postal address, the electronic address, the summary, keywords, MSC or PACS index, article text, the list of references.
2. Files with illustrations, files with tables.
3. The covering letter in English containing the article information (article name, MSC or PACS index, keywords, the summary, the literature) and about all authors (the surname, names, the full name of places of work, the mailing address with the postal code, contact phone number with a city code, the electronic address).
4. The expert judgement on possibility of publication of the article in open press (for authors from Russia).

Authors can submit a paper and the corresponding files to the following addresses: nanojournal.ifmo@gmail.com, popov1955@gmail.com.

### **Text requirements**

Articles should be prepared with using of text editors MS Word or LaTeX (preferable). It is necessary to submit source file (LaTeX) and a pdf copy. In the name of files the English alphabet is used. The recommended size of short communications (letters) is 4-6 pages, research articles– 6-15 pages, reviews – 30 pages.

#### Recommendations for text in MS Word:

Formulas should be written using Math Type. Figures and tables with captions should be inserted in the text. Additionally, authors present separate files for all figures and Word files of tables.

**Recommendations for text in LaTeX:**

Please, use standard LaTeX without macros and additional style files. The list of references should be included in the main LaTeX file. Source LaTeX file of the paper with the corresponding pdf file and files of figures should be submitted.

References in the article text are given in square brackets. The list of references should be prepared in accordance with the following samples:

- [1] Surname N. *Book Title*. Nauka Publishing House, Saint Petersburg, 2000, 281 pp.
- [2] Surname N., Surname N. Paper title. *Journal Name*, 2010, **1** (5), P. 17-23.
- [3] Surname N., Surname N. Lecture title. In: Abstracts/Proceedings of the Conference, Place and Date, 2000, P. 17-23.
- [4] Surname N., Surname N. Paper title, 2000, URL: <http://books.ifmo.ru/ntv>.
- [5] Surname N., Surname N. Patent Name. Patent No. 11111, 2010, Bul. No. 33, 5 pp.
- [6] Surname N., Surname N. Thesis Title. Thesis for full doctor degree in math. and physics, Saint Petersburg, 2000, 105 pp.

**Requirements to illustrations**

Illustrations should be submitted as separate black-and-white files. Formats of files – jpeg, eps, tiff.



# **NANOSYSTEMS:**

**PHYSICS, CHEMISTRY, MATHEMATICS**

**Журнал зарегистрирован**

Федеральной службой по надзору в сфере связи, информационных технологий и массовых коммуникаций

(свидетельство ПИ № ФС 77 - 49048 от 22.03.2012 г.)

ISSN 2220-8054

**Учредитель:** федеральное государственное автономное образовательное учреждение высшего образования

«Санкт-Петербургский национальный исследовательский университет информационных технологий, механики и оптики»

**Издатель:** федеральное государственное автономное образовательное учреждение высшего образования

«Санкт-Петербургский национальный исследовательский университет информационных технологий, механики и оптики»

**Отпечатано** в Учреждении «Университетские телекоммуникации»

Адрес: 197101, Санкт-Петербург, Кронверкский пр., 49

**Подписка на журнал НФХМ**

На первое полугодие 2021 года подписка осуществляется через

ОАО Агентство «Роспечать»

Подписной индекс 57385 в каталоге «Издания органов научно-технической информации»